Modelling Removal of Sulphur Dioxide from Flue Gas in Purification Devices

Kristian Branimirov Kiradjiev

University College

University of Oxford

A thesis submitted for the degree of

Doctor of Philosophy

Trinity 2020

I dedicate this thesis to my family, who have always supported and inspired me in my endeavours.

Acknowledgements

Firstly, I would like to thank my academic supervisors, Prof. Christopher Breward and Prof. Ian Griffiths, for their endless enthusiasm, perseverance, and excellent insight.

Secondly, I am immensely grateful to my industrial supervisors Dr Uwe Beuscher and Dr Vasudevan Venkateshwaran from W. L. Gore and Associates, Inc., who introduced this problem and were an endless source of valuable insight regarding both the theoretical and practical issues involved. I would also like to thank Prof. Donald Schwendeman from the Rensselaer Polytechnic Institute, who has often helped me with various aspects of the problem.

This thesis is based on work partially supported by the EPSRC Centre for Doctoral Training in Industrially Focused Mathematical Modelling (EP/L015803/1) in collaboration with W. L. Gore and Associates, Inc., both of whom I would like to thank for their financial support.

Most importantly, I would like to thank my family, in particular, my wife, my parents, and my grandparents, for all their support. I could not have done it without you.

Abstract

Many chemical filters contain reactive components where harmful substances are removed or transformed. In this thesis, we consider the problem of removal of sulphur dioxide from flue gas using filters made from a porous catalytic medium. This is inspired by a filter, designed by W. L. Gore and Associates, Inc., which converts gaseous sulphur dioxide into liquid sulphuric acid via a chemical reaction that occurs on the surface of microscopic catalytic pellets. During the device operation, the liquid sulphuric acid accumulates within the filter and reduces its efficiency. We derive a series of mathematical models that explore various aspects of this problem and ultimately serve to predict the performance of the device. We begin by considering a fundamental fluid dynamics problem of spreading of a thin film under surface tension with liquid injection due to the chemical reaction. We then formulate a microscale model for the gas and liquid transport within the porous filter material and, separately, present a radially symmetric model for a single catalytic pellet, which we use to estimate the unknown reaction rate constant based on real observations. Although we do not explicitly account for the porous scaffold of the filter, the model set-up is appropriate for the case of hydrophobic material. We move on to upscale the microscale equations to a set of device-scale equations using homogenisation techniques. We obtain numerical solutions and asymptotic predictions for various limits that compare well, and also explore the effect of changing the system parameters, such as the gas speed, on the effective cleansing of flue gas. In addition, we develop a model for two neighbouring pellets, one of which is completely submerged by sulphuric acid, which is useful to understand the long-term behaviour of the system once a continuous layer of liquid forms near the surface of the filter sheets. We also study a simplified problem where the filter is made from hydrophilic material and identify the key differences in the resulting liquid transport. Finally, we present a model for the hygroscopy of sulphuric acid, which helps evaluate the effect of water absorption on the liquid growth within the filter. All the models we develop retain generality and can be applied to other physical and industrial processes.

Contents

List of Figures

Chapter 1

Introduction

1.1 Desulphurisation of Flue Gas

In the drive to protect the environment, reducing the concentrations of harmful chemicals that are released into the atmosphere has become a priority for industry. One key example is the removal of sulphur dioxide (SO_2) from flue (exhaust) gas. Sulphur dioxide is formed in vast quantities in industrial processes and power plants as a by-product of processing of raw materials such as coal, crude oil in refineries, and various ores in smelters (Fioletov *et al.*, 2016; Poullikkas, 2015; Sardar & Roy, 2015). In fact, more than half of the total sulphur dioxide emissions, or around $30,000\,\mathrm{kt/year}$, comes from man-made processes (see figure 1.1).

Sulphur dioxide is a highly toxic gas, which can cause acid rain and is linked to respiratory illnesses (Brown *et al.*, 2003; Sardar & Roy, 2015). According to Guttikunda & Jawahar (2014), 30–40% of the deaths in India in 2011 caused by power plants are attributed to SO_2 emissions. In order to decrease its concentration in flue gas before it is released into the atmosphere, filtering procedures such as wet and dry "gas scrubbing," where flue gas is sprayed with wet and dry reagents, respectively

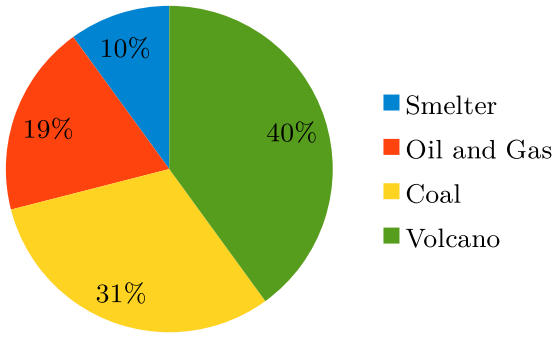

Figure 1.1: Sources of SO_2 (Dahiya & Myllyvirta, 2019).

(Damle, 1986; Hashemi *et al.*, 2019; Peschen, 2002), dry sorbent injection (Bourne *et al.*, 2018), membrane gas absorption (Klaassen, 2003), and packed-bed absorption (Jiang *et al.*, 2011) are often used. In all of these, SO_2 reacts with a sorbent substance, such as limestone in wet scrubbing, to form a new compound such as gypsum (Bourne *et al.*, 2018). However, most existing methods require high input power and the gas to be routed to a specific operation site within the plant where the desulphurisation is to be carried out (Mussatti, 2002). In addition, some of these processes are associated with the production of a large amount of waste, such as gypsum that contains impurities (Poullikkas, 2015). These processes cost between £100,000 and £400,000 per kilotonne of SO_2 removed (Bourne *et al.*, 2018). Thus, it is quite expensive and time-consuming for companies to remove SO_2.

1.2 Catalytic Filters

One specific type of technology used in flue gas desulphurisation is the catalytic filter. These are chemical filters that contain some catalyst, such as activated carbon particles, which are normally embedded in a porous structure to maximise the available surface area and, therefore, exposure to the unfiltered gas. This is different from the sorbent-injection scrubber methods in that the flue gas stream is not sprayed by sorbent but rather flows past it. Such technology is used, for example, in removal of sulphur dioxide, nitric oxides, and hydrogen sulphide (Breivik, 2020; Osaka *et al.*, 2015; Saracco & Specchia, 1995).

1.2.1 Structure of the GMCS Device

Our work is motivated by the Gore Mercury Control System (GMCS) device, designed by W. L. Gore and Associates, Inc., which captures gas-phase mercury via chemisorption processes and, in addition, removes sulphur dioxide from flue gas by catalytically converting it into liquid sulphuric acid (Knotts & Guenioui, 2017). This filtering device is made from stackable modules, each of which consists of a series of open channels made of folded porous sheets (see figure 1.2 for a schematic of a single module).

Each filter sheet contains multiple microscopic hydrophilic catalytic pellets that are held together by a network of hydrophobic fibres that can also be coated with hydrophilic material. Together with the catalyst, the fibrous matrix is referred to as a sorbent–polymer composite (SPC) (Knotts & Guenioui, 2017). Flue gas flows from one end of the filter to the other through the channels and diffuses into the porous

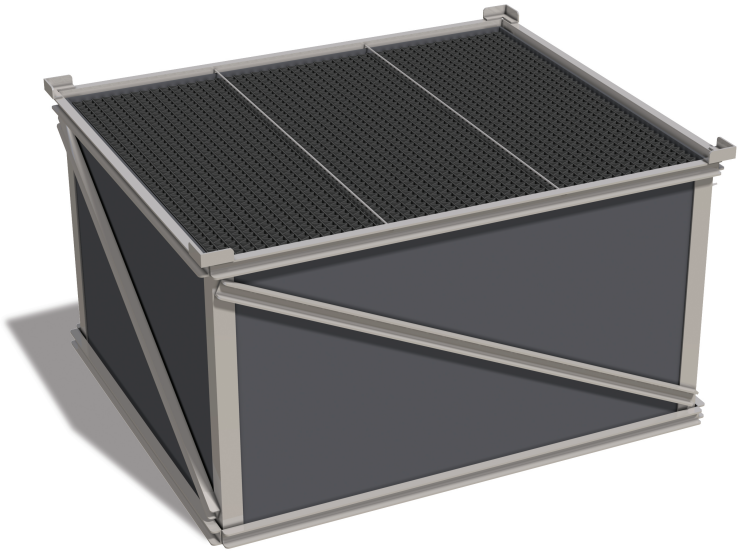

Figure 1.2: One module of the GMCS filter device (taken from Knotts & Guenioui, 2017).

sheets. We note that the entry of the gas from the channels into the filter sheets is by diffusion only, since no external pressure drop is imposed across the filter sheets. The catalyst in the sheets triggers a series of chemical reactions that turn sulphur dioxide together with oxygen and water vapour from the environment into liquid sulphuric acid. The sulphuric acid accumulates within the device and eventually seeps out from the surface of the filter sheets in the form of droplets. The droplets grow and slide down the channels walls under gravity when they become sufficiently large. The sulphuric acid is subsequently collected and stored away (see figure 1.3 for an illustration of the filter structure and a schematic of the filtration process).

1.2.2 Underlying Chemistry

In reality, there are multiple intermediate reactions that take place in the filter sheets (see, for example, Govindarao & Gopalakrishna, 1995; Mochida *et al.*, 1997) before acid is produced. These involve adsorption of sulphur dioxide to the catalyst, oxidation and formation of sulphur trioxide, and hydration, formation, and desorption of sulphuric acid. For simplicity and for the purposes of modelling, however, these steps can be summarised by the following single *effective* chemical reaction

$$2\,\mathrm{SO}_{2(\star)} + 2\,\mathrm{H_2O}_{(\star)} + \mathrm{O}_{2(\star)} \xrightarrow[k]{\text{carbon catalyst}} 2\,\mathrm{H_2SO}_{4(\mathrm{l})}, \tag{1.1}$$

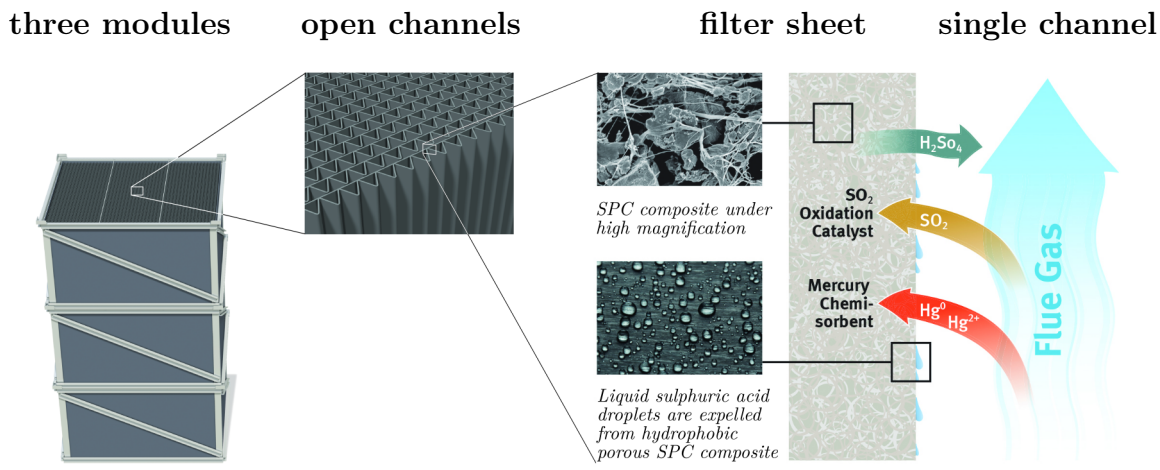

Figure 1.3: Three modules of the GMCS filter device and a schematic of the filtration process together with micrographs of the SPC composite and liquid sulphuric acid droplets on the surface of a filter sheet (taken from Knotts & Guenioui, 2017).

where k is the overall reaction rate taking into account all intermediate steps, and $(\star)$ denotes gaseous state (g) initially, before a liquid layer has formed around the catalytic pellet, and aqueous solution (aq) afterwards. This simplification allows us to formulate rate laws for the concentrations of the reactants with a single *effective* rate constant. In addition, under normal operating conditions, oxygen and water vapour are abundant during the filtration process, and so their concentrations can be taken to be constant. This means that a single rate law for the concentration of sulphur dioxide and a complementary law for liquid sulphuric acid accumulation is enough to describe the chemical kinetics from a modelling point of view. In general, for a multi-step reaction, we might expect a complex rate law, such as Michaelis-Menten kinetics, where the order of the reaction for all the chemicals cannot necessarily be defined in a unique way (Johnson & Goody, 2011). However, assuming that the concentrations of oxygen and water vapour are much larger than the concentration of sulphur dioxide, the assumed rate law for the reaction reduces to a simple mass action law for the sulphur dioxide concentration alone, where the relevant numerical coefficients in such an expression are given by the stoichiometry of the problem (Mochida *et al.*, 1997).

With regards to the reaction site, the activated carbon pellets used in the GMCS device are not solid but are porous. This means that the reaction happens on a larger surface area. Again, for simplicity, we may assume that the reaction happens on the surface of the pellets with an *effective* rate constant that takes into account the larger surface area of the substrate. In Martin *et al.* (2002), they describe the adsorbing capacity of various carbon catalytic beds to sulphur dioxide. They vary the catalyst mass and show the corresponding "breakthrough" curves of sulphur dioxide

concentration, i.e., profiles of the temporal evolution of the outlet sulphur dioxide concentration from zero to the concentration of the gas that is fed to the bed. As expected, they find that the total amount of adsorbed sulphur dioxide is proportional to the mass of the catalyst.

One prominent feature of the chemical reactions taking place in the porous filter sheets is the presence of a phase change from gaseous sulphur dioxide to liquid sulphuric acid. This gives rise to the existence of an evolving gas–liquid interface inside the porous medium. At thermodynamic equilibrium, balancing chemical potential on either side of the interface leads to Henry's law, which states that the sulphur dioxide concentration in the gas phase is proportional to the sulphur dioxide concentration in the liquid phase with a constant of proportionality known as the Henry's law constant (Sander, 2015). This means that, in a realistic mathematical model, we have to account for both the gas and the liquid domain and track the evolution dynamics of sulphur dioxide in both.

Another aspect of the chemical reaction that is worth discussing is the change in temperature. The oxidation of sulphur dioxide and water absorption by sulphuric acid (known as hygroscopy) are both exothermic reactions (Perry & Green, 1997), and so, in general, there is an increase in the temperature. However, in the context of catalytic filters used for flue gas, this change is limited to a few degrees in the case of the most polluted gases, since the concentration is not high enough to cause a substantial temperature change. Thus, assuming isothermal conditions is realistic. Furthermore, in an experimental reactor set-up at W. L. Gore and Associates, Inc., where the filtration process is recreated, they maintain isothermal conditions (Beuscher & Venkateshwaran, 2019).

An important chemistry aspect of the filtration process is that sulphuric acid is a hygroscopic substance, i.e., it absorbs water from the environment (House, 2013). This provides another mechanism for liquid accumulation within the filter apart from the sulphuric acid generation. This effect is directly dependent on the relative humidity of the environment, which may vary across different operating conditions.

1.2.3 Advantages and Challenges with the GMCS Device

There are a few notable benefits when using the GMCS device in flue gas purification, which makes it a desirable method for use in industrial plants (Knotts & Guenioui, 2017). These include

- Lower total cost of ownership – when considering the total maintenance costs, the GMCS device proves to be more cost-effective than regular scrubbers.

- Production of sulphuric acid "for free" – the chemical reaction in the filter produces liquid sulphuric acid of varying concentration (depending on the operating conditions, such as the relative humidity). It can subsequently be stored and used for commercial purposes or in other industrial applications, such as lead-acid (accumulator) batteries (Sander *et al.*, 1984). In addition, since sulphuric acid is continuously expelled from the filter sheets, facilitated by the hydrophobic fibrous matrix, it acts as a natural cleanser of the filter by removing external contaminant particles, such as dust.

- No generation of solid waste – this filter does not generate solid products, such as contaminated gypsum in scrubbing devices.

- Simultaneous removal of gas-phase mercury – the GMCS device also filters out toxic mercury from flue gas streams through the process of chemisorption with a long (order of months) storage capacity.

- Easy installation – the device consists of stackable modules, which can easily be assembled and placed across the stream of flue gas in a flue stack.

Despite all these positive attributes, the filter has one deficiency. As the chemical reaction proceeds within the filter sheets, liquid sulphuric acid accumulates in the void space (that is, the volume that is neither solid nor liquid) between the catalytic pellets and fibres and dramatically reduces the amount of sulphur dioxide that can be processed by the device, resulting in a drop in the device efficiency over time. Our aim is to understand the dynamics of the liquid and gas transport in the filter sheets during operation in order to gain insight into the details of the efficiency reduction and to be able to advise on an optimal operating regime. This modelling will be beneficial to W. L. Gore and Associates, Inc., since currently physical experiments with various filter designs are very expensive and time consuming to undertake. Rigorous and systematic mathematical analysis will provide the company with invaluable insight into the underlying system dynamics and develop necessary machinery for a simplified model that captures the essential characteristics of the problem without the need for overly expensive experimental tests and computational simulations. This analysis will then carry over to other systems, where similar filters made of porous catalytic media are being utilised.

1.2.4 Typical Parameter Values

In the first half of table 1.1, we present typical parameter values for the GMCS device operating regime, which are taken from Knotts & Guenioui (2017) and Beuscher & Venkateshwaran (2019). In addition, in the second half of the table, we list some well-known physical and chemical properties of sulphur dioxide, oxygen, and aqueous sulphuric acid, which we will exploit in our modelling.

Parameter	Definition	Value	Units
d	Radius of filter channels	5×10^{-3}	m
k	Rate of chemical reaction	6×10^{-5}	$\mathrm{m^4\,mol^{-1}\,s^{-1}}$
l	Inter-pellet distance	3×10^{-5}	m
C_0	Inlet concentration of oxygen in the filter channels	2	$\mathrm{mol\,m^{-3}}$
H	Thickness of filter sheets	10^{-3}	m
L	Length of filter channels	3×10^{-1}	m
R	Pellet radius	5×10^{-6}	m
S_0	Inlet concentration of sulphur dioxide in the filter channels	10^{-2}	$\mathrm{mol\,m^{-3}}$
U	Speed of gas flow in filter channels	3×10^{-1}	$\mathrm{m\,s^{-1}}$
W	Width of filter sheets	10^{-2}	m
β_c	Henry's law constant for oxygen	4×10	–
β_s	Henry's law constant for sulphur dioxide	4×10^{-2}	–
γ	Surface tension of sulphuric acid	7.5×10^{-2}	$\mathrm{N\,m^{-1}}$
μ	Viscosity of sulphuric acid	2×10^{-3}	Pa s
ρ	Density of sulphuric acid	1.83×10^{3}	$\mathrm{kg\,m^{-3}}$
D_{c_g}	Diffusivity of oxygen in flue gas	1.6×10^{-5}	$\mathrm{m^2\,s^{-1}}$
D_{c_l}	Diffusivity of oxygen in aqueous sulphuric acid	2.2×10^{-9}	$\mathrm{m^2\,s^{-1}}$
D_{s_g}	Diffusivity of sulphur dioxide in flue gas	1×10^{-5}	$\mathrm{m^2\,s^{-1}}$
D_{s_l}	Diffusivity of sulphur dioxide in aqueous sulphuric acid	2×10^{-9}	$\mathrm{m^2\,s^{-1}}$
$M_{\mathrm{SO_2}}$	Molar mass of sulphur dioxide	6.4×10^{-2}	$\mathrm{kg\,mol^{-1}}$
V_{m}	Molar volume of sulphuric acid	5×10^{-5}	$\mathrm{m^3\,mol^{-1}}$

Table 1.1: Parameter values (taken from Beuscher & Venkateshwaran, 2019; Ferrell & Himmelblau, 1967; Govindarao & Gopalakrishna, 1993; Hayduk *et al.*, 1988; Hetherington, 1968; Kaskiala, 2002; Knotts & Guenioui, 2017; Leaist, 1984; Massman, 1998; Perry & Green, 1997; Rattigan *et al.*, 2000; Rohling *et al.*, 2007; Sanaei & Ciocanel, 2016; Zhang *et al.*, 1998).

We note that the rate of chemical reaction, k, introduced in this table, is an effective rate, and its value is determined indirectly from experimental data using a

procedure described in Section 3.5. The inter-pellet distance, l, may vary slightly depending on the porous material used, but the order of magnitude is the same (Beuscher & Venkateshwaran, 2019). The length of the filter channels, L, may be increased as much as necessary by stacking filter modules on top of each other. Usually, it can be increased up to the order of metres; the value presented in table 1.1 is for a single filter module. In terms of inlet concentrations, there is little variation in the oxygen concentration, C_0, whereas the sulphur dioxide concentration, S_0, may vary by an order of magnitude depending on the degree of contamination of flue gas (Beuscher & Venkateshwaran, 2019).

Henry's law constant can be expressed as a ratio of various quantities, including partial pressure and concentration. We use its dimensionless representation, namely, the ratio of sulphur dioxide concentration in the gas to that in the liquid. A further discussion on the various expressions of the Henry's law constant and how to convert between them can be found in Appendix A.

The surface tension, viscosity and diffusivities depend on the ambient temperature (Ferrell & Himmelblau, 1967; Leaist, 1984; Massman, 1998; Perry & Green, 1997; Rhodes & Barbour, 1923; Suggitt *et al.*, 1949; Young & Grinstead, 1949), but this dependence is weak in the temperature range relevant to the operating conditions of the filter.

Finally, the molar volume of sulphuric acid, V_{m}, refers to the volume occupied by one mole of liquid sulphuric acid.

1.3 Summary of Methodology and Mathematical Techniques

We aim to derive mathematical models that describe the operation of catalytic porous filters, and apply these to study desulphurisation of flue gas by the GMCS device. The physical and chemical nature of the problem motivate the use of reaction–advection–diffusion and reaction–diffusion equations to describe the evolution of the gaseous chemical concentrations. The phase change in the reaction means that there will be a moving gas–liquid interface, and, thus, in general, we will have a free-boundary problem in a porous medium along with liquid production. Since we will be dealing with porous domains, one possible approach will be to use techniques from mathematical homogenisation, whereby we systematically upscale the governing equations that hold on the complicated microscale to obtain effective macroscale equations that describe the overall system behaviour and still capture the effect of the underlying

microstructure (see, for example, Bensoussan *et al.*, 1978; Bruna & Chapman, 2015; Hornung, 1997). We are also interested in a careful and more detailed investigation of the problem on the pellet scale, and, in particular, how capillarity affects the liquid flow. Due to the small length scale, gravity and inertia are not important (the relevant Reynolds and Bond numbers are small), and the governing equations will be Stokes equations. We will also make further simplifications due to the geometry and will use the lubrication approach (see, for example, Howison, 2005). Throughout the thesis, we will make use of matched asymptotic expansions to obtain simplified problems that accurately represent the behaviour of the full problems but are significantly computationally cheaper to solve, and, hence, of good value to industrialists. For a general review of asymptotic techniques, see, for example, Bender & Orszag (1999). We will also explore the case of flow through filter sheets composed of hydrophilic fibres. This will call on the use of mathematical tools for flow in saturated–unsaturated media, and, in particular, Darcy's law and Richards equation for unsaturated flow of two immiscible phases, namely, gas and liquid in our case (see, for example, Bear, 1979).

1.4 Literature Review

Although various models exist for other purification methods, including gas scrubbing (Damle, 1986; De Blasio *et al.*, 2013; Hashemi *et al.*, 2019; Kiil *et al.*, 1998; Michalski, 2001) and absorption (Cao & Nastac, 2019; Qi & Cussler, 1985), reactive-pellet chemical filters that involve a phase change of the contaminant are less well studied. Mochida *et al.* (1997) study the removal of sulphur dioxide using activated carbon fibres, again producing sulphuric acid. They develop a power-law model for the chemical kinetics to describe the concentration of sulphur dioxide at the outlet of the device and find that the rate of sulphur dioxide conversion is proportional to the weight of the catalyst and to a specific power of the starting concentrations of sulphur dioxide, oxygen, and water vapour. In addition, they assert that the rate-limiting step of the reaction is the dissociation of sulphuric acid into an aqueous solution around the carbon. Similar findings appear in Gaur *et al.* (2006), where they develop a detailed kinetic model and then describe the evolution of the gas concentration. They observe that increasing the inlet sulphur dioxide concentration or decreasing the oxygen and water-vapour concentrations increases the outlet concentration of sulphur dioxide. In neither of these models is the evolution of the liquid sulphuric acid explicitly modelled. Furthermore, in the second model the functional form of the concentration of

sulphur dioxide in the fibre pores is assumed, and, in addition, the governing equations, which make use of an effective take-up rate of sulphur dioxide, are derived from a simple averaging over the pore domain. A summary of various similar models for breakthrough-time predictions, i.e., the time it takes for the effluent gas concentration to reach a specific pre-determined value, for gas removal using catalysts can be found in Vizhemehr (2014). In Kiss *et al.* (2010), they present a mass- and energy-balance mathematical model of a multi-component converter in an industrial sulphuric acid plant. They do not explicitly account for the microscale dynamics and the effect of liquid generation but rather use simple one-dimensional reaction–advection–diffusion equations with bulk reaction rates fitted to data. They simultaneously model multiple components of the catalytic reactor and, based on their numerical solutions, determine optimal flow rates of the gas in each of the components. Similar modelling has been conducted by Güthenke *et al.* (2007) and Chen & Tan (2012) in the context of the removal of nitric oxides. In the first of these, a one-dimensional model of a catalytic monolith (reactor) is presented that can be applied to a passenger car for minimising nitric oxides emissions. They use a global kinetic approach incorporating 22 reactions that describe the whole conversion and storage problem using again bulk reaction rates. Chen & Tan (2012) consider a three-dimensional model of a porous solid catalyst for the removal of nitric oxides and solve this using finite-element software. They use Brinkman equation (Brinkman, 1949) for the flow through the porous medium and mass-balance equations with constant bulk reaction terms fitted to data to find the optimal concentration ratio of reacting gases, flow speed, and temperature that maximise removal.

Other previous relevant theoretical work, where the problem of sulphur dioxide removal from flue gas has been studied in the context of porous catalytic media, includes Anderson *et al.* (2015) and Sanaei & Ciocanel (2016). Part of the work in Sanaei & Ciocanel (2016) involves analysis of a one-dimensional microscale problem of liquid film growth on top of a single catalytic region considering only sulphur dioxide concentration as a dependent variable. This is coupled with a simple macroscale model of advection–diffusion of the flue gas. The filter efficiency is shown to decrease with time as a result of gradual filter blockage in this set-up. This model, however, uses simple volume averaging to account for multiple catalysts and ignores the spatial effect of the filter sheets thickness on the gas diffusion and liquid evolution. Furthermore, in the same paper, a network model is presented, in which the filter fibres are modelled as slender flexible rods. They predict how compression of the fibrous material affects various transport parameters. In Anderson *et al.* (2015), there is a detailed local

model of the chemical reactions that take place on the surface of the catalytic pellets, accounting for intermediate steps and number of active sites on the pellet, and an expression for the rate of change of sulphuric acid volume is derived. Similarly to the model in Sanaei & Ciocanel (2016), they couple the local model to a simple advection–diffusion equation for the flue gas in the filter channels. They obtain numerical solutions for a reduced model and track the sulphur dioxide concentration within the device. However, they consider a one-dimensional microscale model and again simple volume averaging is used to arrive at the device-scale equations rather than a careful treatment of the effect of the evolving porous microstructure. An initial network model, based on mass balance, is also briefly considered without accounting for transfer of liquid between nodes.

A relevant problem of desulphurisation of natural gas for fuel cells has been studied in Campbell & Edwards (2015). They consider catalytic removal of sulphur, in which there is only adsorption without liquid generation. A careful analysis of separation of timescales at the pore-level and device-level is presented, and the chemical kinetics explicitly incorporate the effect of the number of active sites on the catalytic pellets. Various asymptotic results are derived for the cases of fast and slow reaction compared to diffusion.

There has also been some work on catalytic filters represented as discrete networks. The general idea is to split the porous sheets into "cells/nodes" that are connected by "throats". Local mass conservation provides the "rules" describing how liquid moves from one cell to another by, for example, appealing to capillary pressure considerations and wettability properties of the porous medium (see, for example, Andrade Jr. *et al.*, 1997; Blunt *et al.*, 1992; Wilmott, 2018; Xiong *et al.*, 2016). The work in Ben-Avraham (1991) and Blunt (2001) provides an overview of diffusion processes in porous structures with catalytic reactions taking place on the solid surface, and uncovers the major role that porous structure of a medium plays on the effectiveness of advection and diffusion and properties such as wettability of the media in multiphase flow. A detailed study of relevant percolation theory concepts and numerical methods for simulating flow in porous media is given in Sahimi *et al.* (1990). The continuum methods presented are, in general, easier to describe and give adequate understanding of solid–liquid interactions in porous media. However, statistical approaches may be easier to implement for describing topological changes in the media as a result of the reactions that take place. Pure statistical methods are also used in evaluating models, as, for example, in Smith *et al.* (2020), where they use machine

learning to explore predictability of catalytic activity from experimental data and find strong predictability across reaction conditions, such as varying temperature.

One approach to studying the physics and chemistry of these reactive filters is to solve a detailed model of the microscale, using an appropriate software package, on the whole device. However, this would be computationally infeasible for realistic filter sizes. Instead, we will appeal to homogenisation theory (see, for example, Bensoussan *et al.*, 1978; Bruna & Chapman, 2015; Hornung, 1997) and upscale the equations that hold on the scale of a catalytic pellet to obtain an averaged model on the macroscale that captures all the microscale physics. A comprehensive review of multiscale modelling in reactive porous media can be found in Molins & Knabner (2019).

Relevant previous work on homogenised models involving reaction–diffusion processes in the bulk of a porous medium have also been studied in Allaire & Piatnitski (2010); Chernyavsky *et al.* (2011); Conca *et al.* (2004); Dalwadi *et al.* (2018); Gahn *et al.* (2016); Meier *et al.* (2007); Peter & Böhm (2009) and Schulz & Knabner (2017). Specific applications amongst these include nutrient transport in porous materials and bioreactors, flows in granular material, and formation and growth of biofilms. The modelling approach is to assume certain sources/sinks due to reactions between one or more species in one of the phases and impose a flux condition on the interface with another phase to describe the adsorption kinetics. The objective is to obtain an upscaled system of equations describing the dynamics of the reacting species. Relevant previous work where chemical reactions are restricted to the interface between two phases residing in a porous medium is contained in Allaire *et al.* (2010); Dalwadi *et al.* (2016, 2015); Luckins *et al.* (2019); Valdés-Parada *et al.* (2017) and Ray *et al.* (2015), where reaction–diffusion equations are coupled with flow problems in porous materials to study processes, such as filtration and decontamination. A similar class of models can describe the growth, precipitation and dissolution of materials, such as crystals and biofilms (see, for example, Bringedal *et al.*, 2016; Bringedal & Kumar, 2017; Fasano & Mikelić, 2000; Landa-Marbán *et al.*, 2020; Peszynska *et al.*, 2016; Ray & Schulz, 2019; van Noorden, 2009*b*,*a*; van Noorden *et al.*, 2010). The objective here is to obtain effective upscaled equations that describe the evolution and deformation of the porous media subject to fluid flow as reactions take place on the interface between the porous scaffold and the fluid. We will discuss the mathematical features of these models in more detail in Section 3.

In a different approach, Chapman & Shabala (2017) and Kropat & Meyer-Nieberg (2012), for example, use a discrete version of homogenisation on a network represen-

tation of a porous medium with reaction–advection–diffusion phenomena. Using periodicity of the underlying microstructure, effective transport properties of the fluid flow are derived.

1.5 Overview

In this thesis, we will develop and analyse models for various aspects of the flue gas desulphurisation process using reactive porous filters. We begin by considering a model problem in Chapter 2 that contains key ingredients of the full problem posed by W. L. Gore and Associates, Inc. and allows us to gain insight into some of the physical phenomena that take place within the GMCS device. We then move on to modelling the operation of the GMCS device in Chapters 3, 4, 5, and 6.

In Chapter 2, we consider a fundamental fluid dynamics problem of injection- and surface-tension-driven spreading of a thin viscous film on a flat substrate. This problem mimics the liquid sulphuric acid generation on the surface of a catalytic pellet and its subsequent flow along a hydrophilic fibre. Here, we derive and solve the governing equations for various injection rates, and obtain asymptotic predictions for the spreading behaviour at early and late times. We then couple this problem with diffusion of sulphur dioxide through the liquid to model a realistic reaction.

In Chapter 3, we use mathematical homogenisation to derive a three-dimensional microscale model for the operation of the GMCS device, and, in fact, any other porous reactive filter that operates in a similar fashion. Although we do not explicitly incorporate the effect of the porous material on the liquid flow, this model is suitable for the case when the porous scaffold is made from hydrophobic material, as in the real GMCS device. We also consider a separate model for liquid sulphuric acid growth around a single catalytic pellet. The aim is to use this model to obtain an estimate for the reaction rate constant using data provided by W. L. Gore and Associates, Inc.

In Chapter 4, we upscale the governing microscale equations for the sulphur dioxide concentration and amount of liquid sulphuric acid to obtain a device-scale model that describes the behaviour of the filter sheets until clogging. We consider various asymptotic limits and possible regimes of operation in a simplified geometry. In order to evaluate the long-term effect of forming a continuous liquid layer near the surface of the filter sheets on the liquid and gas transport deeper into the sheets, we then consider the problem of two neighbouring pellets, where, initially, the first one is completely submerged in liquid sulphuric acid while the second one is coated with a layer of sulphuric acid. We track the relative motion of the flat gas–liquid interface

away from the submerged pellet as sulphur dioxide is converted to sulphuric acid on the pellet surface, and the growth of the spherical interface around the second pellet.

In Chapter 5, we present a simplified model for a porous reactive filter composed of hydrophilic fibres. We derive a model for saturated–unsaturated fluid flow, based on Darcy's law and Richards equation and elucidate the effects the hydrophilicity of the porous medium plays on the fluid transport within the device.

We devote Chapter 6 to investigating the effect of the hygroscopy of sulphuric acid on the liquid accumulation within the filter. Here, we derive a one-dimensional model and validate it through a set of experiments performed at W. L. Gore and Associates, Inc. We use this to estimate the rate of growth of a moisture-absorbing aqueous sulphuric acid layer. We also formulate a microscale model, analogous to the model considered in Chapter 3, which incorporates hygroscopy of sulphuric acid. Finally, we draw conclusions, outline possible future work, and discuss various implications of our work in Chapter 7.

1.6 Statement of Originality

The research presented in this thesis was conducted between October 2017 and July 2020 at the Mathematical Institute, University of Oxford under the supervision of Professors Chris Breward and Ian Griffiths with additional guidance from Professor Donald Schwendeman from the Rensselaer Polytechnic Institute, and Dr Uwe Beuscher and Dr Vasudevan Venkateshwaran from W. L. Gore and Associates, Inc.

Most of the material in Chapter 2 has been published in the *Journal of Fluid Mechanics* (Kiradjiev *et al.*, 2018), and most of the material in Chapters 3 and 4 has been accepted for a publication in the *SIAM Journal on Applied Mathematics* (Kiradjiev *et al.*, 2020*a*). Most of the material on hygroscopy in Chapter 6 has been published in *Industrial & Engineering Chemistry Research* (Kiradjiev *et al.*, 2020*b*). The remaining material in these chapters is also original work or extensions to these journal articles. The experimental data on hygroscopy in Chapter 6 was provided by W. L. Gore and Associates, Inc., and this is acknowledged. Chapter 5 and Chapter 7 are original work.

Chapter 2

Surface-Tension- and Injection-Driven Spreading of a Thin Viscous Film

The microscale problem for the GMCS filtering device involves liquid generation on the surface of catalytic pellets and the subsequent drainage through a network of fibres that connect the pellets within the filter sheets. Inspired by this, we investigate a fundamental problem in fluid dynamics, where a thin film spreads along a rigid substrate under the influence of surface tension, with injection of liquid from a finite-width region on the substrate. Our aim is to gain insight into the evolution dynamics of such a system and will then couple this with diffusion of sulphur dioxide through the liquid and reaction on the substrate to capture the reaction kinetics in the filter.

2.1 Introduction

Surface-tension-driven thin-film flows arise in a wide range of physical applications. For example, they are crucial in understanding the spreading of liquid films (Oron *et al.*, 1997; Craster & Matar, 2009; Zheng *et al.*, 2018), drying of paints (Howison *et al.*, 1997), biological processes such as coating of the internal sides of the airways (Halpern & Grotberg, 1992) and spreading of liquid on the eye (Bruna & Breward, 2014), contact-lens manufacture (Murphy & Lee, 2017), a vast variety of coating processes in industry (Wilson, 1982; Howell *et al.*, 2013) including spin-coating (Fraysse & Homsy, 1994; Wilson *et al.*, 2000), and spreading of chemical reaction fronts in liquids (Guzman & Vasquez, 2016). While the spreading of a fixed volume of fluid is well-studied (see, e.g., Voinov (1976), Hocking (1980), Lacey (1982), Hocking (1983), Cox (1986), Ehrhard & Davis (1991), Hocking (1992), King & Bowen (2001), Bonn *et al.* (2009), Savva & Kalliadasis (2009), Howell (2010), Ajaev (2012), Savva & Kalliadasis (2013)), the analysis of thin-film flows with sources and sinks is much less

common. These flows arise in numerous interesting applications, such as oozing of lava from a volcanic crater (Schwartz & Michaelides, 1988), spreading of films on a porous bed such as textile fabric (Davis & Hocking, 1999, 2000; Mason & Momoniat, 2004; Thompson *et al.*, 2015), and droplet spreading with evaporation (Anderson & Davis, 1995; Oliver *et al.*, 2015; Saxton *et al.*, 2016). Injection-spreading problems have been studied in the case when gravity is the driving force for thin-film source flow on an inclined plate (Smith, 1973; Huppert, 1982; Schwartz & Michaelides, 1988; Lister, 1992), and numerical and similarity solutions have been obtained for the resulting film thickness profile. In particular, Huppert (1982) considers the case of a time-dependent source. Duffy & Moffatt (1997) study a three-dimensional gravity-driven source flow down an almost vertical plane with surface-tension effects included in the steady-flow regime. They find power-law dependencies on the distance down the plane for the width and the height of the resulting film. Further analysis of gravity-driven rivulet flow of Newtonian and power-law fluids down an inclined plane is given in Yatim *et al.* (2010), whereas shear-stress-driven flow is considered in Yatim *et al.* (2012). Corresponding travelling-wave similarity solutions are found in Yatim *et al.* (2013). Momoniat *et al.* (2010) consider a similar problem but for radially symmetric spreading with an annular injection slot and investigate the flow behaviour numerically. In Mason & Momoniat (2004) and Momoniat & Mason (2007), symmetry methods from Lie algebras are used to study thin-film flow with injection/suction acting over a porous bed. The related problem of the flow of a viscous film with injection on an inclined porous plane is studied by Thompson *et al.* (2015). Here, both surface tension and gravity are included, but the spatial variations of the source term are assumed to be periodic and have zero mean, so that steady-state solutions can be analysed. In addition, the linear stability of these steady states is considered, which reveals that suction and blowing can either increase or decrease the critical Reynolds number for linear stability of these steady states. Problems involving thin-film flow with injection of liquid are also studied in the context of elasticity. A concise treatment of the problem of determining the spreading behaviour of a continuously injected viscous fluid under an elastic sheet is presented in Lister *et al.* (2013). Here, the process under consideration is the peeling of the sheet by bending and pulling at the front facilitated by the injected liquid, and they derive specific propagation laws (governed by the effect of elasticity of the covering membrane) with power-law dependence on time. They also assume the viscous film is situated over a thin pre-wetted layer. A similar problem is considered in Zheng *et al.* (2015), where buoyancy-driven

spreading of a thin film over a membrane with constant injection of liquid is studied. Neglecting the effect of surface tension, they obtain similarity solutions for the position of the liquid front for late time.

A comprehensive review of thin-film equations and spreading is given in Myers (1998), where various thin-film equations are derived. There is a well-known stress singularity at the moving contact line, which is often regularised by assuming that there is a precursor layer that pre-wets the substrate and removes the singularity. Such precursor layers are also experimentally observed in many physical systems (Bonn *et al.*, 2009; Ajaev, 2012). Another common regularisation is the slip regularisation, where the liquid is allowed to slip along the substrate following a linear relationship between the velocity and the shear stress (see, for example, Münch *et al.*, 2005). A comparison between different regularisations (in particular, slip and precursor regularisations) is presented in Savva & Kalliadasis (2011) and Sibley *et al.* (2015). The authors conclude that, for certain parameter regimes, these regularisations lead to equivalent droplet-spreading behaviours. Asymptotic results for the depth and extent of a steady thin-film flow down an inclined plane that is pre-wetted with a thin precursor layer are given in Benilov *et al.* (2010). In our work, we will be guided by the results obtained in King & Bowen (2001), in which they analyse a general mass-preserving surface-tension-dominated lubrication equation with a very thin precursor layer. However, their results only hold for the spreading of a fixed volume of fluid and do not account for injection of liquid. Lacey (1982) takes a different approach by assuming a slip regularisation, and derives asymptotic results for the spreading of a viscous droplet due to surface tension for late time. Anderson & Davis (1995) consider steady and unsteady spreading of an evaporating droplet on a heated surface. They find a relationship between the contact angle and the rate of evaporation, and use asymptotic analysis in the large-capillary-number regime to determine the shape of the droplet. Oliver *et al.* (2015) consider the surface-tension-driven spreading of a partially wetting drop, assuming a slip regularisation, with mass transfer along the entire free surface of the resulting film and, in particular, at the contact line. This leads to appropriate generalisations of Tanner's law. Similar results are obtained in Saxton *et al.* (2016), where the effect of evaporation on the evolution of the contact-set radius is studied, while in Saxton *et al.* (2017), vapour transport and kinetic effects are used to regularise the mass-flux singularity at the contact line in an evaporating spreading droplet.

In this chapter, we will study the surface-tension-driven flow of liquid from a finite-width injection region over a precursor layer, inspired by the microscale problem of

liquid generation around catalytic pellets in the GMCS device. We will explore the problem in which the precursor thickness tends to zero. Initially, we will consider the situation where the production rate is constant, and, therefore, the possibility of a steady state is ruled out. In Section 2.2, we formulate our model, explain and employ the precursor-layer regularisation and then non-dimensionalise the equations. In Section 2.3, we present our asymptotic analysis of the problem for early and late time, and briefly consider the $O(1)$-time problem. We will look for power-law predictions for the film thickness in the centre of the injection region, where it attains its maximum, and for the position of the apparent contact line in these temporal regimes. We will present numerical solutions to the full problem and compare them with the asymptotic predictions in Section 2.4. In Section 2.5 and Section 2.6, we will consider generalisations to our problem, in which we take more general time- and thickness-dependent source functions, respectively. Further, for power-law-in-time injection, we will suggest a way of predicting the power-law exponent by examining the film thickness profile and the position of the apparent contact line. Finally, in Section 2.7, we present a coupled model that takes into account diffusion and reaction of sulphur dioxide and oxygen. We draw conclusions in Section 2.8.

2.2 Mathematical Model

2.2.1 Formulation of the Problem

We consider an infinite one-dimensional substrate, on which viscous liquid is injected uniformly through the surface in the region $|\hat{x}| \leq L_R$ at a constant speed W. We let $\hat{x}$ measure the distance along the substrate and $\hat{z}$ measure the distance perpendicular to the substrate, and we show a schematic of the geometry under consideration in figure 2.1. We expect the reduced Reynolds number to be very small for flows of practical interest in purification devices, and so, we ignore the effect of inertia. Further, assuming that gravity can also be neglected, the flow is surface-tension driven and governed by Stokes' equations

$$-\nabla\hat{p} + \mu\nabla^2\hat{\boldsymbol{u}} = 0, \tag{2.1}$$

$$\nabla \cdot \hat{\boldsymbol{u}} = 0, \tag{2.2}$$

where $\hat{\boldsymbol{u}} = (\hat{u}, \hat{w})$ is the fluid velocity, $\hat{p}$ is the pressure, and μ is the viscosity of the liquid. We have the following no-slip[1], kinematic and stress boundary conditions,

$$\hat{u} = 0 \qquad \text{on} \qquad \hat{z} = 0, \tag{2.4}$$

$$\hat{w} = W\Theta\left(L_R - |\hat{x}|\right) \qquad \text{on} \qquad \hat{z} = 0, \tag{2.5}$$

$$\hat{w} = \frac{\partial \hat{h}}{\partial \hat{t}} + \hat{u}\frac{\partial \hat{h}}{\partial \hat{x}} \qquad \text{on} \qquad \hat{z} = \hat{h}(\hat{x}, \hat{t}\,), \tag{2.6}$$

$$\hat{\boldsymbol{n}} \cdot \hat{\boldsymbol{T}} \cdot \hat{\boldsymbol{n}} = \gamma(-\nabla \cdot \hat{\boldsymbol{n}}) = \gamma \frac{\partial^2 \hat{h}}{\partial \hat{x}^2} \left(1 + \left(\frac{\partial \hat{h}}{\partial \hat{x}}\right)^2\right)^{-3/2} \qquad \text{on} \qquad \hat{z} = \hat{h}(\hat{x}, \hat{t}\,), \tag{2.7}$$

$$\hat{\boldsymbol{n}} \cdot \hat{\boldsymbol{T}} \cdot \hat{\boldsymbol{t}} = 0 \qquad \text{on} \qquad \hat{z} = \hat{h}(\hat{x}, \hat{t}\,), \tag{2.8}$$

where $\Theta(\hat{x})$ is the Heaviside step function, $\hat{\boldsymbol{t}}$ and $\hat{\boldsymbol{n}}$ are the unit tangent and outward-pointing normal vectors to the free surface $\hat{z} = \hat{h}(\hat{x}, \hat{t})$, defined by

$$\hat{\boldsymbol{t}} = \left(1 + \left(\frac{\partial \hat{h}}{\partial \hat{x}}\right)^2\right)^{-1/2} \left(1, \frac{\partial \hat{h}}{\partial \hat{x}}\right), \qquad \hat{\boldsymbol{n}} = \left(1 + \left(\frac{\partial \hat{h}}{\partial \hat{x}}\right)^2\right)^{-1/2} \left(-\frac{\partial \hat{h}}{\partial \hat{x}}, 1\right), \tag{2.9}$$

γ is the (constant) surface tension, and $\hat{\boldsymbol{T}}$ is the stress tensor, defined by

$$\hat{\boldsymbol{T}} = \begin{pmatrix} -\hat{p} + 2\mu\dfrac{\partial \hat{u}}{\partial \hat{x}} & \mu\left(\dfrac{\partial \hat{u}}{\partial \hat{z}} + \dfrac{\partial \hat{w}}{\partial \hat{x}}\right) \\ \mu\left(\dfrac{\partial \hat{u}}{\partial \hat{z}} + \dfrac{\partial \hat{w}}{\partial \hat{x}}\right) & -\hat{p} + 2\mu\dfrac{\partial \hat{w}}{\partial \hat{z}} \end{pmatrix}, \tag{2.10}$$

and evaluated on the free surface.

We choose to incorporate a precursor-film regularisation. In this regularisation, we assume that the whole substrate is initially covered in a thin layer of liquid of thickness h_∞ (see figure 2.2). Thus, we assume that

$$\hat{h} \to h_\infty \qquad \text{as} \qquad \hat{x} \to \infty, \tag{2.11}$$

[1] An alternative approach would be to assume that, at the moving front, $\hat{x} = \hat{a}(\hat{t}\,)$, say, we impose zero-thickness and no-flux conditions along with a slip law along the whole of the substrate. For late time, as in the non-injection case we expect a quasi-static profile for the film thickness, where the relationship between the dynamic contact angle, θ_d, and the speed of the contact line, $\dot{\hat{a}}$ (where a dot ($\dot{}$) denotes differentiation with respect to time), is given by a version of Tanner's law (Tanner, 1979). For small contact angles, this can be written as

$$\frac{\partial \hat{h}}{\partial \hat{x}} = \hat{k}\dot{\hat{a}}^{1/3}, \tag{2.3}$$

for some constant of proportionality $\hat{k}$, depending on the system under consideration (Myers, 1998).

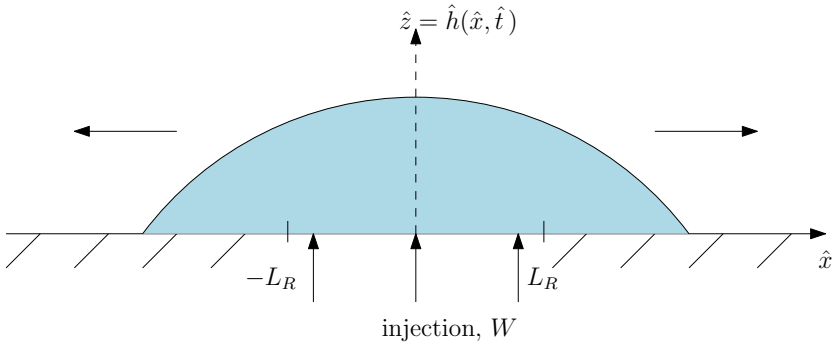

Figure 2.1: Schematic diagram of the thin-film flow problem with injection in the region $-L_R < \hat{x} < L_R$.

and

$$\hat{h} = h_\infty \qquad \text{at} \qquad \hat{t} = 0. \tag{2.12}$$

This regularisation is sufficient to close the problem (King & Bowen, 2001), it resolves the well-known stress singularity that occurs at the moving contact line in film-spreading problems (Huh & Scriven, 1971), and we will find that this recovers a version of Tanner's law describing the motion of the *apparent* contact line, $\hat{a}$. The position of the apparent contact line, which lies in a narrow region where the film thickness adjusts to the precursor thickness, is sometimes defined as the point where the curvature of the free surface attains a local maximum (see, for example, Carlson *et al.*, 2015; Ajaev, 2012). However, any point in the narrow transition region can serve as a definition for the contact line. For concreteness, we define the position of the contact line to be the smallest value of $\hat{x}$ at which $\hat{h}$ equals the precursor layer thickness, h_∞ (see figure 2.2).

Finally, at the centre of the injection region, we assume symmetry, and thus we set

$$\hat{u} = \frac{\partial \hat{p}}{\partial \hat{x}} = \frac{\partial \hat{h}}{\partial \hat{x}} = \frac{\partial^3 \hat{h}}{\partial \hat{x}^3} = 0 \qquad \text{at} \qquad \hat{x} = 0. \tag{2.13}$$

From now on, we assume that the solution is symmetric about $\hat{x} = 0$ and only consider $x \geq 0$. We will therefore drop the modulus sign on the right-hand side of (2.5).

2.2.2 Dimensionless Model

We non-dimensionalise (2.1)–(2.8) using

$$\begin{gathered}(\hat{x}, \hat{a}) = L_R(x, a), \quad (\hat{z}, \hat{h}) = \left(\mu L_R^4 W/\gamma\right)^{1/4}(z, h), \\ \hat{u} = \left(\gamma W^3/\mu\right)^{1/4} u, \quad \hat{w} = W w, \quad \hat{t} = \left(\mu L_R^4/\gamma W^3\right)^{1/4} t, \quad \hat{p} = \left(\gamma^3 \mu W/L_R^4\right)^{1/4} p.\end{gathered} \tag{2.14}$$

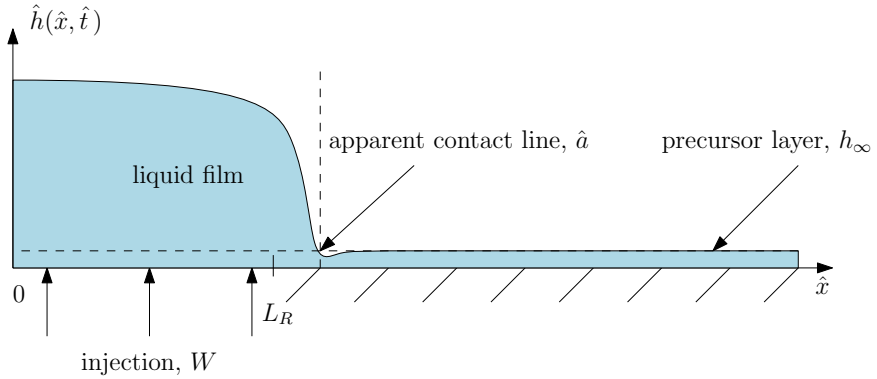

Figure 2.2: A schematic diagram of the thin-film problem on half-space with injection and a precursor layer of thickness h_∞.

We note that we have chosen the intrinsic scale for $\hat{z}$ and $\hat{h}$ that emerges as a result of non-dimensionalising (2.7) and balancing stress in the normal direction with surface-tension forces. We assume that the aspect ratio $\epsilon = (\mu W/\gamma)^{1/4} \ll 1$, and expand the dependent variables in asymptotic series in powers of ϵ^2. This gives the following leading-order dimensionless problem

$$-\frac{\partial p}{\partial x} + \frac{\partial^2 u}{\partial z^2} = 0, \tag{2.15}$$

$$-\frac{\partial p}{\partial z} = 0, \tag{2.16}$$

$$\frac{\partial u}{\partial x} + \frac{\partial w}{\partial z} = 0, \tag{2.17}$$

together with

$$u = 0 \qquad \text{on} \qquad z = 0, \tag{2.18}$$

$$w = \Theta\,(1-x) \qquad \text{on} \qquad z = 0, \tag{2.19}$$

$$w = \frac{\partial h}{\partial t} + u\frac{\partial h}{\partial x} \qquad \text{on} \qquad z = h(x,t), \tag{2.20}$$

$$p = -\frac{\partial^2 h}{\partial x^2} \qquad \text{on} \qquad z = h(x,t), \tag{2.21}$$

$$\frac{\partial u}{\partial z} = 0 \qquad \text{on} \qquad z = h(x,t). \tag{2.22}$$

Integrating (2.17), and using (2.15)–(2.16) together with (2.18)–(2.22), we find that h satisfies the lubrication equation

$$\frac{\partial h}{\partial t} + \frac{1}{3}\frac{\partial}{\partial x}\left(h^3\frac{\partial^3 h}{\partial x^3}\right) = \Theta(1-x). \tag{2.23}$$

The dimensionless boundary and initial conditions become

$$\frac{\partial h}{\partial x} = \frac{\partial^3 h}{\partial x^3} = 0 \qquad \text{at} \qquad x = 0, \tag{2.24}$$

$$h \to \delta \qquad \text{as} \qquad x \to \infty, \tag{2.25}$$

$$h = \delta \qquad \text{at} \qquad t = 0, \tag{2.26}$$

where $\delta = h_\infty/(\epsilon L_R) \ll 1$ is the dimensionless precursor film thickness and the only remaining parameter in the system. Although we have only three boundary conditions for our fourth-order equation, the precursor-layer regularisation (2.25) is enough to ensure a unique solution (King & Bowen, 2001; Myers, 1998).

Integrating (2.23) with respect to both x and t and applying (2.24) and (2.26), we obtain

$$\int_0^\infty (h(x,t) - \delta)\, \mathrm{d}x = t. \tag{2.27}$$

Equation (2.27) is an expression describing global conservation of mass which will be convenient to use in the following analysis.

In the next section, we will explore the behaviour of the film thickness for early, $O(1)$, and late time, which will enable us to make substantial analytical progress with the problem.

2.3 Asymptotic Analysis in the Limit $\delta \ll 1$

We begin by considering the asymptotic behaviour of the solution to (2.23)–(2.27) for early, $O(1)$, and late time in the relevant limit $\delta \ll 1$, and will later compare the results with the full numerical solution. We will find that (i) it is straightforward to determine the early-time behaviour, (ii) the $O(1)$-time behaviour is identical to the case of zero injection and the apparent contact line does not move, and (iii) the interesting injection-dependent behaviour occurs at late time.

2.3.1 Early-Time Behaviour

To examine the early-time behaviour of h, we rescale the thickness h with the initial thickness, δ, and scale time to balance the film growth with the liquid supply, i.e., we set

$$h = \delta\tilde{h}, \qquad t = \delta\tilde{t}. \tag{2.28}$$

We pose the asymptotic expansions

$$\tilde{h}(x,\tilde{t}\,) \sim \tilde{h}_0(x,\tilde{t}\,) + \delta\tilde{h}_1(x,\tilde{t}\,) + \cdots \qquad \text{as} \qquad \delta \to 0, \tag{2.29}$$

$$a(\tilde{t}\,) \sim 1 + \delta a_1(\tilde{t}\,) + \cdots \qquad \text{as} \qquad \delta \to 0, \tag{2.30}$$

and assume, following King & Bowen (2001), that on this timescale the apparent contact line moves only an $O(\delta)$ distance from its original location at the end of the injection region. Thus, to leading order, (2.23) reduces to

$$\frac{\partial \tilde{h}_0}{\partial \tilde{t}} = \Theta(1-x), \tag{2.31}$$

with initial condition

$$\tilde{h}_0 = 1 \qquad \text{at} \qquad \tilde{t} = 0. \tag{2.32}$$

The solution, in terms of the original variables, is

$$h_0(x,t) = \delta + t\,\Theta(1-x). \tag{2.33}$$

We immediately note that, since this solution is spatially uniform on either side of $x = 1$, the boundary conditions (2.24) are automatically satisfied. The global conservation of mass (2.27) also holds. However, there is a discontinuity in our solution at $x = 1$ and, to determine the smooth transition between the two solutions given in (2.33), we need to consider a boundary layer near $x = 1$. Specifically, we rescale

$$x = 1 + \delta\tilde{x}. \tag{2.34}$$

In this boundary layer, we obtain the following problem

$$\frac{\partial \tilde{h}}{\partial \tilde{t}} + \frac{1}{3}\frac{\partial}{\partial \tilde{x}}\left(\tilde{h}^3 \frac{\partial^3 \tilde{h}}{\partial \tilde{x}^3}\right) = \Theta(-\tilde{x}), \tag{2.35}$$

subject to

$$\tilde{h} \to 1 \qquad \text{as} \qquad \tilde{x} \to \infty, \tag{2.36}$$

$$\tilde{h} \to 1 + \tilde{t} \qquad \text{as} \qquad \tilde{x} \to -\infty, \tag{2.37}$$

$$\tilde{h} = 1 \qquad \text{at} \qquad \tilde{t} = 0. \tag{2.38}$$

This problem cannot be solved explicitly. We will present the numerical solutions to this boundary-layer problem along with the solutions to the full system (2.23)–(2.26) in Section 2.4.

Before we focus on the behaviour of the thickness of the liquid film $h(x,t)$ for late time when we expect $O(1)$ movement of the contact line, we look at the $O(1)$-time problem and discuss the behaviour of the apparent contact line.

2.3.2 $O(1)$-Time Behaviour

For $O(1)$ time, all terms in (2.23) come into play, and analytical progress is difficult. However, we will carefully analyse the motion of the apparent contact line with the purpose of exploiting these results during the late-time analysis. The scalings that we obtain in this section are identical to those used in the no-injection case considered in King & Bowen (2001). They find that the apparent contact line is stationary for $O(1)$ times, which is supported by our numerical solutions found in Section 2.4. We will focus on the next-order correction to this leading-order behaviour. Following the work of King & Bowen (2001), we note that the leading-order (in δ) solution for h in the injection region has the following behaviour as $x \to 1^-$:

$$h_0 \sim A(t)(1-x) \qquad \text{as} \qquad x \to 1^-, \tag{2.39}$$

where $A(t) > 0$ is some function that can, in theory, be determined from solving the leading-order problem

$$\frac{\partial h_0}{\partial t} + \frac{1}{3}\frac{\partial}{\partial x}\left(h_0^3 \frac{\partial^3 h_0}{\partial x^3}\right) = 1, \tag{2.40}$$

together with

$$\frac{\partial h_0}{\partial x} = \frac{\partial^3 h_0}{\partial x^3} = 0 \qquad \text{at} \qquad x = 0, \tag{2.41}$$

$$h_0 = 0 \qquad \text{at} \qquad x = 1, \tag{2.42}$$

$$h_0 = 0 \qquad \text{at} \qquad t = 0, \tag{2.43}$$

and conservation of mass

$$\int_0^1 h_0(x,t)\,\mathrm{d}x = t. \tag{2.44}$$

In a transition region at the contact line near $x = 1$, we write

$$x = 1 + \psi c(t) + \varphi d(t)\eta, \qquad h = \delta H, \tag{2.45}$$

to account for the time-dependent motion of the contact line, where we take $d = \dot{c}^{-1/3}$ for convenience in subsequent manipulations, and $\psi = \psi(\delta)$ and $\varphi = \varphi(\delta)$ are anticipated to be small parameters, since the contact line is expected to be close to $x = 1$. Noting that the spatial and time derivatives transform to

$$\frac{\partial}{\partial t} \to \frac{\partial}{\partial t} - \left(\frac{\psi\dot{c}}{\varphi d} + \frac{\eta\dot{d}}{d}\right)\frac{\partial}{\partial \eta}, \qquad \frac{\partial}{\partial x} \to \frac{1}{\varphi d}\frac{\partial}{\partial \eta}, \tag{2.46}$$

after rearranging, equation (2.23) becomes

$$\delta d^4 \frac{\partial H}{\partial \bar{t}} - \left(\frac{\delta\psi}{\varphi} + \eta\delta\dot{d}d^3\right)\frac{\partial H}{\partial \eta} + \frac{\delta^4}{3\varphi^4}\frac{\partial}{\partial \eta}\left(H^3\frac{\partial^3 H}{\partial \eta^3}\right) = d^4\Theta\left(-\psi c - \varphi d\eta\right). \tag{2.47}$$

In order to obtain a non-trivial dominant balance in (2.47), we balance the second and fourth terms, which requires

$$\psi = \frac{\delta^3}{\varphi^3}, \qquad \varphi \ll \psi \qquad \text{as} \qquad \delta \to 0. \tag{2.48}$$

The second condition tells us that for $O(1)$ time, in the limit $\delta \to 0$, the apparent contact line moves by an amount that is much greater in extent than the width of the transition region. Thus, we may ignore injection in the transition region, and the corresponding equation for H becomes

$$-\frac{\partial H}{\partial \eta} + \frac{1}{3}\frac{\partial}{\partial \eta}\left(H^3 \frac{\partial^3 H}{\partial \eta^3}\right) = 0. \tag{2.49}$$

Analysing the behaviour of (2.49) as $\eta \to -\infty$, matching it to the outer solution (2.39), as has been done in King & Bowen (2001), and using (2.48), we obtain the necessary scalings for ψ and φ, namely

$$\psi = \frac{1}{\log(1/\delta)}, \qquad \varphi = \delta \log^{1/3}(1/\delta). \tag{2.50}$$

We immediately note that (2.48) hold true. These scalings will be further verified by the numerical solutions presented in Section 2.4. Thus, we conclude that for $O(1)$ time, the contact line is indeed stationary to leading order in δ, and moves a distance $O(1/\log(1/\delta))$ at next order.

2.3.3 Late-Time Behaviour

To explore the late-time behaviour of the system, we rescale both time and the film thickness appropriately to arrive at a limit in which the surface-tension term in (2.23) is the only dominant term at leading order in the relevant asymptotic parameter (which will be determined as part of the analysis). This leading-order problem constitutes the solution in an outer region, the region to the left of the moving apparent contact line (see figure 2.3). At this stage, though, the position of the apparent contact line is an unknown function of time. We will solve for the film thickness in the transition region near the apparent contact line and match the solutions from the outer, transition and precursor-layer regions to obtain the full profile of the film thickness and the leading-order solution for the location of the moving boundary $a(t)$. We will also see at the end of this section, and in Section 2.5, that the late-time behaviour of our model is a generalisation of the classical droplet-spreading problem when we allow the volume of liquid to be time dependent. However, unlike the classical droplet-spreading problem, we will obtain unbounded growth of the film, which is

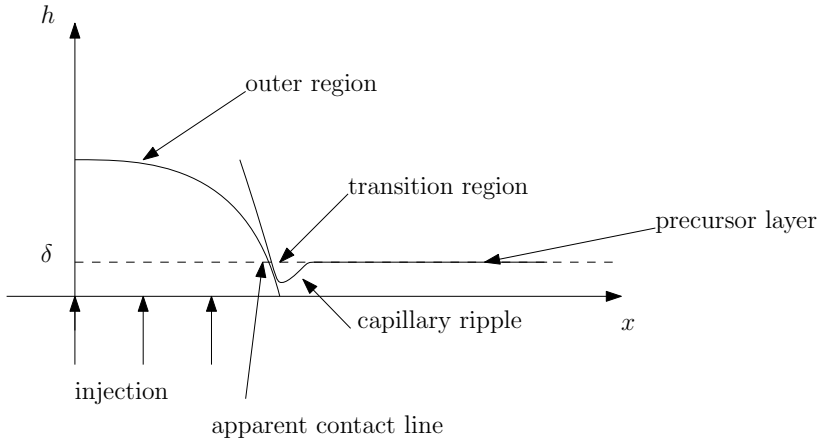

Figure 2.3: A schematic diagram of the outer, transition and precursor layer regions, and the position of the apparent contact line. The film thicknesses are not drawn to scale.

entirely due to the finite-width injection region. In Section 2.5 we will consider some generalisations to our injection-spreading problem, and we will see that unbounded growth is not always guaranteed and depends on the functional form of the injection rate.

2.3.3.1 The Outer Region

Unlike the spreading-droplet scenario considered in King & Bowen (2001), here we anticipate that the injection results in a film thickness that is much larger than δ for late time. Thus, we scale

$$t = \frac{\bar{t}}{\lambda}, \qquad h = \frac{\bar{h}}{\lambda}, \tag{2.51}$$

where $\lambda = \lambda(\delta) \ll 1$ is to be determined. We note that we do not scale x, because we anticipate that a will move by an $O(1)$ amount on this timescale. After rearranging, (2.23) becomes

$$\lambda^4 \frac{\partial \bar{h}}{\partial \bar{t}} + \frac{1}{3}\frac{\partial}{\partial x}\left(\bar{h}^3 \frac{\partial^3 \bar{h}}{\partial x^3}\right) = \lambda^4 \Theta(1-x). \tag{2.52}$$

The surface-tension term in (2.52) is dominant to leading order in λ^4. We assume $\delta \ll \lambda^4 \ll 1$ as $\delta \to 0$, and will verify this assertion *a posteriori*. Expanding the dependent variables as

$$\bar{h}(x,\bar{t}\,) \sim \bar{h}_0(x,\bar{t}\,) + \lambda^4 \bar{h}_1(x,\bar{t}\,) + \cdots \qquad \text{as} \qquad \lambda \to 0, \tag{2.53}$$

$$a(\bar{t}\,) \sim a_0(\bar{t}\,) + \lambda^4 a_1(\bar{t}\,) + \cdots \qquad \text{as} \qquad \lambda \to 0, \tag{2.54}$$

the leading-order problem becomes

$$\frac{\partial}{\partial x}\left(\bar{h}_0^3 \frac{\partial^3 \bar{h}_0}{\partial x^3}\right) = 0, \tag{2.55}$$

with

$$\frac{\partial \bar{h}_0}{\partial x} = \frac{\partial^3 \bar{h}_0}{\partial x^3} = 0 \qquad \text{at} \qquad x = 0, \tag{2.56}$$

$$\bar{h}_0 = 0 \qquad \text{at} \qquad x = a_0(\bar{t}\,). \tag{2.57}$$

The leading-order version of the conservation-of-mass equation (2.27) becomes

$$\bar{t} = \int_0^{a_0(\bar{t})} \bar{h}_0(x, \bar{t}\,)\,\mathrm{d}x. \tag{2.58}$$

Equation (2.55) with conditions (2.56)–(2.58) has a parabolic solution, namely,

$$\bar{h}_0(x, \bar{t}\,) = \frac{3\bar{t}(a_0^2 - x^2)}{2a_0^3}, \tag{2.59}$$

where $a_0(\bar{t}\,)$ is unknown. In order to determine $a_0(\bar{t}\,)$, we will explore the solution in the transition region near the moving boundary and then match to (2.59).

2.3.3.2 The Transition Region

In the transition region near the moving front, we write

$$t = \frac{\bar{t}}{\lambda}, \qquad x = a_0(\bar{t}\,) + \nu s(\bar{t})\xi, \qquad h = \delta H, \tag{2.60}$$

where $\nu \ll 1$, and we set $s(\bar{t}\,) = \dot{a}_0^{-1/3}$ for convenience in subsequent manipulations. With this change of variables, the spatial and time derivatives transform to

$$\frac{\partial}{\partial \bar{t}} \to \frac{\partial}{\partial \bar{t}} - \left(\frac{\dot{a}_0}{\nu s} + \frac{\xi \dot{s}}{s}\right)\frac{\partial}{\partial \xi}, \qquad \frac{\partial}{\partial x} \to \frac{1}{\nu s}\frac{\partial}{\partial \xi}. \tag{2.61}$$

Furthermore, from Section 2.3.2, we know that a moves $O(1/\log(1/\delta))$ away from the end of the injection region for $O(1)$ time. Therefore, assuming that $\nu \ll 1/\log(1/\delta)$ as $\delta \to 0$ (to be verified *a posteriori*), the transition region will lie outside the injection region for late time, and equation (2.23) becomes

$$\lambda\left(s^4 \frac{\partial H}{\partial \bar{t}} - \left(\frac{1}{\nu} + \xi \dot{s} s^3\right)\frac{\partial H}{\partial \xi}\right) + \frac{\delta^3}{3\nu^4}\frac{\partial}{\partial \xi}\left(H^3 \frac{\partial^3 H}{\partial \xi^3}\right) = 0. \tag{2.62}$$

In order to obtain a non-trivial dominant balance in (2.62), we balance the second and fourth terms, which requires that

$$\nu = \frac{\delta}{\lambda^{1/3}}. \tag{2.63}$$

After rearranging, (2.62) then becomes

$$\nu\left(s^4\frac{\partial H}{\partial \bar{t}} - \xi \dot{s} s^3 \frac{\partial H}{\partial \xi}\right) - \frac{\partial H}{\partial \xi} + \frac{1}{3}\frac{\partial}{\partial \xi}\left(H^3\frac{\partial^3 H}{\partial \xi^3}\right) = 0. \tag{2.64}$$

We expand the dependent variables in powers of $\nu = \nu(\delta)$, assuming $\delta \ll \nu \ll 1$ as $\delta \to 0$, which we will also check *a posteriori*, and, thus, we write

$$H(\xi, \bar{t}\,) \sim H_0(\xi, \bar{t}\,) + \nu H_1(\xi, \bar{t}\,) + \cdots \qquad \text{as} \qquad \nu \to 0. \tag{2.65}$$

Substituting (2.65) into (2.64), retaining leading-order terms, integrating once, and applying the matching condition with the precursor layer

$$H_0 \to 1 \qquad \text{as} \qquad \xi \to \infty, \tag{2.66}$$

we find that H_0 satisfies

$$-H_0 + \frac{1}{3}H_0^3\frac{\partial^3 H_0}{\partial \xi^3} = -1. \tag{2.67}$$

To match with the outer solution, we need to understand the behaviour of the transition-region solution as $\xi \to -\infty$. We assume the solution is of the form $H_0 \sim B(-\xi)^m \log^n(-\xi)$, as $\xi \to -\infty$, for some values of B, m and n. Choosing $m = 1$, $n = 1/3$, and $B = 9^{1/3}$ gives the leading-order balance as $\xi \to -\infty$ between the two terms on the left-hand side of (2.67). Thus, our second matching condition is

$$H_0 \sim 9^{1/3}(-\xi)\log^{1/3}(-\xi) \qquad \text{as} \qquad \xi \to -\infty. \tag{2.68}$$

We note that (2.67) has been solved by Duffy & Wilson (1997) for the case when the right-hand side is zero. Furthermore, they also obtain the asymptotic behaviour (2.68) (modulo the pre-factor), which confirms our result, since as $\xi \to -\infty$, $H_0 \to \infty$, and the right-hand side of (2.67), which is constant, does not appear in the dominant balance. We solve for H_0 using a shooting method. Specifically, we expand H_0 using

$$H_0 \sim 1 + \tilde{H}_0 \qquad \text{as} \qquad \xi \to \infty, \tag{2.69}$$

where $\tilde{H}_0 \ll 1$. The equation for $\tilde{H}_0$ is

$$\frac{1}{3}\frac{\partial^3 \tilde{H}_0}{\partial \xi^3} - \tilde{H}_0 = 0, \tag{2.70}$$

which has a solution that is a combination of exponentials. Retaining only decaying solutions and appropriately choosing the origin, we may write the solution as

$$H_0 \sim 1 + \tilde{A}\exp(-3^{1/3}\xi/2)\cos(3^{5/6}\xi/2) \qquad \text{as} \qquad \xi \to \infty. \tag{2.71}$$

We will present the solution to (2.67) in Section 2.4. The solution is found numerically, utilising H_0, H_0', H_0'' given by (2.71) evaluated at some large value of ξ (we used $\xi = 10$); $\tilde{A}$ is our shooting parameter. We note that we can restrict the interval for possible values for $\tilde{A}$ to, for example, $[1, \exp(2\pi/\sqrt{3})]$ (McEwan & Taylor, 1966; Tuck & Schwartz, 1990). We vary $\tilde{A}$ in order to match the behaviour as $\xi \to -\infty$ specified by (2.68). As in Tuck & Schwartz (1990), we use the fact that $H_0 H_0' H_0'' \to -3$ as $\xi \to -\infty$ to provide us with an accurate indicator of how close we are to the required solution.

2.3.3.3 Matching

We first match the transition region with the outer region. We write (2.68) in outer variables as

$$\begin{aligned} \bar{h}_0 &\sim \frac{9^{1/3}\lambda^{4/3}(a_0 - x)\log^{1/3}\left(\lambda^{1/3}(a_0 - x)/(\delta s)\right)}{s} \\ &\sim \frac{9^{1/3}\lambda^{4/3}(a_0 - x)\log^{1/3}(1/\delta)}{s} \qquad \text{as} \qquad \delta \to 0. \end{aligned} \tag{2.72}$$

The leading-order term in the outer solution (2.59) is

$$\bar{h}_0 \sim \frac{3\bar{t}(a_0 - x)}{a_0^2} \qquad \text{as} \qquad x \to a_0^-. \tag{2.73}$$

This suggests that, to match (2.72) and (2.73), the appropriate scaling for λ should be

$$\lambda = \frac{1}{\log^{1/4}(1/\delta)}. \tag{2.74}$$

Thus, (2.63) gives

$$\nu = \delta \log^{1/12}(1/\delta). \tag{2.75}$$

We note that this confirms the hypotheses that $\delta \ll \nu \ll \lambda^4 \ll \lambda \ll 1$, as $\delta \to 0$. Logarithmic scales also appear in similar problems described in Lacey (1982), Hocking (1983), and King & Bowen (2001), for example. However, for the classical problem of a spreading droplet, the relevant scale is $1/\log(1/\delta)$ (King & Bowen, 2001), which is asymptotically smaller (in the limit $\delta \to 0$) than our result (2.74) in the injection case. Matching (2.72) with (2.73), we obtain

$$\dot{a}_0 = \frac{3\bar{t}^{\,3}}{a_0^6}, \tag{2.76}$$

which can be solved to determine $a_0(\bar{t})$. We also remark that (2.76) is a version of Tanner's law, since it follows that, at the contact line,

$$\frac{\partial \bar{h}_0}{\partial x} = -(9\dot{a}_0)^{\frac{1}{3}}. \tag{2.77}$$

We match the late-time behaviour for the contact line with the behaviour for $O(1)$ time, which results in imposing the initial condition $a_0 \to 1$ as $t \to 0$. Thus, (2.76) can be solved to yield

$$a_0(\bar{t}\,) = \left(1 + \frac{21\bar{t}^{\,4}}{4}\right)^{1/7}, \tag{2.78}$$

and so,

$$\bar{h}_0(0, \bar{t}\,) = \frac{3\bar{t}}{2a_0} = \frac{3\bar{t}}{2}\left(1 + \frac{21\bar{t}^{\,4}}{4}\right)^{-1/7}. \tag{2.79}$$

In terms of the original variables, $h_0 = \bar{h}_0/\lambda$ and $t = \bar{t}/\lambda$,

$$a_0(t) = \left(1 + \frac{21\lambda^4 t^4}{4}\right)^{1/7}, \quad h_0(0,t) = \frac{3t}{2}\left(1 + \frac{21\lambda^4 t^4}{4}\right)^{-1/7} \text{ for } \quad t = O(1/\lambda). \tag{2.80}$$

We observe that, for late time, the apparent contact line moves much faster ($\sim t^{4/7}$) than the classical non-injection case ($\sim t^{1/7}$) considered in King & Bowen (2001). We also note that, through λ, the leading-order results (2.80) have a dependence on the precursor thickness, δ. In physical systems where precursor layers are not observed, δ can be treated as an adjustable parameter to be determined from experimental data.

As mentioned at the beginning of Section 2.3, we can generalise results from the classical droplet-spreading problem (see, for example, Voinov, 1976; Cox, 1986; Bonn *et al.*, 2009) to the case of a time-dependent injection rate using the Cox–Voinov law (Bonn *et al.*, 2009) to obtain the full late-time ($t \gg 1/\lambda$) behaviour of the film spreading.

Our starting point is the relationship between the apparent and microscopic contact angles $\theta_{o,i}$ given by the well-known Cox–Voinov law (Bonn *et al.*, 2009)

$$\theta_o^3 - \theta_i^3 = \frac{9\mu\dot{a}}{\gamma}\log(L_o/L_i), \tag{2.81}$$

where $L_{o,i}$ are the length scales of the outer and inner regions of the problem (in analogy to the terminology used in Section 2.3). We use (2.59), (2.60) and (2.74)–(2.76) to find that $\log(L_o/L_i) = \log(a_0/\nu s) \sim \log(t/\delta a_0) = \log(h(0,t)/\delta)$ to leading

order in δ. Thus, with our non-dimensionalisation and remembering that $\theta_i = 0$ in our precursor-film regularisation, we write $a_0 = 1 + b$ to give

$$\dot{b} \sim \frac{\theta_o^3}{9 \log\left(h_0(0,t)/\delta\right)}. \tag{2.82}$$

For $1 \ll t \ll 1/\lambda = \log^{1/4}(1/\delta)$, we linearise (2.80) and we find that

$$b \sim \frac{3t^4}{4 \log\left(1/\delta\right)} \ll 1. \tag{2.83}$$

This can also be obtained from the Cox–Voinov law using (2.59) with $a_0 = 1$, $\theta_o = 3t$, and $h_0(0,t) \propto t$, and noting that $\log\left(t/\delta\right) \sim \log\left(1/\delta\right)$ for the specified range of t. In the case where $t = O(\log^{1/4}(1/\delta))$, we have $b = O(1)$, and the behaviour of the film spreading is given by our result (2.80). For the late-time regime, $t \gg \log^{1/4}(1/\delta)$, $a_0 \sim b \gg 1$, and, using (2.81), but this time with $\theta_o = 3t/a_0^2$ and $h_0(0,t) \propto t/a_0$ from (2.59), we obtain

$$\dot{a}_0 \sim \frac{3t^3}{a_0^6 \log\left(t/\delta a_0\right)}. \tag{2.84}$$

Integrating the leading-order version of (2.84) in which we treat the logarithm as constant (which can be confirmed *a posteriori*), we find that a_0 scales as

$$a_0 \sim \left(\frac{21t^4}{4 \log\left(t^{3/7}/\delta\right)}\right)^{1/7}. \tag{2.85}$$

We see that, for $t \gg \log^{1/4}(1/\delta)$, $a_0(t)$ has a true power-law dependence on time, provided $t \ll 1/\delta^{7/3}$.

We further note that we can also obtain the power-law dependence on time in (2.80) using scaling arguments. The matching condition (2.76) can also simply be deduced from a comparison of the slopes of h in the inner and outer regions obtained from (2.72) and (2.73), respectively. Scaling $x \sim a$, the slope of the outer solution $\sim h/a \sim t/a^2$ from (2.59), while the inner region has height $\sim \delta$ and length $\sim \delta \dot{a}^{-1/3}$ from (2.60) (with $\lambda = 1$) and, thus, has slope $t/a^2 \sim \dot{a}^{1/3}$ confirming the scalings $a \sim t^{4/7}$ and $h \sim t^{3/7}$. Furthermore, if we look for a similarity solution to the problem for late time (essentially, away from the injection region) of the form $t^m f(x/t^n)$, for some exponents m and n, we can recover $m = 3/7$ and $n = 4/7$ and the parabolic profile for the outer solution. This is confirmed by the late-time asymptotic analysis. Thus, for late time the aspect ratio is given by $h_0(0,t)/a_0(t) \sim t^{-1/7}$, and so remains small for all time.

2.4 Numerical Results and Discussion

We now present numerical solutions to the system (2.23)–(2.26). We approximate the boundary condition (2.25) by imposing

$$h = \delta \qquad \text{on} \qquad x = l, \tag{2.86}$$

$$\frac{\partial h}{\partial x} = 0 \qquad \text{on} \qquad x = l, \tag{2.87}$$

where l is some large number. We used $l = 60$.

We employ a transformation of the coordinates that yields an adaptive mesh, which allows us to solve the problem for large time for a moderate computational cost (see Appendix B for details). We solve the problem using MATLAB with a linear implicit Euler scheme. We use the exact expression for the Heaviside function $\theta(x)$ and note that the discontinuity associated with it in (2.23) does not pose numerical difficulties and is not visible in the solutions, since the discontinuity appears in the fourth derivative of h. In figure 2.4(a), we show the numerical solutions for the spatial profile of the thickness $h(x, t)$ for various times where we have imposed a dimensionless precursor-layer thickness of $\delta = 10^{-3}$. As anticipated, the film thickness increases with time, and the front advances. We observe that the solutions appear self-similar, which indeed is the case for late time as found at the end of Section 2.3.3.3. In figure 2.4(b), we show a zoom-in of the height profile near the apparent contact line, where we see characteristic capillary ripples, or ridges, (Bonn *et al.*, 2009). In figure 2.4(c), we show the numerical solutions for the spatial profile of the thickness $h(x, t)$ for various early times with a zoom-in of the apparent contact line near $x = 1$. We see that capillary ripples form on either side of $x = 1$ and subsequently travel outwards in both directions. In Section 2.3.1, we formulated the boundary-layer problem (2.35)–(2.38) for the transition between the spatially uniform solutions for early time given in (2.33). In figure 2.4(d), we show a plot of the film height near $x = 1$, found by solving (2.35)–(2.38) numerically, compared with the full numerical solution. We see good agreement between the two solutions.

In figure 2.5, we compare the thickness profile of the film at time $t = 10$ with the asymptotic predictions for late time for the outer- and transition-region profiles, given by (2.59) and (2.67), respectively, for two different precursor-layer thicknesses. We see excellent agreement between the numerical solution and the asymptotic solution as δ decreases. We have translated the asymptotic solution for the inner region to allow for a detailed comparison with the numerical solution near the capillary ripple. This is shown in the small panels in the figures. In general, the positions of $x = a$

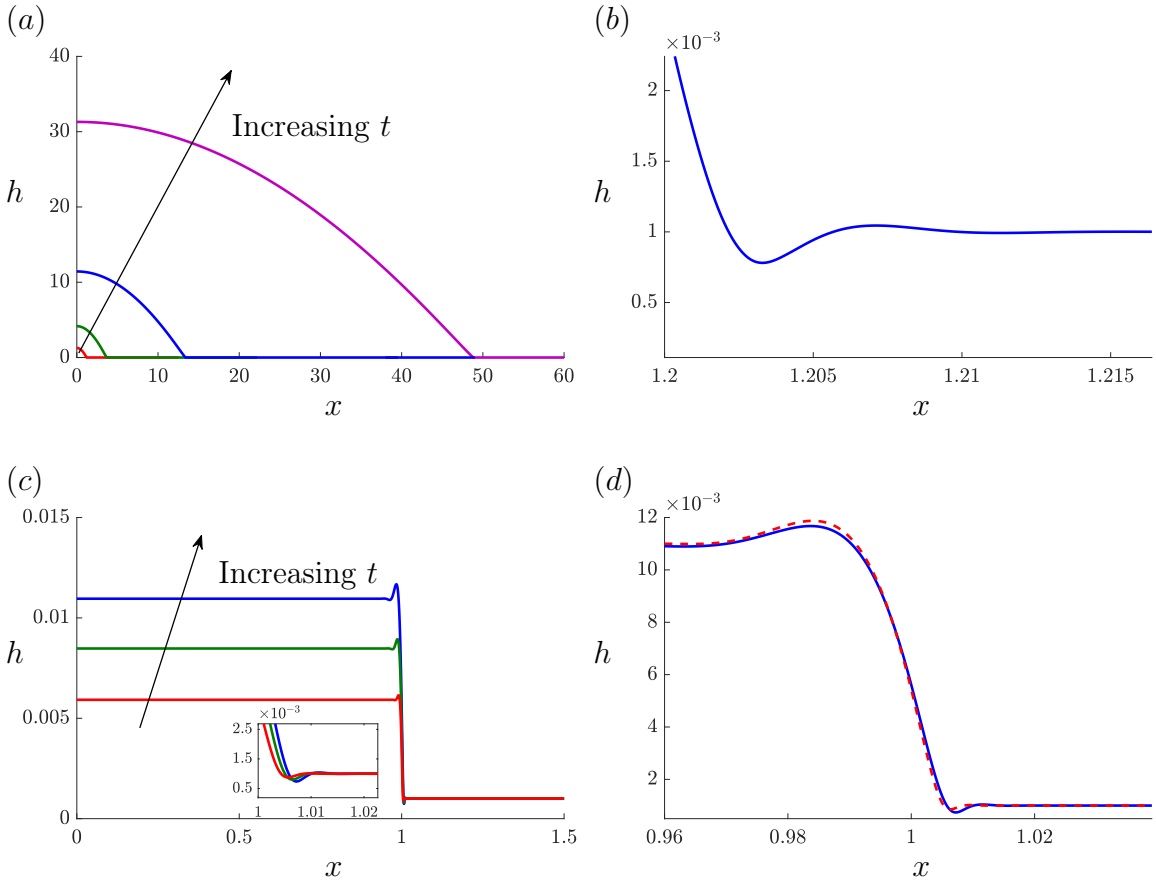

Figure 2.4: Plots of the film thickness, $h(x,t)$, satisfying (2.23)–(2.26) (a) at $t = 1$ (red), $t = 10$ (green), $t = 100$ (blue), $t = 1000$ (purple), (b) near $h = \delta$ and $x = 1.2$ for $t = 1$, and (c) at $t = 0.005$ (red), $t = 0.0075$ (green), $t = 0.01$ (blue). In (d), we show the film thickness (solid blue) along with the solution to (2.35)–(2.38) (dashed red) near $x = 1$ for $t = 0.01$. In all figures, $\delta = 10^{-3}$.

for the outer and inner regions are expected to differ, because the corrections to the leading-order outer solution for a ($O(\lambda^4) = O(1/\log(1/\delta))$ from (2.54) and (2.74)) are large compared to the length scale of the inner region ($O(\nu) = O(\delta \log^{1/12}(1/\delta))$ from (2.60) and (2.75)). We note that the predicted convergence is quite slow since our asymptotic sequence for $h(x,t)$ is logarithmic in nature. This slow logarithmic convergence is also present when slip regularisation is used (see, for example, Lacey, 1982; Hocking, 1983).

In figure 2.6, we show log–log plots of $h(0,t)$ and the position of the apparent contact line, $a(t)$, given by the numerical solution to (2.23)–(2.26), together with our asymptotic predictions for early time, (2.33), and late time, (2.78)–(2.79). The asymptotic solutions match well for the early and late time behaviours, and, in fact,

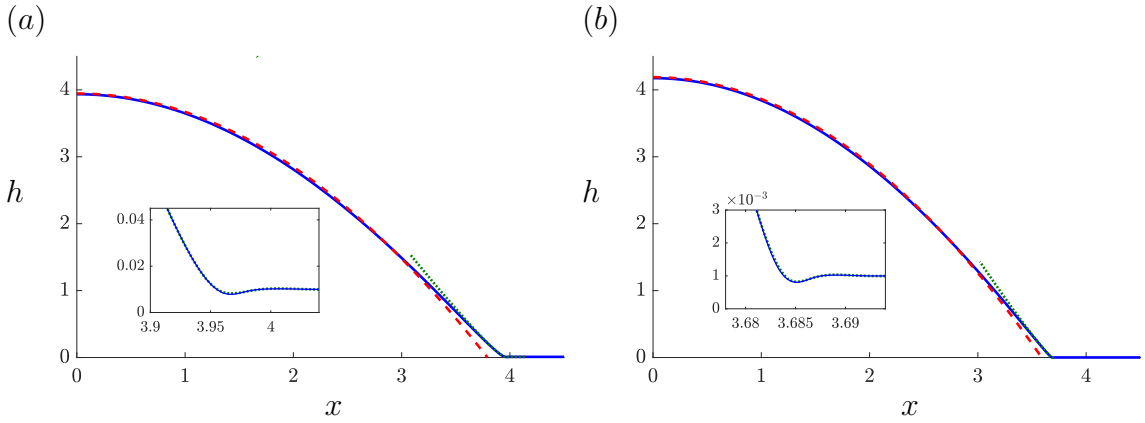

Figure 2.5: Plots of the film thickness, h, satisfying (2.23)–(2.26), at $t = 10$: numerical solution (solid blue), asymptotic solution in the outer region (2.59) (dashed red), asymptotic solution in the transition region (2.67) (dotted green) for (a) $\delta = 10^{-2}$ and (b) $\delta = 10^{-3}$.

are valid for a much wider range of times than expected. We also note that the contact line does not move to leading order in δ for early time, as shown in Section 2.3.1, and moves $O(1/\log(1/\delta))$ for $O(1)$ time, as shown in Section 2.3.2.

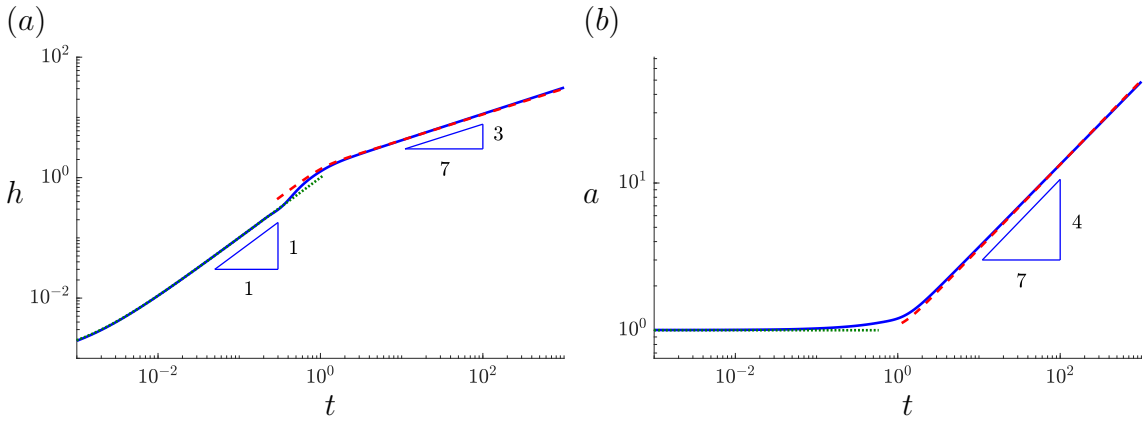

Figure 2.6: Log–log plots of the numerical solution to (2.23)–(2.26) (solid blue) for (a) $h(0,t)$ and (b) $a(t)$. The asymptotic predictions for early time, (2.33) (dotted green), and late time, (2.78)–(2.79) (dashed red) are also shown. Here, $\delta = 10^{-3}$.

2.5 General Injection Rates

In this section, we extend the model to the case of non-constant injection by replacing (2.5) with

$$\hat{w} = \hat{f}(\hat{x}, \hat{t}\,)\Theta\,(L_R - \hat{x}) \qquad \text{on} \qquad \hat{z} = 0, \tag{2.88}$$

for some dimensional supply function $\hat{f}(\hat{x}, \hat{t}\,)$.

2.5.1 Power-Law Injection

We first consider the case in which $\hat{f}$ has a power-law dependence in time, i.e., $\hat{f} = \hat{t}^c \hat{g}(\hat{x})$, where $\hat{g}$ is some integrable function on $[0, 1]$, and c is some real exponent whose range we will specify later on. We expect that $c < 0$ for physically sensible models, such as a chemical reaction whose rate decreases with time. However, we will also study the case $c > 0$. We note that, for $-1 < c < 0$, the injection rate is singular at $t = 0$, but the volume of liquid (which is the time integral of the flux) is still finite. The case $c \leq -1$ corresponds to an infinite volume of liquid injected at $t = 0$, which we exclude on physical grounds. For simplicity, in the following analysis we assume that $\hat{g} = W$ is constant, even though more general spatial variance could be incorporated using the same approach. Thus, the boundary condition on the surface $\hat{z} = 0$ becomes

$$\hat{w} = W\hat{t}^c\Theta\,(L_R - \hat{x}) \qquad \text{on} \qquad \hat{z} = 0. \tag{2.89}$$

In this case, we require a different non-dimensionalisation and we use

$$\begin{gathered}(\hat{x}, \hat{a}) = L_R(x, a), \quad (\hat{z}, \hat{h}) = \left(\mu L_R^4 W^{1/(c+1)}/\gamma\right)^{(c+1)/(3c+4)}(z, h), \\ \hat{u} = \left(\gamma L_R^{3c} W^3/\mu\right)^{1/(3c+4)} u, \quad \hat{w} = \left(\mu L_R^4 W^{4/c}/\gamma\right)^{c/(3c+4)} w, \\ \hat{t} = \left(\mu L_R^4/\gamma W^3\right)^{1/(3c+4)} t, \quad \hat{p} = \left(\gamma^{2c+3}\mu^{c+1} W/L_R^{2c+4}\right)^{1/(3c+4)} p.\end{gathered} \tag{2.90}$$

We assume a long and thin geometry, i.e., that the aspect ratio

$$\epsilon = \left(\mu L_R^{c/c+1} W^{1/(c+1)}/\gamma\right)^{(c+1)/(3c+4)} \ll 1, \tag{2.91}$$

and that we have a thin precursor film, i.e., $\delta = h_\infty/(\epsilon L_R) \ll 1$. Following the same steps as in Section 2.2.2, we manipulate the dimensionless versions of (2.1)–(2.4), (2.6)–(2.8) and (2.89) and we arrive at the evolution equation for h, namely

$$\frac{\partial h}{\partial t} + \frac{1}{3}\frac{\partial}{\partial x}\left(h^3 \frac{\partial^3 h}{\partial x^3}\right) = t^c \Theta(1 - x), \tag{2.92}$$

together with the boundary conditions given by (2.24)–(2.26).

For early time, we use a scaling similar to (2.28), but take account of the exponent c in the injection function by setting

$$h = \delta\tilde{h}, \qquad t = \delta^{1/(c+1)}\tilde{t}, \tag{2.93}$$

where we recall that $c > -1$ so that the scalings are valid for early time. After asymptotically expanding h and a in powers of δ as before, we arrive at a dominant balance between the first and third term in (2.92). Using the same notation as in Section 2.3, we obtain

$$\tilde{h}_0(x,\tilde{t}\,) = 1 + \frac{\tilde{t}^{c+1}}{c+1}\Theta(1-x). \tag{2.94}$$

As in Section 2.3.1, it is possible to obtain a problem for the boundary layer near $x = 1$, analogous to (2.35)–(2.38), which smoothly joins the two solutions given in (2.94), but we do not pursue that here. Instead, we point out that we can consider two distinct temporal regimes in which more analytical progress can be made.

We begin by rewriting the unscaled early-time result for the film thickness above the injection slot, (2.94), namely

$$h(x,t) = \delta + \frac{t^{c+1}}{c+1}. \tag{2.95}$$

For $t \ll \delta^{1/(c+1)}$, we have $h \sim \delta$, and, thus, the inner solution satisfies the linear *hyperdiffusion* equation

$$\frac{\partial h}{\partial t} + \frac{\delta^3}{3}\frac{\partial^4 h}{\partial x^4} = t^c\Theta(1-x). \tag{2.96}$$

Scaling analysis suggests a spreading rate of the form $x - 1 \sim (\delta^3 t)^{1/4}$. Thus, we seek a solution of the form

$$h \sim \delta + \frac{t^{c+1}}{c+1}\mathcal{H}(\xi), \tag{2.97}$$

where $\xi = (1-x)/(\delta^3 t)^{1/4}$, and $\mathcal{H}$ satisfies

$$(c+1)\mathcal{H} - \frac{1}{4}\xi\frac{\partial \mathcal{H}}{\partial \xi} + \frac{1}{3}\frac{\partial^4 \mathcal{H}}{\partial \xi^4} = (c+1)\Theta(\xi), \tag{2.98}$$

with $\mathcal{H}(\xi) \to \Theta(\xi)$ as $\xi \to \pm\infty$.

When $t = O(\delta^{1/(c+1)})$, both terms in (2.95) are comparable in magnitude, and the non-linearity of h^3 in the original equation becomes important. For $t \gg \delta^{1/(c+1)}$, we can consider both regions $x < 1$ and $x > 1$ separately. In $x < 1$, $h \sim t^{c+1}/(c+1)$, and the spreading rate is $x - 1 \sim (h^3 t)^{1/4} \sim t^{(3c+4)/4}/(c+1)^{3/4}$. We, thus, seek a solution of the form

$$h \sim \frac{t^{c+1}}{c+1}\mathcal{H}(\xi), \tag{2.99}$$

where $\xi = (1-x)/(t^{3c+4}/(c+1)^3)^{1/4}$, and $\mathcal{H}$ satisfies

$$(c+1)\mathcal{H} - \frac{3c+4}{4}\xi\frac{\partial \mathcal{H}}{\partial \xi} + \frac{1}{3}\frac{\partial}{\partial \xi}\left(\mathcal{H}^3\frac{\partial^3 \mathcal{H}}{\partial \xi^3}\right) = (c+1)\Theta(\xi), \tag{2.100}$$

with

$$\mathcal{H}(\xi) \to 1 \qquad \text{as} \quad \xi \to \infty, \tag{2.101}$$

$$\mathcal{H} = \mathcal{H}^3(\partial^3\mathcal{H}/\partial\xi^3) = 0 \qquad \text{at} \quad \xi = 0. \tag{2.102}$$

The first condition ensures that the two non-decaying modes $\mathcal{H} - 1 \propto 1$ and $\exp\left((3/4)(3(3c+4)/4)^{1/3}\xi^{4/3}\right)$ are excluded.

For $\xi \ll 1$ (i.e., near $x = 1$), we balance the capillary and injection terms in (2.100). Assuming the solution is of the form $\mathcal{H} \propto \xi \log^p(\xi^r)$ for some exponents p and r, this yields

$$\frac{\partial \mathcal{H}}{\partial \xi} \sim (12(c+1))^{1/4}\log^{1/4}(1/\xi), \tag{2.103}$$

for which the first and second terms in (2.100) are indeed sub-dominant. Writing the position of the apparent contact line $a = 1+b$, we expect to find a quasi-static region near $x = 1$ with an apparent contact line at $x - 1 = b$. In this region, the capillary term dominates and the profile of the film is linear to leading order, $h \propto (1+b-x)$, with slope given by matching with (2.103), resulting in

$$\frac{\partial h}{\partial x} = -12^{1/4}t^{c/4}\log^{1/4}\left(t^{(3c+4)/4}/(b(c+1)^{3/4})\right). \tag{2.104}$$

Using the Cox–Voinov law, we obtain the spreading speed (and, thus, b) as

$$\dot{b} \sim \frac{12^{3/4}t^{3c/4}\log^{3/4}\left(t^{(3c+4)/4}/(b(c+1)^{3/4})\right)}{9\log\left(bt^{c/4}/\delta\right)}, \tag{2.105}$$

which holds for early time.

For late time, we scale

$$h = \frac{\bar{h}}{\lambda_c}, \qquad t = \frac{\bar{t}}{\lambda_c^{1/(c+1)}}, \tag{2.106}$$

where we assume $\lambda_c \ll 1$. Repeating the analysis in Section 2.3.3, we find the appropriate choice of λ_c is (*cf.* (2.74))

$$\lambda_c = \frac{1}{\log^{(c+1)/(3c+4)}(1/\delta)}, \tag{2.107}$$

which is indeed small for $c > -1$. Therefore, we obtain the following leading-order results for the position of the apparent contact line and the maximum film thickness

$$a_0(\bar{t}\,) = \left(1 + \frac{21\bar{t}^{3c+4}}{(c+1)^3(3c+4)}\right)^{1/7}, \tag{2.108}$$

$$\bar{h}_0(0,\bar{t}\,) = \frac{3\bar{t}^{c+1}}{2(c+1)a_0} = \frac{3\bar{t}^{c+1}}{2(c+1)}\left(1 + \frac{21\bar{t}^{3c+4}}{(c+1)^3(3c+4)}\right)^{-1/7}. \tag{2.109}$$

In an analogous way to Section 2.3, we can use the Cox–Voinov law to obtain the full late-time behaviour of the film spreading when $t \gg 1/\lambda_c^{1/(c+1)}$. Again writing $a_0 = 1 + b$ and repeating the analysis in (2.81)–(2.85), we find that, for $1 \ll t \ll \log^{1/(3c+4)}(1/\delta)$, $b \ll 1$ and is given by

$$b \sim \frac{3t^{3c+4}}{(c+1)^3(3c+4)\log(1/\delta)}, \tag{2.110}$$

which is the linearisation of (2.108). For $t = O(\log^{1/(3c+4)}(1/\delta))$, we have $b = O(1)$, and the behaviour of the film spreading is given by our result (2.108).

Thus, for the late-time regime, $t \gg \log^{1/(3c+4)}(1/\delta)$, $a_0 \sim b \gg 1$, and we have

$$a_0 \sim \left(\frac{21t^{3c+4}}{(c+1)^3(3c+4)\log(t^{(4c+3)/7}/\delta)}\right)^{1/7}. \tag{2.111}$$

We note that, in the case when $c = 0$, we recover the results (2.78) and (2.79). Furthermore, when $c = -3/4$, $\bar{h}_0$ tends to a constant, i.e., injection is just enough to balance the surface-tension flow. Consequently, for $-1 < c < -3/4$, injection can no longer support a growing or constant film thickness, and, thus, the film thickness decreases at large time. For very large time, we expect capillarity to force the film to approach the thickness of the precursor layer again, and, thus, using the scaling from (2.109), $h \sim t^{(4c+3)/7}$ gives $t = \delta^{7/(4c+3)}t^\star$ as the required scaling for t. We note that the same scaling can be derived from the balance $h - \delta \sim t^{c+1}/x, x \sim (\delta^3 t)^{1/4}$ between the growth and the surface-tension term in (2.92). We do not pursue this situation further.

In figure 2.7, we show log–log plots of the numerical solution and our asymptotic predictions for the maximum film thickness at the origin and the position of the apparent contact line as functions of time for different values of c. We see a good agreement between the numerical solution and the asymptotic results for early and late time in all three cases.

Additionally, we observe that the aspect ratio, given by $h_0(0,t)/a_0(t) \sim t^{(c-1)/7}$, grows in time if $c > 1$. In this case, for late time, the thin-film hypothesis will eventually break down.

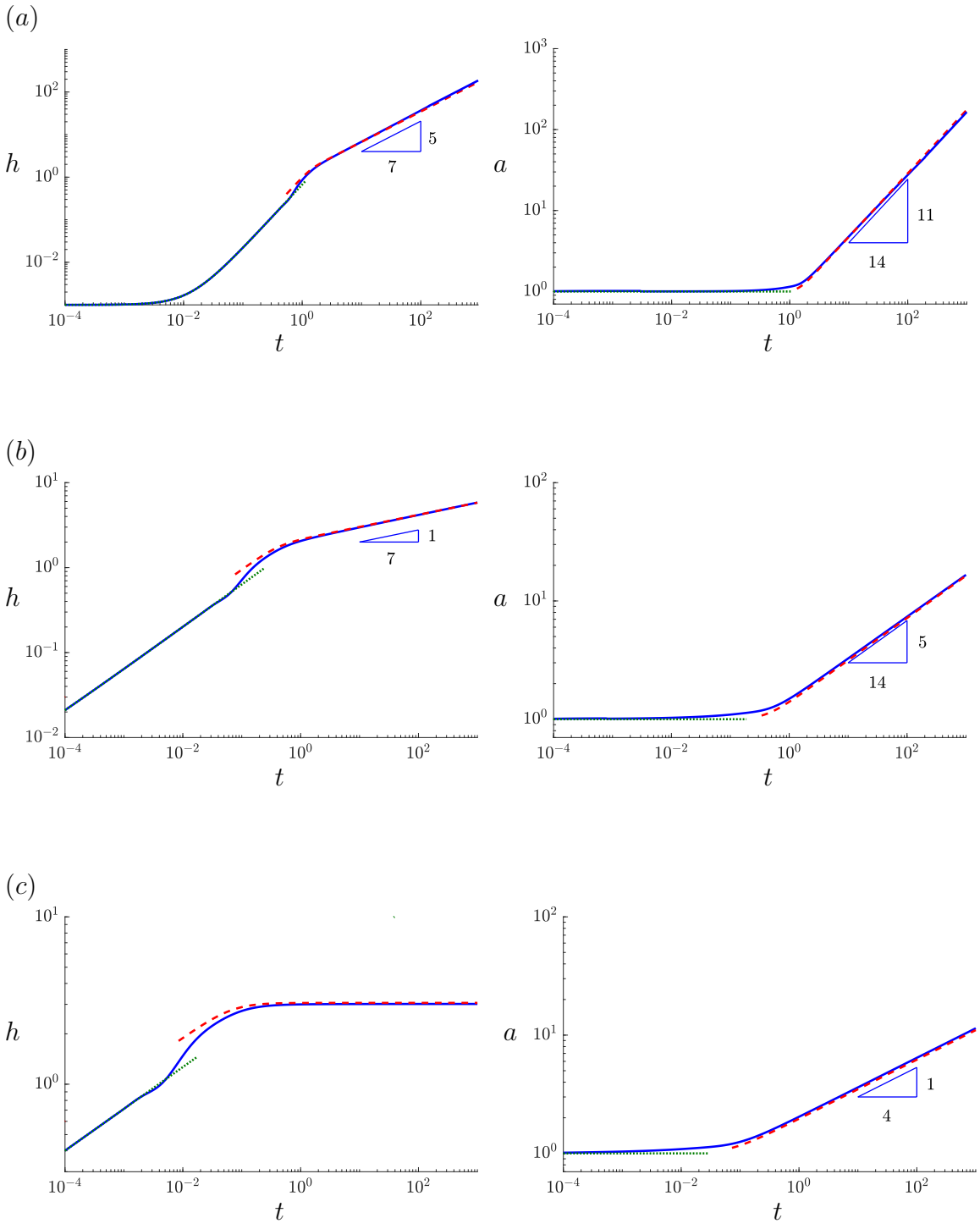

Figure 2.7: Log–log plots of the numerical solution to (2.92) with (2.24)–(2.26) (solid blue) for $h(0,t)$ (left column) and $a(t)$ (right column) for (a) $c = 1/2$, (b) $c = -1/2$, (c) $c = -3/4$. The asymptotic predictions for early time, (2.94) (dotted green), and late time, (2.108)–(2.109) (dashed red) are also shown. In all figures, $\delta = 10^{-3}$.

Finally, we note that the results (2.108)–(2.109) can be used in a simple inverse problem, in which we can determine the exponent of the injection rate, assuming it has a power-law dependence, by observing the spreading of the film front or the evolution of its maximum thickness at the origin for late time. Thus, if the film front is observed to spread like t^r for some exponent r, then the exponent of the injection rate is given by $c = (7r - 4)/3$. For example, if experimental data reveals a linear spread of the film front, then the liquid is also injected linearly in time.

2.5.2 Point-Source Injection

We now consider the case when liquid is injected at the origin only, i.e., a point-source injection with $\hat{f} = Q\delta(\hat{x})$ in (2.88), where Q is a given liquid flux. We note that, due to the definition of the delta function, $Q = 2LW$ in terms of the notation in Section 2.3. The boundary condition on $\hat{z} = 0$ then becomes

$$\hat{w} = Q\delta(\hat{x}) \qquad \text{on} \qquad \hat{z} = 0. \tag{2.112}$$

We non-dimensionalise using

$$\begin{gathered}(\hat{x}, \hat{a}) = \left(\gamma\tau^4 Q^3/\mu\right)^{1/7}(x, a), \quad (\hat{z}, \hat{h}) = \left(\mu\tau^3 Q^4/\gamma\right)^{1/7}(z, h), \\ \hat{u} = \left(\gamma Q^3/\mu\tau^3\right)^{1/7} u, \quad \hat{w} = \left(\mu Q^4/\gamma\tau^4\right)^{1/7} w, \quad \hat{t} = \tau t, \quad \hat{p} = \left(\gamma^4\mu^3/\tau^5 Q^2\right)^{1/7} p.\end{gathered} \tag{2.113}$$

We choose the timescale $\tau = (\gamma h_\infty^7/\mu Q^4)^{1/3}$ so that the dimensionless precursor-layer thickness $\delta = h_\infty \left(\mu\tau^3 Q^4/\gamma\right)^{-1/7} = 1$ and we remove all dimensionless parameters from the model. However, we are interested in the situation where the film thickness is much larger than the precursor thickness and a long timescale over which the aspect ratio $\epsilon = \left(\mu^2 Q/\gamma^2\tau\right)^{1/7} \ll 1$ so that the thin-film hypothesis is valid. Thus, we rescale our problem using

$$t \to Tt, \quad (x, a) \to T^{4/7}(x, a), \quad (z, h) \to T^{3/7}(z, h) \tag{2.114}$$

for some arbitrary $T \gg 1$. The evolution equation for h becomes

$$\frac{\partial h}{\partial t} + \frac{1}{3}\frac{\partial}{\partial x}\left(h^3 \frac{\partial^3 h}{\partial x^3}\right) = \delta(x), \tag{2.115}$$

together with (2.24)–(2.26), in which the dimensionless precursor thickness now appears as $\delta = 1/T^{3/7} \ll 1$, and where we have used the fact that $\delta(\kappa x) = \delta(x)/\kappa$ for any $\kappa > 0$. We note that the thin-film hypothesis will hold as long as the new aspect ratio $\epsilon = \left(\mu^2 Q/\gamma^2\tau T\right)^{1/7} \ll 1$, which is true for sufficiently large T. The appropriate

limit of the late-time analysis presented in Section 2.3.3 holds in this case too, since the width of the slot is asymptotically small for late time, and so, can be described by a delta function. We, thus, recover the power-law dependencies

$$a_0(\bar{t}\,) = \left(\frac{21}{32}\right)^{1/7} \bar{t}^{\,4/7}, \tag{2.116}$$

$$\bar{h}_0(0,\bar{t}\,) = \frac{3}{4}\left(\frac{32}{21}\right)^{1/7} \bar{t}^{\,3/7}, \tag{2.117}$$

where, again, we can use the Cox–Voinov law, as mentioned in Section 2.3, to obtain the full late-time behaviour. However, we note that the numerical pre-factors are not the same as those in (2.78) and (2.79), since the strength of the source in this case is half that considered in Section 2.3.3.

In figure 2.8, we show log–log plots of the maximum film thickness and the position of the apparent contact line as functions of time for the case of point-source injection. To simulate the behaviour of the delta function, we have used two approaches. First, we approximate a point-source injection using the original numerical solution with a finite injection slot of small width $\hat{L}_s = (\gamma\tau^4 Q^3/\mu)^{1/7} L_s$, keeping the total flux of liquid constant by increasing the injection rate, i.e., replacing (2.115) with

$$\frac{\partial h}{\partial t} + \frac{1}{3}\frac{\partial}{\partial x}\left(h^3 \frac{\partial^3 h}{\partial x^3}\right) = \frac{\Theta(L_s - x)}{2L_s}, \tag{2.118}$$

where $L_s \ll 1$. Second, we prescribe the flux at the origin by solving the problem

$$\frac{\partial h}{\partial t} + \frac{1}{3}\frac{\partial}{\partial x}\left(h^3 \frac{\partial^3 h}{\partial x^3}\right) = 0, \tag{2.119}$$

subject to (2.25), (2.26), and

$$\frac{\partial h}{\partial x} = 0, \qquad \frac{1}{3}h^3\frac{\partial^3 h}{\partial x^3} = \frac{1}{2} \qquad \text{at} \qquad x = 0. \tag{2.120}$$

We also plot the asymptotic results (2.116) and (2.117) across the entire t range (despite them only being formally valid for $t \gg 1$). We see a very good agreement between the numerical results obtained using the second approach and the asymptotic results for a wider range of time than anticipated. The asymptotic results provide a good estimate at late time, because, in this case, the slot has been shrunk to a point. For early time, we observe a slight discrepancy between the numerical and the asymptotic results, which can be explained by the finite precursor film, which is present everywhere on the substrate at $t = 0$ and is not reflected by our "late-time"

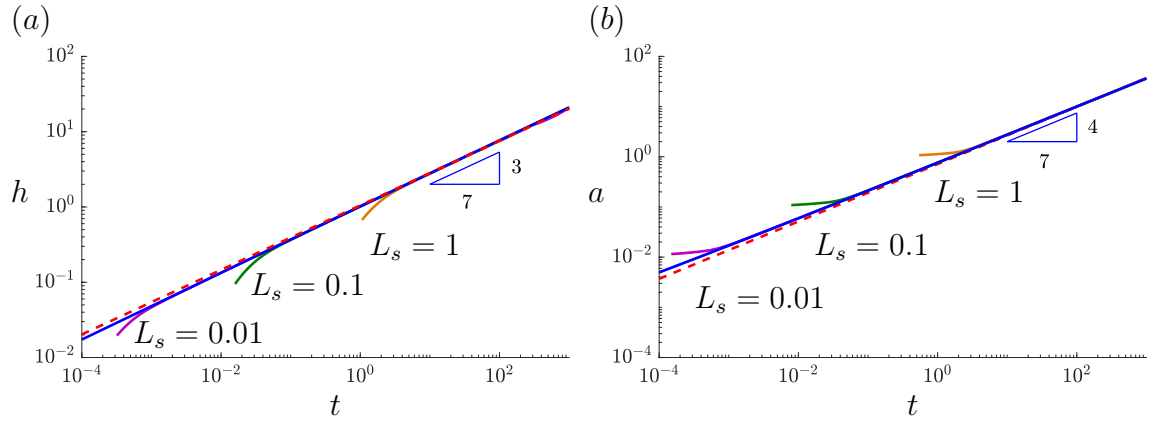

Figure 2.8: Log–log plots of the numerical solution to (2.119) with (2.120) and (2.25)–(2.26) (solid blue), the numerical solutions to (2.118) with (2.24)–(2.26) with $L_s = 1$ (orange), $L_s = 0.1$ (green), and $L_s = 0.01$ (purple) for (a) $h(0,t)$ and (b) $a(t)$, compared with the asymptotic predictions for late time (2.80) (dashed red). Here, $\delta = 10^{-3}$.

results. We also see that, as time increases, the numerical solution from the first approach converges to the numerical solution from the second approach (as anticipated) and to the asymptotic predictions (2.116) and (2.117), and the time to convergence decreases as L_s decreases. To illustrate this, we consider the early-time behaviour. As before, we determine the linear growth for early time by balancing the first and third terms in (2.118), which gives

$$h = \delta + \frac{t}{L_s}\Theta(L_s - x). \tag{2.121}$$

We obtain the range of validity of the early-time solution (2.121) by requiring that the "discontinuous" step that is initially at $x = L_s$ has not spread to the origin. By considering (2.121), we see that, if $t \ll \delta L_s$, then $h \sim \delta$, and the validity condition, found using a scaling argument on (2.119), reads

$$(\delta^3 t)^{1/4} \ll L_s. \tag{2.122}$$

If $\delta L_s \ll t \ll 1$, then $h \sim t/L_s$ from (2.121), and the validity condition is instead

$$(h^3 t)^{1/4} \ll L_s. \tag{2.123}$$

The two conditions (2.122) and (2.123) can be combined into a single range of validity, $t \ll \min\{L_s^4/\delta^3, L_s^{7/4}\}$. We note that when $L_s = 1$, the validity condition becomes $t \ll 1$, as seen in Section 2.3.1.

2.6 Thickness-Inhibited Injection

A final regime of interest is one in which the rate of injection decreases as the liquid thickness grows. Such a scenario might arise when liquid forms through a chemical reaction on the surface, which requires the chemical to diffuse through the liquid film to reach the surface. This may be captured by considering a dimensional supply flux $W/\hat{h}^q$, where $q > 0$ is a constant. We note that the case $q = 1$ is a good proxy for the problem of liquid generation caused by diffusion across the liquid layer, since, in the dimensional scenario with a strong reaction removing all the molecules at the bottom of the layer, the gas concentration adopts a linear profile across the layer, which is inversely proportional to the thickness of the layer, and thus the diffusive flux generating liquid will also be inversely proportional to the film thickness. The boundary condition on $\hat{z} = 0$ then becomes

$$\hat{w} = \frac{W}{\hat{h}^q}\Theta\left(L_R - \hat{x}\right) \qquad \text{on} \qquad \hat{z} = 0. \tag{2.124}$$

This time, we non-dimensionalise (2.1)–(2.4), (2.6)–(2.8) and (2.124) using

$$\begin{gathered}(\hat{x}, \hat{a}) = L_R(x, a), \quad (\hat{z}, \hat{h}) = \left(\mu W L_R^4/\gamma\right)^{1/(q+4)}(z, h), \\ \hat{u} = \left(\gamma^{q+1}W^3/\mu^{q+1}L_R^{3q}\right)^{1/(q+4)}u, \quad \hat{w} = \left(\gamma W^{4/q}/\mu L_R^4\right)^{q/(q+4)}w, \\ \hat{t} = \left(\mu L_R^4/\gamma W^{3/(q+1)}\right)^{(q+1)/(q+4)}t, \quad \hat{p} = \left(\gamma^{q+3}\mu W/L_R^{2q+4}\right)^{1/(q+4)}p.\end{gathered} \tag{2.125}$$

We continue assuming a long and thin geometry, i.e., that the aspect ratio

$$\epsilon = \left(\mu W/\gamma L_R^q\right)^{1/(q+4)} \ll 1, \tag{2.126}$$

and that the precursor layer is thin, i.e., $\delta = h_\infty/(\epsilon L_R) \ll 1$. The evolution equation for h is then

$$\frac{\partial h}{\partial t} + \frac{1}{3}\frac{\partial}{\partial x}\left(h^3\frac{\partial^3 h}{\partial x^3}\right) = \frac{1}{h^q}\Theta(1 - x), \tag{2.127}$$

together with (2.24)–(2.26).

For early time, we rescale the film thickness and time according to

$$h = \delta\tilde{h}, \qquad t = \delta^{q+1}\tilde{t}. \tag{2.128}$$

The leading-order (in δ) solution satisfies

$$\frac{\partial \tilde{h}_0}{\partial \tilde{t}} = \frac{1}{\tilde{h}_0^q}\Theta(1 - x) \tag{2.129}$$

with an initial condition given by

$$\tilde{h}_0 = 1 \qquad \text{at} \qquad \tilde{t} = 0. \tag{2.130}$$

The solution to (2.129) with (2.130) has a power-law behaviour in $0 \leq x \leq 1$ and is constant in $x > 1$, with

$$\tilde{h}_0(x, \tilde{t}\,) = \left(1 + (q+1)\tilde{t}\Theta(1-x)\right)^{1/(q+1)}. \tag{2.131}$$

A boundary-layer analysis near $x = 1$ analogous to the one in Section 2.3.1 provides a continuous solution smoothly joining the film thicknesses on either side of $x = 1$, but the solution cannot be solved explicitly.

For late time, we scale

$$h = \frac{\bar{h}}{\lambda_q}, \qquad t = \frac{\bar{t}}{\lambda_q^{q+1}}, \tag{2.132}$$

where we assume $\lambda_q \ll 1$. Repeating the analysis in Section 2.3.3, we find the appropriate choice of λ_q is (*cf.* (2.74))

$$\lambda_q = \frac{1}{\log^{1/(q+4)}(1/\delta)}, \tag{2.133}$$

which is indeed small for $q > 0$. We note that the analogue of (2.58) is

$$V(\bar{t}\,) = \int_0^{\bar{t}} \int_0^1 \frac{1}{\bar{h}_0^q(x,s)}\,\mathrm{d}x\,\mathrm{d}s = \int_0^{a_0(\bar{t}\,)} \bar{h}_0\,(x, \bar{t}\,)\,\mathrm{d}x, \tag{2.134}$$

where V is the leading-order volume of the liquid.

Repeating the analysis in Section 2.3.3, we obtain the outer solution for the leading-order film thickness, $\bar{h}_0$

$$\bar{h}_0\,(x, \bar{t}\,) = A(\bar{t}\,)\left(a_0^2 - x^2\right), \tag{2.135}$$

where $A(\bar{t}\,)$ satisfies

$$A(\bar{t}\,) = \frac{3V(\bar{t}\,)}{2a_0(\bar{t}\,)^3} = \frac{3}{2a_0(\bar{t}\,)^3} \int_0^{\bar{t}} \int_0^1 \frac{1}{A(s)^q (a_0^2(s) - x^2)^q}\,\mathrm{d}x\,\mathrm{d}s. \tag{2.136}$$

In this case, we end up with the following integro-differential equation for $a_0(\bar{t}\,)$

$$\dot{a}_0 = \frac{8}{9} a_0^3 A^3 = \frac{3V^3}{a_0^6} = \frac{3}{a_0^6}\left(\int_0^{\bar{t}} \int_0^1 \frac{1}{A(s)^q (a_0^2(s) - x^2)^q}\,\mathrm{d}x\,\mathrm{d}s\right)^3. \tag{2.137}$$

We note that setting $q = 0$ recovers (2.76).

In order to make further analytical progress, we first transform (2.137) into an ordinary differential equation by differentiating both sides with respect to time and using (2.136). We then obtain

$$\ddot{a}_0 = -6\frac{\dot{a}_0^2}{a_0} + 4\chi(\bar{t}\,)\left(\frac{9\dot{a}_0}{8a_0^3}\right)^{(2-q)/3}, \tag{2.138}$$

where

$$\chi(\bar{t}\,) = \int_0^1 \frac{1}{(a_0(\bar{t}\,)^2 - x^2)^q}\,\mathrm{d}x. \tag{2.139}$$

Anticipating that $a_0 \gg 1$ for large $\bar{t}$, we approximate (2.138) by

$$\ddot{a}_0 = -6\frac{\dot{a}_0^2}{a_0} + 4\left(\frac{9\dot{a}_0}{8a_0^3}\right)^{(2-q)/3}\frac{1}{a_0^{2q}}. \tag{2.140}$$

If we now try an ansatz of the form $a_0 = C\bar{t}^{\,D}$ in (2.140), we find

$$D = \frac{q+4}{4q+7}, \qquad C = \left(\frac{2^{3q}3^{1-2q}(4q+7)^{q+4}}{(q+4)^{q+1}(q+7)^3}\right)^{1/(4q+7)}. \tag{2.141}$$

We, thus, obtain the power-law behaviour of the maximum film thickness and the position of the apparent contact line for $\bar{t} \gg 1$

$$\bar{h}_0(0,\bar{t}\,) \sim \left(\frac{9(q+4)}{8(4q+7)}\right)^{1/3} C^{4/3}\bar{t}^{\,3/(4q+7)}, \tag{2.142}$$

$$a_0(\bar{t}\,) \sim C\bar{t}^{\,(q+4)/(4q+7)}. \tag{2.143}$$

We see that setting $q = 0$ recovers (2.78) and (2.79). We note that we can obtain the exponents of these power-law dependencies using the scaling arguments, found at the end of Section 2.3. Also, as mentioned in Section 2.3, it is possible to use the Cox–Voinov law in the case of thickness-dependent injection to obtain the true late-time behaviour of the film spreading. In particular, our results (2.142) and (2.143) are valid for $1 \ll \bar{t} = \lambda_q^{q+1}t \ll \lambda_q^{q+1}/\delta^{(4q+7)/3}$, which agrees with the range for t found at the end of Section 2.3.3.3 for the case $q = 0$. We also remark that the aspect ratio for the problem is $\epsilon = h_0/a_0 \sim t^{-(q+1)/(4q+7)} \ll 1$ for large t and $q > 0$, and so, the thin-film hypothesis holds.

To illustrate our analysis for a particular value of q, we take $q = 2$, for which (2.138) simplifies substantially, and we can perform the integration in (2.139):

$$\int_0^1 \frac{1}{(a_0^2 - x^2)^2}\,\mathrm{d}x = \frac{(a_0^2-1)\coth^{-1}(a_0) - a_0}{2a_0^3(a_0^2-1)} \sim \frac{1}{a_0^4} \qquad \text{for} \qquad a_0 \gg 1. \tag{2.144}$$

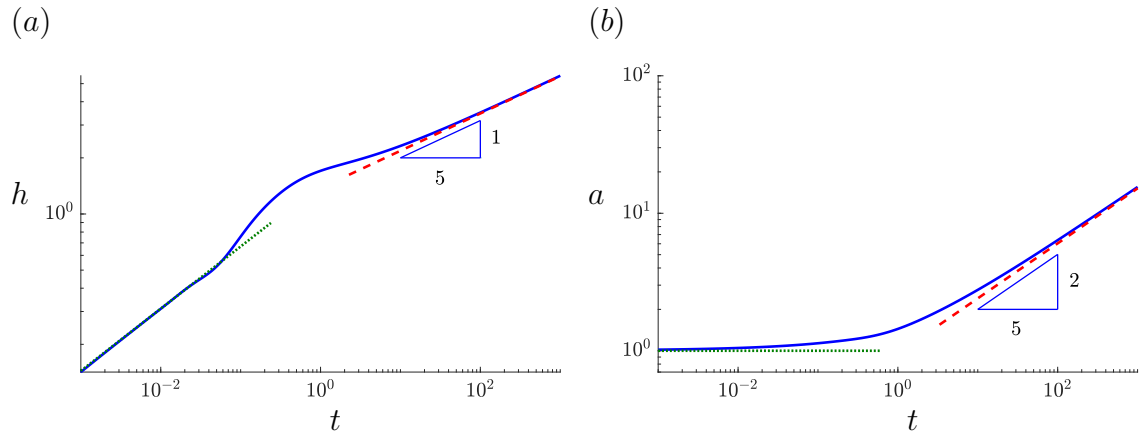

Figure 2.9: Log–log plots of the numerical solution to (2.127) with (2.24)–(2.26) (solid blue) with $q = 2$ for (a) $h(0,t)$ and (b) $a(t)$, compared with the asymptotic predictions for early time, (2.131) (dotted green), and late time, (2.145)–(2.146) (dashed red). Here, $\delta = 10^{-3}$.

We then have

$$a_0(\bar{t}\,) \sim \left(\frac{50}{9}\right)^{1/5} \bar{t}^{\,2/5}, \tag{2.145}$$

$$\bar{h}_0(0,\bar{t}\,) \sim \left(\frac{5 \times 9^{1/3}}{4}\right)^{1/5} \bar{t}^{\,1/5}. \tag{2.146}$$

In figure 2.9, we show log–log plots of the maximum film thickness and the position of the apparent contact line for the case of thickness-inhibited injection with $q = 2$. We see a very good agreement between the numerical solutions and the asymptotic results for early time, given by (2.131), and late time, given by (2.145)–(2.146).

2.7 A Coupled Diffusion Model for Liquid-Film Growth

We will now extend our paradigm problem by incorporating diffusion of sulphur dioxide through the gas and the liquid, and a chemical reaction on part of the substrate, where sulphur dioxide is converted into liquid sulphuric acid. This is an idealised representation of the microscale fluid flow over a pellet–fibre pair in the filter sheets. We use the same geometrical set-up as in Section 2.2, in which the injection region will now be the reaction site. Our aim is to explore how the diffusive transport of sulphur dioxide alters the resulting flow problem.

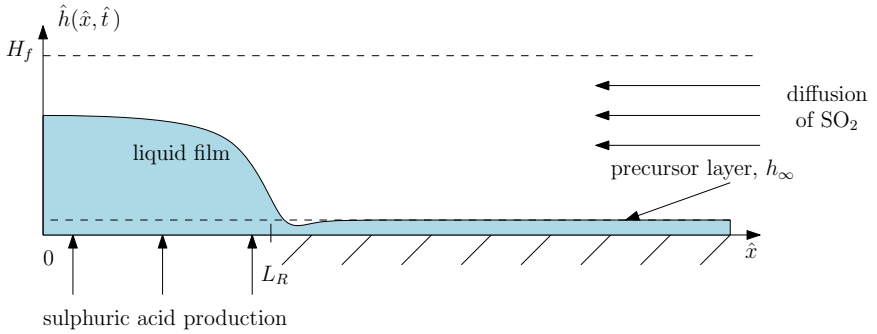

Figure 2.10: A schematic diagram for the geometrical set-up of the coupled model with gas transport.

2.7.1 Mathematical Model

Our paradigm problem is shown schematically in figure 2.10. Gas enters the system from the right-hand side of the system and diffuses inwards, through the liquid layer, and reacts to form new liquid on the substrate in the region between 0 and L_R. We note that the gas is assumed to move by diffusion only, as, in the real application, the gas diffuses into the filter sheets from the channels. We assume symmetry at $\hat{x} = 0$ and also at $\hat{z} = H_f$. Initially, we assume that a thin layer of sulphuric acid of thickness h_∞ resides above the substrate. We denote sulphur dioxide concentration in the gas and in the liquid by $\hat{s}_g$ and $\hat{s}_l$, respectively. Appealing to conservation of mass, we have

$$\frac{\partial \hat{s}_g}{\partial \hat{t}} = D_{s_g}\left(\frac{\partial^2 \hat{s}_g}{\partial \hat{x}^2} + \frac{\partial^2 \hat{s}_g}{\partial \hat{z}^2}\right) \qquad \text{in } \hat{z} > \hat{h}(\hat{x},\hat{t}), \tag{2.147}$$

$$\frac{\partial \hat{s}_l}{\partial \hat{t}} + \nabla\cdot(\hat{\boldsymbol{u}}_{\boldsymbol{l}}\hat{s}_l) = D_{s_l}\left(\frac{\partial^2 \hat{s}_l}{\partial \hat{x}^2} + \frac{\partial^2 \hat{s}_l}{\partial \hat{z}^2}\right) \qquad \text{in } \hat{z} < \hat{h}(\hat{x},\hat{t}), \tag{2.148}$$

where $\hat{\boldsymbol{u}}_{\boldsymbol{l}} = (\hat{u}_{l,1}, \hat{u}_{l,2})$ $\hat{u}_{l,1}$ is the liquid velocity, $\hat{h}(\hat{x},\hat{t}\,)$ is the thickness of the liquid layer, and D_{s_g} and D_{s_l} are the diffusivities of sulphur dioxide in the gas and in the liquid, respectively. We note that, in writing (2.147) and (2.148), we have assumed that, in the liquid, sulphur dioxide is transported by diffusion and advection that results from the liquid flow. However, as we will see in Section 2.7.3 after we non-dimensionalise the model and use parameters from table 1.1, we will ignore the advective terms, since the advective timescale associated with fluid transport due to the reaction (on the order of days) is slower than the diffusive timescale in the liquid (on the order of seconds). Thus, in order to close the system, we need an evolution equation for the film thickness, $\hat{h}$. We follow the derivation in Section 2.2.1, except

for the boundary condition on $\hat{z} = 0$, which we modify to take account of the sulphuric acid production due to the chemical reaction that takes place there. We model the rate of production of sulphuric acid using mass-action kinetics applied to sulphur dioxide molecules with stoichiometry given by (1.1), i.e., two molecules of sulphur dioxide react to produce two molecules of sulphuric acid. We recall that we do not include dependence on oxygen and water vapour at this stage, as we assume they are abundant in the system. We present the case of non-constant oxygen concentration in Appendix C and derive a model for hygroscopy of sulphuric acid that takes account of water vapour in Chapter 6. Thus, the relevant boundary condition on $\hat{z} = 0$ is

$$\hat{w} = 2kV_{\mathrm{m}}\hat{s}_l^2\Theta(L_R - \hat{x}) \qquad \text{on} \qquad \hat{z} = 0, \tag{2.149}$$

where k is the reaction rate constant, and V_{m} is the molar volume of sulphuric acid. Thus, the evolution equation for $\hat{h}$ becomes

$$\frac{\partial \hat{h}}{\partial \hat{t}} + \frac{\gamma}{3\mu}\frac{\partial}{\partial \hat{x}}\left(\hat{h}^3\frac{\partial^3 \hat{h}}{\partial \hat{x}^3}\right) = 2kV_{\mathrm{m}}\hat{s}_l^2|_{\hat{z}=0}\Theta(L_R - \hat{x}), \tag{2.150}$$

where we have the notation from Section 2.2. We note that in writing (2.150) we have already assumed a thin-film (lubrication) approximation, as in Section 2.2. In particular, $\hat{\boldsymbol{u}}_{\boldsymbol{l}}$ is given by solving the dimensional version of (2.15)–(2.18), (2.20)–(2.22), together with (2.149). We give the dimensionless expression for $\hat{\boldsymbol{u}}_{\boldsymbol{l}}$ in the next section.

At the substrate surface, we use local conservation of mass to balance the total flux of sulphur dioxide into the reaction region with the amount being consumed by the reaction. These can be written as

$$D_{s_l}\frac{\partial \hat{s}_l}{\partial \hat{z}} - \hat{u}_{l,2}\hat{s}_l = 2k\hat{s}_l^2\Theta(L_R - \hat{x}) \qquad \text{at} \qquad \hat{z} = 0. \tag{2.151}$$

At the gas–liquid interface, we assume that the flux of sulphur dioxide is conserved, and that the concentrations on either side of the interface are related via Henry's law, with constant related to the ratio of the solubility of sulphur dioxide in the gas and the liquid (see discussion in Section 1.2.4 and Appendix A). Thus, we write

$$D_{s_g}\frac{\partial \hat{s}_g}{\partial \hat{n}} = D_{s_l}\frac{\partial \hat{s}_l}{\partial \hat{n}} \qquad \text{at} \qquad \hat{z} = \hat{h}(\hat{x}, \hat{t}), \tag{2.152}$$

$$\hat{s}_g = \beta_s \hat{s}_l \qquad \text{at} \qquad \hat{z} = \hat{h}(\hat{x}, \hat{t}), \tag{2.153}$$

where $\partial/\partial\hat{n}$ denotes the directional derivative in the direction of the outwards-pointing unit normal to the film, and β_s is the Henry's law constant for sulphur

dioxide. Using the symmetry about $\hat{z} = H_f$, we have the no-flux condition

$$\frac{\partial \hat{s}_g}{\partial \hat{z}} = 0 \qquad \text{at} \qquad \hat{z} = H_f. \tag{2.154}$$

We assume that the reaction region is symmetric about $\hat{x} = 0$, and so we also write

$$\frac{\partial \hat{s}_g}{\partial \hat{x}} = \frac{\partial \hat{s}_l}{\partial \hat{x}} = \frac{\partial \hat{h}}{\partial \hat{x}} = \frac{\partial^3 \hat{h}}{\partial \hat{x}^3} = 0 \qquad \text{at} \qquad \hat{x} = 0. \tag{2.155}$$

We assume that, far away from the reaction region, the concentration of sulphur dioxide in the gas is given by a constant concentration, S_0. Furthermore, we require that, away from the reaction region, the film thickness approaches that of the precursor film, h_∞. Thus, we have

$$\hat{s}_g \to S_0, \quad \hat{s}_l \to \frac{S_0}{\beta_s}, \quad \hat{h} \to h_\infty \qquad \text{as} \qquad \hat{x} \to \infty. \tag{2.156}$$

We use initial conditions that are consistent with the boundary conditions (2.156), so that we write

$$\hat{s}_g = S_0, \quad \hat{s}_l = \frac{S_0}{\beta_s}, \quad \hat{h} = h_\infty \qquad \text{at} \qquad \hat{t} = 0. \tag{2.157}$$

2.7.2 Dimensionless Model

We non-dimensionalise the model (2.147)–(2.157) using

$$\hat{x} = L_R x, \quad (\hat{z}, \hat{h}) = H_f(z, h), \quad \hat{t} = (\mu L_R^4/\gamma H_f^3)t,$$
$$\hat{u}_{l,1} = (kL_R S_0^2 V_\mathrm{m}/\beta_s^2 H_f)u_{l,1}, \quad \hat{u}_{l,2} = (kS_0^2 V_\mathrm{m}/\beta_s^2)u_{l,2}, \quad \hat{s}_g = S_0 s_g, \quad \hat{s}_l = (S_0/\beta_s)s_l, \tag{2.158}$$

where we have chosen the timescale associated with capillary spreading due to surface tension, in which the two terms on the left-hand side of the film-evolution equation (2.150) balance, the velocity scale in the $\hat{z}$-direction, associated with liquid growth due to the reaction, and have rescaled the velocity scale in the $\hat{x}$-direction appropriately due to the small aspect ratio $\epsilon = H_f/L_R \ll 1$. The corresponding equations, and initial and boundary conditions become

$$\eta_s \tau_s \frac{\partial s_g}{\partial t} = \left(\epsilon^2 \frac{\partial^2 s_g}{\partial x^2} + \frac{\partial^2 s_g}{\partial z^2}\right) \qquad \text{in} \qquad z > h(x,t), \tag{2.159}$$

$$\tau_s \frac{\partial s_l}{\partial t} + \alpha_s \kappa_s \nabla \cdot (\boldsymbol{u_l} s_l) = \left(\epsilon^2 \frac{\partial^2 s_l}{\partial x^2} + \frac{\partial^2 s_l}{\partial z^2}\right) \qquad \text{in} \qquad z < h(x,t), \tag{2.160}$$

and

$$\frac{\partial h}{\partial t} + \frac{1}{3}\frac{\partial}{\partial x}\left(h^3 \frac{\partial^3 h}{\partial x^3}\right) = \frac{2\alpha_s \kappa_s}{\tau_s} s_l^2|_{z=0} \Theta(1-x), \tag{2.161}$$

where

$$\begin{aligned} u_{l,1} &= -\frac{\tau_s}{2\alpha_s\kappa_s}\frac{\partial^3 h}{\partial x^3}z(z-2h), \\ u_{l,2} &= \frac{\tau_s}{2\alpha_s\kappa_s}\left(\frac{\partial^4 h}{\partial x^4}z^2\left(\frac{z}{3}-h\right)-\frac{\partial^3 h}{\partial x^3}\frac{\partial h}{\partial x}z^2\right)+2s_l^2|_{z=0}\Theta(1-x), \end{aligned} \tag{2.162}$$

which we obtain by solving (2.15)–(2.18), (2.20)–(2.22), together with the dimensionless version of (2.149). These equations are subject to the boundary conditions

$$\frac{\partial s_l}{\partial z}-\alpha_s\kappa_s u_{l,2}s_l = 2\kappa_s s_l^2\Theta(1-x) \qquad \text{at} \qquad z=0, \tag{2.163}$$

$$\frac{\partial s_g}{\partial z}-\epsilon^2\frac{\partial h}{\partial x}\frac{\partial s_g}{\partial x} = \sigma_s\left(\frac{\partial s_l}{\partial z}-\epsilon^2\frac{\partial h}{\partial x}\frac{\partial s_l}{\partial x}\right) \qquad \text{at} \qquad z=h(x,t), \tag{2.164}$$

$$s_g = s_l \qquad \text{at} \qquad z=h(x,t), \tag{2.165}$$

$$\frac{\partial s_g}{\partial z} = 0 \qquad \text{at} \qquad z=1, \tag{2.166}$$

$$\frac{\partial s_g}{\partial x} = \frac{\partial s_l}{\partial x} = \frac{\partial h}{\partial x} = \frac{\partial^3 h}{\partial x^3} = 0 \qquad \text{at} \qquad x=0, \tag{2.167}$$

$$s_g \to 1, \quad s_l \to 1, \quad h \to \delta \qquad \text{as} \qquad x\to\infty, \tag{2.168}$$

and the initial conditions

$$s_g = 1, \quad s_l = 1, \quad h=\delta \qquad \text{at} \qquad t=0, \tag{2.169}$$

where we have introduced seven dimensionless parameters

$$\begin{gathered} \alpha_s = \frac{S_0 V_{\mathrm{m}}}{\beta_s} \approx 10^{-5},\ \delta = \frac{h_\infty}{H_f} \approx 2\times10^{-3},\ \epsilon = \frac{H_f}{L_R} \approx 3\times10^{-2},\ \eta_s = \frac{D_{s_l}}{D_{s_g}} \approx 2\times10^{-4}, \\ \kappa_s = \frac{kH_f S_0}{\beta_s D_{s_l}} \approx 4\times10^{-3},\ \sigma_s = \frac{D_{s_l}}{\beta_s D_{s_g}} \approx 5\times10^{-3},\ \tau_s = \frac{\gamma H_f^5}{\mu D_{s_l} L_R^4} \approx 4\times10^{-3}, \end{gathered} \tag{2.170}$$

where we have used the parameter values from table 1.1, along with $H_f = 5\times10^{-7}\,\mathrm{m}$ and $L_R = 2\times10^{-5}\,\mathrm{m}$, chosen to be representative of the real problem.

We conclude with a remark about the small-aspect-ratio assumption. In principle, the external restriction that $H_f/L_R \ll 1$ is not necessary. For the liquid problem, we could instead follow the analysis in Section 2.2 and pick an intrinsic scale for the film thickness that is consistent with the long and thin hypothesis. For the gas problem, we could make use of slender-body theory, where the film is assumed to be sufficiently thin, so that the equation for the sulphur dioxide concentration holds everywhere above the substrate and the reaction can be treated as a point sink, as far as the outer problem is concerned (see, for example, Dunn *et al.*, 2008; Schofield *et al.*, 2020; Wray *et al.*, 2020, where they consider evaporation of droplets with vapour transport above them).

2.7.3 Relevant Distinguished Limit: $\kappa_s = O(1), \alpha_s, \sigma_s, \tau_s = O(\epsilon^2)$

We will now explore a distinguished limit of the model presented in Section 2.7.2. Since the coefficients in front of the time derivatives in (2.159) and (2.160) are small, we consider a distinguished limit, in which we balance them with diffusion in the horizontal direction. This amounts to choosing $\tau_s = \epsilon^2\tilde{\tau}_s$, where $\tilde{\tau}_s = O(1)$. In addition, for the richest asymptotic limit, we assume $\eta_s = O(1)$. We can then distil the relevant sub-limits for our set-up when $\eta_s \ll 1$, for example.

We identify κ_s as a relevant parameter that has an immediate physical significance and measures the ratio of the reaction rate to the diffusive mass transfer rate (which is commonly called the Damköhler number). For a distinguished limit, we assume that $\kappa_s = O(1)$, i.e., diffusion balances the reaction in (2.163). We also take $\sigma_s = \epsilon^2\tilde{\sigma}_s$, where $\tilde{\sigma}_s = O(1)$ and $\alpha_s = \epsilon^2\tilde{\alpha}_s$, where $\tilde{\alpha}_s = O(1)$.

We asymptotically expand s_g, s_l and h in powers of ϵ^2

$$s_g \sim s_g^{(0)} + \epsilon^2 s_g^{(1)} + \epsilon^4 s_g^{(2)} + \cdots \qquad \text{as} \qquad \epsilon \to 0, \tag{2.171}$$

$$s_l \sim s_l^{(0)} + \epsilon^2 s_l^{(1)} + \epsilon^4 s_l^{(2)} + \cdots \qquad \text{as} \qquad \epsilon \to 0, \tag{2.172}$$

$$h \sim h^{(0)} + \epsilon^2 h^{(1)} + \epsilon^4 h^{(2)} + \cdots \qquad \text{as} \qquad \epsilon \to 0. \tag{2.173}$$

The leading-order problem for s_g, s_l and h is

$$\frac{\partial^2 s_g^{(0)}}{\partial z^2} = 0 \qquad \text{in} \qquad z > h(x,t), \tag{2.174}$$

$$\frac{\partial^2 s_l^{(0)}}{\partial z^2} = 0 \qquad \text{in} \qquad z < h(x,t), \tag{2.175}$$

and

$$\frac{\partial h^{(0)}}{\partial t} + \frac{1}{3}\frac{\partial}{\partial x}\left(h^{(0)3}\frac{\partial^3 h^{(0)}}{\partial x^3}\right) = \frac{2\tilde{\alpha}_s\kappa_s}{\tilde{\tau}_s} s_l^{(0)2}|_{z=0}\Theta(1-x), \tag{2.176}$$

subject to the boundary conditions

$$\frac{\partial s_l^{(0)}}{\partial z} = 2\kappa_s s_l^{(0)2}\Theta(1-x) \qquad \text{at} \qquad z = 0, \tag{2.177}$$

$$\frac{\partial s_g^{(0)}}{\partial z} = 0 \qquad \text{at} \qquad z = h(x,t), \tag{2.178}$$

$$s_g^{(0)} = s_l^{(0)} \qquad \text{at} \qquad z = h(x,t), \tag{2.179}$$

$$\frac{\partial s_g^{(0)}}{\partial z} = 0 \qquad \text{at} \qquad z = 1, \tag{2.180}$$

$$\frac{\partial s_g^{(0)}}{\partial x} = \frac{\partial s_l^{(0)}}{\partial x} = \frac{\partial h^{(0)}}{\partial x} = \frac{\partial^3 h^{(0)}}{\partial x^3} = 0 \qquad \text{at} \qquad x = 0, \tag{2.181}$$

$$s_g^{(0)} \to 1, \quad s_l^{(0)} \to 1, \quad h^{(0)} \to \delta \qquad \text{as} \qquad x \to \infty, \tag{2.182}$$

and the initial conditions

$$s_g^{(0)} = 1, \quad s_l^{(0)} = 1, \quad h^{(0)} = \delta \qquad \text{at} \qquad t = 0. \tag{2.183}$$

Integrating (2.174) and using (2.178) and (2.180), we find that $s_g^{(0)}$ is independent of z, i.e.,

$$s_g^{(0)} = s_g^{(0)}(x,t). \tag{2.184}$$

For $x < 1$, integrating (2.175) and using (2.177), we obtain

$$s_l^{(0)} = 2\kappa_s \mathcal{G}(x,t)^2 z + \mathcal{G}(x,t) \qquad \text{in} \qquad 0 \le x \le 1, \tag{2.185}$$

where, using (2.179),

$$\mathcal{G}(x,t) = \frac{-1 + \sqrt{1 + 8\kappa_s h^{(0)} s_g^{(0)}}}{4\kappa_s h^{(0)}} = \frac{2 s_g^{(0)}}{1 + \sqrt{1 + 8\kappa_s h^{(0)} s_g^{(0)}}}, \tag{2.186}$$

and we have obtained the second equality after using the formula $A^2 - B^2 = (A - B)(A + B)$. We note that we have taken the positive square root for $\mathcal{G}$ to ensure the concentration is non-negative.

For $x > 1$, integrating (2.175) and using (2.177), we obtain that $s_l^{(0)}$ is independent of z, i.e.,

$$s_l^{(0)} = s_l^{(0)}(x,t). \tag{2.187}$$

The boundary condition (2.179), together with (2.187), dictate that

$$s_l^{(0)} = s_g^{(0)} \qquad \text{in} \qquad x > 1. \tag{2.188}$$

The apparent discontinuity in $s_l^{(0)}$ at $x = 1$, behind which $s_l^{(0)}$ is linear in z, and ahead of which it is independent of z, can be resolved via a boundary-layer analysis, where we need to scale $x = 1 + \epsilon\tilde{x}$ so that the second term (diffusion in the horizontal direction) in (2.160) contributes at leading order. The resulting problem is not explicitly solvable.

Since $s_g^{(0)}$ is undetermined at this stage, we need to consider the equations and boundary conditions at $O(\epsilon^2)$ in order to close the problem. The relevant equation for $s_g^{(1)}$ is

$$\eta_s \tilde{\tau}_s \frac{\partial s_g^{(0)}}{\partial t} = \frac{\partial^2 s_g^{(0)}}{\partial x^2} + \frac{\partial^2 s_g^{(1)}}{\partial z^2}. \tag{2.189}$$

We also need the following boundary conditions, which follow from evaluating (2.166) and (2.164) at $O(\epsilon^2)$

$$\frac{\partial s_g^{(1)}}{\partial z} - \frac{\partial h^{(0)}}{\partial x}\frac{\partial s_g^{(0)}}{\partial x} = \tilde{\sigma}_s \frac{\partial s_l^{(0)}}{\partial z} \qquad \text{at} \qquad z = h(x,t), \tag{2.190}$$

$$\frac{\partial s_g^{(1)}}{\partial z} = 0 \qquad \text{at} \qquad z = 1. \tag{2.191}$$

Integrating (2.189) with respect to z from h to 1 and noting that $s_g^{(0)}$ does not depend on z, we obtain

$$\begin{aligned}(1-h^{(0)})\left(\eta_s\tilde{\tau}_s\frac{\partial s_g^{(0)}}{\partial t} - \frac{\partial^2 s_g^{(0)}}{\partial x^2}\right) = \frac{\partial s_g^{(1)}}{\partial z}\bigg|_{z=h}^{z=1} &= -\tilde{\sigma}_s\frac{\partial s_l^{(0)}}{\partial z} - \frac{\partial h^{(0)}}{\partial x}\frac{\partial s_g^{(0)}}{\partial x} \\ &= -2\tilde{\sigma}_s\kappa_s\mathcal{G}^2\Theta(1-x) - \frac{\partial h^{(0)}}{\partial x}\frac{\partial s_g^{(0)}}{\partial x},\end{aligned} \tag{2.192}$$

using (2.191), (2.190), and (2.185). Thus, we have (dropping the superscripts on the variables for convenience)

$$\eta_s\tilde{\tau}_s(1-h)\frac{\partial s_g}{\partial t} - \frac{\partial}{\partial x}\left((1-h)\frac{\partial s_g}{\partial x}\right) = -2\tilde{\sigma}_s\kappa_s\left(\frac{2s_g}{1+\sqrt{1+8\kappa_s h s_g}}\right)^2\Theta(1-x), \tag{2.193}$$

$$\frac{\partial h}{\partial t} + \frac{1}{3}\frac{\partial}{\partial x}\left(h^3\frac{\partial^3 h}{\partial x^3}\right) = \frac{2\tilde{\alpha}_s\kappa_s}{\tilde{\tau}_s}\left(\frac{2s_g}{1+\sqrt{1+8\kappa_s h s_g}}\right)^2\Theta(1-x), \tag{2.194}$$

subject to the boundary conditions

$$\frac{\partial s_g}{\partial x} = \frac{\partial h}{\partial x} = \frac{\partial^3 h}{\partial x^3} = 0 \qquad \text{at} \qquad x = 0, \tag{2.195}$$

$$s_g \to 1, \quad h \to \delta \qquad \text{as} \qquad x \to \infty, \tag{2.196}$$

and the initial conditions

$$s_g = 1, \quad h = \delta \qquad \text{at} \qquad t = 0. \tag{2.197}$$

We note an important feature of (2.194), namely, that the film growth depends inversely on its thickness. This is reminiscent of the thickness-inhibited injection presented in Section 2.6.

In Appendix C, we present a similar analysis in the case when the oxygen concentration is not constant.

2.7.4 Particular Sub-Limits

Our final model (2.193)–(2.197) and (2.185)–(2.188) involves five dimensionless groups, namely, $\eta_s\tilde{\tau}_s$, $\tilde{\sigma}_s$, κ_s, $\tilde{\alpha}_s$, and δ. This suggests that our problem is likely to possess a rich structure depending on the parameter values. To illustrate this, we now show how we can distil a few distinct and important sub-limits of potential interest from (2.193) and (2.194). In all of them, for simplicity, we keep $\eta_s\tilde{\tau}_s = O(1)$.

Firstly, we look at the case when diffusion in the liquid happens much faster than the reaction. Thus, letting $\kappa_s \to 0$ and having $\tilde{\sigma}_s\kappa_s = O(1)$ and $\tilde{\alpha}_s\kappa_s = O(1)$, which correspond to having small reaction rate but large mass transfer across the gas–liquid interface ($\tilde{\sigma}_s \gg 1$) and large amount of sulphur dioxide ($\tilde{\alpha}_s \gg 1$), respectively, the resulting governing equations (2.193) and (2.194) for s_g and h (with the same initial and boundary conditions) read

$$\eta_s\tilde{\tau}_s(1-h)\frac{\partial s_g}{\partial t} - \frac{\partial}{\partial x}\left((1-h)\frac{\partial s_g}{\partial x}\right) = -2\tilde{\sigma}_s\kappa_s s_g^2\Theta(1-x), \tag{2.198}$$

$$\frac{\partial h}{\partial t} + \frac{1}{3}\frac{\partial}{\partial x}\left(h^3\frac{\partial^3 h}{\partial x^3}\right) = \frac{2\tilde{\alpha}_s\kappa_s s_g^2}{\tilde{\tau}_s}\Theta(1-x). \tag{2.199}$$

In this limit, the "source" terms on the right-hand sides of (2.198) and (2.199) lose the h-dependence.

If we now further look at the case of moderate mass transfer across the gas–liquid interface ($\tilde{\sigma}_s = O(1)$, for example), but still have large amount of sulphur dioxide in the gas ($\tilde{\alpha}_s\kappa_s = O(1)$), the right-hand side of (2.198) becomes zero. Equation (2.198) admits the solution $s_g = 1$. Thus, the right-hand side of (2.199) is constant, which corresponds to the constant-injection case we considered in Section 2.2, with the sulphur dioxide removed from the gas by the reaction instantaneously replenished by diffusion.

Similarly, if we look at the case when there is moderate amount of sulphur dioxide in the gas ($\tilde{\alpha}_s = O(1)$, for example), but we still have large mass transfer across the gas–liquid interface ($\tilde{\sigma}_s\kappa_s = O(1)$), the right-hand side of (2.199) is zero, and thus the solution for h is given by $h = \delta$. In this case, we have absorption of sulphur dioxide with no growth of the film.

Ultimately, if both $\tilde{\sigma}_s$ and $\tilde{\alpha}_s$ are $O(1)$, we get the expected trivial constant solutions, $s_g = 1$ and $h = \delta$. All of these sub-limits apply equally well to the case of non-constant oxygen concentration in the liquid, presented in Appendix C.

Secondly, if we consider a reaction that occurs much faster than diffusion in the liquid, then we let $\kappa_s \to \infty$ in (2.193) and (2.194) to obtain

$$\eta_s \tilde{\tau}_s (1-h)\frac{\partial s_g}{\partial t} - \frac{\partial}{\partial x}\left((1-h)\frac{\partial s_g}{\partial x}\right) = -\frac{\tilde{\sigma}_s s_g}{h}\Theta(1-x), \tag{2.200}$$

$$\frac{\partial h}{\partial t} + \frac{1}{3}\frac{\partial}{\partial x}\left(h^3\frac{\partial^3 h}{\partial x^3}\right) = \frac{\tilde{\alpha}_s s_g}{h}\Theta(1-x). \tag{2.201}$$

In this case, we have an example of the simple thickness-inhibited injection, considered in Section 2.6, with a rate that is proportional to $1/h$.

If we allow $\tilde{\sigma}_s \to 0$, i.e., small mass transfer across the gas–liquid interface, but keep $\tilde{\alpha}_s = O(1)$, i.e., a moderate amount of sulphur dioxide, then we again obtain $s_g = 1$. However, this time the right-hand side of (2.201) takes the form of the thickness-inhibited-injection case we considered in Section 2.6 with $q = 1$.

Similarly, one can look at the case of small amount of sulphur dioxide in the gas, $\tilde{\alpha}_s \to 0$, with moderate mass transfer, $\tilde{\sigma}_s = O(1)$, which gives the constant solution $h = \delta$.

If both $\tilde{\sigma}_s, \tilde{\alpha}_s \to 0$, we recover the trivial constant solutions as before. This has an important implication and shows that provided $\tilde{\sigma}_s$ and $\tilde{\alpha}_s$ are sufficiently small, the problem will not exhibit spatially or temporally varying behaviour for any values of κ_s. Again, we consider these limits in the case of non-constant oxygen concentration in Appendix C.

2.7.5 Numerical Results

We solve the problem (2.193)–(2.197) numerically using the method of lines in *Mathematica*. We again use the exact expression for the Heaviside function $\theta(x)$ and note that this time the discontinuity associated with it in (2.193) can be detected in the solutions for s_g, unlike for h, since the discontinuity appears in the second derivative of s_g. In figure 2.11(a), we show the spatial profile of the film thickness, h, at three different times before it has reached the symmetry line at $z = 1$. We see the characteristic parabolic profile and capillary ripple as in Section 2.4. Initially, the film grows faster near the end of the reaction region, since this is the closest point to the incoming sulphur dioxide, but, as time increases, the film spreads along the substrate, and the fastest increase occurs in the middle of the reaction region. In figure 2.11(b), we show the spatial profile of the sulphur dioxide concentration, s_g, in the gas for a given time. We see that the concentration is lowest above the middle of the reaction region, and that the deviation from the outer concentration extends much further than the

width of the reaction region. As time increases, the sulphur dioxide concentration decreases the most over the reaction region. We focus on the effect of varying κ_s,

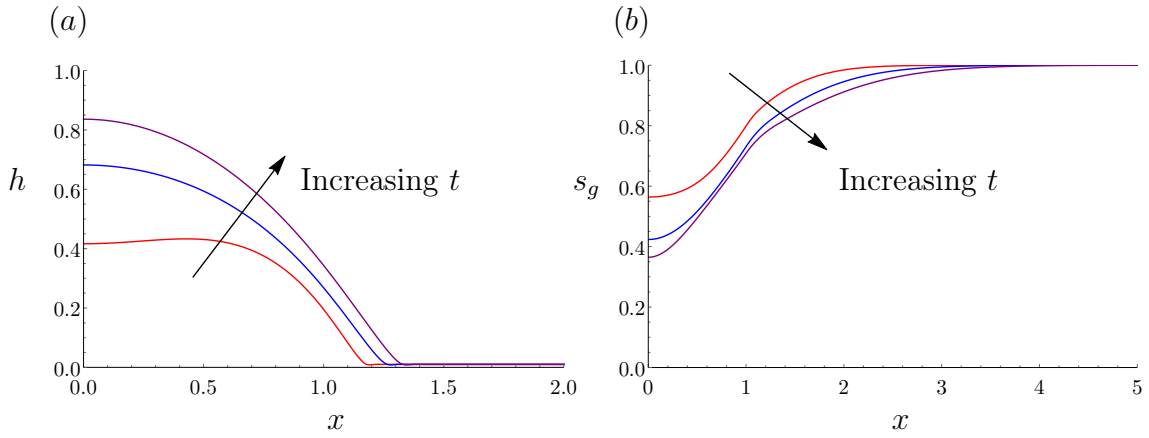

Figure 2.11: Spatial profiles of (a) the film thickness, h, and (b) the concentration of sulphur dioxide, s_g, for $t = 0.5$ (red), $t = 1$ (blue), and $t = 1.5$ (purple). In these plots, $\eta_s = \tilde{\tau}_s = \tilde{\sigma}_s = \tilde{\alpha}_s = \kappa_s = 1$.

which we recall is a measure of the relative importance of reaction to diffusion in the liquid, and we use the values: $\kappa_s = 0, 0.1, 1, 10$. We aim to illustrate some of the sub-limits mentioned towards the end of Section 2.7.3. We assume $\eta_s = \tilde{\tau}_s = \tilde{\sigma}_s = \tilde{\alpha}_s = 1$ for simplicity. In figure 2.12(a), we show how the film thickness, h, varies with x at a given time for various κ_s. We observe that, as we increase κ_s, the film thickness increases, which is expected, since large κ_s corresponds to large reaction rate (if we keep the rest of the parameters constant). We have also plotted the case $\kappa_s = 0$, which corresponds to a constant film thickness (given by the precursor thickness), as discussed in Section 2.7.3, and the case $\kappa_s = \infty$, given by (2.200) and (2.201). In order to compare these results with the results from the model considered in Sections 2.1–2.6, we have further plotted curves corresponding to the constant-injection rate, considered in Section 2.2, and thickness-inhibited injection with $q = 1$, presented in Section 2.6. We see that the thickness-inhibited injection gives fastest film growth, and the film reaches the symmetry line $z = 1$ at $t = 0.33$, which is the time at which the plots were taken. The constant-injection rate is qualitatively similar to the $\kappa_s = 1$ case. In figure 2.12(b), we plot the total volume of fluid, V, to the left of the apparent contact line at $x = a(t)$, given by

$$V = \int_0^{a(t)} h \, \mathrm{d}x, \tag{2.202}$$

as a function of κ_s at time $t = 0.87$, which is when the curve for the film thickness that corresponds to $\kappa_s = \infty$ reaches the symmetry line. As κ_s increases, the total volume

approaches a maximum value when $\kappa_s = \infty$, obtained by solving (2.200) and (2.201). In figure 2.13(a), we show the spatial profile of sulphur dioxide concentration in the gas, s_g, as κ_s varies. As we increase κ_s, the concentration drops down as expected, given the increased reaction rate. We have also plotted the case $\kappa_s = 0$, in which the sulphur dioxide concentration is constant and given by the initial condition, as discussed in Section 2.7.3, and the case $\kappa_s = \infty$, given by (2.200) and (2.201). We note that the bounding profile for $\kappa_s = \infty$ reaches a concentration of zero at the origin. In figure 2.13(b), we show the instantaneous amount of sulphur dioxide, S, removed from the gas, given by

$$S = \int_0^\infty (1 - s_g)\,\mathrm{d}x, \tag{2.203}$$

as a function of κ_s, again at time $t = 0.87$. As we increase κ_s, this amount again approaches a maximum value given by the case when $\kappa_s = \infty$.

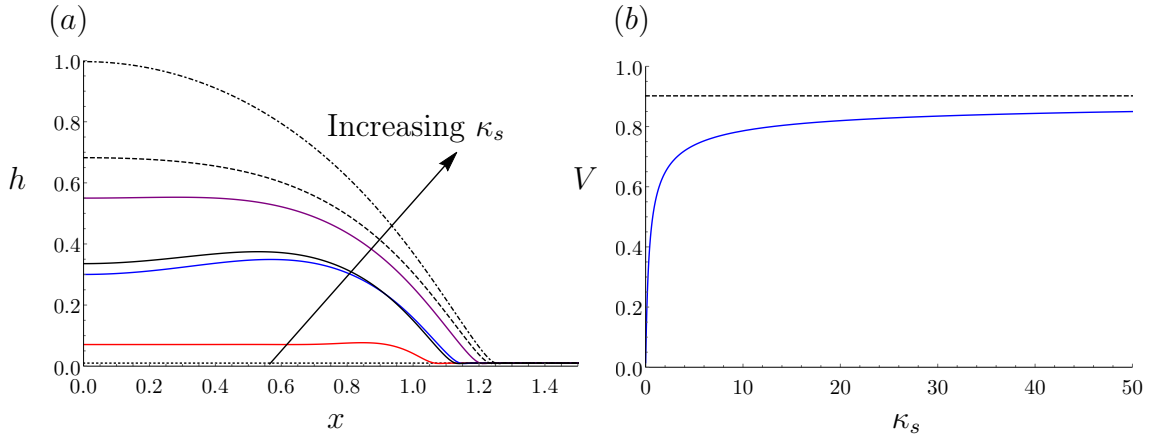

Figure 2.12: Plots of (a) the spatial profile of the film thickness, h, for $\kappa_s = 0$ (dotted black), $\kappa_s = 0.1$ (red), $\kappa_s = 1$ (blue), $\kappa_s = 10$ (purple), $\kappa_s = \infty$ (dashed black), constant injection from Section 2.2 (black), and thickness-inhibited injection with $q = 1$ from Section 2.6 (dot-dashed black) at time $t = 0.33$, and (b) the total volume of fluid, V, as a function of κ_s at time $t = 0.87$ when the $\kappa_s = \infty$-curve in (a) reaches the symmetry line at $z = 1$. The dashed line in (b) corresponds to $\kappa_s = \infty$.

A key output of our model is the time, t_{final}, taken for the film to reach the symmetry line, at which point it will coalesce with the fluid growing over the neighbouring fibre. In figure 2.14, we show a plot of the time t_{final} when the film reaches $z = 1$ as a function of κ_s. We see that, as κ_s increases, t_{final} approaches the time for the case $\kappa_s = \infty$ (shown in dashed black). In fact, as soon as $\kappa_s = O(1)$ the reaching time has already become very close to the time corresponding to $\kappa_s = \infty$.

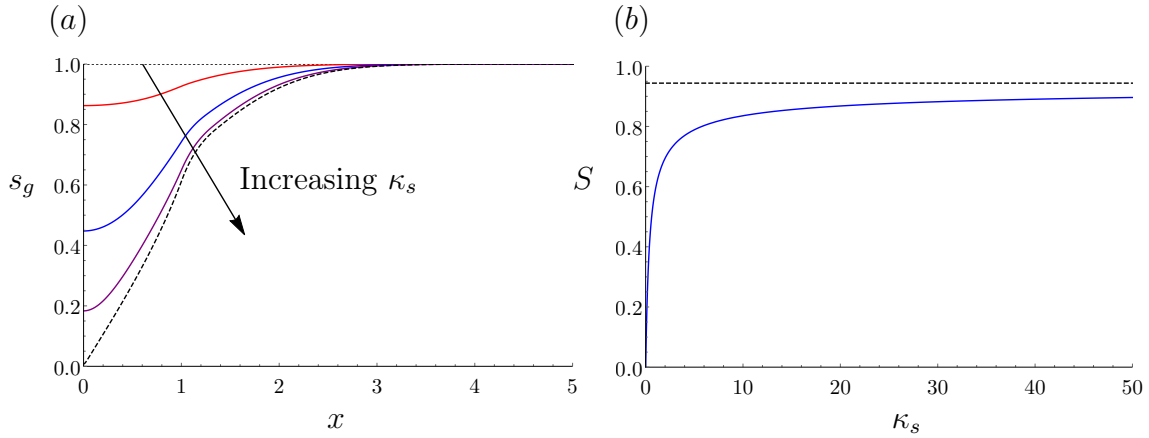

Figure 2.13: Plots of (a) the spatial profile of sulphur dioxide concentration in the gas, s_g, for $\kappa_s = 0$ (dotted black), $\kappa_s = 0.1$ (red), $\kappa_s = 1$ (blue), $\kappa_s = 10$ (purple), and $\kappa_s = \infty$ (dashed black), and (b) the instantaneous amount of removed sulphur dioxide, S, from the gas as a function of κ_s. The dashed line in (b) corresponds to $\kappa_s = \infty$, and the plots are again taken at time $t = 0.87$.

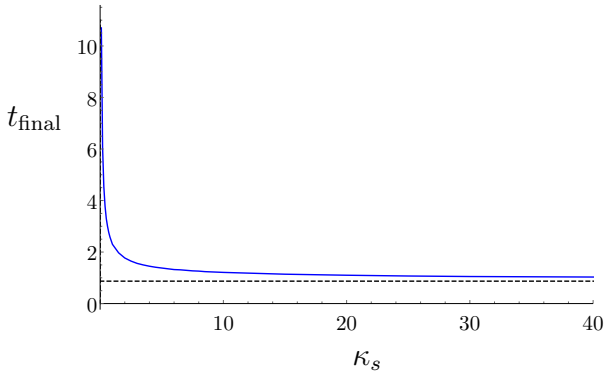

Figure 2.14: Plot of the time taken until the film reaches the symmetry line $z = 1$ as a function of κ_s and the time corresponding to $\kappa_s = \infty$ (dashed black).

2.8 Conclusions

In this chapter, we considered the problem of surface-tension-driven flow of a viscous liquid along a flat surface with injection through part of the substrate. We initially focused on the situation in which the injection rate was constant. We derived a fourth-order parabolic evolution equation for the thickness profile, along with appropriate boundary conditions, reflecting the injection in a fixed region. We assumed that a thin precursor layer was present initially along the surface, which resolved the stress singularity at the moving contact line. We used asymptotic analysis for early, $O(1)$, and late time in order to examine the behaviour of the solution, and obtained power-law dependencies on time for the maximum film thickness at the centre of the injection region, $h_0(0,t)$, and the position of the apparent contact line, $a_0(t)$. We recovered

a version of Tanner's law at the apparent contact line, namely, $\partial h_0/\partial x \propto -(\dot{a}_0)^{1/3}$. For early time, we established a linear growth of the film thickness in the injection region and no movement of the contact line to leading order. We justified the absence of motion of the contact line to leading order for $O(1)$ time, while for late time, t, the maximum film thickness scales as $t^{3/7}$ and the position of the apparent contact line scales as $t^{4/7}$. Up to a multiplicative constant, the time-dependent aspect ratio is $h_0(0,t)/a_0(t) \sim t^{-1/7}$, as $t \to \infty$, which is consistent with the thin-film assumption. We observed that the leading-order results for h and a depend on the precursor thickness, δ. We also showed how to generalise classical results (such as the Cox–Voinov law) from the droplet-spreading problem in the case of injection to obtain the full late-time behaviour of the film.

We then considered three generalisations to the problem: a power-law, point-source and thickness-dependent injection rate. In the first case, we looked at injection of the form t^c with an exponent in the range $-1 < c < 1$, and established power-law behaviours for the maximum film thickness and the position of the apparent contact line as functions of time. We showed that, for late time, the film thickness increased for $c > -3/4$, tended to a constant for $c = -3/4$, and decreased for $c < -3/4$. For $c \geq 1$, the aspect ratio of the problem grows unboundedly with time and eventually invalidates the thin-film hypothesis. We also presented a simple inverse problem for determining the exponent of the power-law injection (assuming this exists) by observing the position of the apparent contact line, for example. In the point-source case, we obtained the same late-time behaviour as in the constant-injection-rate case. With regards to the thickness-dependent injection, we formulated the problem with injection of the form $1/h^q$ for some exponent $q > 0$. We obtained an integro-differential equation for the position of the apparent contact line for late time and simplified it to an ordinary differential equation. We found power-law behaviours for the maximum thickness of the film and the position of the apparent contact line, which were confirmed using scaling arguments. Unlike the time-dependent-injection case, we observed unbounded growth and spreading of the film for all $q > 0$. We note that, as q increases, the exponents in the spreading behaviour decrease, corresponding to a slowing down of the film growth and front spreading. Furthermore, we see a close relationship between the behaviour for $a(t)$ and $h(0,t)$ between the power-law-injection and the thickness-inhibited-injection cases; they are identical if $c = -3q/(4q+7)$. Interestingly, since $q > 0$, $c \to -3/4$ as $q \to \infty$. This recovers the critical exponent for time-dependent injection at which the film thickness stops increasing for late time. This gives a relationship between the qualitative behaviours

for late time of the maximum film thickness and the position of the apparent contact line with power-law-in-time and thickness-inhibited injection rates.

Finally, we derived a paradigm model coupling the film growth with diffusion of chemical species through the gas and the liquid and a liquid-producing reaction on part of the surface. The key parameter that emerged as part of the analysis is κ_s, which is a Damköhler number that measures the ratio of the reaction rate to the diffusive mass transfer rate. Increasing this parameter enhances film growth and removes more sulphur dioxide from the gas, as expected. Interestingly, we note that, for the case of infinite κ_s, i.e., infinitely fast reaction, we do not obtain complete removal of sulphur dioxide above the reaction region, but rather a monotonic profile for the sulphur dioxide concentration which reaches zero only at the origin and approaches the far-field value away from the reaction region.

Our ultimate aim is to use the insight we have obtained by studying these surface-tension- and injection-driven flows to provide a better understanding of the operation of the GMCS purification devices. Due to the precursor-layer regularisation, we note that this analysis will be appropriate for filters made of hydrophilic fibres, although we expect similar scalings for the spreading of the film to be valid if one uses a Navier-slip regularisation (Sibley *et al.*, 2015), for example, which will be more appropriate for hydrophobic fibres. The case $q = 1$ in the thickness-inhibited injection proved to be relevant in describing the coupled problem of liquid generation and sulphur dioxide diffusion in the case of instantaneous reaction on the injection region.

We now move on to study a more detailed and rigorous model of the operation of the GMCS device that systematically upscales the problem valid on the microscale to a device-scale model of the whole filter using the theory of homogenisation.

Chapter 3

A Homogenised Model for Porous Catalytic Media with Hydrophobic Porous Structure

3.1 Introduction

As mentioned in Section 1.4, numerically solving a detailed model of the microscale throughout the filter that incorporates all the relevant physics and chemistry would be computationally infeasible. We would like to have a simpler model that describes the macroscale dynamics of the filter that takes into account the effect of the complex porous microstructure. A rigorous and systematic way to do this is to use mathematical homogenisation (see, for example, Bensoussan *et al.*, 1978; Bruna & Chapman, 2015; Hornung, 1997). This will provide the necessary mathematical framework to obtain upscaled equations that govern the gas and liquid transport within the filter.

Mathematical homogenisation is a useful technique to study problems in which there are multiple length scales (or timescales) present. This is often the case in a porous structure, where the pore scale is much smaller than the length scale of the macroscale structure. The goal in such problems is to obtain the macroscale behaviour of the system while capturing the effect of the microstructure on the macroscale without having to solve the full problem everywhere on the microscale. In the homogenisation procedure, the key step is to utilise the separation of length scales between the microscale and the macroscale level by assuming that the variables depend on both the microscale and the macroscale independently. This assumption means that any derivative operators will then transform to a combination of derivatives with respect to the microscale and the macroscale variables. The next stage is to expand

the governing equations asymptotically together with the boundary and initial conditions in powers of the ratio of the length scales, which is assumed to be a small parameter. The leading-order problem normally implies that the dependent variables are independent of the microscale variables, and thus vary only over the macroscale. A cell problem, usually involving a system of equations that arise from considering the first-order correction in the asymptotic expansion of the original system, is then formulated and needs to be solved once for a given geometry. The final step in the homogenisation procedure is to obtain the macroscale equations by averaging the microscale equations over the relevant microscale domain and applying the boundary conditions, which might appear at higher order in the asymptotic expansion. The resulting macroscale equations often have parameters in them that depend on the microscale through the solution of the cell problem.

We recall that, as described in Chapter 1, there are many physical situations that can be modelled using reaction–diffusion processes that occur in the microscale in a porous medium. In these situations, the microscale models often describe conservation of mass and momentum of the phases involved, coupled with advection–diffusion equations describing the transport of chemicals, and surface or bulk reactions that contribute to the evolution. These microscale problems can be homogenised by performing a multiple-scales analysis, and the resulting macroscale equations often have a reaction–diffusion–advection form. As one example, Dalwadi *et al.* (2018) consider the problem of bacterial nutrient uptake in a bioreactor. They derive upscaled equations for the nutrient concentration, and the resulting macroscale equations are of a reaction–diffusion form. The reactor is modelled as a fluid medium with dissolved nutrients that diffuse around, and into, a periodic array of spherical bacteria, where the nutrients are absorbed. They study three different distinguished limits based on the ratio of diffusivities of nutrients in the ambient and bacterial media, the strength of absorption, and the size of the bacteria. They find that, in the case when the bacteria are of a comparable size to the distance between them, the effective uptake scales either with the bacterial volume for a weak uptake, or with the surface area of the bacteria for a strong uptake; in the case when the size of the bacteria is much smaller than the distance between them, the effective uptake is found to scale with the radius of the bacteria. Here, the interface between the ambient medium and bacteria is static.

In cases where there are moving interfaces on the microscale, there are two main approaches normally adopted: using a level-set formulation or explicitly tracking the position of the interface. In the level-set formulation, the moving interface is given

by the zero set of a time-dependent function $f(\boldsymbol{x}, t)$, such as $f = |\boldsymbol{x}| - R(\boldsymbol{x}, t)$ in the case of an asymmetric interface with radius $R(\boldsymbol{x}, t)$, that is evolved according to the reactions that take place at the interface. As part of the homogenisation procedure, the equation for the level-set function that defines the interface needs to be asymptotically expanded, and a separate equation, which evolves the level-set function according to the reactions that take place at the interface, is necessary. The advantage of this approach is the ability to capture spatially non-uniform evolution of any microscale interfaces. This approach has been used by van Noorden (2009*a*), for example, to derive homogenised equations incorporating fluid flow for the evolution of a solid–liquid interface in crystal precipitation and dissolution. In Ray *et al.* (2015), they consider the transport by advection, diffusion, and potential interactions of colloid particles suspended in a fluid moving past circular obstacles, to which they can attach or detach. A level-set function is used to separate the solid from the liquid regions in the system. A homogenisation procedure yields a set of upscaled equations describing the coupled flow, transport, and interaction of the particles. Similar modelling has also been done in Schulz & Knabner (2017) to describe the growth, around solid particles, of a biofilm produced by mobile microorganisms that are transported in a moving fluid and can attach to, and detach from, the biofilm. Since the biofilm grows non-uniformly around the particles, they use a level-set formulation to locate its boundary. They solve their cell problem, which is used to obtain effective diffusivity, until the time when the biofilms reach the boundary of the cell.

In some situations, the homogenisation procedure leads to a cell problem for two variables on either side of an interface. In Bringedal *et al.* (2016) and Bringedal & Kumar (2017), for example, they study the evolution of reactive grains using a level-set function to track the solid–liquid interface and derive and numerically solve effective macroscale equations, whose cell problem includes two domains patched together with appropriate boundary conditions.

Explicit interface tracking is often used when the evolution of the microscale interface is simple, for example, if it remains spherical. Here, the homogenisation procedure differs from the level-set formulation, because the problem can be explicitly written down in terms of the interface location, $|\boldsymbol{x}| = R(t)$, say. The interface evolution is often determined by appealing to conservation of mass and incorporating the effect of the reactions that occur on the interface. Another feature of this approach is that the unit normal to the interface needs to be expanded in both microscale and macroscale variables to take into account variations occurring over the macroscale. The rest of the homogenisation procedure follows that for the level-set formulation and consists

of formulating a cell problem and averaging over the microscale domain, where the only difference is that the relevant boundary conditions can be applied at the explicit interface location. For example, in Luckins *et al.* (2019), the problem of removal of toxic contaminant in a porous medium using a cleanser is considered. The removal is modelled using a first-order (linear) reaction between the two phases that occurs on the interface between them. They obtain a homogenised model that describes the effective removal of the toxic component in the case when it is surrounded by a layer of cleanser, and in the case when there is a sharp macroscale interface between the two phases. Even though there are two phases present, solutions are sought on only one side of the interface between them. In Dalwadi *et al.* (2015, 2016), they consider adsorption of small contaminant particles, transported by a fluid, to microscopic obstacles in a filter medium. They obtain a homogenised model describing the effective removal of contaminant assuming linear adsorption kinetics, and they analyse how a porosity gradient in the filter can improve its performance. In van Noorden (2009*b*) and van Noorden *et al.* (2010), they obtain a one-dimensional equation for deposition and detachment in a biofilm that coats a thin pore and is subject to fluid flow. In Ray & Schulz (2019), they investigate the effect of Taylor and electro-osmotically induced dispersion under flow-dominated conditions in reactive ion transport and derive the effective equations for a thin evolving pore.

For our filter problem, we need to solve for the sulphur dioxide concentration in both the gas and the liquid media, along with the position of the interface between them, which moves due to the production of liquid sulphuric acid on the surface of the pellets that eventually become submerged by the produced liquid. This is fundamentally different to the situation studied in Luckins *et al.* (2019), for example, where the reaction occurs at the moving interface, or Dalwadi *et al.* (2018), where it occurs in the whole bacterial region with a static interface.

In this chapter, we will adopt a classical homogenisation-based approach in which we treat the filter medium as an array of cubic cells each containing a spherical pellet coated with a growing uniform layer of liquid sulphuric acid. We will exploit the separation of length scales on the pore and the device level and use homogenisation theory to derive averaged equations for the concentration of sulphur dioxide and the thickness of the acid layer within the filter. In Section 3.2, we will present a mathematical model for the microscale problem in the porous sheets. We will non-dimensionalise the model in Section 3.3 and introduce the key dimensionless parameters governing the behaviour of the system. In Section 3.4, we will use homogenisation to obtain averaged equations for the concentration of sulphur dioxide and the thickness of the

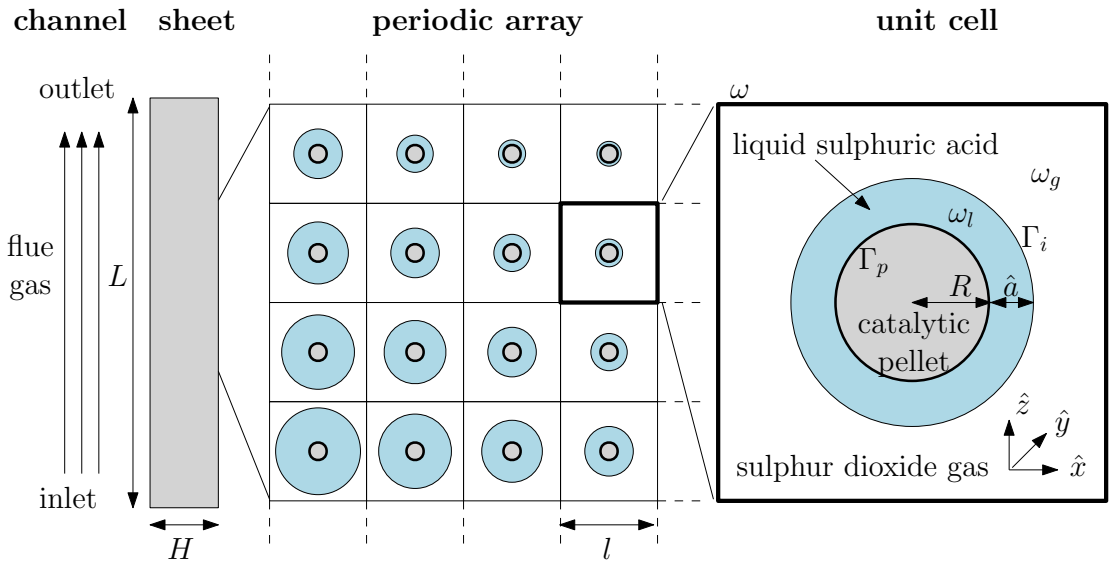

Figure 3.1: Schematic cross-sectional representation of the porous structure of the filter. The catalytic pellets (grey) are held together by a network of fibres, not shown in the schematic.

liquid-acid layer throughout the filter. We will identify two distinct regimes of operation and derive the equations corresponding to each of them. In Section 3.5, we will consider a model for liquid growth around a single pellet and compare the results with experimental observations to estimate the reaction rate constant, which is unknown *a priori*. We draw conclusions in Section 3.6.

3.2 Microscale Model

Our aim is to obtain a homogenised model for the operation of the filter device (see figure 3.1 left) that incorporates the effect of the porous microstructure of the filter sheets (see figure 3.1 middle). We begin by presenting the mathematical model that holds in a microscopic region within the filter sheets containing a single spherical pellet (see figure 3.1 right). We suppose that the microscale problem is periodic in a cubic cell of size l (taken to be the average inter-pellet distance) containing a pellet of radius $R < l/2$ at the centre, where we ignore the presence of the surrounding scaffold of thin fibres. We assume that l is much smaller than the typical thickness, width, and length of the filter sheets, H, W, and L, respectively. We represent a single filter sheet as a periodic array of these cubic cells and employ a Cartesian coordinate system $(\hat{x}, \hat{y}, \hat{z})$ in each of them. We assume that the pellet catalyses the reaction presented in (1.1), and a layer of thickness $\hat{a}$ of liquid sulphuric acid forms around the pellet. Although we do not explicitly model the hydrophobic fibres in the filter

sheet, we expect such a behaviour, since the liquid will be repelled from the fibres and will tend to accumulate around the hydrophilic pellets. We further assume that surface tension keeps the gas–liquid interface spherical to a good approximation, and neglect the effect of gravity on the shape of the liquid layer, since we find that the Bond number, $\mathrm{Bo} = \rho g l^2/\gamma$, which measures the relative effect of gravity to surface tension, is small, namely, $\mathrm{Bo} \approx 6 \times 10^{-4} \ll 1$ (using the parameters in table 1.1), where ρ is the density of sulphuric acid, g is the gravitational acceleration, and γ is the surface tension of sulphuric acid. We denote the cubic cell and its boundary by ω and $\partial\omega$, respectively, and the regions of gas and liquid, the interface between the two phases, and the surface of the pellet by ω_g, ω_l, Γ_i, Γ_p, respectively, as shown in figure 3.1 (right). We denote the concentration of sulphur dioxide in the gas and the liquid by $\hat{s}_g$ and $\hat{s}_l$, respectively. We assume that sulphur dioxide is transported by diffusion and advection induced by the liquid production at the surface of the pellet. Thus, we have the following governing equations

$$\frac{\partial \hat{s}_g}{\partial \hat{t}} + \nabla \cdot (\hat{\boldsymbol{u}}_{\boldsymbol{g}} \hat{s}_g) = D_{s_g} \nabla^2 \hat{s}_g \qquad \text{in} \qquad \omega_g, \tag{3.1}$$

$$\frac{\partial \hat{s}_l}{\partial \hat{t}} + \nabla \cdot (\hat{\boldsymbol{u}}_{\boldsymbol{l}} \hat{s}_l) = D_{s_l} \nabla^2 \hat{s}_l \qquad \text{in} \qquad \omega_l, \tag{3.2}$$

where $\hat{\boldsymbol{u}}_{\boldsymbol{g}}$ and $\hat{\boldsymbol{u}}_{\boldsymbol{l}}$ are the velocities of the gas and the liquid phase, respectively, D_{s_g} and D_{s_l} are the corresponding diffusivities of sulphur dioxide in the gas and the liquid, respectively, and $\hat{t}$ denotes time. We assume that the fluid in both phases is incompressible but will not write in full the equations satisfied by $\hat{\boldsymbol{u}}_{\boldsymbol{g}}$ and $\hat{\boldsymbol{u}}_{\boldsymbol{l}}$, since, as we shall see, the advection terms in (3.1) and (3.2) will be negligible in the physically relevant limit that we consider in which the liquid layer around the catalytic pellet grows slowly. We assume that water vapour and oxygen are abundant in the system and, thus, assume that their concentrations are constant. As in the previous chapter, we use the Law of Mass Action to determine the flux, $\hat{Q}$, of sulphur dioxide removed from the system at the surface of the pellets, which gives us that

$$\hat{Q} = 2k\hat{s}^2, \tag{3.3}$$

where $\hat{s} = \hat{s}_l|_{|\hat{\boldsymbol{x}}|=R}$, and k is the reaction rate constant, with units $\mathrm{m}^4\,\mathrm{mol}^{-1}\,\mathrm{s}^{-1}$. We close the system using a global conservation law that links the growth of the liquid layer to the amount of liquid produced on the surface of the catalytic pellet, namely

$$\frac{\mathrm{d}}{\mathrm{d}\hat{t}} \left(\frac{4\pi\rho}{3} \left((R + \hat{a})^3 - R^3 \right) \right) = \int_{\Gamma_p} \rho V_{\mathrm{m}} \hat{Q} \, \mathrm{d}\hat{S} = 4\pi\rho R^2 V_{\mathrm{m}} \hat{Q}, \tag{3.4}$$

where ρ is the density of sulphuric acid, with units $\mathrm{kg\,m^{-3}}$, and V_m is the molar volume of liquid sulphuric acid, with units $\mathrm{m^3\,mol^{-1}}$. We note that we can ignore the mass of the dissolved sulphur dioxide in this calculation, because, in one cubic metre of liquid sulphuric acid, there are approximately 16 g of sulphur dioxide, compared to the 1830 kg of acid (Perry & Green, 1997). We rewrite (3.4) as

$$\frac{\mathrm{d}\hat{a}}{\mathrm{d}\hat{t}} = \frac{V_\mathrm{m}\hat{Q}}{(1+\hat{a}/R)^2} = \frac{2kV_\mathrm{m}\hat{s}^2}{(1+\hat{a}/R)^2}. \tag{3.5}$$

In this case, at the pellet's surface, the velocity of the liquid is given by its production rate

$$\hat{\boldsymbol{u}}_{\boldsymbol{l}} \cdot \boldsymbol{n}_p = V_\mathrm{m}\hat{Q} = 2kV_\mathrm{m}\hat{s}_l^2, \tag{3.6}$$

where $\boldsymbol{n}_p$ denotes the outwards-pointing unit normal to the surface of the pellet, which is in the radial direction $\boldsymbol{e}_r$. We also balance the flux of sulphur dioxide into the pellet with the amount being consumed by the reaction, i.e.,

$$(D_{s_l}\nabla\hat{s}_l - \hat{\boldsymbol{u}}_{\boldsymbol{l}}\hat{s}_l)\cdot\boldsymbol{n}_p = \hat{Q} = 2k\hat{s}_l^2, \tag{3.7}$$

which we can rewrite, using (3.6), to be

$$D_{s_l}\nabla\hat{s}_l \cdot \boldsymbol{n}_p = \hat{Q}(1+V_\mathrm{m}\hat{s}_l) = 2k(1+V_\mathrm{m}\hat{s}_l)\hat{s}_l^2. \tag{3.8}$$

At the gas–liquid interface, we impose continuity of flux of sulphur dioxide, and we assume local thermodynamic equilibrium (which leads to Henry's law), and, thus, we write

$$-D_{s_g}\nabla\hat{s}_g \cdot \boldsymbol{n}_i = -D_{s_l}\nabla\hat{s}_l \cdot \boldsymbol{n}_i, \tag{3.9}$$

$$\hat{s}_g = \beta_s\hat{s}_l, \tag{3.10}$$

where β_s is Henry's law constant, which measures the relative solubility of the gas in each phase, and

$$\boldsymbol{n}_i = \frac{\nabla\left(|\hat{\boldsymbol{x}}| - R - \hat{a}\right)}{\left|\nabla\left(|\hat{\boldsymbol{x}}| - R - \hat{a}\right)\right|} \tag{3.11}$$

denotes the outwards-pointing unit normal to the liquid layer.

To close the microscale model, we prescribe periodicity of $\hat{s}_g$ along the boundary of each cell and also assume

$$\hat{s}_g = S_0 \quad \text{and} \quad \hat{a} = 0 \qquad \text{at} \qquad \hat{t} = 0, \tag{3.12}$$

where S_0 is the concentration of sulphur dioxide in the incoming flue gas. Once we obtain the macroscale equations that hold over the domain of the whole device in Chapter 4, we will prescribe the necessary macroscale boundary and initial conditions.

We conclude this section by noting that we could use a general flux function $\hat{Q}$ in (3.5)–(3.8), which would allow us to employ different kinetic laws or model other chemical reactions of a similar type. For the purposes of this model, though, we will take $\hat{Q}$ as in (3.3).

3.3 Dimensionless Model

We non-dimensionalise (3.1), (3.2), (3.5)–(3.10), and (3.12) using

$$\begin{gathered}(\hat{\boldsymbol{x}}, \hat{a}) = l\,(\boldsymbol{x}, a)\,, \quad \hat{t} = \left(\beta_s^2 l / k S_0^2 V_{\mathrm{m}}\right) t, \quad \hat{s}_g = S_0 s_g, \quad \hat{s}_l = (S_0/\beta_s)\, s_l, \\ (\hat{\boldsymbol{u}}_{\boldsymbol{g}}, \hat{\boldsymbol{u}}_{\boldsymbol{l}}) = \left(k S_0^2 V_{\mathrm{m}}/\beta_s^2\right) (\boldsymbol{u}_{\boldsymbol{g}}, \boldsymbol{u}_{\boldsymbol{l}}),\end{gathered} \tag{3.13}$$

where we have chosen to non-dimensionalise using the timescale over which the liquid layer grows to fill the void space. Using the typical parameter values in table 1.1 we find this timescale is approximately equal to one day, which is longer than the timescale for diffusive transport in the gas ($l^2/D_{s_g} = 9 \times 10^{-5}\,\mathrm{s}$), or in the liquid ($l^2/D_{s_l} = 4.5 \times 10^{-1}\,\mathrm{s}$). We also note that we have chosen different scales for the concentrations of sulphur dioxide in the gas and in the liquid to simplify (3.10), and so that both concentrations are $O(1)$. The dimensionless model reads

$$\nu_s^2 \eta_s \left(\frac{\partial s_g}{\partial t} + \boldsymbol{u}_{\boldsymbol{g}} \cdot \nabla s_g\right) = \nabla^2 s_g \qquad \text{in} \qquad \omega_g, \tag{3.14}$$

$$\nu_s^2 \left(\frac{\partial s_l}{\partial t} + \boldsymbol{u}_{\boldsymbol{l}} \cdot \nabla s_l\right) = \nabla^2 s_l \qquad \text{in} \qquad \omega_l, \tag{3.15}$$

$$\frac{\mathrm{d}a}{\mathrm{d}t} = \frac{2s^2}{(1 + a/\Lambda)^2}, \tag{3.16}$$

subject to the boundary conditions and initial conditions

$$\nabla s_l \cdot \boldsymbol{n}_p = 2\left(\kappa_s + \nu_s^2 s_l\right) s_l^2 \qquad \text{on} \qquad \Gamma_p, \tag{3.17}$$

$$-\nabla s_g \cdot \boldsymbol{n}_i = -\frac{\eta_s}{\beta_s} \nabla s_l \cdot \boldsymbol{n}_i \qquad \text{on} \qquad \Gamma_i, \tag{3.18}$$

$$s_g = s_l \qquad \text{on} \qquad \Gamma_i, \tag{3.19}$$

$$s_g \text{ periodic} \qquad \text{on} \qquad \partial\omega, \tag{3.20}$$

$$s_g = 1 \qquad \text{at} \qquad t = 0, \tag{3.21}$$

$$a = 0 \qquad \text{at} \qquad t = 0, \tag{3.22}$$

where $s = s_l|_{|\boldsymbol{x}|=\Lambda}$, and we have introduced the following four dimensionless parameters:

$$\eta_s = \frac{D_{s_l}}{D_{s_g}} \approx 10^{-4}, \quad \kappa_s = \frac{klS_0}{\beta_s D_{s_l}} \approx 10^{-1}, \quad \Lambda = \frac{R}{l} \approx 10^{-1}, \quad \nu_s = \sqrt{\frac{klS_0^2 V_{\mathrm{m}}}{\beta_s^2 D_{s_l}}} \approx 10^{-3}. \tag{3.23}$$

Here, η_s is the ratio of the diffusivities of sulphur dioxide in the liquid and gas phase, κ_s (sometimes called a Damköhler number) measures the relative strength of the reaction on the surface of the pellet to diffusion of sulphur dioxide in the liquid sulphuric acid, Λ is a measure of how densely packed the catalytic pellets are, and ν_s is the Péclet number,[1] i.e., the ratio of the diffusive timescale in the liquid over the pore scale to the timescale associated with the liquid-layer growth. We also introduce the ratio of the pore length scale to the filter sheet thickness, $\epsilon = l/H \approx 10^{-2} \ll 1$, which we will use later in the homogenisation. We note that $\nu_s = \epsilon\sqrt{\tau_s}$, where $\tau_s = kH^2 S_0^2 V_{\mathrm{m}}/\beta_s^2 l D_{s_l} \approx 10^{-3} \ll 1$ is the ratio of the diffusive timescale in the liquid over the thickness of the filter sheet to the timescale associated with the liquid-layer growth.

3.4 Homogenisation

Our goal is to obtain macroscale equations, valid over the whole filter domain, by averaging over the complicated porous microstructure of the filter sheets, in order to obtain the effective removal of sulphur dioxide by the filter. We introduce the macroscale spatial variables

$$\boldsymbol{X} = \epsilon \boldsymbol{x}, \tag{3.24}$$

and let s_g, s_l, and a also depend independently on the macroscale variables. Using (3.24) together with the Chain Rule, the gradient operator transforms as $\nabla \to \nabla_x + \epsilon\nabla_X$. We also note that, using the fact that $\nabla_x|\boldsymbol{x}| = \boldsymbol{x}/|\boldsymbol{x}| = \boldsymbol{e}_r$,

$$\nabla\left(|\boldsymbol{x}| - \Lambda - a\right) = \boldsymbol{e}_r - \epsilon\nabla_X a, \tag{3.25}$$

and we see that, due to the dependence on the macroscale variables, $\boldsymbol{n}_i$, defined by (3.11) is not equal to $\boldsymbol{e}_r$. Rewriting (3.14)–(3.20), we have

$$\begin{aligned}
&\epsilon^2\tau_s\eta_s\left(\frac{\partial s_g}{\partial t} + \boldsymbol{u_g}\cdot\left(\nabla_x + \epsilon\nabla_X\right)s_g\right)\\
&\qquad = \nabla_x^2 s_g + \epsilon\left(\nabla_x\cdot\nabla_X + \nabla_X\cdot\nabla_x\right)s_g + \epsilon^2\nabla_X^2 s_g \qquad \text{in} \qquad \omega_g, \qquad (3.26)\\
&\epsilon^2\tau_s\left(\frac{\partial s_l}{\partial t} + \boldsymbol{u_l}\cdot\left(\nabla_x + \epsilon\nabla_X\right)s_l\right)\\
&\qquad = \nabla_x^2 s_l + \epsilon\left(\nabla_x\cdot\nabla_X + \nabla_X\cdot\nabla_x\right)s_l + \epsilon^2\nabla_X^2 s_l \qquad \text{in} \qquad \omega_l, \qquad (3.27)\\
&\frac{\partial a}{\partial t} = \frac{2s^2}{(1 + a/\Lambda)^2}, \qquad (3.28)
\end{aligned}$$

[1] We have used ν_s here for the Péclet number, reserving Pe for the Péclet number in the outer flow, as described in Section 4.1.

subject to the boundary conditions

$$(\nabla_x + \epsilon\nabla_X)\, s_l \cdot \boldsymbol{e}_r = 2\left(\kappa_s + \epsilon^2\tau_s s_l\right) s_l^2 \quad \text{on} \quad \Gamma_p, \tag{3.29}$$

$$-(\nabla_x + \epsilon\nabla_X)\, s_g \cdot (\boldsymbol{e}_r - \epsilon\nabla_X a) = -\sigma_s\,(\nabla_x + \epsilon\nabla_X)\, s_l \cdot (\boldsymbol{e}_r - \epsilon\nabla_X a) \quad \text{on} \quad \Gamma_i, \tag{3.30}$$

$$s_g = s_l \quad \text{on} \quad \Gamma_i, \tag{3.31}$$

$$s_g \text{ is periodic} \quad \text{on} \quad \partial\omega, \tag{3.32}$$

the initial conditions (3.21) and (3.22), which we will not explicitly mention again until we derive the macroscale model in Chapter 4, and we have also defined

$$\sigma_s = \frac{\eta_s}{\beta_s}. \tag{3.33}$$

We note that, since $\tau_s \ll 1$, we have that $\nu_s^2 = \epsilon^2\tau_s = o(\epsilon^2)$. Thus, the left-hand sides of (3.26) and (3.27) are negligible and the sulphur dioxide concentration in the gas and in the liquid evolves quasi-statically, while the time dependence is retained only in (3.28), which describes the liquid growth. At the end of the section, we will also mention the physically less relevant limit when $\tau_s = O(1)$. However, in this case little analytical progress can be made due to the non-linearity and complexity of the system of equations and boundary conditions. The parameters that most significantly control the behaviour of our system are σ_s and κ_s, as they dictate respectively how much and how fast sulphur dioxide can be transported to the pellets in order to produce liquid sulphuric acid that eventually clogs up the filter. There is a rich underlying asymptotic structure associated with the order of magnitude of these parameters. In particular, we will find later on that, if the product of these parameters, $\sigma_s\kappa_s$ is not sufficiently small, then sulphur dioxide is completely consumed in the filter medium, and non-zero solutions appear as higher-order corrections only. This, for example, corresponds to the case when the dimensionless rate of mass transfer of sulphur dioxide into the liquid is $O(1)$ and comparable to the rate at which it is being consumed by the reaction. It transpires that, when $\sigma_s\kappa_s = O(\epsilon^2)$, which is the physically relevant case, we have a non-trivial behaviour at leading order in the sulphur dioxide concentration in both the gas and the liquid phases. We, therefore, first present two distinguished limits when $\sigma_s\kappa_s = O(\epsilon^2)$, and then briefly discuss what happens when $\sigma_s\kappa_s \gg \epsilon^2$.

3.4.1 Limit I: $\sigma_s = O(\epsilon^2)$ and $\kappa_s = O(1)$

We begin by exploring the case when the mass transfer of sulphur dioxide into the liquid $\sigma_s = O(\epsilon^2)$, but the dimensionless reaction rate $\kappa_s = O(1)$. For convenience, we write $\sigma_s = \epsilon^2\tilde{\sigma}_s$, where $\tilde{\sigma}_s = O(1)$. We expand each of the dependent variables in (3.26)–(3.32) as

$$f \sim f^{(0)} + \epsilon f^{(1)} + \epsilon^2 f^{(2)} + \cdots, \tag{3.34}$$

and obtain the following leading-order problem for s_g, s_l, and a:

$$\nabla_x^2 s_g^{(0)} = 0 \qquad \text{in} \qquad \omega_g^{(0)}, \tag{3.35}$$

$$\nabla_x^2 s_l^{(0)} = 0 \qquad \text{in} \qquad \omega_l^{(0)}, \tag{3.36}$$

$$\frac{\partial a^{(0)}}{\partial t} = \frac{2s^{(0)2}}{(1 + a^{(0)}/\Lambda)^2}, \tag{3.37}$$

subject to the boundary conditions

$$\nabla_x s_l^{(0)} \cdot \boldsymbol{e}_r = 2\kappa_s s_l^{(0)2} \qquad \text{on} \qquad \Gamma_p, \tag{3.38}$$

$$-\nabla_x s_g^{(0)} \cdot \boldsymbol{e}_r = 0 \qquad \text{on} \qquad \Gamma_i^{(0)}, \tag{3.39}$$

$$s_g^{(0)} = s_l^{(0)} \qquad \text{on} \qquad \Gamma_i^{(0)}, \tag{3.40}$$

$$s_g^{(0)} \text{ is periodic} \qquad \text{on} \qquad \partial\omega, \tag{3.41}$$

where $s^{(0)} = s_l^{(0)}|_{|\boldsymbol{x}|=\Lambda}$, $\omega_g^{(0)} = \omega \backslash \{|\boldsymbol{x}| \leq \Lambda + a^{(0)}\}$, $\omega_l^{(0)} = \{\Lambda < |\boldsymbol{x}| < \Lambda + a^{(0)}\}$, and $\Gamma_i^{(0)} = \{|\boldsymbol{x}| = \Lambda + a^{(0)}\}$. We first solve the problem in the liquid layer. We rewrite (3.36) in spherical polar coordinates, assume radial symmetry, integrate, and apply (3.38) to find that

$$\frac{\partial s_l^{(0)}}{\partial r} = \frac{2\Lambda^2\kappa_s s^{(0)2}}{r^2}, \tag{3.42}$$

where we note that, due to radial symmetry, $s^{(0)}$ is a function of the macroscale variables only. Following the remark at the end of Section 3.2, we note that, for a general flux of sulphur dioxide, the right-hand side of (3.42) becomes $\Lambda^2 Q/r^2$, where Q, which is a function of $s^{(0)}$, is the flux, non-dimensionalised appropriately and of $O(1)$ magnitude.

Integrating once again and using (3.40), we obtain

$$s_l^{(0)} = 2\Lambda^2\kappa_s s^{(0)2}\left(\frac{1}{\Lambda + a^{(0)}} - \frac{1}{r}\right) + s_g^{(0)}|_{r=\Lambda+a^{(0)}}. \tag{3.43}$$

Evaluating (3.43) at $r = \Lambda$ and rearranging yields the following quadratic equation for $s^{(0)}$

$$\frac{2\Lambda\kappa_s a^{(0)}}{\Lambda + a^{(0)}} s^{(0)2} + s^{(0)} - s_g^{(0)}|_{r=\Lambda+a^{(0)}} = 0. \tag{3.44}$$

The physically relevant solution, which is non-negative and bounded as $\kappa_s \to 0$, is, therefore,

$$s^{(0)} = \frac{1 + a^{(0)}/\Lambda}{4\kappa_s a^{(0)}} \left(-1 + \sqrt{1 + \frac{8\Lambda\kappa_s a^{(0)} s_g^{(0)}|_{r=\Lambda+a^{(0)}}}{\Lambda + a^{(0)}}} \right). \tag{3.45}$$

Now considering (3.35), we multiply both sides by $s_g^{(0)}$, integrate over $\omega_g^{(0)}$, use the Divergence Theorem and rearrange to obtain

$$\iiint_{\omega_g^{(0)}} \left| \nabla_x s_g^{(0)} \right|^2 \mathrm{d}V = \iint_{\partial\omega_g^{(0)}} s_g^{(0)} \nabla_x s_g^{(0)} \cdot \mathbf{d}\boldsymbol{S}. \tag{3.46}$$

Since $s_g^{(0)}$ is periodic on the boundary of the unit cell ω, the surface integral in (3.46) over $\partial\omega$ evaluates to zero. On $\Gamma_i^{(0)} = \{|\boldsymbol{x}| = \Lambda + a^{(0)}\}$, we use (3.39) to obtain

$$\iiint_{\omega_g^{(0)}} \left| \nabla_x s_g^{(0)} \right|^2 \mathrm{d}V = 0. \tag{3.47}$$

Thus,

$$s_g^{(0)} = s_g^{(0)}(\boldsymbol{X}, t), \tag{3.48}$$

i.e., $s_g^{(0)}$ depends only on the macroscale spatial variables. We manipulate (3.45) (utilising the formula $A - B = (A^2 - B^2)\,/\,(A + B)$) to find

$$s^{(0)} = 2s_g^{(0)} \left(1 + \sqrt{1 + \frac{8\Lambda\kappa_s a^{(0)} s_g^{(0)}}{\Lambda + a^{(0)}}} \right)^{-1}, \tag{3.49}$$

where we have rationalised $s^{(0)}$ to further simplify it. We note that, as $\kappa_s \to 0$ (small reaction rate), $s^{(0)} \to s_g^{(0)}$, i.e., the concentration on the surface of the pellet is the same as the concentration in the gas, while, as $\kappa_s \to \infty$ (large reaction rate), $s^{(0)} \to 0$, i.e., sulphur dioxide is taken up instantaneously on the surface of the pellet.

We now consider the $O(\epsilon)$ terms in (3.26)–(3.32) in order to determine the problem for $s_g^{(1)}$. We have

$$\nabla_x^2 s_g^{(1)} = 0 \qquad \text{in} \qquad \omega_g^{(0)}, \tag{3.50}$$

subject to the boundary conditions

$$-\left(\nabla_X s_g^{(0)} + \nabla_x s_g^{(1)}\right) \cdot \boldsymbol{e}_r = 0 \qquad \text{on} \qquad \Gamma_i^{(0)}, \tag{3.51}$$

$$s_g^{(1)} \text{ is periodic} \qquad \text{on} \qquad \partial\omega. \tag{3.52}$$

We use the linearity of the problem for $s_g^{(1)}$ to write the solution in the form

$$s_g^{(1)} = \boldsymbol{\Phi} \cdot \nabla_X s_g^{(0)}, \tag{3.53}$$

where the function $\boldsymbol{\Phi}(\boldsymbol{x},t)=(\Phi_1,\Phi_2,\Phi_3)$ satisfies the cell problem

$$\nabla_x^2\Phi_i=0 \qquad \text{in} \qquad \omega_g^{(0)}, \tag{3.54}$$

subject to

$$(\nabla_x\Phi_i+\boldsymbol{e}_i)\cdot\boldsymbol{e}_r=0 \qquad \text{on} \qquad \Gamma_i^{(0)}, \tag{3.55}$$

$$\Phi_i \text{ is periodic} \qquad \text{on} \qquad \partial\omega, \tag{3.56}$$

for $i=1,2,3$, and where $\boldsymbol{e}_i$ is the unit vector in the x,y,z direction, respectively.

We now look at the $O(\epsilon^2)$ terms in (3.26)–(3.32) in order to determine the problem for $s_g^{(2)}$. Rearranging and remembering that $\tau_s\ll 1$, we have

$$0=\nabla_x\cdot\left(\nabla_x s_g^{(2)}+\nabla_X s_g^{(1)}\right)+\nabla_X\cdot\left(\nabla_x s_g^{(1)}+\nabla_X s_g^{(0)}\right) \qquad \text{in} \qquad \omega_g^{(0)}, \tag{3.57}$$

subject to the boundary conditions

$$\begin{aligned}-\left(\nabla_x s_g^{(2)}+\nabla_X s_g^{(1)}\right)\cdot\boldsymbol{e}_r+\nabla_X a^{(0)}\cdot\left(\nabla_x s_g^{(1)}+\nabla_X s_g^{(0)}\right)&\\ =-\tilde{\sigma}_s\nabla_x s_l^{(0)}\cdot\boldsymbol{e}_r=-\frac{2\tilde{\sigma}_s\kappa_s s^{(0)2}}{\left(1+a^{(0)}/\Lambda\right)^2} \qquad &\text{on} \qquad \Gamma_i^{(0)},\end{aligned} \tag{3.58}$$

$$s_g^{(2)} \text{ is periodic} \qquad \text{on} \qquad \partial\omega, \tag{3.59}$$

where we have used (3.42) and (3.51) to simplify (3.58) and remove the terms that come from expanding s_g on the boundary $\Gamma_i^{(0)}=\{|\boldsymbol{x}|=\Lambda+a^{(0)}\}$.

We now integrate (3.57) over $\omega_g^{(0)}$, remembering that $s_g^{(0)}$ does not depend on the microscale variables, and use the Divergence Theorem to obtain

$$0=\iiint_{\omega_g^{(0)}}\nabla_X\cdot\left(\nabla_x s_g^{(1)}+\nabla_X s_g^{(0)}\right)\,\mathrm{d}V+\iint_{\partial\omega_g^{(0)}}\left(\nabla_X s_g^{(1)}+\nabla_x s_g^{(2)}\right)\cdot\mathbf{d}\boldsymbol{S}, \tag{3.60}$$

where

$$\mathcal{V}_g\left(\omega_g^{(0)}\right)=\iiint_{\omega_g^{(0)}}\mathrm{d}V \tag{3.61}$$

is the volume of the gas phase in the unit cell. To rewrite the volume integral in (3.60), we use a generalisation of Leibniz Rule in the form

$$\nabla_X\cdot\iiint_{\omega_g^{(0)}(\boldsymbol{X},t)}\boldsymbol{g}\left(\boldsymbol{X},\boldsymbol{x},t\right)\,\mathrm{d}V=\iiint_{\omega_g^{(0)}}\nabla_X\cdot\boldsymbol{g}\,\mathrm{d}V-\iint_{\{|\boldsymbol{x}|=\Lambda+a^{(0)}\}}\nabla_X a^{(0)}\cdot\boldsymbol{g}\,\mathrm{d}S. \tag{3.62}$$

With $\boldsymbol{g}=\nabla_x s_g^{(1)}+\nabla_X s_g^{(0)}$, we obtain

$$\begin{aligned}\iiint_{\omega_g^{(0)}} \nabla_X \cdot \left(\nabla_x s_g^{(1)} + \nabla_X s_g^{(0)}\right) \mathrm{d}V &= \nabla_X \cdot \iiint_{\omega_g^{(0)}} \nabla_x s_g^{(1)} + \nabla_X s_g^{(0)} \,\mathrm{d}V \\ &\quad + \iint_{\Gamma_i^{(0)}} \nabla_X a^{(0)} \cdot \left(\nabla_x s_g^{(1)} + \nabla_X s_g^{(0)}\right) \mathrm{d}S \\ &= \nabla_X \cdot \left(\mathcal{V}_g \left(\mathbf{I} + \frac{1}{\mathcal{V}_g} \iiint_{\omega_g^{(0)}} \nabla_x \boldsymbol{\Phi} \,\mathrm{d}V\right) \nabla_X s_g^{(0)}\right) \\ &\quad + \iint_{\Gamma_i^{(0)}} \nabla_X a^{(0)} \cdot \left(\nabla_x s_g^{(1)} + \nabla_X s_g^{(0)}\right) \mathrm{d}S, \end{aligned} \tag{3.63}$$

where $\mathbf{I}$ is the identity matrix, and we have used (3.53) to obtain the final line in (3.63). Since $s_g^{(1)}$ and $s_g^{(2)}$ are periodic on $\partial\omega$, the surface integral in (3.60) can be reduced to an integral over $\Gamma_i^{(0)}$ only and so, using (3.58), we find that

$$\begin{aligned}\iint_{\partial\omega_g^{(0)}} \left(\nabla_X s_g^{(1)} + \nabla_x s_g^{(2)}\right) \cdot \mathbf{d}\boldsymbol{S} &= -\frac{2\tilde{\sigma}_s \kappa_s s^{(0)2} \mathcal{S}_{gl}}{\left(1 + a^{(0)}/\Lambda\right)^2} \\ &\quad - \iint_{\Gamma_i^{(0)}} \nabla_X a^{(0)} \cdot \left(\nabla_x s_g^{(1)} + \nabla_X s_g^{(0)}\right) \mathrm{d}S, \end{aligned} \tag{3.64}$$

where

$$\mathcal{S}_{gl}\left(\Gamma_i^{(0)}\right) = \iint_{\Gamma_i^{(0)}} \mathrm{d}S \tag{3.65}$$

is the surface area of the gas–liquid interface. Rewriting (3.60), using (3.63) and (3.64), we obtain the macroscale equations that govern the evolution of $s_g^{(0)}$ and $a^{(0)}$, which, dropping the superscripts, read

$$0 = \nabla_X \cdot \left(\mathcal{V}_g \mathbf{D} \nabla_X s_g\right) - \frac{2\tilde{\sigma}_s \kappa_s s^2 \mathcal{S}_{gl}}{\left(1 + a/\Lambda\right)^2}, \tag{3.66}$$

$$\frac{\partial a}{\partial t} = \frac{2s^2}{(1 + a/\Lambda)^2}, \tag{3.67}$$

where

$$s = 2s_g \left(1 + \sqrt{1 + \frac{8\Lambda\kappa_s a s_g}{\Lambda + a}}\right)^{-1}, \tag{3.68}$$

$$\mathbf{D}_{ij} = \delta_{ij} + \frac{1}{\mathcal{V}_g} \iiint_{\omega_g} \frac{\partial \Phi_j}{\partial x_i} \,\mathrm{d}V, \tag{3.69}$$

is the macroscopic diffusivity tensor which depends on the microscale structure, δ_{ij} is the Kronecker delta, and

$$\mathcal{V}_g = 1 - \frac{4}{3}\pi \left(\Lambda + a\right)^3, \qquad \mathcal{S}_{gl} = 4\pi \left(\Lambda + a\right)^2. \tag{3.70}$$

Due to the spatial symmetry of the cubic cell, $\mathbf{D}$ is proportional to the identity matrix, i.e., $\mathbf{D} = D\mathbf{I}$. We solve for D numerically using COMSOL Multiphysics. In figure

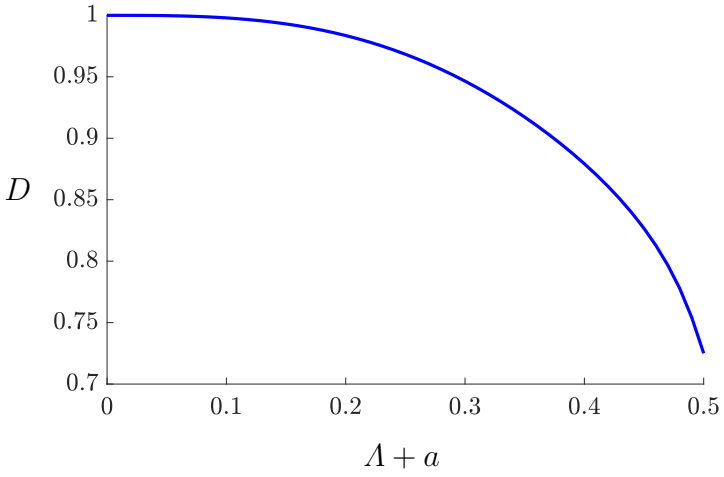

Figure 3.2: Effective diffusivity, D, as a function of the dimensionless radius of the pellet and thickness of the liquid layer around it.

3.2, we plot D as a function of $\Lambda + a$, and we observe that D decreases non-linearly as the liquid layer increases in thickness, as expected.

We conclude with a remark about the physical significance of the variable s_g. Since s_g is independent of the microscale, it is identical to the volume average of the sulphur dioxide concentration over the gas phase (which is an experimentally measurable quantity), since

$$s_g = \frac{1}{\mathcal{V}_g} \iiint_{\omega_g} s_g \, \mathrm{d}V. \tag{3.71}$$

Another useful quantity is the volume-averaged concentration over the whole space, defined as

$$\begin{aligned} S_g &= \frac{1}{\mathcal{V}_\omega} \left(\iiint_{\omega_g} s_g \, \mathrm{d}V + \frac{1}{\beta_s} \iiint_{\omega_l} s_l \, \mathrm{d}V \right) = \mathcal{V}_g s_g + \frac{1}{\beta_s} \iiint_{\omega_l} s_l \, \mathrm{d}V, \\ &= \left(\mathcal{V}_g + \frac{\mathcal{V}_l}{\beta_s} \right) s_g + \frac{2\Lambda^2 \kappa_s s^2}{\beta_s} \left(\frac{\mathcal{V}_l}{\Lambda + a} - \frac{\mathcal{S}_{gl} - \mathcal{S}_{ls}}{2} \right), \end{aligned} \tag{3.72}$$

where the factor of $1/\beta_s$ comes from scaling the sulphur dioxide concentration differently in the gas and in the liquid, $\mathcal{V}_\omega = 1$ is the volume of ω, $\mathcal{V}_l = 1 - 4\pi\Lambda^3/3 - \mathcal{V}_g$ is the volume of the liquid phase, $\mathcal{S}_{ls} = 4\pi\Lambda^2$ is the surface area of the pellet, and we have used (3.43) to obtain the third equality. S_g is important when we are interested in the total amount of sulphur dioxide in the filter, and how it is partitioned between both gaseous and dissolved form.

3.4.2 Limit II: $\boldsymbol{\sigma_s = O(1)}$ and $\boldsymbol{\kappa_s = O(\epsilon^2)}$

The second distinguished limit is the case when the mass transfer of sulphur dioxide into the liquid happens at an $O(1)$ rate and the dimensionless reaction rate is small. For convenience, we write $\kappa_s = \epsilon^2 \tilde{\kappa}_s$, where $\tilde{\kappa}_s = O(1)$. In this case, the $O(1)$ problem for s_g, s_l, and a becomes

$$\nabla_x^2 s_g^{(0)} = 0 \qquad \text{in} \qquad \omega_g^{(0)}, \tag{3.73}$$

$$\nabla_x^2 s_l^{(0)} = 0 \qquad \text{in} \qquad \omega_l^{(0)}, \tag{3.74}$$

$$\frac{\partial a^{(0)}}{\partial t} = \frac{2 s^{(0)2}}{(1 + a^{(0)}/\Lambda)^2}, \tag{3.75}$$

subject to the boundary conditions

$$\nabla_x s_l^{(0)} \cdot \boldsymbol{e}_r = 0 \qquad \text{on} \qquad \Gamma_p, \tag{3.76}$$

$$-\nabla_x s_g^{(0)} \cdot \boldsymbol{e}_r = -\sigma_s \nabla_x s_l^{(0)} \cdot \boldsymbol{e}_r \qquad \text{on} \qquad \Gamma_i^{(0)}, \tag{3.77}$$

$$s_g^{(0)} = s_l^{(0)} \qquad \text{on} \qquad \Gamma_i^{(0)}, \tag{3.78}$$

$$s_g^{(0)} \text{ is periodic} \qquad \text{on} \qquad \partial\omega, \tag{3.79}$$

where the changes from the limit in Section 3.4.1 are contained in (3.76) and (3.77). Returning to (3.73) and using (3.77) in an identical way as in Section 3.4.1, we obtain

$$\begin{aligned} \iiint_{\omega_g^{(0)}} \left|\nabla_x s_g^{(0)}\right|^2 \mathrm{d}V = -\iint_{\Gamma_i^{(0)}} s_g^{(0)} \nabla_x s_g^{(0)} \cdot \boldsymbol{e}_r \mathrm{d}S = -\iint_{\Gamma_i^{(0)}} \sigma_s s_l^{(0)} \nabla_x s_l^{(0)} \cdot \boldsymbol{e}_r \mathrm{d}S \\ = -\iint_{\Gamma_p} \sigma_s s_l^{(0)} \nabla_x s_l^{(0)} \cdot \boldsymbol{e}_r \mathrm{d}S = 0, \end{aligned} \tag{3.80}$$

where we have used the Divergence Theorem twice, together with (3.76) and (3.78). We conclude that $s_g^{(0)}$ is a function of the macroscale variables only. Solving the problem in the liquid layer given by (3.74), together with (3.76) and (3.78), we obtain

$$s_l^{(0)} = s_g^{(0)}. \tag{3.81}$$

In this case, we have to consider $O(\epsilon)$ problems for both s_g and s_l. The $O(\epsilon)$ components of (3.26)–(3.32) are

$$\nabla_x^2 s_g^{(1)} = 0 \qquad \text{in} \qquad \omega_g^{(0)}, \tag{3.82}$$

$$\nabla_x^2 s_l^{(1)} = 0 \qquad \text{in} \qquad \omega_l^{(0)}, \tag{3.83}$$

subject to the boundary conditions

$$(\nabla_x s_l^{(1)} + \nabla_X s_l^{(0)}) \cdot \boldsymbol{e}_r = 0 \qquad \text{on} \qquad \Gamma_p, \tag{3.84}$$

$$-\left(\nabla_X s_g^{(0)} + \nabla_x s_g^{(1)}\right) \cdot \boldsymbol{e}_r = -\sigma_s \left(\nabla_X s_l^{(0)} + \nabla_x s_l^{(1)}\right) \cdot \boldsymbol{e}_r \qquad \text{on} \qquad \Gamma_i^{(0)}, \tag{3.85}$$

$$s_g^{(1)} = s_l^{(1)} \qquad \text{on} \qquad \Gamma_i^{(0)}, \tag{3.86}$$

$$s_g^{(1)} \text{ is periodic} \qquad \text{on} \qquad \partial\omega, \tag{3.87}$$

again evaluating to zero the terms involving $\nabla_x s_l^{(0)}$ on the right-hand sides of (3.85) and (3.86) that arise from expanding the variables around the moving boundary.

In this limit, we use the linearity of the problem for both $s_g^{(1)}$ and $s_l^{(1)}$ to write the solution in the form

$$s_g^{(1)} = \boldsymbol{\Omega} \cdot \nabla_X s_g^{(0)}, \tag{3.88}$$

$$s_l^{(1)} = \boldsymbol{\Theta} \cdot \nabla_X s_l^{(0)}, \tag{3.89}$$

where we note that $s_l^{(0)} = s_g^{(0)}$ from (3.81), and the functions $\boldsymbol{\Omega}(\boldsymbol{x}, t) = (\Omega_1, \Omega_2, \Omega_3)$ and $\boldsymbol{\Theta}(\boldsymbol{x}, t) = (\Theta_1, \Theta_2, \Theta_3)$ satisfy the cell problem

$$\nabla_x^2 \Omega_i = 0 \qquad \text{in} \qquad \omega_g^{(0)}, \tag{3.90}$$

$$\nabla_x^2 \Theta_i = 0 \qquad \text{in} \qquad \omega_l^{(0)}, \tag{3.91}$$

subject to, for $i = 1, 2, 3$,

$$(\nabla_x \Omega_i + \boldsymbol{e}_i) \cdot \boldsymbol{e}_r = \sigma_s \left(\nabla_x \Theta_i + \boldsymbol{e}_i\right) \cdot \boldsymbol{e}_r \qquad \text{on} \qquad \Gamma_i^{(0)}, \tag{3.92}$$

$$\Omega_i = \Theta_i \qquad \text{on} \qquad \Gamma_i^{(0)}, \tag{3.93}$$

$$(\nabla_x \Theta_i + \boldsymbol{e}_i) \cdot \boldsymbol{e}_r = 0 \qquad \text{on} \qquad \Gamma_p, \tag{3.94}$$

$$\Omega_i \text{ is periodic} \qquad \text{on} \qquad \partial\omega. \tag{3.95}$$

We now look at the $O(\epsilon^2)$ problem of (3.26)–(3.32) for $s_g^{(2)}$ and $s_l^{(2)}$ (again remembering that $\tau_s \ll 1$), which becomes

$$0 = \nabla_x \cdot \left(\nabla_x s_g^{(2)} + \nabla_X s_g^{(1)}\right) + \nabla_X \cdot \left(\nabla_x s_g^{(1)} + \nabla_X s_g^{(0)}\right) \qquad \text{in} \qquad \omega_g^{(0)}, \tag{3.96}$$

$$0 = \nabla_x \cdot \left(\nabla_x s_l^{(2)} + \nabla_X s_l^{(1)}\right) + \nabla_X \cdot \left(\nabla_x s_l^{(1)} + \nabla_X s_l^{(0)}\right) \qquad \text{in} \qquad \omega_l^{(0)}, \tag{3.97}$$

subject to the relevant boundary conditions

$$
\begin{aligned}
&- \left(\nabla_x s_g^{(2)} + \nabla_X s_g^{(1)}\right) \cdot \boldsymbol{e}_r + \nabla_X a^{(0)} \cdot \left(\nabla_x s_g^{(1)} + \nabla_X s_g^{(0)}\right) \\
&= \sigma_s \left(- \left(\nabla_x s_l^{(2)} + \nabla_X s_l^{(1)}\right) \cdot \boldsymbol{e}_r + \nabla_X a^{(0)} \cdot \left(\nabla_x s_l^{(1)} + \nabla_X s_l^{(0)}\right)\right) \quad \text{on} \quad \Gamma_i^{(0)}, \qquad (3.98) \\
&\left(\nabla_x s_l^{(2)} + \nabla_X s_l^{(1)}\right) \cdot \boldsymbol{e}_r = 2\tilde{\kappa}_s s_l^{(0)2} \quad \text{on} \quad \Gamma_p, \qquad (3.99) \\
&s_g^{(2)} \text{ is periodic} \quad \text{on} \quad \partial\omega, \qquad (3.100)
\end{aligned}
$$

where we have used (3.85) to simplify (3.98).

Integrating (3.96) and (3.97) over $\omega_g^{(0)}$ and $\omega_l^{(0)}$, respectively, and applying first the Divergence Theorem and then Leibniz Rule together with periodicity of $s_g^{(1)}$ and $s_g^{(2)}$ we obtain

$$
\begin{aligned}
0 = \nabla_X \cdot &\left(\mathcal{V}_g \left(\mathbf{I} + \frac{1}{\mathcal{V}_g} \iiint_{\omega_g^{(0)}} \nabla_x \boldsymbol{\Omega} \, \mathrm{d}V \right) \nabla_X s_g^{(0)} \right) \\
&+ \iint_{\Gamma_i^{(0)}} \nabla_X a^{(0)} \cdot \left(\nabla_x s_g^{(1)} + \nabla_X s_g^{(0)}\right) - \left(\nabla_X s_g^{(1)} + \nabla_x s_g^{(2)}\right) \cdot \boldsymbol{e}_r \, \mathrm{d}S, \qquad (3.101) \\
0 = \nabla_X \cdot &\left(\mathcal{V}_l \left(\mathbf{I} + \frac{1}{\mathcal{V}_l} \iiint_{\omega_l^{(0)}} \nabla_x \boldsymbol{\Theta} \, \mathrm{d}V \right) \nabla_X s_l^{(0)} \right) \\
&- \iint_{\Gamma_i^{(0)}} \nabla_X a^{(0)} \cdot \left(\nabla_x s_l^{(1)} + \nabla_X s_l^{(0)}\right) + \left(\nabla_X s_l^{(1)} + \nabla_x s_l^{(2)}\right) \cdot \boldsymbol{e}_r \, \mathrm{d}S \\
&- \iint_{\Gamma_p} \left(\nabla_X s_l^{(1)} + \nabla_x s_l^{(2)}\right) \cdot \boldsymbol{e}_r \, \mathrm{d}S. \qquad (3.102)
\end{aligned}
$$

We now multiply (3.102) by σ_s, combine with (3.101), remembering that $s_l^{(0)} = s_g^{(0)}$ from (3.81), and use the boundary conditions (3.98) and (3.99) to obtain the macroscale equations that govern the evolution of $s_g^{(0)}$ and $a^{(0)}$ which, dropping the superscripts, read

$$
0 = \nabla_X \cdot (\mathcal{V} \mathbf{D} \nabla_X s_g) - \frac{2\sigma_s \tilde{\kappa}_s s_g^2 \mathcal{S}_{gl}}{(1 + a/\Lambda)^2}, \qquad (3.103)
$$

$$
\frac{\partial a}{\partial t} = \frac{2 s_g^2}{(1 + a/\Lambda)^2}, \qquad (3.104)
$$

where

$$
\mathbf{D}_{ij} = \delta_{ij} + \frac{1}{\mathcal{V}} \left(\iiint_{\omega_g} \frac{\partial \Omega_j}{\partial x_i} \, \mathrm{d}V + \sigma_s \iiint_{\omega_l} \frac{\partial \Theta_j}{\partial x_i} \, \mathrm{d}V \right), \qquad (3.105)
$$

$$
\mathcal{V} = \mathcal{V}_g + \sigma_s \mathcal{V}_l. \qquad (3.106)
$$

In this limit, since the mass transfer of sulphur dioxide between the gas and the liquid phase is $O(1)$, we must solve two cell problems, and the diffusivity tensor takes account of the diffusivities in both the gas and the liquid domain (unlike the previous limit, which only depended on the diffusivity in the gas domain).

3.4.3 Uniformly Valid Equations

We combine the results from the limits in Sections 3.4.1 and 3.4.2 into a uniformly valid set of macroscale equations to obtain

$$0 = \nabla_X \cdot (\mathcal{V}\mathbf{D}\nabla_X s_g) - \frac{2\sigma_s\kappa_s s^2 \mathcal{S}_{gl}}{\epsilon^2 \left(1 + a/\Lambda\right)^2}, \tag{3.107}$$

$$\frac{\partial a}{\partial t} = \frac{2s^2}{(1 + a/\Lambda)^2}, \tag{3.108}$$

where s, $\mathbf{D}$, and $\mathcal{V}$ are defined as in (3.49), (3.105), and (3.106), respectively. Setting either σ_s or κ_s to be $O(\epsilon^2)$ recovers the previous distinguished limits for effective uptake and effective diffusion, respectively, while further simplifications can be made if both $\sigma_s, \kappa_s \ll 1$.

3.4.4 A Comment on the Limit When Both $\sigma_s, \kappa_s = O(1)$

In the limit when both $\sigma_s, \kappa_s = O(1)$, sulphur dioxide will be depleted at a much faster rate than in the previous two limits. The leading-order governing equations for $s_g^{(0)}$ and $s_l^{(0)}$ in this case are

$$\nabla_x^2 s_g^{(0)} = 0 \qquad \text{in} \qquad \omega_g^{(0)}, \tag{3.109}$$

$$\nabla_x^2 s_l^{(0)} = 0 \qquad \text{in} \qquad \omega_l^{(0)}, \tag{3.110}$$

subject to the boundary conditions

$$\nabla_x s_l^{(0)} \cdot \boldsymbol{e}_r = 2\kappa_s s_l^{(0)2} \qquad \text{on} \qquad \Gamma_p, \tag{3.111}$$

$$-\nabla_x s_g^{(0)} \cdot \boldsymbol{e}_r = -\sigma_s \nabla_x s_l^{(0)} \cdot \boldsymbol{e}_r \qquad \text{on} \qquad \Gamma_i^{(0)}, \tag{3.112}$$

$$s_g^{(0)} = s_l^{(0)} \qquad \text{on} \qquad \Gamma_i^{(0)}, \tag{3.113}$$

$$s_g^{(0)} \text{ is periodic} \qquad \text{on} \qquad \partial\omega, \tag{3.114}$$

i.e., the right-hand sides of (3.111) and (3.112) are both non-zero. Applying the Divergence Theorem to (3.109) and (3.110), and using (3.111), (3.112), and (3.114), we conclude that

$$s_l^{(0)} = 0 \qquad \text{on} \qquad \Gamma_p. \tag{3.115}$$

Then, solving (3.110), with (3.111), (3.115) and the radial symmetry of $s_l^{(0)}$, we obtain

$$s_l^{(0)} = 0 \qquad \text{in} \qquad \omega_l^{(0)}. \tag{3.116}$$

Following the previous arguments in (3.46)–(3.48) (where (3.112) and (3.116) reduce to (3.39)), we see that $s_g^{(0)}$ is independent of the microscale variables and, thus, using (3.113), we establish that

$$s_g^{(0)} = 0 \qquad \text{in} \qquad \omega_g^{(0)}, \tag{3.117}$$

i.e., all the sulphur dioxide is consumed on the timescale of liquid growth. In order to explore how the sulphur dioxide concentration evolves in this case, we assume that $\tau_s = O(1)$, i.e., the reaction rate is comparable to the diffusive rate through the liquid. This means that the advective terms in (3.26) and (3.27) should now enter the leading-order equations for $s_g^{(0)}$ and $s_l^{(0)}$. As in Dalwadi *et al.* (2018), in this regime, there is a limit in which $\eta_s \ll 1$, which simplifies the leading-order version of (3.26), but retains the advective term in the leading-order version of (3.27). In either case, we need to add another equation for the velocity of the fluid (e.g., conservation of momentum). However, unlike in Dalwadi *et al.* (2018), the resulting equations cannot be solved explicitly due to the non-linearity in the boundary conditions on the surface of the catalytic pellet and the moving boundary that is present.

We note that we obtain the same conclusions if we assume $\sigma_s\kappa_s = O(\epsilon)$ and one of κ_s or σ_s is $O(1)$. In these limits, the combined effect of the mass transfer and reaction is strong enough to consume all the sulphur dioxide to leading order on our chosen timescale. This means that, in the limits we considered, where $\kappa_s\sigma_s = O(\epsilon^2)$, macroscale diffusion balances macroscale uptake.

3.4.5 Physically Relevant Limit

It is clear that the limits in which $\sigma_s\kappa_s = O(\epsilon^2)$ provide the largest values of the parameters for which we obtain non-trivial solutions for the sulphur dioxide concentration on our timescale. Furthermore, the values of the physical parameters also suggest that these are the physically relevant regimes, since otherwise the device would fill with liquid and lose efficiency much faster than the experiments indicate. In fact, using actual parameter values, the most relevant limit is where κ_s and σ_s are both $O(\epsilon)$. This is a sub-limit of the other two considered in Sections 3.4.1 and 3.4.2, and the governing equations in this case can be obtained, for example, by letting $\kappa_s \to 0$ in (3.66) and (3.67) or using the equations in Section 3.4.3 with $\kappa_s, \sigma_s = O(\epsilon)$. Writing $\kappa_s = \epsilon\bar{\kappa}_s, \sigma_s = \epsilon\bar{\sigma}_s$, where $\bar{\kappa}_s, \bar{\sigma}_s = O(1)$, we find that

$$0 = \nabla_X \cdot (\mathcal{V}_g D \nabla_X s_g) - \frac{2\bar{\sigma}_s\bar{\kappa}_s\mathcal{S}_{gl}s_g^2}{(1 + a/\Lambda)^2}, \tag{3.118}$$

$$\frac{\partial a}{\partial t} = \frac{2s_g^2}{(1 + a/\Lambda)^2}, \tag{3.119}$$

where D, $\mathcal{V}_g$, and $\mathcal{S}_{gl}$ are as defined in (3.69) and (3.70).

3.5 Using the Microscale Model to Determine the Reaction Rate Constant $\boldsymbol{k}$

We conclude this chapter by formulating and analysing a model of what happens around a single catalytic pellet producing liquid sulphuric acid. The goal of such a model will be estimation of the unknown *a priori* effective chemical rate constant for the reaction, in which sulphur dioxide is converted into sulphuric acid. Knowing how long it takes for the first droplets of sulphuric acid to appear on the outside surface of the filter sheets will help determine the reaction rate that appears in table 1.1 and is used as an input parameter in our models. Sanaei & Ciocanel (2016) consider a similar problem but assume a simplified one-dimensional Cartesian geometry, where there is an infinite catalytic plate rather than a pellet. In addition, they do not analyse the microscale problem further, nor do they explicitly solve for the evolution of the thickness of the liquid layer.

3.5.1 Model Formulation

We consider the microscale model presented in Section 3.2 in a spherically symmetric coordinate system, centred at the pellet (see figure 3.3 for a schematic of the pellet). The governing equations for sulphur dioxide concentration in the gas and in the liquid, and the liquid-layer growth are

$$\frac{\partial \hat{s}_g}{\partial \hat{t}} + \hat{u}_{g,r}\frac{\partial \hat{s}_g}{\partial \hat{r}} = \frac{D_{s_g}}{\hat{r}^2}\frac{\partial}{\partial \hat{r}}\left(\hat{r}^2\frac{\partial \hat{s}_g}{\partial \hat{r}}\right) \qquad \text{in} \qquad \hat{r} > R + \hat{a}, \tag{3.120}$$

$$\frac{\partial \hat{s}_l}{\partial \hat{t}} + \hat{u}_{l,r}\frac{\partial \hat{s}_l}{\partial \hat{r}} = \frac{D_{s_l}}{\hat{r}^2}\frac{\partial}{\partial \hat{r}}\left(\hat{r}^2\frac{\partial \hat{s}_l}{\partial \hat{r}}\right) \qquad \text{in} \qquad R < \hat{r} < R + \hat{a}, \tag{3.121}$$

$$\left(1 + \frac{\hat{a}}{R}\right)^2 \frac{\mathrm{d}\hat{a}}{\mathrm{d}\hat{t}} = 2kV_{\mathrm{m}}\hat{s}^2, \tag{3.122}$$

where $\hat{u}_{g,r}$ and $\hat{u}_{l,r}$ are the radial velocities of the gas and the liquid, respectively, and we recall that $\hat{s} = \hat{s}_l|_{\hat{r}=R}$. We note that the liquid layer of sulphuric acid around the pellet grows until it reaches a thickness of half the typical inter-pellet distance $l_p = l - 2R$, measured from the edge of one pellet to the closest edge of the next pellet, when it will coalesce with the growing liquid layer from a neighbouring pellet.

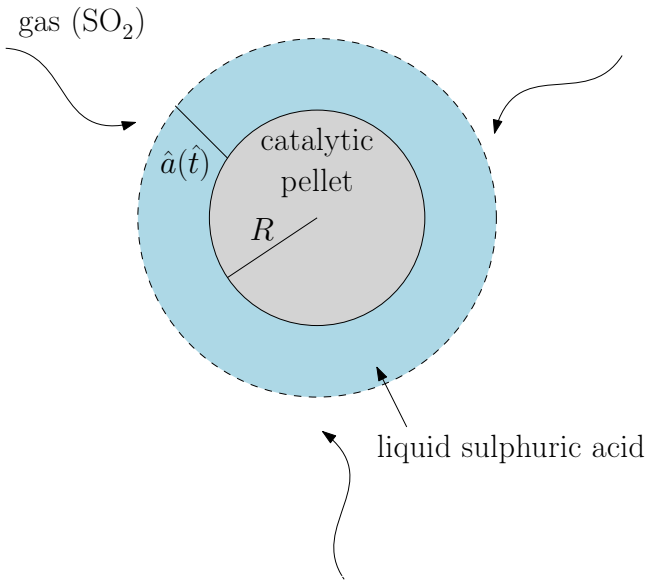

Figure 3.3: Radially symmetric catalytic pellet.

The flue-gas source of sulphur dioxide, at constant concentration S_0, is assumed to be located far away from the pellet, and, thus, we write

$$\hat{s}_g \to S_0 \qquad \text{as} \qquad \hat{r} \to \infty. \tag{3.123}$$

The rest of the boundary and initial conditions are the same as in Section 3.2, namely,

$$D_{s_g}\frac{\partial \hat{s}_g}{\partial \hat{r}} = D_{s_l}\frac{\partial \hat{s}_l}{\partial \hat{r}} \qquad \text{at} \qquad \hat{r} = R + \hat{a}, \tag{3.124}$$

$$\hat{s}_g = \beta_s \hat{s}_l \qquad \text{at} \qquad \hat{r} = R + \hat{a}, \tag{3.125}$$

$$D_{s_l}\frac{\partial \hat{s}_l}{\partial \hat{r}} = 2k\hat{s}^2 \qquad \text{at} \qquad \hat{r} = R, \tag{3.126}$$

$$\hat{s}_g = S_0 \qquad \text{at} \qquad \hat{t} = 0, \tag{3.127}$$

$$\hat{a} = 0 \qquad \text{at} \qquad \hat{t} = 0. \tag{3.128}$$

3.5.2 Non-Dimensionalisation

We non-dimensionalise the model using the following scalings

$$\begin{gathered}(\hat{r}, \hat{a}\,) = l_p(r, a), \quad \hat{t} = T_{\text{clog}}t, \quad (\hat{u}_{g,r}, \hat{u}_{l,r}) = (l_p/T_{\text{clog}})(u_{g,r}, u_{l,r}), \\ \hat{s}_g = S_0 s_g, \quad \hat{s}_l = (S_0/\beta_s)s_l,\end{gathered} \tag{3.129}$$

where, for the purposes of this model, we have non-dimensionalised time with T_{clog}, which is the average time until liquid droplets appear on the filter sheets for the

first time, as reported by W. L. Gore and Associates, Inc. This number varies with the operating conditions and the inlet concentration of sulphur dioxide, but for a moderate amount of sulphur dioxide (the value stated in table 1.1), $T_{\text{clog}} \approx 1$ day. We assume that, on average, at T_{clog} the liquid layer will have grown to half the inter-pellet distance, l_p, at which point it will have coalesced with the layer growing around a neighbouring pellet in the actual filter sheets, i.e., we identify the time for coalescence of neighbouring liquid layers with the observation of the first droplets on the filter sheets. Thus, when estimating the value of the reaction rate constant k, we will be looking for k, such that $a = 0.5$ at $t = 1$. We note that, this timescale is indeed much longer than the corresponding diffusive timescale through the liquid, $l_p^2/D_{s_l} \approx 0.1\,\text{s}$, which again justifies neglecting advection associated with the fluid flow. The governing equations become

$$\eta_s \upsilon \left(\frac{\partial s_g}{\partial t} + u_{g,r} \frac{\partial s_g}{\partial r} \right) = \frac{1}{r^2} \frac{\partial}{\partial r} \left(r^2 \frac{\partial s_g}{\partial r} \right) \qquad \text{in} \qquad r > \Lambda_p + a, \tag{3.130}$$

$$\upsilon \left(\frac{\partial s_l}{\partial t} + u_{l,r} \frac{\partial s_l}{\partial r} \right) = \frac{1}{r^2} \frac{\partial}{\partial r} \left(r^2 \frac{\partial s_l}{\partial r} \right) \qquad \text{in} \qquad \Lambda_p < r < \Lambda_p + a, \tag{3.131}$$

$$\left(1 + \frac{a}{\Lambda_p} \right)^2 \frac{\mathrm{d}a}{\mathrm{d}t} = \frac{\alpha \kappa_s s^2}{\beta_s \upsilon} \qquad \text{at} \qquad r = \Lambda_p, \tag{3.132}$$

which are subject to the following boundary and initial conditions

$$s_g \to 1 \qquad \text{as} \qquad r \to \infty, \tag{3.133}$$

$$\frac{\partial s_g}{\partial r} = \frac{\eta_s}{\beta_s} \frac{\partial s_l}{\partial r} \qquad \text{at} \qquad r = \Lambda_p + a, \tag{3.134}$$

$$s_g = s_l \qquad \text{at} \qquad r = \Lambda_p + a, \tag{3.135}$$

$$\frac{\partial s_l}{\partial r} = \kappa_s s^2 \qquad \text{at} \qquad r = \Lambda_p, \tag{3.136}$$

$$s_g = 1 \qquad \text{at} \qquad t = 0, \tag{3.137}$$

$$a = 0 \qquad \text{at} \qquad t = 0, \tag{3.138}$$

where $s = s_l|_{r=\Lambda_p}$, and we have defined the following five dimensionless numbers

$$\alpha = S_0 V_{\text{m}}, \quad \eta_s = \frac{D_{s_l}}{D_{s_g}}, \quad \kappa_s = \frac{2klS_0}{\beta_s D_{s_l}}, \quad \Lambda_p = \frac{R}{l_p}, \quad \upsilon = \frac{l_p^2}{D_{s_l} T_{\text{clog}}}. \tag{3.139}$$

Here, α measures the volumetric change in the gas-to-liquid conversion between sulphur dioxide and sulphuric acid, η_s is the ratio of diffusivities of sulphur dioxide in the gas and in the liquid, respectively, κ_s captures the relative strength of reaction to diffusion and can be thought of as a Damköhler number for the reaction, Λ_p is

the ratio of the pellet radius to the inter-pellet distance, and, thus, is a measure for the pellet density inside the filter sheets, and υ represents the ratio between the diffusive timescale in the liquid sulphuric acid and the timescale for the first droplets to appear on the surface of the filter sheets. Using the parameter values in table 1.1, $\alpha \approx 5 \times 10^{-7}, \eta_s \approx 2 \times 10^{-4}, \Lambda_p \approx 2.5 \times 10^{-1}$ and $\upsilon \approx 2.3 \times 10^{-6}$. We note that the value of κ_s is *a priori* unknown, as it depends on the reaction rate, which is what we want to estimate. However, we anticipate that the grouping in (3.132), $\alpha\kappa_s/\beta_s\upsilon = O(1)$, by our choice of non-dimensionalisation. We also note that, for the purposes of numerical simulations, we have incorporated the numerical pre-factor from the kinetics law in the definition of κ_s.

3.5.3 Asymptotic Simplifications

We now exploit the fact that some of our dimensionless numbers are negligible in magnitude to simplify the governing equations and boundary conditions. In particular, since the parameters in front of the time derivatives in (3.130) and (3.131) are small, we can assume that the sulphur dioxide concentration in the gas and in the liquid evolves quasi-statically, according to

$$0 = \frac{1}{r^2}\frac{\partial}{\partial r}\left(r^2\frac{\partial s_g}{\partial r}\right) \qquad \text{in} \qquad r > \Lambda_p + a, \tag{3.140}$$

$$0 = \frac{1}{r^2}\frac{\partial}{\partial r}\left(r^2\frac{\partial s_l}{\partial r}\right) \qquad \text{in} \qquad \Lambda_p < r < \Lambda_p + a. \tag{3.141}$$

In addition, due to the small diffusivity ratio, η_s, the left-hand side of (3.134) dominates over the right-hand side, and the boundary condition can be simplified to

$$\frac{\partial s_g}{\partial r} = 0 \qquad \text{at} \qquad r = \Lambda_p + a. \tag{3.142}$$

Equation (3.140) and conditions (3.133) and (3.142) indicate that the concentration of sulphur dioxide in the gas is constant and is given by its far-field value, i.e.,

$$s_g(r, t) = 1. \tag{3.143}$$

Together with (3.135), equation (3.143) gives a Dirichlet condition for the sulphur dioxide concentration in the liquid, namely,

$$s_l = 1 \qquad \text{at} \qquad r = \Lambda_p + a. \tag{3.144}$$

Thus, we have decoupled the problem for s_l from that for s_g. In order to solve for s_l, we need to solve (3.141) together with (3.136) and (3.144). Integrating (3.141) and applying (3.136) gives

$$\frac{\partial s_l}{\partial r} = \frac{\kappa_s \Lambda_p^2 s^2}{r^2}. \tag{3.145}$$

Integrating (3.145) and applying (3.144) yields

$$s_l = \kappa_s \Lambda_p^2 s^2 \left(\frac{1}{\Lambda_p + a} - \frac{1}{r} \right) + 1. \tag{3.146}$$

Thus, evaluating (3.146) at $r = \Lambda_p$, we see that s can be found by solving

$$s = \kappa_s \Lambda_p^2 s^2 \left(\frac{1}{\Lambda_p + a} - \frac{1}{\Lambda_p} \right) + 1, \tag{3.147}$$

which rearranges to the following quadratic equation for s

$$s^2 + \frac{\Lambda_p + a}{\kappa_s \Lambda_p a} s - \frac{\Lambda_p + a}{\kappa_s \Lambda_p a} = 0. \tag{3.148}$$

The solution for s_l given by (3.146) depends on a. Therefore, we need to solve (3.132) with (3.138) and the value for s, obtained by solving (3.148), to determine s_l everywhere.

Equation (3.148) has two solutions

$$s_\pm = \frac{\Lambda_p + a}{2\kappa_s \Lambda_p a} \left(-1 \pm \sqrt{1 + \frac{4\kappa_s \Lambda_p a}{\Lambda_p + a}} \right) = 2 \left(1 \pm \sqrt{1 + \frac{4\kappa_s \Lambda_p a}{\Lambda_p + a}} \right)^{-1}, \tag{3.149}$$

where we have used the formula $(A - B)(A + B) = A^2 - B^2$ to rationalise the term after the first equality. This makes it clear how to choose the physically relevant solution, since we require that the sulphur dioxide concentration in the liquid layer should approach the concentration prescribed by the boundary condition (3.144) as the reaction rate tends to zero, i.e., $s \to 1$ as $\kappa_s \to 0$. Thus, we see that the relevant solution is

$$s = s_+ = 2 \left(1 + \sqrt{1 + \frac{4\kappa_s \Lambda_p a}{\Lambda_p + a}} \right)^{-1}. \tag{3.150}$$

We now use (3.150) to reduce the system of equations to a single non-linear equation for a, namely,

$$\left(1 + \frac{a}{\Lambda_p} \right)^2 \frac{\mathrm{d}a}{\mathrm{d}t} = \frac{4\alpha\kappa_s}{\beta_s \upsilon} \left(1 + \sqrt{1 + \frac{4\kappa_s \Lambda_p a}{\Lambda_p + a}} \right)^{-2}. \tag{3.151}$$

We can gain insight into the qualitative behaviour of the solutions to (3.151) by considering what happens in the cases of very slow ($\kappa_s \to 0$) and very fast ($\kappa_s \to \infty$) reaction. In the first case, we see that the right-hand side of (3.151) tends to zero as $\kappa_s \to 0$. Thus, we conclude that the film is stationary to leading order in κ_s. In the second case, taking the limit as $\kappa_s \to \infty$ in (3.150), we obtain

$$s \sim \sqrt{\frac{\Lambda_p + a}{\kappa_s \Lambda_p a}} \to 0 \qquad \text{as} \qquad \kappa_s \to \infty. \tag{3.152}$$

Therefore, to leading order in $1/\kappa_s$, (3.132) becomes

$$\left(1 + \frac{a}{\Lambda_p}\right) \frac{\mathrm{d}a}{\mathrm{d}t} = \frac{\alpha}{\beta_s \upsilon a}. \tag{3.153}$$

Together with (3.138), this can be solved implicitly to yield

$$t = \frac{\beta_s \upsilon}{3\alpha\Lambda_p} a^2 \left(a + \frac{3\Lambda_p}{2}\right). \tag{3.154}$$

This asymptotic limit gives an upper bound for the thickness of the liquid layer and corresponds to instantaneous conversion of all sulphur dioxide reacting on the surface of the pellet.

3.5.4 Numerical Solution

We now solve (3.151) with (3.138) numerically using the NDSolve package in *Mathematica* and the parameter values presented in Section 3.5.2. We first examine the behaviour of a and s_l, where we take $\kappa_s = 0.45$, which is the value we find after fitting the model to experimental observations. We present this procedure later in the section. In figure 3.4(a), we show the temporal profile of the thickness of the liquid sulphuric acid layer, a. We see that, as time increases, the layer grows more slowly. In figure 3.4(b), we show a spatial profile of the sulphur dioxide concentration in the liquid, s_l, for various times. The curves are monotonic across the thickness of the layer. At $t = 1$, the concentration at the pellet surface has dropped by less than 10% of its initial value, which is a result of the small magnitude of the dimensionless reaction rate, κ_s.

In order to find the quoted value of κ_s, we vary κ_s and examine the value of $a(1)$, recalling that our goal is to find κ_s, such that $a(1) = 0.5$, which corresponds to filling half the inter-pellet distance by the time the first droplets appear on the surface of the filter sheets (*cf.* the beginning of Section 3.5.2). We recall that κ_s is indeed the

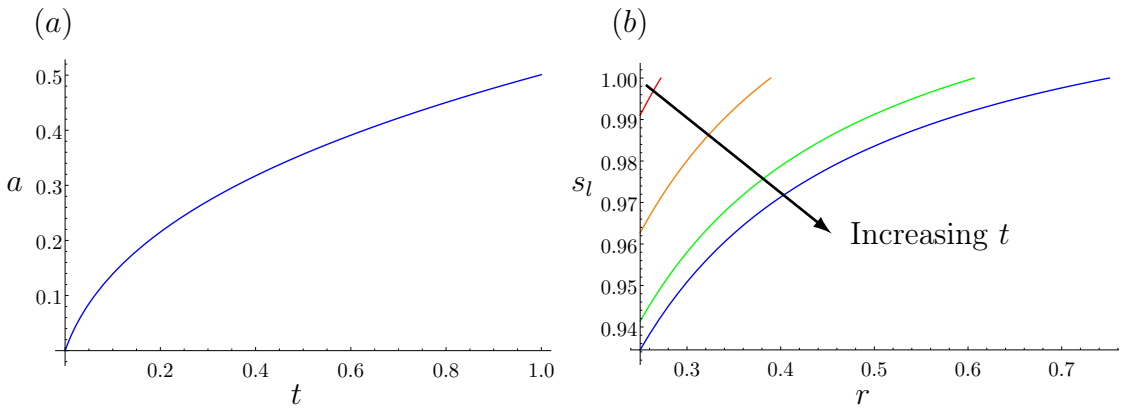

Figure 3.4: (a) Temporal profile of a and (b) spatial profile of s_l for $t = 0.01$ (red), 0.1 (orange), 0.5 (green), and 1 (blue). Here, $\alpha = 5 \times 10^{-7}, \kappa_s = 4.5 \times 10^{-1}, \Lambda_p = 2.5 \times 10^{-1}, \upsilon = 2.3 \times 10^{-6}$.

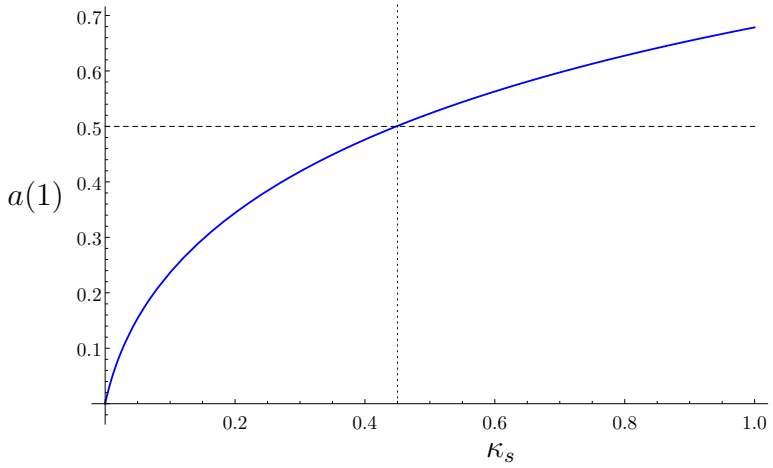

Figure 3.5: Plot of $a(1)$ as a function of the dimensionless parameter κ_s (blue) and the constant value of 0.5 (dashed). The value of κ_s where the curves cross is indicated by a dotted line. Here, $\alpha = 5 \times 10^{-7}, \Lambda_p = 2.5 \times 10^{-1}, \upsilon = 2.3 \times 10^{-6}$.

only unknown parameter in our model, and once fixed, the reaction rate constant, k, can be recovered using (3.139) as

$$k = \frac{\kappa_s \beta_s D_{s_l}}{2lS_0}. \tag{3.155}$$

In figure 3.5, we show how $a(1)$ varies with κ_s. We see a monotonic behaviour, and, thus, we can identify a unique value $\kappa_s \approx 0.45$ that corresponds to $a(1) = 0.5$. Therefore, the estimated value for the reaction rate constant is $k = 6 \times 10^{-5}\,\mathrm{m}^4\,\mathrm{mol}^{-1}\,\mathrm{s}^{-1}$, which is the value that appears in table 1.1.

We finish this section with a remark regarding the uncertainty in the estimate for κ_s. In practice, the time T_{clog} may vary depending on the operating conditions of the filter. The estimate that we used, $T_{\text{clog}} \approx 1$ day, is the value that is known to the least

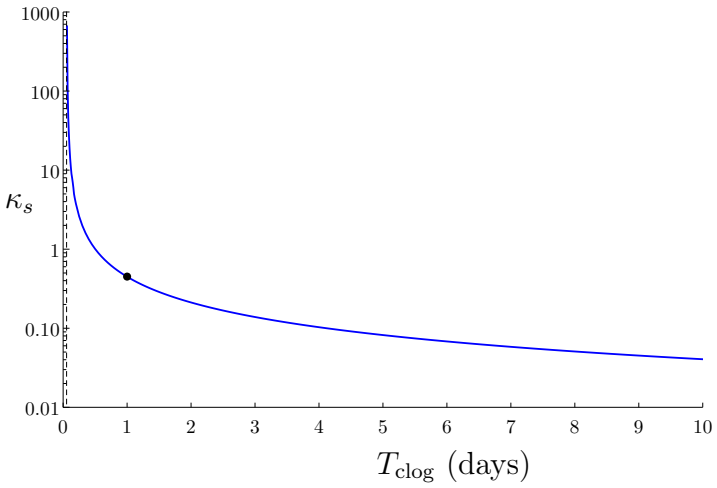

Figure 3.6: Log-plot of κ_s as a function of T_{clog} (blue) and the corresponding asymptote at $T_{\text{clog}} = 0.054$ day (dashed). The black dot corresponds to the point $(1, 0.45)$. Here, $\alpha = 5 \times 10^{-7}, \Lambda_p = 2.5 \times 10^{-1}$.

degree of accuracy in our model. We would, thus, like to understand how changes in T_{clog} affect the estimated value of κ_s should we be supplied with a more accurate value. In figure 3.6, we show a log-plot of κ_s as a function of T_{clog} (measured in days), which is obtained by varying v in (3.151). We also indicate the point (1,0.45) that we have already found, which provides the value of κ_s that corresponds to a clogging time of one day. The graph has a vertical asymptote as $T_{\text{clog}} \to 0.054^+$ day. This suggests that no value of κ_s can be identified with a scenario in which $T_{\text{clog}} \leq 0.054$ day. This is due to the fact that there is a time associated with the diffusive transport of sulphur dioxide through the liquid layer before it reacts on the pellet surface, which provides an upper bound on the rate of generation of sulphuric acid.

3.6 Conclusions

In this chapter, we developed a mathematical model to describe the operation of a device that converts gaseous sulphur dioxide into liquid sulphuric acid through a chemical reaction that occurs on the surface of catalytic pellets contained in a porous filter sheet. Our aim was to track the spatial and temporal evolution of the concentration of sulphur dioxide and the local amount of acid in the filter. We began by describing the model that holds on the scale of a single catalytic pellet in the filter sheet, around which a uniform layer of liquid sulphuric acid forms. We then systematically homogenised these equations and derived a set of macroscale equations that describe the whole filter and capture the effect of the porous microstructure via (i) an effective

"sink" term in the macroscale equation for the concentration of sulphur dioxide in the filter, and (ii) an effective diffusivity. We presented two distinguished limits based on the order of magnitude of two dimensionless numbers, κ_s and σ_s, which measure the relative strength of reaction to diffusion and the relative mass transfer on either side of the gas–liquid interface, respectively. In the first limit, when $\kappa_s = O(1)$ and $\sigma_s = O(\epsilon^2)$, the sink term for sulphur dioxide was a complicated non-linear function of the concentration of sulphur dioxide and the thickness of the sulphuric acid. In the second limit, when $\kappa_s = O(\epsilon^2)$ and $\sigma_s = O(1)$, this term simplified considerably but the effective diffusivity became more difficult to calculate. We identified a physically relevant sub-limit, in which both κ_s and σ_s are both small, which simplified the governing equations in the filter sheet. In each case, we established a quasi-static evolution of the sulphur dioxide concentration.

In the last section, we used the mathematical framework we had developed with the microscale model to consider a radially symmetric model for growth of a layer of liquid sulphuric acid around a single catalytic pellet inside the porous filter sheets of the GMCS device. We reduced the system of equations governing the concentration of sulphur dioxide in the gas and in the liquid, and the equation for the thickness of the liquid layer to a single non-linear initial-value problem for the layer thickness. We solved this equation numerically and, by varying the unknown reaction rate, we found a unique value that matched the experimental observations by W. L. Gore and Associates, Inc. on the average time taken for the liquid to fill the void space in the filter sheets and to be expelled on their surface. We, thus, found that the reaction rate constant in our formulation is $k = 6 \times 10^{-5}\,\mathrm{m}^4\,\mathrm{mol}^{-1}\,\mathrm{s}^{-1}$, which is the value that appears in table 1.1. We also explored the relationship between reaction rate and the corresponding time taken for the liquid to be expelled on the surface of the filter sheets and found that there was a minimum time for which liquid could be expelled from the surface. This corresponds to the limit of infinite reaction rate when the process is limited by diffusion transport. We investigated this behaviour in detail by analysing the asymptotic limit of infinite reaction rate. Our analysis can be used to model reactions with a phase change of the reactants in other industrial processes.

We now move on to a macroscale model of the GMCS device that includes both the filter sheets and the filter channels, where the flue gas flows.

Chapter 4

Device-Scale Model

4.1 Introduction

Now that we have derived the macroscale equations for the sulphur dioxide concentration and the thickness of the liquid acid layer within the filter sheets, we need to incorporate these in a model for the whole device. Our goal is to couple these macroscale equations with the equations that describe how the flue gas is transported within the filter channels. This will link important system parameters, such as the inlet sulphur dioxide concentration, to output quantities that describe the operation of the device, such as the outlet sulphur dioxide concentration.

In Section 4.2, we formulate the mathematical model and derive the system of governing equations identifying key dimensionless parameters. In Section 4.3, we present asymptotic results for a slender filter geometry and consider two limits that depend on the amount of sulphur dioxide at the inlet of the device and the aspect ratio of the filter channels. In Section 4.4, we show numerical results of the problem and compare with the asymptotic predictions, and, in Section 4.5, we show numerical results for an extended macroscale model, valid beyond the point of first liquid-layer coalescence. In Section 4.6, we present a radially symmetric version of the device-scale model and compare the results with the Cartesian version. We discuss general features and practical implications of the macroscale model in Section 4.7 and consider a simple model of what happens once all gaseous pathways in the filter sheets are blocked with liquid sulphuric acid in Section 4.8. We draw conclusions in Section 4.9.

4.2 Model Formulation

We begin by considering the filter as shown on the left in figure 1.2, which we reproduce with the relevant coordinate system (with macroscale variables $\hat{X}, \hat{Y}, \hat{Z}$) and length scales in figure 4.1. This is a representation of a single channel of the GMCS device, where the sheets are assumed to be parallel to each other and the flue gas flows between them. However, it contains all necessary mathematical features that can be incorporated in another geometrical set-up.

As shown in figure 4.1, we assume the flue gas flows up through a channel of half-width d and length L alongside a filter sheet of thickness H, width W, and length L. In the filter channel, since the gas flow is uniform in the $\hat{Z}$-direction and we assume no flux of gas at $\hat{Y} = \pm W/2$, we anticipate negligible variation in the $\hat{X}$-direction and no variation in the $\hat{Y}$-direction. The Reynolds number, associated with the flow under normal operating conditions, is estimated to be $\mathrm{Re} = 2\rho_{\mathrm{gas}} U d/\mu_{\mathrm{gas}} = O(10^3) \gg 1$, where we use $\rho_{\mathrm{gas}} \approx 1\mathrm{kg\,m^{-3}}$ and $\mu_{\mathrm{gas}} \approx 10^{-5}\mathrm{Pa\,s}$ (Perry & Green, 1997). Thus, any boundary layer near the surface of the channel walls will be small, and, for simplicity, we assume a plug flow in the channel. We note that, on the surface of the filter sheet, we could have applied the boundary condition found in Beavers & Joseph (1967) to account for the transmission of longitudinal flow from the channel into the porous medium. This would introduce a thin layer, near the surface, across which the gas velocity is reduced to zero. Since our focus is on the generation of liquid inside the filter sheet, for simplicity we assume the channel wall provides no retardation to the flow. Thus, conservation of mass of sulphur dioxide in the filter channel with cross-sectionally averaged concentration $\hat{S}(\hat{z}, \hat{t})$ reads

$$d\left(\frac{\partial \hat{S}}{\partial \hat{t}} + U\frac{\partial \hat{S}}{\partial \hat{Z}}\right) = \left[\mathcal{V}_g\,(\hat{a})\,\hat{D}(\hat{a})\frac{\partial \hat{s}_g}{\partial \hat{X}}\right]_{\hat{X}=0}, \tag{4.1}$$

where U is the constant speed of the gas flow, $\mathcal{V}_g$ is the void fraction in the filter sheet (defined in (3.70)), and $\hat{D}(\hat{a}) = D_{s_g} D(a)$ with D defined in (3.69). The right-hand side of (4.1) accounts for the uptake of sulphur dioxide by the filter sheet at $\hat{X} = 0$, while we have assumed zero flux in the middle of the channel at $\hat{X} = -d$ and on its borders located at $\hat{Y} = \pm W/2$. We note that we have neglected diffusion along the channel, which is justifiable, since the Péclet number $\mathrm{Pe} = UL/D_{s_g} \approx 10^4 \gg 1$.[1] In the filter sheet, we track the concentration, $\hat{s}_g$, of sulphur dioxide and the void

[1] Of course, it is possible that a thin diffusive boundary layer exists on the channel walls, but, due to the largeness of the Péclet number, we assume its effect is negligible.

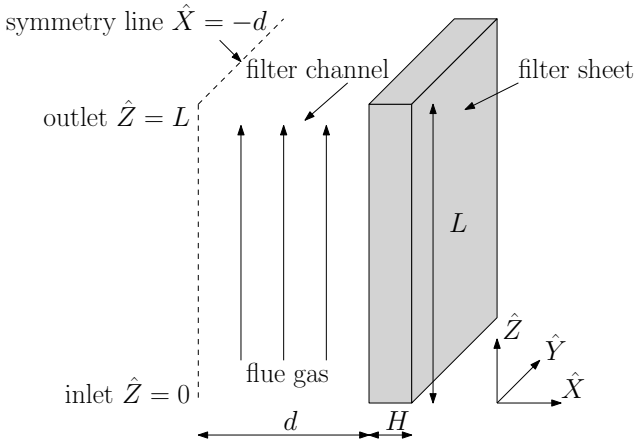

Figure 4.1: Schematic of a rectangular filter channel.

fraction $\mathcal{V}_g$. The dimensional forms of (3.118) and (3.119), in which we have used the dimensional form of (3.70), to convert $\hat{a}$ into $\mathcal{V}_g$, read

$$0 = \nabla_{\hat{X}} \cdot \left(\mathcal{V}_g \hat{D} \nabla_{\hat{X}} \hat{s}_g \right) - 8\pi \mathcal{K} \hat{s}_g^2, \tag{4.2}$$

$$\frac{\partial \mathcal{V}_g}{\partial \hat{t}} = -8\pi V_{\mathrm{m}} \mathcal{K} \hat{s}_g^2, \tag{4.3}$$

where we have introduced the effective reaction rate $\mathcal{K} = kR^2/\beta_s^2 l^3$.

At the surface of the sheet, we assume that the concentration is continuous, and so we write

$$\hat{s}_g = \hat{S} \qquad \text{at} \qquad \hat{X} = 0. \tag{4.4}$$

We note that the void fraction does not appear in (4.4), since $\hat{s}_g$ is the concentration of sulphur dioxide averaged over the gas phase and not the whole space. At the back of the filter sheet, we assume that no sulphur dioxide can escape and write

$$\frac{\partial \hat{s}_g}{\partial \hat{X}} = 0 \qquad \text{at} \qquad \hat{X} = H. \tag{4.5}$$

At the inlet of the filter, both the channel and the filter sheet are exposed to the incoming gas stream. We assume that sulphur dioxide of constant concentration S_0 is supplied to the filter

$$\hat{s}_g = \hat{S} = S_0 \qquad \text{at} \qquad \hat{Z} = 0. \tag{4.6}$$

At the top of the sheet, the filter is open, and, thus, we assume that the two concentrations are the same, and so we have that

$$\hat{s}_g = \hat{S} \qquad \text{at} \qquad \hat{Z} = L. \tag{4.7}$$

At the two ends along the width of the sheet, we assume no flux of sulphur dioxide

$$\frac{\partial \hat{s}_g}{\partial \hat{Y}} = 0 \qquad \text{at} \qquad \hat{Y} = \pm\frac{W}{2}. \tag{4.8}$$

Finally, we assume no sulphur dioxide or liquid sulphuric acid are initially present in the filter; these conditions read

$$\hat{S} = 0, \qquad \mathcal{V}_g = 1 - \frac{4}{3}\pi(R/l)^3 \qquad \text{at} \qquad \hat{t} = 0. \tag{4.9}$$

We non-dimensionalise (4.1)–(4.9) using

$$\hat{X} = HX, \quad \hat{Y} = WY, \quad \hat{Z} = LZ, \quad \hat{t} = (L^2/D_{s_g})t, \quad \hat{S} = S_0 S, \quad \hat{D} = D_{s_g} D, \tag{4.10}$$

where we have picked the timescale based on diffusion along the length of the filter sheet. We note that the diffusive timescale in the transverse, X, direction is much smaller than this timescale and not of particular interest with regards to the long-term operation of the device. In addition, since the flue gas flows uniformly along the channel, and we prescribe zero flux of sulphur dioxide at $Y = \pm 1/2$, there are no variations in the Y-direction of s_g or S. The dimensionless equations thus become

$$\delta\varepsilon\left(\frac{\partial S}{\partial t} + \mathrm{Pe}\frac{\partial S}{\partial Z}\right) = \left(\mathcal{V}_g D\frac{\partial s_g}{\partial X}\right)\bigg|_{X=0}, \tag{4.11}$$

$$0 = \frac{\partial}{\partial X}\left(\mathcal{V}_g D\frac{\partial s_g}{\partial X}\right) + \delta^2\frac{\partial}{\partial Z}\left(\mathcal{V}_g D\frac{\partial s_g}{\partial Z}\right) - \frac{\delta^2\Upsilon s_g^2}{\alpha}, \tag{4.12}$$

$$\frac{\partial \mathcal{V}_g}{\partial t} = -\Upsilon s_g^2, \tag{4.13}$$

subject to

$$s_g = S \qquad \text{at} \qquad X = 0, \tag{4.14}$$

$$\frac{\partial s_g}{\partial X} = 0 \qquad \text{at} \qquad X = 1, \tag{4.15}$$

$$s_g = S = 1 \qquad \text{at} \qquad Z = 0, \tag{4.16}$$

$$s_g = S \qquad \text{at} \qquad Z = 1, \tag{4.17}$$

$$S = 0 \qquad \text{at} \qquad t = 0, \tag{4.18}$$

$$\mathcal{V}_g = 1 - \frac{4\pi\Lambda^3}{3} \qquad \text{at} \qquad t = 0, \tag{4.19}$$

where we have the following six dimensionless parameters with corresponding orders of magnitude

$$\begin{gathered}\alpha = S_0 V_\mathrm{m} \approx 10^{-6}, \quad \delta = \frac{H}{L} \approx 10^{-2}, \quad \varepsilon = \frac{d}{L} \approx 10^{-2}, \quad \Lambda = \frac{R}{l} \approx 10^{-1}, \\ \Upsilon = \frac{8\pi k L^2 R^2 S_0^2 V_\mathrm{m}}{\beta_s^2 l^3 D_{s_g}} \approx 10^{-1}, \quad \mathrm{Pe} = \frac{LU}{D_{s_g}} \approx 10^4.\end{gathered} \tag{4.20}$$

Here, α measures the change in volume in the gas-to-liquid transition in the chemical reaction, δ is the aspect ratio of the filter sheet, ε is the aspect ratio of the filter channel, Λ is the ratio of the catalytic pellet radius to the inter-pellet distance (as introduced in (3.23)), Υ is a ratio of the diffusive timescale to the timescale over which the liquid layer grows, and Pe is the Péclet number.

4.3 Asymptotic Results for a Slender Filter Device

As seen in (4.20), $\delta \ll 1$. Furthermore, under normal operating conditions, the gas flow is advection-dominated, so that $\mathrm{Pe} \gg 1$. We exploit these facts to further simplify the system of equations presented in the previous section. In particular, we systematically explore two physically relevant distinguished limits by varying α and ε which control the system behaviour. In all the limits, based on experimental evidence, we assume $\mathrm{Pe} = O(1/\delta^2)$ and, for the richest asymptotic limit, we assume that the reaction rate and diffusive rate are in balance, i.e., $\Upsilon = O(1)$.

4.3.1 Limit I: $\alpha = O(\delta^2)$ and $\varepsilon = O(\delta)$

We first study the case when the channel thickness and sheet thickness are similar, and the concentration of sulphur dioxide supplied at the entrance of the channel is small. We set $\alpha = \delta^2\tilde{\alpha}$, and $\varepsilon = \delta\bar{\varepsilon}$, where $\tilde{\alpha}, \bar{\varepsilon} = O(1)$. Expanding the dependent variables as power series in powers of δ^2, the leading-order versions of (4.11) and (4.12) become quasi-static, and we find that

$$\bar{\varepsilon}\,\widetilde{\mathrm{Pe}}\frac{\partial S}{\partial Z} = \left(\mathcal{V}_g D\frac{\partial s_g}{\partial X}\right)\bigg|_{X=0}, \tag{4.21}$$

$$0 = \frac{\partial}{\partial X}\left(\mathcal{V}_g D\frac{\partial s_g}{\partial X}\right) - \frac{\Upsilon s_g^2}{\tilde{\alpha}}, \tag{4.22}$$

$$\frac{\partial \mathcal{V}_g}{\partial t} = -\Upsilon s_g^2, \tag{4.23}$$

where $\widetilde{\mathrm{Pe}} = \delta^2\mathrm{Pe} = O(1)$. We note that, alternatively, this limit can be specified more generally by taking $\delta^2\Upsilon/\alpha = O(1)$ and $\delta\epsilon\mathrm{Pe} = O(1)$. Equations (4.21)–(4.23) must be solved subject to (4.14)–(4.19). We will solve these numerically in Section 4.4 and will find a monotonically decreasing quasi-static solution for the sulphur dioxide concentration that agrees well with the solution to the full numerical solution as δ decreases.

We note that, the strategy for solving the quasi-steady system (4.21)–(4.23) numerically is the following: first, using the initial condition for $\mathcal{V}_g$, we solve (4.22) at $Z = 0$; we then feed the result into (4.21) to calculate S at the next location in Z and repeat the procedure until we have s_g and S at each location in Z; finally, we update $\mathcal{V}_g$ according to (4.23) and repeat the whole procedure for each time step.

4.3.2 Limit II: $\boldsymbol{\alpha = O(\delta)}$ and $\boldsymbol{\varepsilon = O(\delta^2)}$

We now turn our attention to the case when the channel width is much thinner than the sheet width, and there is a moderate amount of sulphur dioxide entering the device. We write $\alpha = \delta\bar{\alpha}$, and $\varepsilon = \delta^2\tilde{\varepsilon}$, where $\bar{\alpha}, \tilde{\varepsilon} = O(1)$. After asymptotically expanding the dependent variables in powers of δ (and dropping the superscripts on the leading-order variables), the leading-order version of (4.12) becomes

$$0 = \frac{\partial}{\partial X}\left(\mathcal{V}_g D \frac{\partial s_g}{\partial X}\right). \tag{4.24}$$

This can be readily integrated, and using (4.15), we obtain

$$s_g = s_g(Z,t) = S(Z,t), \tag{4.25}$$

using (4.14). The $O(\delta)$ versions of (4.11) and (4.12) read

$$\tilde{\varepsilon}\widetilde{\mathrm{Pe}}\frac{\partial S}{\partial Z} = \left(\mathcal{V}_g D \frac{\partial s_g^{(1)}}{\partial X}\right)\bigg|_{X=0}, \tag{4.26}$$

$$0 = \frac{\partial}{\partial X}\left(\mathcal{V}_g D \frac{\partial s_g^{(1)}}{\partial X}\right) - \frac{\Upsilon s_g^2}{\bar{\alpha}}. \tag{4.27}$$

Integrating (4.27) with respect to X from 0 to 1, and using (4.15), (4.25), and (4.26) we obtain

$$0 = -\frac{\Upsilon}{\bar{\alpha}}S^2 - \tilde{\varepsilon}\widetilde{\mathrm{Pe}}\frac{\partial S}{\partial Z}, \tag{4.28}$$

which we solve alongside

$$\frac{\partial \mathcal{V}_g}{\partial t} = -\Upsilon S^2, \tag{4.29}$$

together with the conditions

$$S = 1 \qquad \text{at} \qquad Z = 0, \tag{4.30}$$

$$\mathcal{V}_g = 1 - \frac{4\pi\Lambda^3}{3} \qquad \text{at} \qquad t = 0. \tag{4.31}$$

Writing $\beta = \Upsilon/\bar{\alpha}\,\tilde{\varepsilon}\,\widetilde{\mathrm{Pe}}$, the solution is

$$S = \frac{1}{1+\beta Z}, \qquad \mathcal{V}_g = 1 - \frac{4\pi\Lambda^3}{3} - \frac{\Upsilon t}{(1+\beta Z)^2}. \tag{4.32}$$

This case can be treated as a sub-limit of the previous case by taking $\delta\varepsilon\mathrm{Pe}, \delta^2\Upsilon/\alpha \to 0$ in (4.11) and (4.12), respectively.

In this limit, we see that S has reached a steady state, while $\mathcal{V}_g$ evolves linearly in time. Furthermore, using (4.32), we can calculate the first time when liquid layers around the pellets adjacent to the inlet of the channel touch each other, after which moment we will need a different model to account for the coalescence. The critical void fraction at which this happens is $\mathcal{V}_{g,c} = 1 - \pi/6$ (the largest sphere that can fit in the unit cube has radius $\pi/6$), and, therefore, using (4.32) evaluated at $Z = 0$, the asymptotic value of the critical time t_c^a is calculated to be

$$t_c^a = \frac{\pi}{6\Upsilon}\left(1 - 8\Lambda^3\right). \tag{4.33}$$

4.4 Numerical Results

We solve (4.11)–(4.19) numerically using a second-order-accurate explicit finite-difference scheme, implemented in MATLAB. In figure 4.2, we show plots of the spatial profiles of S in the channel and $\mathcal{V}_g$ at the edge of the filter at $X = 0$ for various times (the parameter values are shown in the figure caption). We stop the simulations at the time when two neighbouring liquid layers adjacent to the inlet of the channel coalesce, i.e., when $\mathcal{V}_g = 1 - \pi/6 \approx 0.48$ ($t_c \approx 0.52$ in this simulation). After this point, our model becomes unphysical, and we would need to consider transport through a fully flooded microstructure. We will discuss a simple model that addresses this issue in Section 4.8. In figure 4.2(a), we see that, as time increases, the concentration of sulphur dioxide increases and approaches a quasi-steady state. In figure 4.2(b), we see that, as time increases, the void fraction decreases and is smallest near the channel inlet, as expected. The temporal behaviour of S can be more easily seen in figure 4.3(a), where we plot a temporal profile of S at the outlet of the channel $Z = 1$. In figure 4.3(a), we can also see the breakthrough curve that describes the steep increase in the concentration of sulphur dioxide and the point in time when the gas initially fills up the channel. The slow increase in concentration at the end of the channel is due to the gradual accumulation of liquid sulphuric acid in the filter sheet. In figure 4.3(b), we plot the temporal profile of the ratio, F, of the total amount of

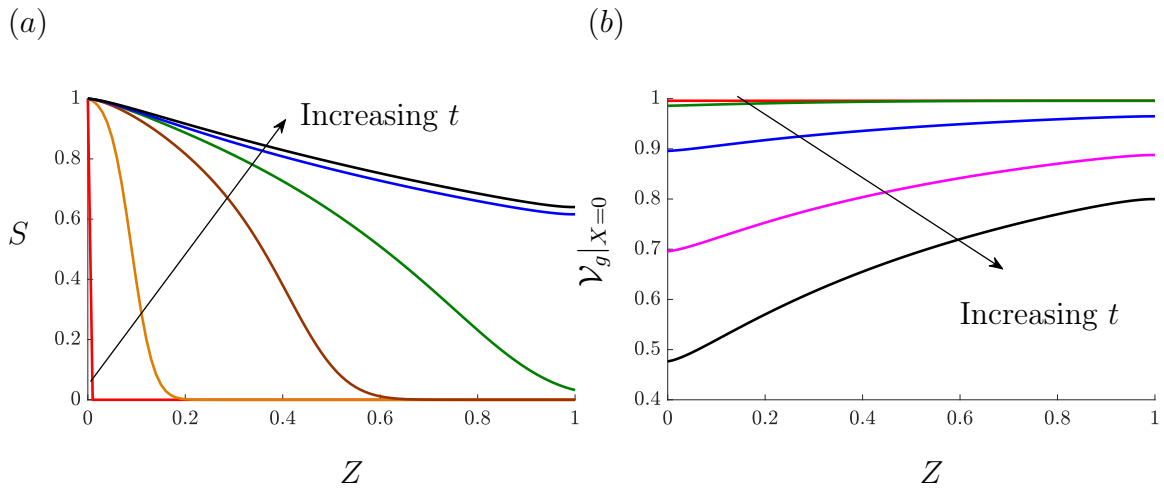

Figure 4.2: (a) Spatial profile of S in the channel and (b) $\mathcal{V}_g$ on the channel wall at $X = 0$ for various times t: 0 (red), 0.001 (orange), 0.005 (brown), 0.01 (green), 0.1 (blue), 0.3 (magenta), 0.52 (black). In these plots, $\alpha = 0.01, \delta = 0.1, \varepsilon = 0.1, \Lambda = 0.1, \Upsilon = 1, \mathrm{Pe} = 100$.

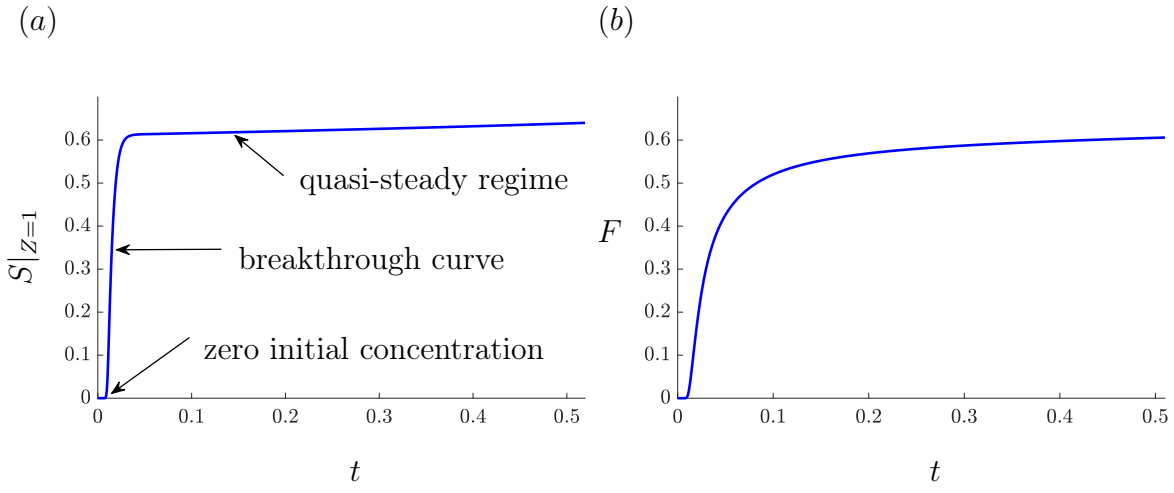

Figure 4.3: Temporal profile of (a) S at the outlet of the channel $Z = 1$ and (b) the ratio, F, of the total amount of sulphur dioxide that has exited the channel at $Z = 1$, compared to the total amount of sulphur dioxide that has entered the channel at $Z = 0$. In these plots, $\alpha = 0.01, \delta = 0.1, \varepsilon = 0.1, \Lambda = 0.1, \Upsilon = 1, \mathrm{Pe} = 100$.

sulphur dioxide that has exited the channel at $Z = 1$, compared to the total amount of sulphur dioxide that has entered the channel at $Z = 0$, calculated according to

$$F = \frac{\int_0^t S(1,s)\,\mathrm{d}s}{\int_0^t S(0,s)\,\mathrm{d}s}. \tag{4.34}$$

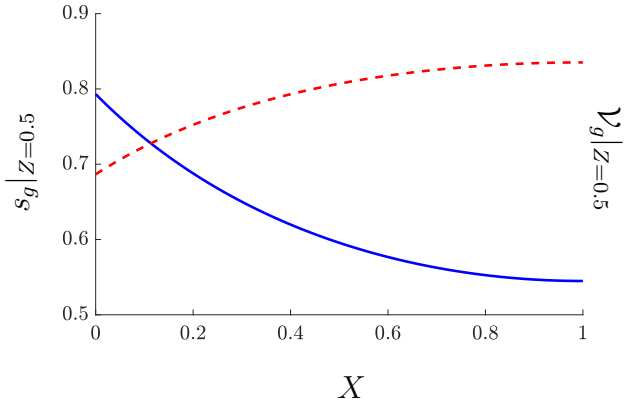

Figure 4.4: Spatial profiles of s_g (blue) and $\mathcal{V}_g$ (dashed red) at $t = 0.52$ in the sheet at the middle of the channel $Z = 0.5$. In this plot, $\alpha = 0.01, \delta = 0.1, \varepsilon = 0.1, \Lambda = 0.1, \Upsilon = 1, \mathrm{Pe} = 100$.

We see that, similar to figure 4.3(a), F is initially zero until the channel is filled with gas. We also see that F then rises steeply as sulphur dioxide exits the channel, and then levels off. In figure 4.4, we show spatial profiles of S and $\mathcal{V}_g$ in the filter sheet at the middle of the channel at $t = t_c$. As anticipated, the concentration of sulphur dioxide decreases deeper into the sheet, and the void fraction increases.

In figure 4.5, we show the temporal evolution of S at the channel outlet $Z = 1$ as we vary four of the dimensionless parameters, namely $\alpha, \varepsilon, \Upsilon$ and Pe. We see that increasing α increases the concentration of sulphur dioxide at the outlet, since this corresponds to larger amounts of sulphur dioxide being fed into the device. However, increasing ε increases the concentration, since this corresponds to a wider channel, which contains more sulphur dioxide. Increasing Υ, though, decreases the critical time for liquid coalescence, t_c, and the sulphur dioxide concentration, which is expected, as this corresponds to increasing the reaction rate k. Increasing Pe increases the concentration, as this corresponds to increasing the speed of the gas. Furthermore, in figure 4.6, we show the temporal profile of F for different values of Pe. We see that increasing Pe increases F and thus decreases the efficiency of the filter. Thus, we can use these results to calculate the maximum flow speed of the gas in order to remove a given proportion of the incoming sulphur dioxide, or keep the outlet concentration of sulphur dioxide below a given threshold. We note that we have used a different set of base parameter values for δ and Pe than in (4.20), since the simulations become computationally challenging in this case. In particular, the values

of Pe we have used are at least two orders of magnitude smaller than in reality, which means that, for real parameter values, the initial rise in the temporal profile of sulphur dioxide concentration will be almost instantaneous. Looking at figure 4.5(d), it may seem that, for the real value of Pe, the outlet concentration of sulphur dioxide will approach its inlet value, but we recall that the realistic values of α and ϵ are much smaller than the values used in the numerical simulations, which will have the effect of substantially reducing the outlet concentration as evident from figures 4.5(a) and 4.5(b). The aim here is to illustrate the general qualitative behaviour of the system, and then to use asymptotic reductions (when $\delta \ll 1$), thus enabling a quicker solution.

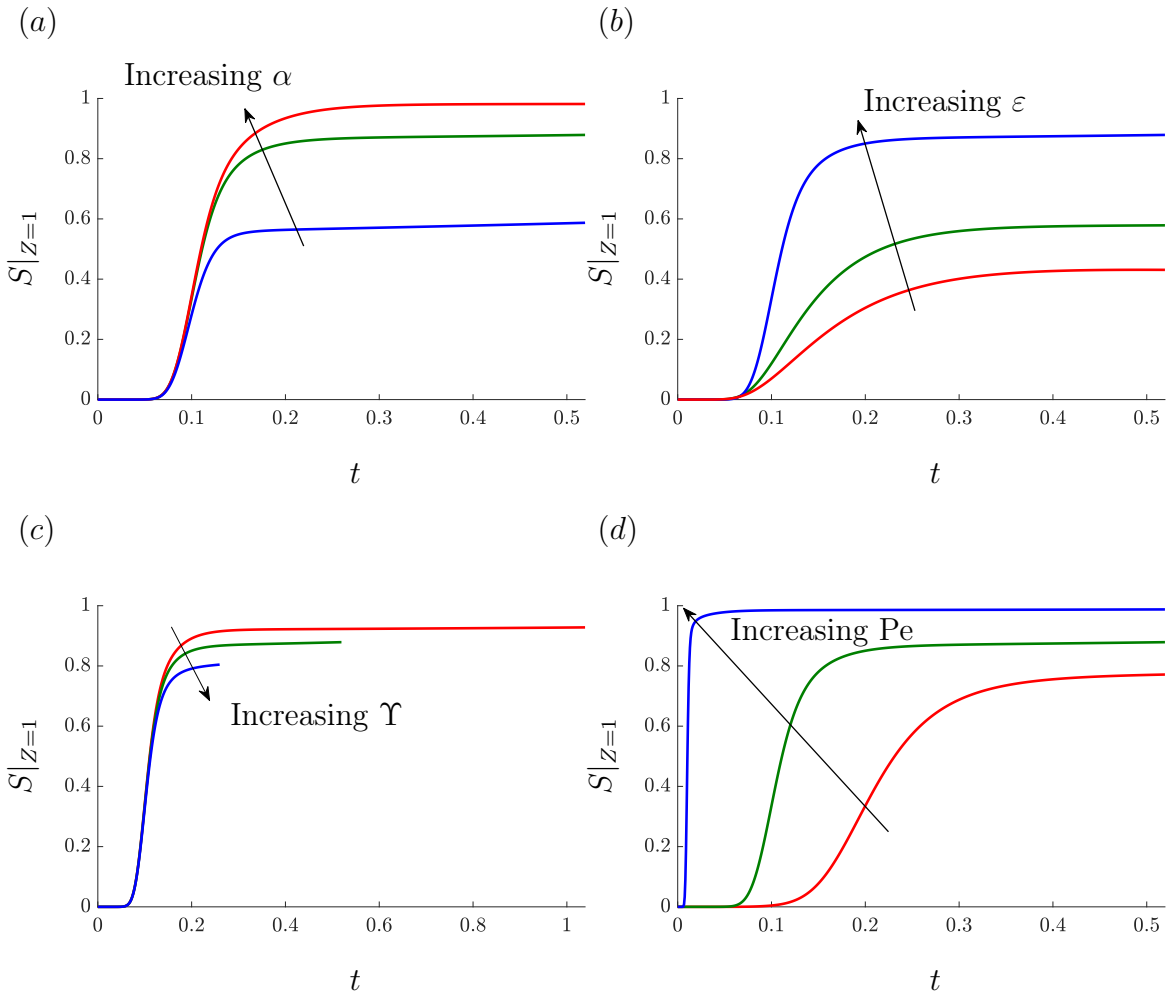

Figure 4.5: Plots of the temporal profile of S at the channel outlet $Z = 1$ varying (a) $\alpha = 1$ (red), 0.1 (green), and 0.01 (blue) keeping $\varepsilon = 1, \Upsilon = 1, \mathrm{Pe} = 10$, ($b$) $\varepsilon = 0.1$ (red), 0.2 (green), and 1 (blue) keeping $\alpha = 0.1, \Upsilon = 1, \mathrm{Pe} = 10$, ($c$) $\Upsilon = 0.5$ (red), 1 (green), and 2 (blue) keeping $\alpha = 0.1, \varepsilon = 1, \mathrm{Pe} = 10$, and ($d$) Pe = 5 (red), 10 (green), and 100 (blue) keeping $\alpha = 0.1, \varepsilon = 1, \Upsilon = 1$. In these plots, $\delta = 0.3, \Lambda = 0.1$.

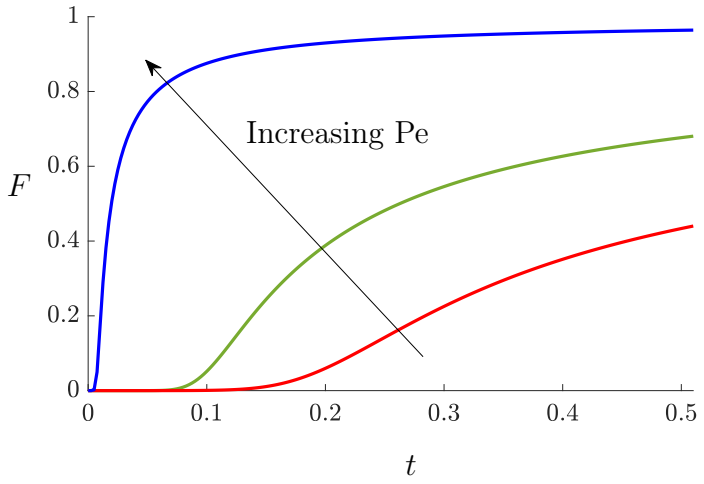

Figure 4.6: Temporal profile of the ratio, F, of the total amount of sulphur dioxide that has exited the channel, compared to the total amount of sulphur dioxide that has entered the channel, varying Pe $= 5$ (red), 10 (green), and 100 (blue) keeping $\alpha = 0.1, \delta = 0.3, \varepsilon = 1, \Lambda = 0.1, \Upsilon = 1$.

Finally, in figure 4.7, we show spatial profiles of the numerical solution to (4.11)–(4.19) for decreasing δ compared to the solution of the asymptotically reduced equations (4.22)–(4.21) and the asymptotic result (4.32), respectively. When we vary δ, we also vary α and ε according to the limits considered in Sections 4.3.1 and 4.3.2, respectively. We see a very good agreement even at moderate values of δ, noting that the convergence in figure 4.7(b) is slower.

4.5 Extended Macroscale Model

We now present an extension to the model considered in this chapter that holds until the filter clogs up with liquid everywhere along the filter channel. As mentioned at the beginning of this section, we stop our numerical simulations once two neighbouring liquid layers coalesce. However, in order to gain insight into the long-term operation of the device, we can run the simulations beyond this point by switching off the uptake of sulphur dioxide and, consequently, the liquid growth, as soon as the void fraction $\mathcal{V}_g = 0$. We do this numerically by multiplying the sink term in (4.12) and the right-hand side of (4.13) by a Heaviside step function $\Theta(\mathcal{V}_g)$. In addition, since the effective

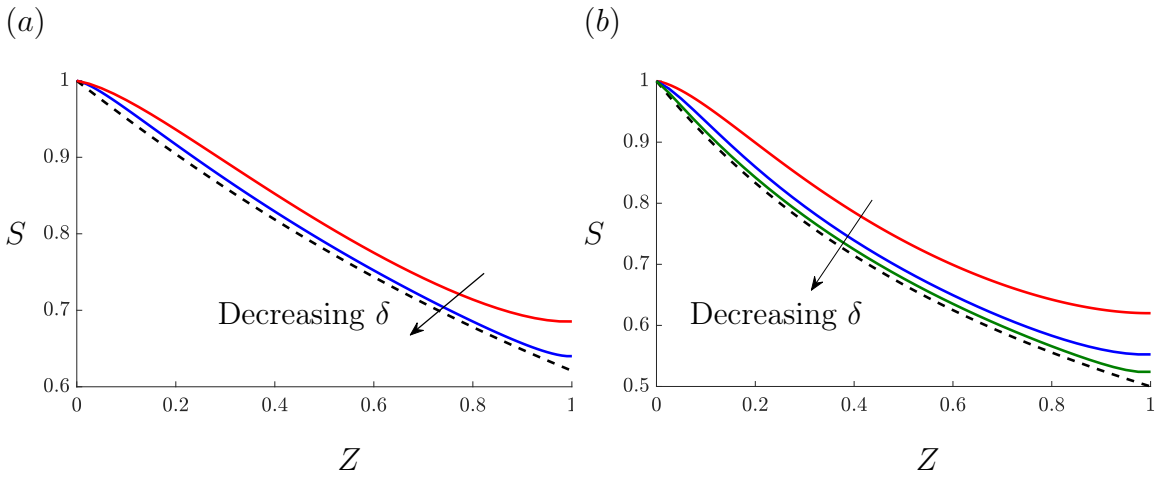

Figure 4.7: Plots of the spatial profile of S at $t = 0.52$ for (a) $\delta = 0.3$ (red), $\delta = 0.1$ (blue), and the corresponding asymptotic results in Section 4.3.1 (dashed black) with $\tilde{\alpha} = 1, \bar{\varepsilon} = 1$, and for (b) $\delta = 0.3$ (red), $\delta = 0.1$ (blue), $\delta = 0.03$ (green) and the corresponding asymptotic results in Section 4.3.2 (dashed black) with $\bar{\alpha} = 1, \tilde{\varepsilon} = 1$. In these plots, $\Lambda = 0.1, \Upsilon = 1, \widetilde{\mathrm{Pe}} = 1$.

diffusivity D is defined until $\mathcal{V}_g = 1 - \pi/6$ (see Section 3.4.1), for simplicity, we extend it linearly until it reaches zero when $\mathcal{V}_g = 0$. We note that this is an idealisation of the problem, but allows us to study the behaviour of the filter until the liquid fills up the filter sheet, and gives a lower bound on the clogging time, as, in reality, diffusion also occurs in the liquid, albeit at a much slower rate. In figure 4.8, we again show the temporal profile of S at the outlet of the channel $Z = 1$, as in figure 4.3(a), but this time until $\mathcal{V}_g$ reaches zero everywhere. We see that, after the point of the first liquid coalescence at $t_c \approx 0.52$ (indicated by a star), the sulphur dioxide concentration rises steeply until it reaches one, the value of the inlet concentration, at time $t_{\mathrm{stop}} \approx 1.8$. In figure 4.9, we also show spatial profiles of the void fraction $\mathcal{V}_g$ along the channel wall at $X = 0$ and transversely into the filter sheet at the middle of the channel at $Z = 0.5$, as in figure 4.4, for various times. We see that, as time increases, the void fraction along the channel wall approaches zero everywhere, whereas the void fraction across the thickness of the filter sheet becomes zero only near the channel and is monotonically increasing deeper into the sheet. We also note that the new clogging time for the whole filter has almost quadrupled compared to figure 4.3(a) for the corresponding parameter regime. We discuss the practical implications of these results in Section 4.7.

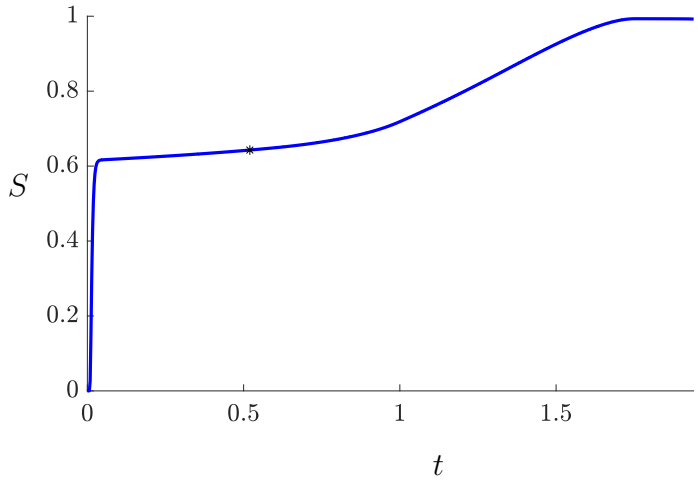

Figure 4.8: Temporal profile of S at the outlet of the channel $Z = 1$. The point of first clogging ($t_c = 0.52$) is indicated by a star. In this plot, $\alpha = 0.01, \delta = 0.1, \varepsilon = 0.1, \Lambda = 0.1, \Upsilon = 1, \mathrm{Pe} = 100$.

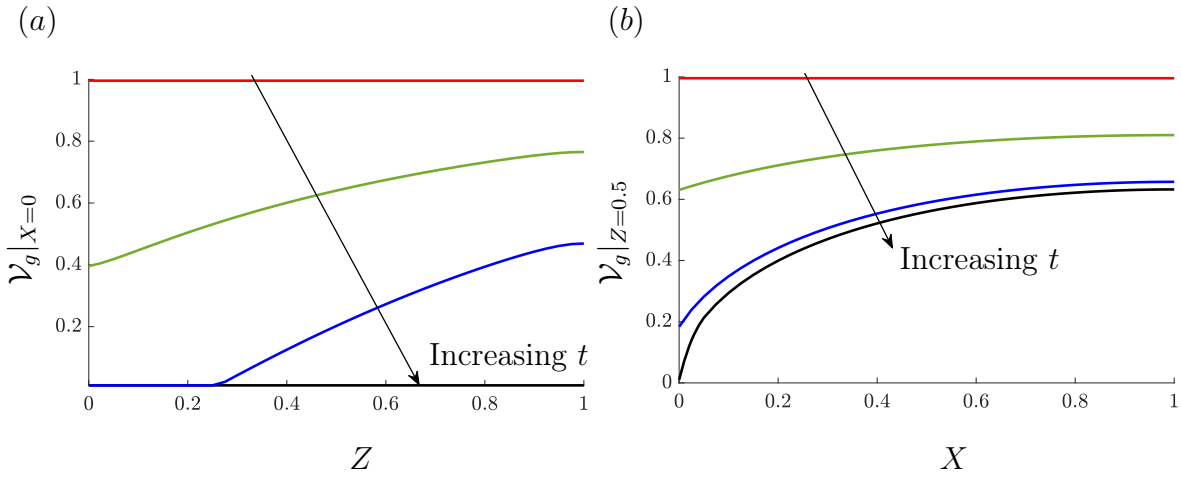

Figure 4.9: Spatial profiles of $\mathcal{V}_g$ (a) on the channel wall at $X = 0$ and (b) in the sheet at the middle of the channel $Z = 0.5$ for various times t: 0 (red), 0.6 (green), 1.2 (blue), 1.8 (black). In these plots, $\alpha = 0.01, \delta = 0.1, \varepsilon = 0.1, \Lambda = 0.1, \Upsilon = 1, \mathrm{Pe} = 100$.

4.6 Radially Symmetric Model

To study another representation, where the channel is enclosed by a filter sheet from all sides, we also consider a radially symmetric geometry, as shown in figure 4.10.

This increases the exposure of flue gas to the filter sheet by increasing the lateral surface area of the channel, which is the reason why the filter sheet is folded within the GMCS device. We will then compare the behaviour of the system in the Cartesian and polar coordinate systems. As we shall see, both models give the same qualitative behaviour.

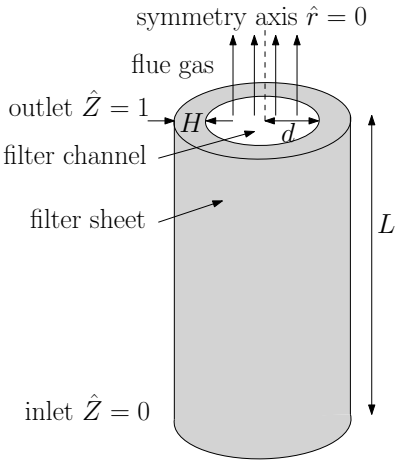

Figure 4.10: Schematic of a cylindrical filter channel.

We note that we can write down the corresponding equations straight away by making the transformation from Cartesian to cylindrical polar coordinates and moving the origin to the centre of the channel. Thus, for the sake of brevity, we directly write down the dimensionless equations, where we have scaled the radial coordinate as $\hat{r} = Hr$:

$$\delta\epsilon\left(\frac{\partial S}{\partial t} + \mathrm{Pe}\frac{\partial S}{\partial Z}\right) = \varrho\left(\mathcal{V}_g D\frac{\partial s_g}{\partial r}\right)\bigg|_{r=\varrho}, \tag{4.35}$$

$$0 = \frac{1}{r}\frac{\partial}{\partial r}\left(r\mathcal{V}_g D\frac{\partial s_g}{\partial r}\right) + \delta^2\frac{\partial}{\partial Z}\left(\mathcal{V}_g D\frac{\partial s_g}{\partial Z}\right) - \frac{\delta^2\Upsilon s_g^2}{\alpha}, \tag{4.36}$$

$$\frac{\partial \mathcal{V}_g}{\partial t} = -\Upsilon s_g^2, \tag{4.37}$$

subject to

$$s_g = S \qquad \text{at} \qquad r = \varrho, \tag{4.38}$$

$$\frac{\partial s_g}{\partial r} = 0 \qquad \text{at} \qquad r = 1 + \varrho, \tag{4.39}$$

$$s_g = S = 1 \qquad \text{at} \qquad Z = 0, \tag{4.40}$$

$$s_g = S \qquad \text{at} \qquad Z = 1, \tag{4.41}$$

$$S = 0 \qquad \text{at} \qquad t = 0, \tag{4.42}$$

$$\mathcal{V}_g = 1 - \frac{4\pi\Lambda^3}{3} \qquad \text{at} \qquad t = 0, \tag{4.43}$$

where we have defined $\varrho = d/H = \epsilon/\delta \approx 1$, which appears on the right-hand side of (4.35) due to the extra radial factors in the cylindrical-coordinates formulation, and the rest of the parameters are as defined in (4.20).

In figure 4.11, we show the temporal profile of S at the outlet of the channel $Z = 1$ from figure 4.3(a), compared to the corresponding profile using the radially symmetric model (4.35)–(4.43). We see that the solutions have the same qualitative behaviour. However, in the radially symmetric case, the outlet concentration is lower than in the Cartesian case, which is due to the different geometrical set-up and the fact that the cylindrical design provides more surface area of the filter sheet which is exposed to the flue gas.

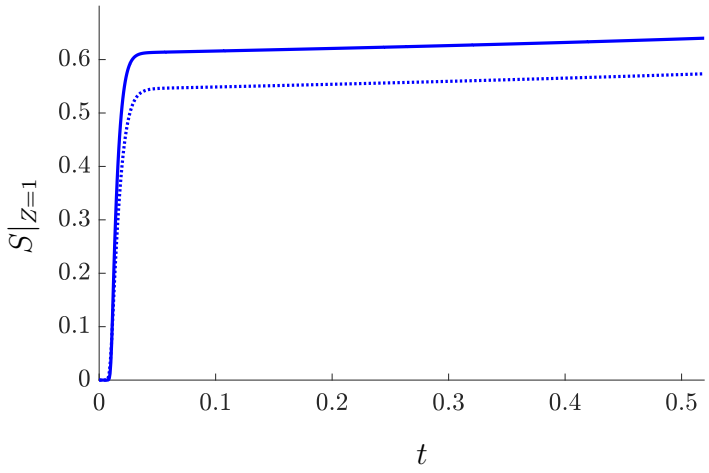

Figure 4.11: Temporal profile of S at the outlet of the channel $Z = 1$ for Cartesian (blue) and cylindrical (dashed) geometry. In this plot, $\alpha = 0.01, \delta = 0.1, \varepsilon = 0.1, \Lambda = 0.1, \varrho = 1, \Upsilon = 1, \mathrm{Pe} = 100$.

4.7 Practical Implications

One of the important outputs of this model that serve as a measure of the device performance is the outlet concentration of sulphur dioxide, $S|_{Z=1}$, since this is controlled by external requirements to be bounded by a given threshold, above which

the flue gas is considered to be toxic for the outside environment. In order to obtain solutions for a physically relevant parameter regime, we appealed to asymptotic reductions of our macroscale model, which significantly decreased the corresponding computational cost. In figure 4.7(a), we see a plot of the asymptotic solution for the spatial profile of the sulphur dioxide concentration in the filter channel for the physically relevant limit considered in Section 4.3.1 when the filter sheet thickness is comparable to the half-width of the channel, and there is a small amount of sulphur dioxide in the flue gas. Our analysis suggested that the outlet sulphur dioxide concentration reduced to about 60% of the inlet concentration. Furthermore, we note that, if we use a realistic value of $\delta = 10^{-2}$, then according to the limit from Section 4.3.1, $\alpha = O(\delta^2) = O(10^{-4})$. However, the true value is lower than that even in the case when there is a large amount of sulphur dioxide in the flue gas, and so, using the results in figure 4.5(a), namely, that the outlet concentration of sulphur dioxide decreases with α, we conclude that the outlet concentration in a physically realistic regime is less than 60%. To illustrate this, in figure 4.12, we show an analogous plot to the asymptotic result from figure 4.7(a) with $\tilde{\alpha} = 10^{-1}$, which corresponds to $\alpha = 10^{-5}$. We see that, in this case, the outlet concentration reduces to about 20% of the inlet concentration.

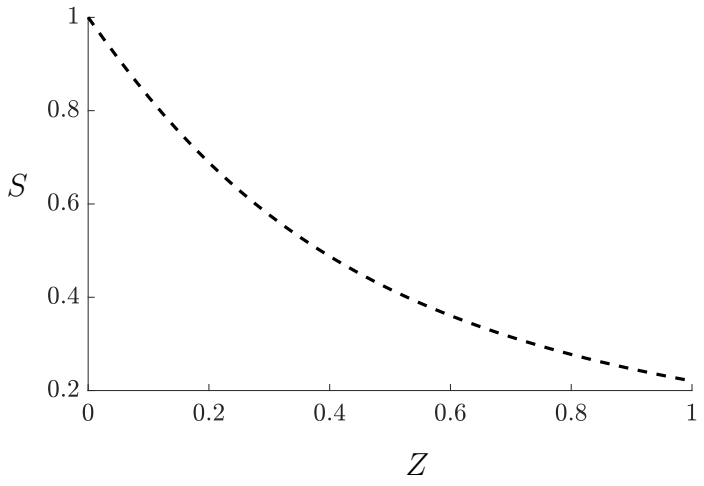

Figure 4.12: Plot of the spatial profile of S at $t = 0.52$ using the asymptotic results in Section 4.3.1 with $\tilde{\alpha} = 0.1, \bar{\varepsilon} = 1, \Lambda = 0.1, \Upsilon = 1, \widetilde{\mathrm{Pe}} = 1$.

As we noted in Section 4.4, we can use the plots in figure 4.5 or the plots, such as

in figure 4.12, associated with asymptotic solutions, to evaluate the effect of changing the system parameters on the outlet concentration. In particular, of special interest to W. L. Gore and Associates, Inc. is how the dimensions of the filter and the gas speed affect the device performance. We see that increasing the channel width and the gas speed both increase the outlet concentration. For example, given a maximum allowed outlet concentration, say, 20% of the inlet concentration, we find the maximum speed the gas can be flowed at to be approximately $0.1\,\mathrm{m\,s^{-1}}$. Similar reasoning applies to another quantity of interest, namely, the percentage of unfiltered sulphur dioxide, F, shown in figure 4.6. This is important when it is required to filter a given percentage of incoming sulphur dioxide.

Finally, we also discuss the implications of our model on the lifetime of the filter. The model we developed is valid until the first time two liquid layers, which grow around neighbouring pellets, coalesce. The key parameter that controls this time is Υ, which we recall is the ratio of the diffusive timescale in the gas across the filter to the timescale associated with liquid growth. In figure 4.5(c), where we vary Υ, we see that this clogging time varies linearly with the reciprocal of Υ. This is further supported by the explicit asymptotic result (4.33) from Section 4.3.2. With $\Upsilon = 1$, used in our simulations, we obtain clogging time on the order of 10^{-1} day, and thus with the realistic value of $\Upsilon = 0.1$, as in (4.20), we obtain clogging time on the order of a single day, which is the expected duration with moderate amount of sulphur dioxide ($10^{-2}\,\mathrm{mol\,m^{-3}}$) in the flue gas, as discussed in Section 3.5. However, provided there is less sulphur dioxide by an order of magnitude, say, $10^{-3}\,\mathrm{mol\,m^{-3}}$, which occurs in the applications of the GMCS device, the clogging time increases by two orders of magnitude to approximately 100 days (or 3 months) due to the quadratic dependence of Υ on the sulphur dioxide concentration. This clogging time is comparable with clogging times seen during long-term industrial operation of the filter. In reality, as already discussed in Section 4.5, the time when the whole filter clogs up with liquid is considerably longer than these estimates. In particular, for the parameter regime considered in figure 4.8, there is a four-fold increase in the clogging time. We also note that, in this extended model, the void fraction does not become zero everywhere, as can be seen in figure 4.9, which indicates that the filter does not clog uniformly everywhere. In order to more accurately capture the filter dynamics beyond the point of first clogging, a different model, where we track diffusion through the liquid, is required. We conclude by noting that the estimate (4.33) also depends on Λ, which is the ratio of the pellet radius to the inter-pellet distance, and thus measures how densely packed the pellets in the filter sheet are. For designs of practical significance

to W. L. Gore and Associates, Inc., $\Lambda < 1$. This means that the cubic dependence of the clogging time on Λ is weak, and changing the pellet density does not dramatically affect the performance of the device.

4.8 A Two-Pellet Model

As we noted in Section 4.4, the model we have developed so far in this chapter is valid until the liquid layers around two neighbouring pellets coalesce. This happens for the first time near the inlet of the filter channel. After that, there will be a continuous layer of liquid forming in the filter sheet along the channel surface until eventually there will be no direct gas pathway from the channel to the pellets deeper into the sheet. In order for the gas to reach the deeper pellets, it then has to diffuse through the liquid layer, where its diffusivity is much lower than in the gas phase. One possible modelling approach would be to consider a region of the filter sheet that is completely saturated with liquid and then track the macroscale sharp interface with the remaining unsaturated region. Such a problem has been studied in Luckins *et al.* (2019) in the context of decontamination, where a reaction occurs on the interface between a toxic chemical and an immiscible cleanser. They use homogenisation to derive a macroscale equation that describes the macroscale interface between the chemical and the cleanser.

In our filter problem, a natural question that arises is whether the gas–liquid interface of the continuous liquid layer or the gas–liquid interface around each of the pellets situated deeper into the sheet moves faster. This will give insight into the global liquid-transport problem in the filtering device and, therefore, the liquid distribution within the filter sheets and change in the efficiency of the device. Therefore, we consider the simplified problem where there are two neighbouring pellets and one is completely submerged in a layer of liquid sulphuric acid, as shown in figure 4.13. We will assume a source of gaseous sulphur dioxide is placed behind this layer, to the left of the first pellet, and we wish to explore the effect the liquid layer has on the gas transport and the resulting motion of the two gas–liquid interfaces.

4.8.1 Model Formulation

For simplicity, we consider a two-dimensional model of two neighbouring catalytic pellets and the space around them represented by two square cells with the pellets at the centres, respectively. We assume that the space around the pellet in the first cell is completely filled with liquid sulphuric acid and forms a moving gas–liquid interface,

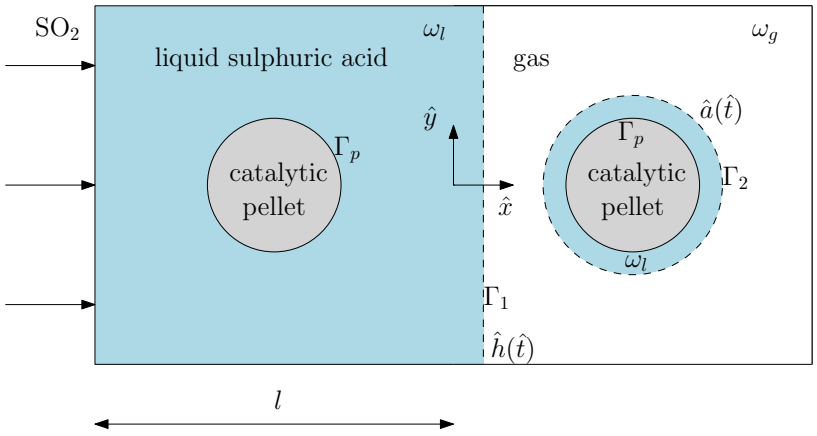

Figure 4.13: Two neighbouring catalytic pellets.

situated between the two pellets at $\hat{x} = \hat{h}(\hat{t})$, whereas, as sulphur dioxide reacts on the surface of the second pellet, a uniform layer of sulphuric acid of thickness $\hat{a}(\hat{t})$ forms around it. We assume that the liquid cannot exit the system through the left-hand boundary. While this is a big simplification, it allows us to focus on the relative production of liquid by the two pellets. The geometry is shown in figure 4.13. We define Γ_i^1 to be the interface between the liquid surrounding the left-hand pellet and the gas surrounding the right-hand pellet, and assume that this interface remains vertical. We define Γ_i^2 to be the gas–liquid interface of the layer growing around the right-hand pellet. Using the results from Section 3.5, we neglect advection effects due to liquid growth and assume that the concentration $\hat{s}_g$ of sulphur dioxide in the gas region ω_g, and $\hat{s}_l$ in the two liquid regions ω_l evolve quasi-statically and satisfy the steady diffusion equation with diffusivities D_{s_g} and D_{s_l}, respectively. Thus, we have

$$0 = D_{s_g} \nabla^2 \hat{s}_g \qquad \text{in} \qquad \omega_g, \tag{4.44}$$

$$0 = D_{s_l} \nabla^2 \hat{s}_l \qquad \text{in} \qquad \omega_l. \tag{4.45}$$

To model the directionality of the gas transport coming from the flue-gas stream, we assume the concentration of gaseous sulphur dioxide at the left-hand end of the two-cell system, $\hat{x} = -l$, is constant, S_0, and thus the concentration of sulphur dioxide in the liquid is given by S_0/β_s, where β_s is Henry's law constant. We impose no flux on the other external sides of the cells. We therefore write

$$\hat{s}_l = \frac{S_0}{\beta_s} \qquad \text{at} \qquad \hat{x} = -l, \tag{4.46}$$

$$\frac{\partial \hat{s}_g}{\partial \hat{x}} = 0 \qquad \text{at} \qquad \hat{x} = l, \tag{4.47}$$

$$\frac{\partial \hat{s}_g}{\partial \hat{y}} = \frac{\partial \hat{s}_l}{\partial \hat{y}} = 0 \qquad \text{at} \qquad \hat{y} = \pm\frac{l}{2}. \tag{4.48}$$

At the two gas–liquid interfaces, Γ_i^1 and Γ_i^2, as before, we impose a flux balance and apply Henry's law. We, thus, obtain

$$D_{s_g}\frac{\partial \hat{s}_g}{\partial \hat{x}} = D_{s_l}\frac{\partial \hat{s}_l}{\partial \hat{x}} \qquad \text{at} \qquad \Gamma_i^{1,2}, \tag{4.49}$$

$$\hat{s}_g = \beta_s \hat{s}_l \qquad \text{at} \qquad \Gamma_i^{1,2}. \tag{4.50}$$

On the surface of the pellets, Γ_p^1 and Γ_p^2, we again balance the diffusive flux of sulphur dioxide with what is consumed by the reaction using the mass-action kinetics from Chapter 3,

$$D_{s_l}\frac{\partial \hat{s}_l}{\partial \hat{n}_p} = 2k\hat{s}_l^2 \qquad \text{at} \qquad \Gamma_p^{1,2}, \tag{4.51}$$

where k is the reaction rate constant, and $\partial/\partial\hat{n}_p$ is the normal derivative to $\Gamma_p^{1,2}$.

To close the system, we need to prescribe the evolution of the gas–liquid interfaces. For Γ_i^2, we have used the two-dimensional analogue of (3.4), namely, we have allowed for non-uniform production around the pellet, with arclength $\hat{s}$,

$$(R+\hat{a})\,\frac{\mathrm{d}\hat{a}}{\mathrm{d}\hat{t}} = \frac{kV_\mathrm{m}}{\pi}\int_{\Gamma_p^2}\hat{s}_l^2\,\mathrm{d}\hat{s}. \tag{4.52}$$

We note that we cannot evaluate the integral in (4.52), since we do not assume radial symmetry. Since we assume Γ_i^1 to be flat, we prescribe its velocity according to how much liquid is produced at the surface of the pellet. Thus, we write

$$l\frac{\mathrm{d}\hat{h}}{\mathrm{d}\hat{t}} = 2kV_\mathrm{m}\int_{\Gamma_p^1}\hat{s}_l^2\,\mathrm{d}\hat{s}. \tag{4.53}$$

Initially, we assume that there is no liquid sulphuric acid on the second pellet, and that Γ_i^1 is situated midway between the two pellets, so

$$\hat{a} = 0 \qquad \text{at} \qquad \hat{t} = 0, \tag{4.54}$$

$$\hat{h} = 0 \qquad \text{at} \qquad \hat{t} = 0. \tag{4.55}$$

4.8.2 Non-Dimensionalisation

We non-dimensionalise the model using the following scalings

$$(\hat{x},\hat{h},\hat{a}\,) = l(x,h,a), \quad \hat{s} = Rs, \quad \hat{t} = (\pi\beta_s^2 l/kS_0^2V_\mathrm{m})t, \quad \hat{s}_g = S_0 s_g, \quad \hat{s}_l = (S_0/\beta_s)s_l, \tag{4.56}$$

where we have chosen the timescale associated with liquid growth around the second pellet. The governing equations are

$$0 = \nabla^2 s_g \qquad \text{in} \qquad \omega_g, \tag{4.57}$$

$$0 = \nabla^2 s_l \qquad \text{in} \qquad \omega_l, \tag{4.58}$$

$$\frac{\mathrm{d}h}{\mathrm{d}t} = 2\pi\Lambda \int_{\Gamma_p^1} s_l^2 \,\mathrm{d}s, \tag{4.59}$$

$$\left(1 + \frac{a}{\Lambda}\right) \frac{\mathrm{d}a}{\mathrm{d}t} = \int_{\Gamma_p^2} s_l^2 \,\mathrm{d}s, \tag{4.60}$$

which are subject to the following boundary and initial conditions

$$s_l = 1 \qquad \text{at} \qquad x = -1, \tag{4.61}$$

$$\frac{\partial s_g}{\partial x} = 0 \qquad \text{at} \qquad x = 1, \tag{4.62}$$

$$\frac{\partial s_g}{\partial x} = \frac{\partial s_l}{\partial x} = 0 \qquad \text{at} \qquad y = \pm\frac{1}{2}, \tag{4.63}$$

$$\frac{\partial s_g}{\partial x} = \frac{\eta_s}{\beta_s}\frac{\partial s_l}{\partial x} \qquad \text{at} \qquad \Gamma_i^{1,2}, \tag{4.64}$$

$$s_g = s_l \qquad \text{at} \qquad \Gamma_i^{1,2}, \tag{4.65}$$

$$\frac{\partial s_l}{\partial n_p} = \kappa_s s_l^2 \qquad \text{at} \qquad \Gamma_p^{1,2}, \tag{4.66}$$

$$a = 0 \qquad \text{at} \qquad t = 0, \tag{4.67}$$

$$h = 0 \qquad \text{at} \qquad t = 0, \tag{4.68}$$

where we have defined the following three dimensionless numbers

$$\eta_s = \frac{D_{s_l}}{D_{s_g}} \approx 2 \times 10^{-4}, \quad \Lambda = \frac{R}{l} \approx 2.5 \times 10^{-1}, \quad \kappa_s = \frac{2klS_0}{\beta_s D_{s_l}} \approx 4.5 \times 10^{-1}, \tag{4.69}$$

which are the same as in Chapter 3, noting that, for the purposes of the numerical computation, we have incorporated the numerical pre-factor from the kinetics law in the definition of κ_s.

4.8.3 Numerical Solution and Asymptotic Reductions

We solve (4.57)–(4.68) numerically using the COMSOL Multiphysics software. In figure 4.14, we show a plot of the concentration of sulphur dioxide in the gas and the liquid at time $t = 1$ using the parameter values in (4.69). We denote the initial positions of the gas–liquid interfaces with black lines and the positions at $t = 1$ with white lines, respectively. We see that the concentration of sulphur dioxide is high near the source at $x = -1$ but then progressively decreases as x increases. This is a result of the dimensionless reaction rate not being small. Thus, the majority of sulphur dioxide is used up in the reaction on the surface of the first pellet, and only a fraction reaches the second pellet. This also explains the larger amount of liquid

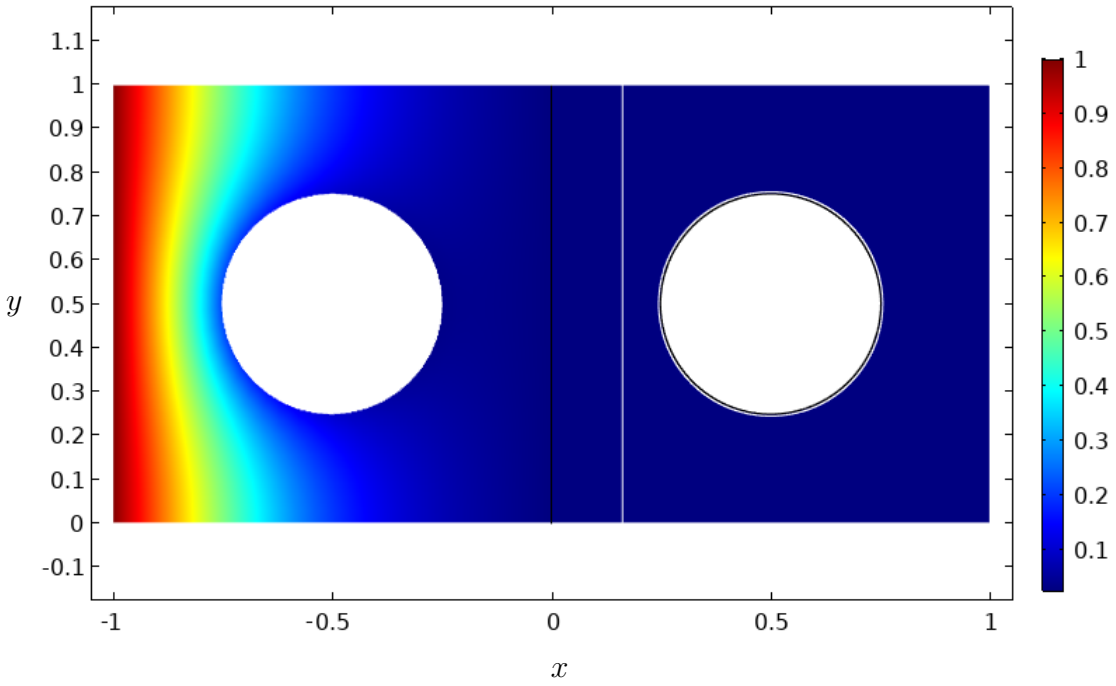

Figure 4.14: Concentration profile in the two-pellet system at time $t = 1$ using the parameter values in (4.69). Initial position of the gas–liquid interfaces is shown in black; position at $t = 1$ is shown in white.

generated around the first pellet, and therefore, the significantly faster motion of the vertical interface relative to the curved one. This is further enhanced by the fact that the curved interface is longer than the vertical one. In figure 4.15, we show a temporal profile of the dimensionless amount of liquid produced by each of the pellets, which can be calculated as

$$V_1 = h, \tag{4.70}$$

$$V_2 = \pi\left((a + \Lambda^2) - \Lambda^2\right). \tag{4.71}$$

We run our simulations until the time of coalescence of the two gas–liquid interfaces. We again see that much more liquid has been generated around the first pellet. In order to explore the effect of changing the reaction rate on the amount of liquid produced, we consider varying κ_s. In figure 4.16, we show temporal profiles of the dimensionless amount of liquid produced around each of the pellets for small and large κ_s (with $\kappa_s = 0.45$ shown in figure 4.15). In both plots, we run our simulations until coalescence of the two interfaces. We note that, since we have non-dimensionalised using the reaction timescale, in order to compare all the figures with each other and with figure 4.15 on the same timescale, we define $\tilde{t} = (0.45/\kappa_s)t$, where $\tilde{t}$ is measured according to the timescale in figure 4.15 (when $\kappa_s = 0.45$). This way

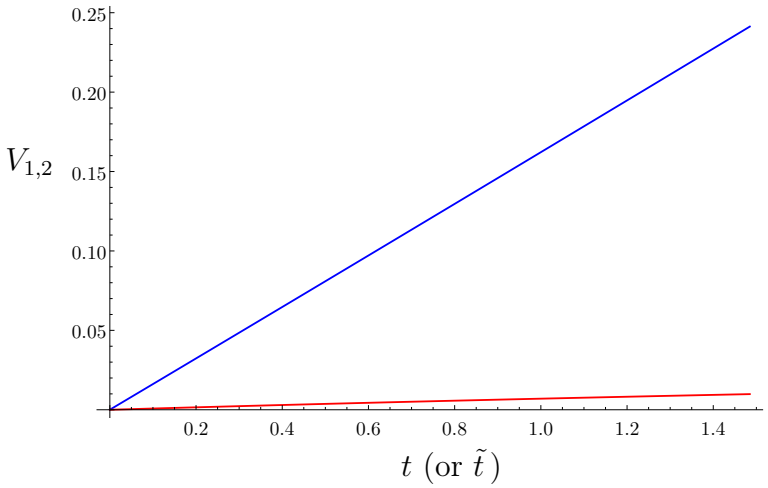

Figure 4.15: Temporal profile of the amount of liquid produced around the first pellet, V_1 (blue), and around the second pellet, V_2 (red), using the parameter values in (4.69). The simulation terminates when the two interfaces coalesce.

each dimensionless unit of time corresponds to the value of the timescale chosen in (4.56) with parameter values from table 1.1. We see that, as κ_s increases, the first pellet generates significantly more liquid relative to the second pellet. The time until coalescence proportionally decreases as well. This suggests that the time until the filter sheets are completely filled with liquid is dictated by the rate at which the saturated layer propagates into the sheets. In fact, once such a continuous layer forms, we expect that the device efficiency will drop due to the much lower diffusivity of sulphur dioxide in liquid than in gas.

We finish this section by considering the asymptotic limit when $\kappa_s \to 0$, which corresponds to the case when the reaction is much slower than diffusion. This will also serve as a benchmark, against which we can compare our numerical solution. The leading-order solution in κ_s for s_g and s_l is constant and given by the boundary condition (4.61)

$$s_g = s_l = 1. \tag{4.72}$$

This gives, using (4.59), (4.60), (4.67), and (4.68),

$$h = 4\pi^2 \Lambda t, \tag{4.73}$$

$$a = \Lambda \left(\sqrt{1 + \frac{4\pi t}{\Lambda}} - 1 \right). \tag{4.74}$$

In terms of the liquid amount produced around each of the pellets, we obtain

$$V_1 = V_2 = 4\pi^2 \Lambda t. \tag{4.75}$$

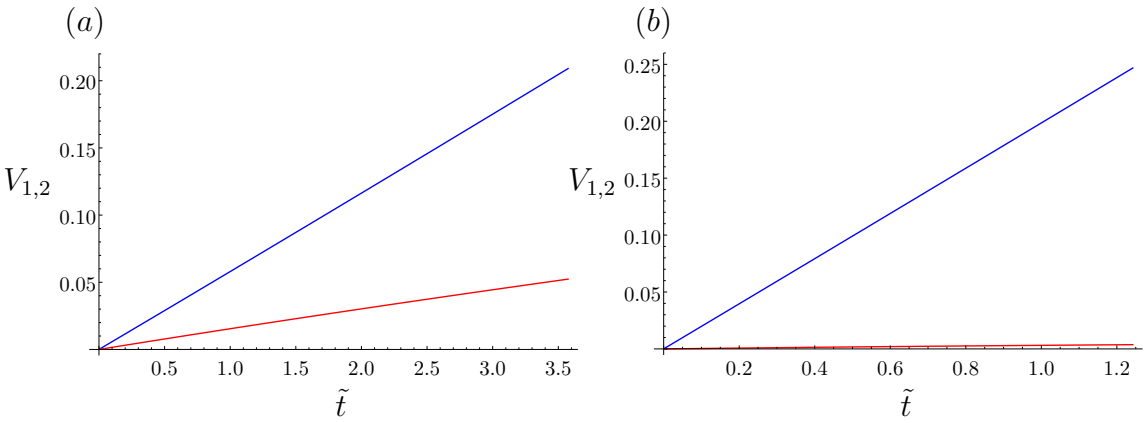

Figure 4.16: Temporal profiles of the amount of liquid produced around the first pellet, V_1 (blue), and around the second pellet, V_2 (red) for (a) $\kappa_s = 0.01$, and (b) $\kappa_s = 100$. The other parameter values are as in (4.69).

In figure 4.17, we show a temporal profile of V_1 and V_2 for $\kappa_s = 10^{-5}$ and the asymptotic prediction (4.75) shown in a dashed line. We see a very good agreement.

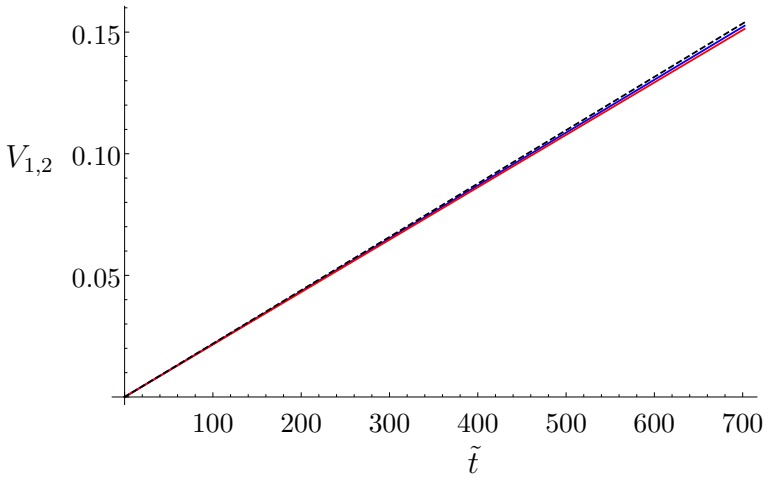

Figure 4.17: Temporal profile of V_1 (blue) and V_2 (red) for $\kappa_s = 10^{-5}$, and the asymptotic result (4.75) (dashed). The other parameter values are as in (4.69).

4.9 Conclusions

In this chapter, we coupled the macroscale equations emerging from the homogenisation in Chapter 3 with a reaction–advection equation for the gas flow in the filter channel between the sheets. We then assumed that the aspect ratio of the filter sheets is small and studied two asymptotic regimes based on the orders of magnitude of two dimensionless numbers, α and ε, which measure the change in volume in the

gas-to-liquid transition in the chemical reaction, and the aspect ratio of the channel, respectively. This analysis proved beneficial in significantly reducing the computational cost of solving the full system of governing equations in parameter regimes of physical relevance. In the first limit, when $\alpha = O(\delta^2)$ and $\varepsilon = O(\delta)$, we obtained a quasi-static equation for the concentration of sulphur dioxide both in the filter sheet and in the channel. In the second limit, when $\alpha = O(\delta)$ and $\varepsilon = O(\delta^2)$, we were able to obtain an explicit solution (4.32) for the concentration of sulphur dioxide and the void fraction. In particular, we found an estimate for the time at which two neighbouring liquid layers around catalytic pellets adjacent to the inlet of the channel will coalesce, which is proportional to the ratio of the timescale over which the liquid layer grows and the diffusive timescale of sulphur dioxide along the channel. From this formula, we see that increasing the inter-pellet distance in the porous sheet increases the time until coalescence, and, thus, increases the device operation time. We solved the full system of macroscale equations numerically until the point of first coalescence and investigated the effect of changing various parameters. Given a target concentration of sulphur dioxide at the outlet or a certain percentage of sulphur dioxide to be removed, our model can be used to find the maximum speed of the gas and the maximum width of the filter channels that achieve this. We compared the numerical results to our asymptotic predictions and found excellent agreement, and thus, in the relevant limit, the reduced system of equations may be used to approximate the performance of the filter in the given regimes. We then presented numerical results for an extended model that holds beyond the point of first coalescence of liquid layers until the whole device clogs up. We found a significant increase in the clogging time in this case and that the filter was not uniformly filled with liquid by the time it stopped working. We also compared the outlet concentration of sulphur dioxide for both Cartesian and cylindrical geometry of the filter and found that the qualitative behaviour of the solution was the same, but in the radially symmetric case, the outlet concentration was lower due to the increased surface area.

At the end of the chapter, we examined the gas and liquid transport in the situation of two neighbouring catalytic pellets, one of which was initially completely submerged in liquid sulphuric acid, while the other did not have a liquid layer around itself initially. The results of such a model have implications in the later stages of the filter operation when it is anticipated that a continuous layer of liquid sulphuric acid will form near the surface of the filter sheets that is exposed to the stream of flue gas. In fact, once such a continuous layer forms, we expect that the device efficiency will drop due to the much lower diffusivity of sulphur dioxide in liquid than in gas. The

goal of this model is to understand how the amount of liquid produced on the second pellet is influenced by the liquid amount produced around the first pellet. This is a non-trivial question since, as gaseous sulphur dioxide diffuses through the layer of sulphuric acid around the first pellet, some of it reacts on its surface, while some reaches the second pellet and then reacts. We found that, for the normal parameter regime the GMCS device operates at, much more liquid was produced around the first pellet compared to the second, and consequently, the vertical gas–liquid interface of the layer moved much faster than the curved interface around the second pellet. Our analysis suggests that the time until the filter sheets are completely filled with liquid is dictated by the rate at which the saturated layer propagates into the sheets. We also found that, as the reaction rate decreased, the amount of liquid produced around each pellet approached a common value, and the time it took until coalescence of the two interfaces increased. While a more realistic representation of the geometry would be obtained by considering a three-dimensional model, we do not expect a qualitative difference in the solutions.

Chapter 5

Hydrophilic Porous Filter Media

5.1 Introduction

In the previous chapters, for simplicity, we ignored the fibrous matrix within which the catalytic pellets are embedded. This modelling approach is appropriate when the fibres are hydrophobic, since any liquid will grow locally around each pellet until neighbouring layers coalesce rather than being drawn away from the pellets by the fibres. Although the GMCS device is manufactured with hydrophobic fibres and hydrophilic pellets (Beuscher & Venkateshwaran, 2019), an interesting question is how the efficiency and the liquid transport within the filter would be affected by the presence of a scaffold of hydrophilic fibres, which can be manufactured by coating the fibrous matrix with a hydrophilic substance. In this case, liquid flow will be enhanced by the fibres.

Models for flow inside hydrophilic porous media often involve variants of Richards equation (Richards, 1931), which governs the temporal and spatial evolution of a fluid in an unsaturated porous medium utilising Darcy's law for the flow problem (see, for example, Bear, 1979). Such modelling approaches are taken in a wide range of applications from modelling infiltration of soil (Zurmühl & Durner, 1996; Borsi *et al.*, 2004; Lewandowska *et al.*, 2004; Marinoschi, 2004; Weill *et al.*, 2009; Herrada *et al.*, 2014; Zeng *et al.*, 2018) to snow melting (Wever *et al.*, 2014; Meyer & Hewitt, 2017) to even nappy modelling (Wein *et al.*, 2019). For example, in Borsi *et al.* (2004), they consider rain water infiltration through the soil above an aquifer with runoff of the excess water. They use Richards equation and derive a boundary condition at the surface of the soil which takes into account the pressure the rain exerts on the soil to accurately capture the amount of water that penetrates into the soil, and incorporates gravitational effects. In their model, they include the effect of

gravity in the governing equations. Marinoschi (2004) models infiltration of water in unsaturated soil until a fully saturated region forms, whose front propagates into the soil. The model features a saturated region, behind the saturation front, where the saturation is constant and the governing equation is Darcy's law with a source, and an unsaturated region, ahead of the saturation front, where Richards equation holds. The boundary conditions at the front enforce continuity of pressure and velocity (or, equally, the pressure gradient using Darcy's law). A detailed analysis of Richards equation and its numerical solutions can be found, for example, in Gilding (1991); Deng & Wang (2017); Farthing & Ogden (2017); Zeng *et al.* (2018). We note that the time-independent Richards equation reduces to Darcy's law with sources/sinks (see, for example, Slodička, 1997).

Homogenisation approaches are also used to model infiltration of porous media and obtain equivalent equations to Richards equation (Lewandowska *et al.*, 2004; Daly & Roose, 2015). In Lewandowska *et al.* (2004), they study double-porosity soil infiltration and derive a macroscale model with effective properties, such as the hydraulic conductivity tensor. In Daly & Roose (2015), they use the Cahn–Hilliard phase field equation for the evolution of two fluids, coupled with the Stokes equations and obtain a homogenised model for the saturation and pressure in a porous medium. The model reduces to Richards equation only in certain regimes, such as constant gas pressure.

A key ingredient to Richards equation is the relationship between the saturation, i.e., the fraction of porous medium filled with a fluid, and either of the hydraulic conductivity (the ease with which a fluid can pass through a porous medium) or the characteristic pressure of the medium, which is the difference between the ambient (normally gas) pressure and the capillary pressure of the fluid (normally liquid). These are often found empirically for different porous structures. Classic non-linear relationships are given in van Genuchten (1980) for the case of unsaturated soils. The degree of wettability of the porous medium is an important factor that determines such relationships between the saturation and the hydraulic conductivity, and the characteristic pressure. Depending on the contact angle between the infiltrating fluid and the solid porous scaffold, the spatial profile of the liquid motion can vary (Cieplak & Robbins, 1990). The liquid–air–solid contact angle can also alter the pressure–saturation relationship (see, for example, Ishakoglu & Baytas, 2005; Gallagher *et al.*, 2008; O'Carroll *et al.*, 2010; Cooper *et al.*, 2017).

In this chapter, we present a simple one-dimensional model for liquid sulphuric acid flow within a hydrophilic filter sheet coupled with the transport of sulphur dioxide

to gain insight into the transport mechanism. In Section 5.2, we set up the mathematical model. We non-dimensionalise the system in Section 5.3 and identify the key dimensionless parameters. In Section 5.4, we consider an asymptotic simplification in the case of fast wetting of the fibres compared to the liquid growth due to the chemical reaction, and show numerical solutions in Section 5.5. We draw conclusions in Section 5.6.

5.2 Mathematical Model

In order to include flow along the fibres in a simple macroscale model for the filter, we modify the upscaled equations (4.2) and (4.3) and incorporate liquid flow through the fibrous medium using Darcy's law. This way we are effectively using a two-level homogenisation: first, homogenising the porous matrix, and then incorporating the catalytic pellets and the species transport. The simplicity of this approach allows us to write down a macroscale model that holds in the filter sheet. In addition, to evaluate the effect of hydrophilic fibres on the fluid flow in the simplest setting, we will focus on a one-dimensional cross-section of the sheet that is transverse to the filter channel. In order to follow the established approaches in infiltration problems closely, we also use the saturation, θ, defined to be the local fraction of liquid volume to volume of the void in the overall porous medium, instead of the void fraction $\mathcal{V}_g$, defined in Chapter 3. The relationship between the two can be expressed as

$$\theta = 1 - \frac{\mathcal{V}_g}{(1-\phi_s)}, \tag{5.1}$$

where $\phi_s \approx 0.3$ (Beuscher & Venkateshwaran, 2019) is the solid fraction in the porous medium (i.e., the fraction of fibres and pellets volume). We immediately note that $\theta = 1$ corresponds to zero void fraction, i.e., a completely saturated medium, while $\theta = 0$ corresponds to void fraction equal to $1 - \phi_s$, i.e., a completely unsaturated porous medium. We modify (4.2) and (4.3) by including advection terms. This turns (4.3) in the form of Richards equation with a source term due to the chemical reaction that takes place on the catalytic pellets. The model then reads

$$0 = -\frac{\partial}{\partial \hat{X}}\left(\hat{u}\hat{s}_g\right) + \frac{\partial}{\partial \hat{X}}\left(\mathcal{V}_g(\theta)\hat{D}(\theta)\frac{\partial \hat{s}_g}{\partial \hat{X}}\right) - 8\pi\mathcal{K}\hat{s}_g^2, \tag{5.2}$$

$$(1-\phi_s)\frac{\partial \theta}{\partial \hat{t}} = -\frac{\partial \hat{u}}{\partial \hat{X}} + 8\pi V_{\mathrm{m}}\mathcal{K}\hat{s}_g^2, \tag{5.3}$$

where $\mathcal{V}_g(\theta)$ is obtained from (5.1),

$$\hat{u} = -\frac{\hat{K}(\theta)}{\mu}\frac{\partial \hat{p}_{\mathrm{c}}}{\partial \hat{X}} \tag{5.4}$$

is the Darcy velocity, $\hat{K}(\theta)$ is the hydraulic conductivity of the porous medium, $\hat{p}_{\mathrm{c}}$ is the characteristic pressure, and, again, μ is the viscosity of sulphuric acid, $\hat{s}_g$ denotes the concentration of sulphur dioxide, R is the radius of the catalytic pellets, k is the reaction rate constant, β_s is Henry's law constant for sulphur dioxide, l is the pore length scale, and V_{m} is the molar volume of sulphuric acid. We take simple functional forms for $\hat{K}(\theta)$ and $\hat{p}_{\mathrm{c}}$ (Bear, 1979; Meyer & Hewitt, 2017), given by

$$\hat{K}(\theta) = k_s \theta^3 \tag{5.5}$$

and

$$\hat{p}_{\mathrm{c}}(\theta) = p_{\mathrm{a}} - \frac{\gamma}{l}\left(\frac{1}{\theta} - \theta\right), \tag{5.6}$$

where $k_s = O(10^{-10}\,\mathrm{m}^2)$ (Beuscher & Venkateshwaran, 2019) is the permeability of a fully saturated porous medium, and p_{a} is the ambient air pressure. We note that, when the medium is fully saturated, i.e., $\theta = 1$, equation (5.6) implies that $\hat{p}_{\mathrm{c}} = p_{\mathrm{a}}$, while, when the medium is dry, i.e., $\theta = 0$, we have that $\hat{p}_{\mathrm{c}} = -\infty$, which represents the effect of infinite suction by the porous medium.[1]

Finally, for simplicity, we assume that the diffusivity is a linear function that depends on the saturation and is given by

$$\hat{D}(\theta) = D_{s_g}(1 - \theta). \tag{5.8}$$

We use this simple form for the diffusivity rather than the effective diffusivity we derived in Chapter 3 to bypass the difficulty of calculating the diffusivity for void fractions less than $1 - \pi/6$. The main purpose of this model is to gain insight into the general mechanisms of transport when there are hydrophilic fibres, rather than focusing on details that will not influence the solutions qualitatively.

We assume that the sheet is sealed at one end, $\hat{X} = H$, and so there is no flow there. Therefore, using (5.4), we obtain

$$\frac{\partial \hat{p}_{\mathrm{c}}}{\partial \hat{X}} = 0 \qquad \text{at} \qquad \hat{X} = H. \tag{5.9}$$

[1]We also note that, if we want to model varying degrees of hydrophilicity of the fibres, we could use different functional forms of the pressure–saturation relationship (5.6), as presented in van Genuchten (1980); Ishakoglu & Baytas (2005); Gallagher *et al.* (2008); O'Carroll *et al.* (2010); Cooper *et al.* (2017). Experiments performed in O'Carroll *et al.* (2010), for example, suggest that increasing the hydrophobicity of the porous material (or, equally, increasing the contact angle) decreases the pressure and reduces the variation with saturation, θ. These effects can be captured by modifying (5.6) to

$$\hat{p}_{\mathrm{c}} = p_{\mathrm{a}} - \frac{\gamma}{l}\left(\frac{1}{\theta^m} - \theta\right)^n. \tag{5.7}$$

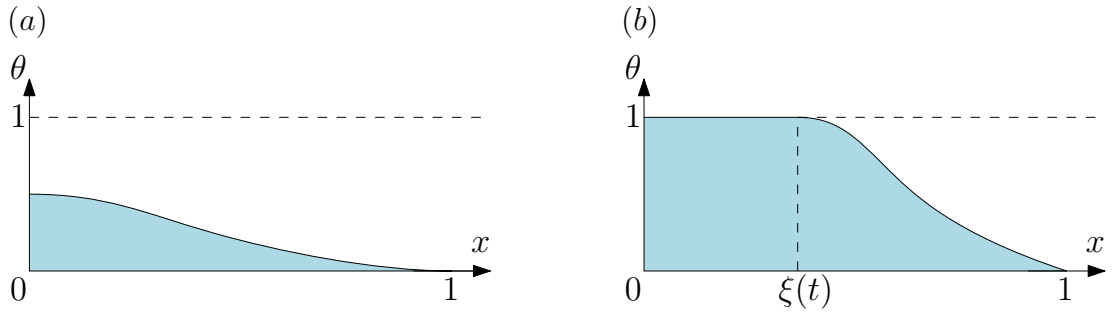

Figure 5.1: Schematic of (a) the start-up problem and (b) the saturation-front problem.

During the saturation process, in general, there will be two distinct stages, as shown in figure 5.1. The first stage, which we call the start-up problem, involves the initial build-up of liquid before full saturation is reached anywhere within the porous medium. During this stage, we assume that there is no outflow at the other end, $\hat{X} = 0$, which faces the channel. This can be thought of as having a growing droplet near that end, which does not fall due to surface tension effects. Thus, we write

$$\frac{\partial \hat{p}_{\mathrm{c}}}{\partial \hat{X}} = 0 \qquad \text{at} \qquad \hat{X} = 0. \tag{5.10}$$

The second stage, which we call the saturation-front problem, involves the formation of a saturation front, behind which the porous medium is fully saturated. As we will see in Sections 5.4 and 5.5, the saturation-front stage will not be present in the parameter regime of interest. Nevertheless, we will describe the governing equations and boundary conditions in this case in Section 5.2.2. We note that, during this stage, since the medium is fully saturated near $\hat{X} = 0$, we prescribe the pressure to be the same as the ambient air pressure. Thus,

$$\hat{p}_{\mathrm{c}} = p_{\mathrm{a}} \qquad \text{at} \qquad \hat{X} = 0. \tag{5.11}$$

We assume that there is a constant source of sulphur dioxide at $\hat{X} = 0$, where the channel is, and that no sulphur dioxide can exit at the other end, which is sealed. Thus,

$$\hat{s}_g = S_0 \qquad \text{at} \qquad \hat{X} = 0, \tag{5.12}$$

$$\frac{\partial \hat{s}_g}{\partial \hat{X}} = 0 \qquad \text{at} \qquad \hat{X} = H. \tag{5.13}$$

We will consider the corresponding problems for the two stages in turn in the following two sections.

5.2.1 Start-Up Problem

We substitute from (5.4) into (5.2) and (5.3), and the model reads

$$0 = \frac{\partial}{\partial \hat{X}}\left(\frac{\hat{s}_g \hat{K}(\theta)}{\mu}\frac{\partial \hat{p}_\mathrm{c}}{\partial \hat{X}}\right) + \frac{\partial}{\partial \hat{X}}\left(\mathcal{V}_g(\theta)\hat{D}(\theta)\frac{\partial \hat{s}_g}{\partial \hat{X}}\right) - 8\pi\mathcal{K}\hat{s}_g^2, \tag{5.14}$$

$$(1-\phi_s)\frac{\partial \theta}{\partial \hat{t}} = \frac{\partial}{\partial \hat{X}}\left(\frac{\hat{K}(\theta)}{\mu}\frac{\partial \hat{p}_\mathrm{c}}{\partial \hat{X}}\right) + 8\pi V_\mathrm{m}\mathcal{K}\hat{s}_g^2, \tag{5.15}$$

with boundary conditions

$$\hat{s}_g = S_0, \quad \frac{\partial \hat{p}_\mathrm{c}}{\partial \hat{X}} = 0 \qquad \text{at} \qquad \hat{X} = 0, \tag{5.16}$$

$$\frac{\partial \hat{s}_g}{\partial \hat{X}} = 0, \quad \frac{\partial \hat{p}_\mathrm{c}}{\partial \hat{X}} = 0 \qquad \text{at} \qquad \hat{X} = H. \tag{5.17}$$

To close the system, we assume that, initially, there is no liquid sulphuric acid in the sheet. Thus,

$$\theta = 0 \qquad \text{at} \qquad \hat{t} = 0. \tag{5.18}$$

5.2.2 Saturation-Front Problem

As the liquid sulphuric acid accumulates within the filter sheet, the region closest to the filter channel at $\hat{X} = 0$ will saturate fully first. A saturation front will form at $\hat{X} = \hat{\xi}(\hat{t})$, say, which will then propagate into the sheet. Behind the front, in $0 < \hat{X} < \hat{\xi}(\hat{t})$, the saturation will be $\theta = 1$. This means that $\mathcal{V}_g = 0$, and so (5.14) becomes

$$0 = \frac{\partial}{\partial \hat{X}}\left(\frac{k_s \hat{s}_g}{\mu}\frac{\partial \hat{p}_\mathrm{c}}{\partial \hat{X}}\right) - 8\pi\mathcal{K}\hat{s}_g^2. \tag{5.19}$$

Richards equation (5.15) reduces to Darcy flow with a source, where the pressure satisfies

$$0 = \frac{k_s}{\mu}\frac{\partial^2 \hat{p}_\mathrm{c}}{\partial \hat{X}^2} + 8\pi V_\mathrm{m}\mathcal{K}\hat{s}_g^2. \tag{5.20}$$

Ahead of the front, we solve the same equations as in the start-up problem, namely, (5.14) and (5.15). The boundary conditions for sulphur dioxide at either end of the sheet are the same and given by (5.16) and (5.17). This time, however, since the medium is fully saturated near $\hat{X} = 0$, we prescribe the pressure to be the same as the ambient air pressure, while, at the other end, $\hat{X} = H$, we still have no flow, as the end is sealed. Thus, we retain (5.9), but replace (5.10) with

$$\hat{p}_\mathrm{c} = p_\mathrm{a} \qquad \text{at} \qquad \hat{X} = 0. \tag{5.21}$$

At the saturation front, we impose continuity of the sulphur dioxide concentration and flux, i.e.,

$$\hat{s}_g = 0 \qquad \text{at} \qquad \hat{X} = \hat{\xi}(\hat{t}), \tag{5.22}$$

$$\frac{\partial \hat{s}_g}{\partial \hat{X}} = 0 \qquad \text{at} \qquad \hat{X} = \hat{\xi}(\hat{t}). \tag{5.23}$$

We also have that the saturation is constant at the front

$$\theta = 1 \qquad \text{at} \qquad \hat{X} = \hat{\xi}(\hat{t}). \tag{5.24}$$

In addition, we impose continuity of the pressure at the front, i.e., this yields

$$\hat{p}_{\mathrm{c}} = p_{\mathrm{a}} \qquad \text{at} \qquad \hat{X} = \hat{\xi}(\hat{t}). \tag{5.25}$$

We also impose continuity of velocity. In the saturated region, the velocity is given by (5.4), while, in the unsaturated region, we substitute (5.6) into (5.4). Equating the two, we find that

$$\frac{\partial \hat{p}_{\mathrm{c}}}{\partial \hat{X}} = \frac{2\gamma}{l}\frac{\partial \theta}{\partial \hat{X}} \qquad \text{at} \qquad \hat{X} = \hat{\xi}(\hat{t}). \tag{5.26}$$

We note that we have imposed an extra condition at the saturation front, since we also need to determine its location. Here, the front propagates into the sheet due to conversion of sulphur dioxide already in the sheet. A less trivial problem arises if we insist that there be a maximum possible saturation of the porous medium, which is less than one. In this case, $\mathcal{V}_g > 0$ and $D > 0$. Thus, there will be a reaction and diffusion occurring behind the front. We do not pursue this further, since, as we shall see, for the parameter regime of interest, the start-up problem will be enough to describe the transport within the filter sheet.

We conclude by noting that the full macroscale version of this model, where we couple the filter sheet dynamics with the gas flow in a channel of length L, will be analogous to the model in Chapter 4.

5.3 Dimensionless Model

We now non-dimensionalise (5.14)–(5.26) using the following scales

$$\begin{gathered} \hat{X} = HX, \qquad \hat{t} = L^2/D_{s_g} t, \qquad \hat{s}_g = S_0 s_g, \\ \hat{p}_{\mathrm{c}} = p_{\mathrm{a}} + (\gamma/l)p_{\mathrm{c}}, \qquad \hat{D} = D_{s_g} D, \end{gathered} \tag{5.27}$$

where L is the length of the filter channel in the whole device, and we have chosen the same timescale as in Chapter 4 (*cf.* (4.10)). This is because we are interested in the device behaviour over the macroscopic timescale when liquid growth is observed, where this model will serve as an essential building block.

The dimensionless model for the start-up problem (5.14)–(5.18) becomes

$$0 = \vartheta \frac{\partial}{\partial X}\left(s_g \theta (1+\theta^2)\frac{\partial \theta}{\partial X}\right) + \frac{\partial}{\partial X}\left(\mathcal{V}_g(\theta) D(\theta)\frac{\partial s_g}{\partial X}\right) - \frac{\delta^2 \Upsilon s_g^2}{\alpha}, \tag{5.28}$$

$$(1-\phi_s)\frac{\partial \theta}{\partial t} = \frac{\vartheta}{\delta^2}\frac{\partial}{\partial X}\left(\theta(1+\theta^2)\frac{\partial \theta}{\partial X}\right) + \Upsilon s_g^2, \tag{5.29}$$

along with the boundary and initial conditions

$$s_g = 1, \quad \frac{\partial \theta}{\partial X} = 0 \qquad \text{at} \qquad X = 0, \tag{5.30}$$

$$\frac{\partial s_g}{\partial X} = 0, \quad \frac{\partial \theta}{\partial X} = 0 \qquad \text{at} \qquad X = 1, \tag{5.31}$$

$$\theta = 0 \qquad \text{at} \qquad t = 0, \tag{5.32}$$

where we have used (5.5) and (5.6) to remove the pressure from (5.28) and (5.29). We have defined four dimensionless parameters

$$\alpha = S_0 V_{\mathrm{m}} \approx 10^{-6},\ \delta = \frac{H}{L} \approx 10^{-2},\ \vartheta = \frac{\gamma k_s}{\mu l D_{s_g}} \approx 10,\ \Upsilon = \frac{8\pi k L^2 R^2 S_0^2 V_{\mathrm{m}}}{\beta_s^2 l^3 D_{s_g}} \approx 10^{-1}, \tag{5.33}$$

where we have used parameter values from table 1.1 and an order of magnitude of $10^{-10}\,\mathrm{m}^2$ for the permeability k_s (Beuscher & Venkateshwaran, 2019). We note that all of the parameters except ϑ are the same as in Chapter 4. Here, ϑ/δ^2 measures the ratio of the macroscopic diffusive timescale (comparable to the timescale over which liquid grows, as indicated by the value of Υ) to the timescale associated with wetting of the porous media.

5.4 Asymptotic Solutions

We explore the fact that the parameter δ is small, and ϑ/δ^2 is large. This means that the wetting timescale associated with Richards equation is much smaller than the diffusive timescale along the filter channel.[2] We can then asymptotically expand

[2]In fact, given that ϑ alone is moderately large, the wetting timescale is smaller than the diffusive timescale across the sheet thickness as well, and our analysis would be similar, had we non-dimensionalised time with this diffusive timescale (H^2/D_{s_g}) instead.

our dependent variables θ and s_g in powers of δ^2. The leading-order versions of (5.28) and (5.29) are

$$0 = \vartheta \frac{\partial}{\partial X}\left(s_g^{(0)}\theta(1+\theta^{(0)2})\frac{\partial \theta^{(0)}}{\partial X}\right) + \frac{\partial}{\partial X}\left(\mathcal{V}_g(\theta^{(0)})D(\theta^{(0)})\frac{\partial s_g^{(0)}}{\partial X}\right) - \frac{\delta^2 \Upsilon s_g^{(0)2}}{\alpha}, \quad (5.34)$$

$$0 = \frac{\partial}{\partial X}\left(\theta^{(0)}(1+\theta^{(0)2})\frac{\partial \theta^{(0)}}{\partial X}\right), \quad (5.35)$$

where the superscript $^{(0)}$ denotes leading order, and the dimensionless grouping $\delta^2\Upsilon/\alpha = O(1)$. Integrating (5.35) together with (5.30) and (5.31), we obtain that the leading-order saturation is a function of time only, i.e., $\theta^{(0)} = \theta^{(0)}(t)$. Proceeding to first order in δ^2 in (5.29), we obtain

$$(1-\phi_s)\frac{\partial \theta^{(0)}}{\partial t} = \vartheta \frac{\partial}{\partial X}\left(\theta^{(0)}(1+\theta^{(0)2})\frac{\partial \theta^{(1)}}{\partial X}\right) + \Upsilon s_g^{(0)2}, \quad (5.36)$$

noting that the term $\partial\theta^{(0)}/\partial X = 0$. Integrating (5.36) from $X = 0$ to $X = 1$ and applying (5.30) and (5.31) yields the governing equation for $\theta^{(0)}$

$$(1-\phi_s)\frac{\partial \theta^{(0)}}{\partial t} = \Upsilon \int_0^1 s_g^{(0)2}\,\mathrm{d}X, \quad (5.37)$$

where $s_g^{(0)}$ satisfies (5.34), which, using (5.35), simplifies to

$$0 = \mathcal{V}_g(\theta^{(0)})D(\theta^{(0)})\frac{\partial^2 s_g^{(0)}}{\partial X^2} - \frac{\delta^2 \Upsilon s_g^{(0)2}}{\alpha}. \quad (5.38)$$

5.5 Numerical Solutions

We solve (5.28) and (5.29), subject to (5.30)–(5.32), numerically using the method of lines on *Mathematica* with the parameter values: $\alpha = 10^{-6}, \delta = 10^{-2}, \vartheta = 10, \Upsilon = 1$, $\phi_s = 0.3$. In figure 5.2, we show a comparison between the numerical solution and the solution to the asymptotically reduced problem from Section 5.4 of the start-up problem for the spatial profile of θ and s_g for various times until the saturation becomes $\theta = 1$ at $X = 0$. We see that the saturation is spatially uniform across the domain, as predicted by the asymptotic analysis, with which there is excellent agreement. This means that the filter sheet saturates with liquid everywhere at the same time, and so there is no saturation-front problem in this case. While, on the face of it, this might be surprising, this is because the wetting timescale is much smaller than the diffusive timescale over the whole device. We note that there is an initial transient growth in the sulphur dioxide concentration, not shown in the graph, until

$t = O(\delta^2)$ when all the terms in (5.28) balance. Then, for larger times, the dominant balance is between the second, the third, and the fourth term, and while θ is not very close to one, the concentration is quasi-steady. However, once θ approaches 1, the fourth term dominates, and the concentration decreases to zero. In figure 5.3, we also show the temporal profile of θ, which again agrees well with the asymptotic prediction.

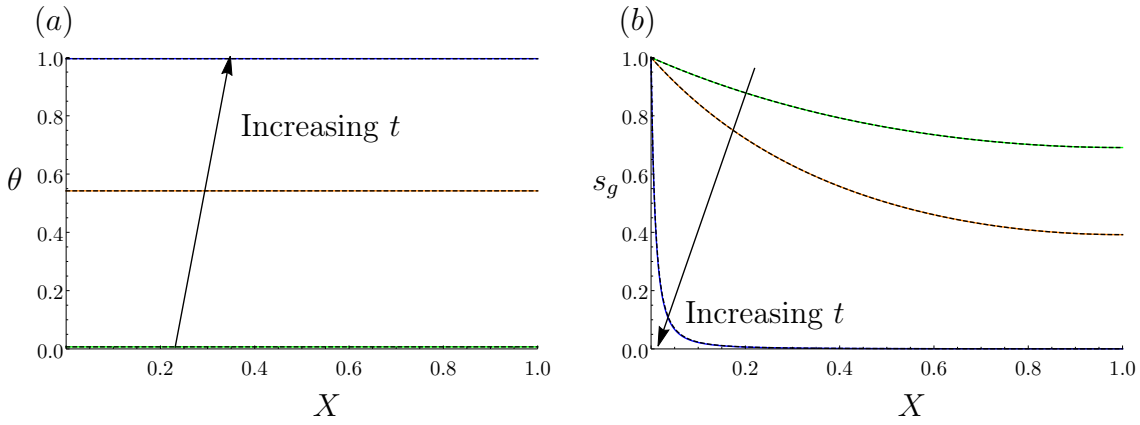

Figure 5.2: Spatial profile of (a) θ and (b) s_g for various times: $t = 0.01$ (green), 1 (orange), 5.4 (blue), and the asymptotic prediction from Section 5.4 (dashed). The parameter values are $\alpha = 10^{-6}, \delta = 10^{-2}, \vartheta = 10, \Upsilon = 1$, $\phi_s = 0.3$.

To illustrate how the solutions depend on ϑ, we also show the spatial profiles of θ and s_g in figure 5.4 varying ϑ. We see that, as ϑ increases, the profile of the saturation becomes more uniform. When ϑ is small, the wetting timescale is large, and so it takes time for the liquid to spread.

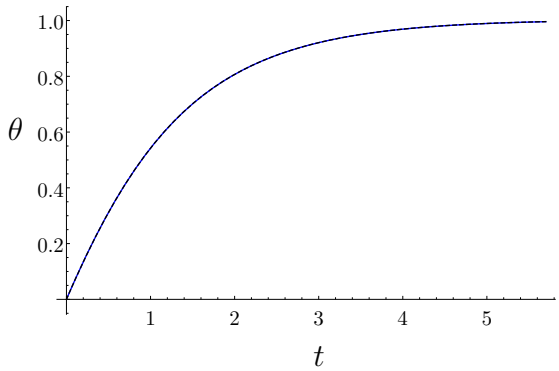

Figure 5.3: Temporal profile of θ (blue) with the asymptotic prediction from Section 5.4 (dashed). The parameter values are $\alpha = 10^{-6}, \delta = 10^{-2}, \vartheta = 10, \Upsilon = 1$, $\phi_s = 0.3$.

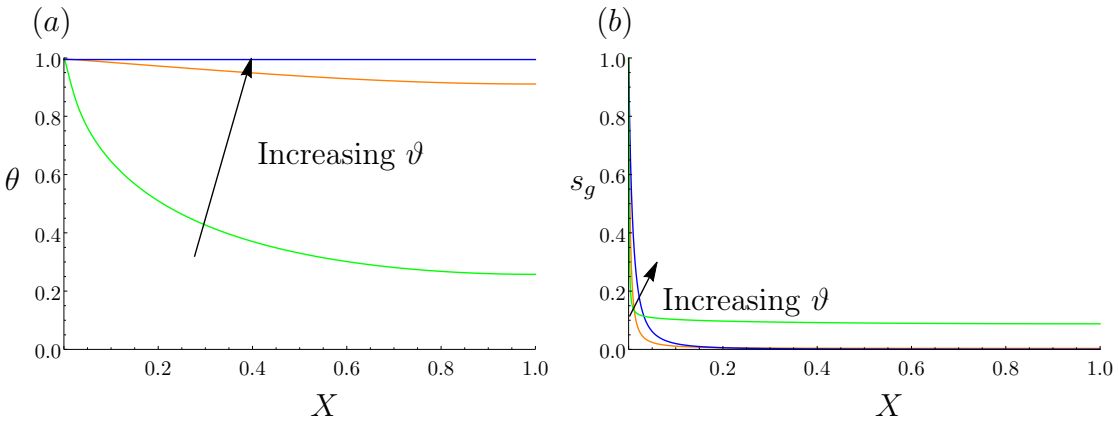

Figure 5.4: Spatial profile of (a) θ and (b) s_g when $\theta = 1$ at $X = 0$ varying $\vartheta = 10^{-8}$ (green), 10^{-6} (orange), 10^{-4} (blue). The other parameters are $\alpha = 10^{-6}, \delta = 10^{-2}, \Upsilon = 1$, $\phi_s = 0.3$.

5.6 Conclusions

In this chapter, we derived a simple one-dimensional model for gas and liquid transport within a filter sheet of the GMCS device that is composed of hydrophilic fibres. We modelled the flow in the porous medium formed by fibres and pellets using a version of Richards equation that incorporates a source term due to the chemical reaction that occurs within the filter. As part of the mathematical analysis, we identified a dimensionless number that measures the ratio of the diffusive timescale over the whole device (comparable to the timescale over which the liquid grows) to the wetting timescale. For realistic parameter values, and on the device timescale, this number is large, which indicates that the sheet wets very fast before any appreciable liquid growth is observed. Thus, over the timescale of liquid growth, the liquid saturation is spatially uniform across the sheet and increases until the whole sheet is filled with liquid. This is very different from the situation in Chapter 4, where we saw that the region near the filter channel is the first to fully saturate with liquid. This suggests that, in the case of hydrophilic fibres, choosing sheets that are thicker will increase the time before the sheets clog. The model can be used to describe filters made from materials of varying wettability. It is an important building block setting up the mathematical machinery, necessary for studying the behaviour of filters made from such materials.

When extending to a two-dimensional or a three-dimensional model, a careful evaluation of the effect of gravity in such liquid flows has to be taken into account, as the actual GMCS device is longer than the thickness of its filter sheets. This might

facilitate flow in the vertical direction, along the channels, and act as a self-cleaning mechanism for the filter.

Chapter 6

A Simple Model for the Hygroscopy of Sulphuric Acid

6.1 Introduction

Sulphuric acid is produced as a by-product in the GMCS device when removing sulphur dioxide from flue gas. However, it is also used in a wide range of industrial processes, including as a catalyst in alkylation reactions, in petroleum refining, in the manufacture of detergents, and as an important component in lead-acid batteries (House, 2013). Its properties have been extensively studied and established empirically (Perry & Green, 1997; Joshi & Kandpal, 2007; Sippola & Taskinen, 2014). A prominent feature of sulphuric acid is its hygroscopy, i.e., its tendency to absorb water vapour from its surroundings (House, 2013). When water vapour is absorbed, the volume of the sulphuric acid solution increases and consequently dilutes the acid concentration.

Water absorption into liquids has been well studied and modelled (see, for example, Lewis & Whitman, 1924; Greenewalt, 1926) as far as the mechanism of the process at the gas–liquid interface is concerned. In Lewis & Whitman (1924), and Greenewalt (1926), they describe the principles of gas absorption in terms of a "two-film" theory, in which thin stationary films of the corresponding phase on either side of the interface are assumed to exist which provide resistance to mass transfer. The absorptive flux depends linearly on the difference between the concentration of water at the gas–liquid interface and the equilibrium value of the concentration of water in the liquid when there is no net absorption.

The hygroscopic growth of materials has mainly been considered in the context of swelling of solid porous materials such as mortar, polymers and powders (Zhou *et al.*, 2006; Delgado *et al.*, 2006; Hsu *et al.*, 2008; Canuto *et al.*, 2013) rather than aqueous

solutions such as aqueous sulphuric acid. In Delgado *et al.* (2006), they present a model for the hygroscopic material that uses a non-linear expression for the rate of increase of water content that has a power-law dependence on the difference between the amount of water at the surface and at equilibrium. However, their model assumes that the water is well mixed in the bulk, and so does not incorporate water transport across the material.

A conservation-of-mass type of model for hygroscopic swelling of porous spherical particles, which incorporates the diffusive transport of water, is presented in Sweijen *et al.* (2017). They track the volume fraction of water and model absorption at the interface as a first-order kinetics process. Furthermore, they investigate numerically the regimes when diffusion and water absorption dominate, respectively, and derive a formula for the particle radius as a function of the water volume fraction. In this model, the water fraction at the particle surface is assumed to be independent of diffusion processes in the bulk and is solved for separately to obtain an exponential evolution in time. This makes the boundary condition at the surface of the particle a time-dependent Dirichlet condition.

Hennessy *et al.* (2017) develop a model for solvent evaporation and adsorption in thin liquid films. They track the volume fraction of the solvent using a non-linear diffusion model, couple this with mass transfer across the moving interface, and fit solutions of their model against experimental data from ternary solutions, to find the mass transfer coefficient for their systems. We will use a simplified version of their model in this chapter in which we set the diffusivity to be constant and track the concentration, rather than volume fraction, of water in the liquid layer. Similar models for solvent diffusion in glassy polymers are presented in Alfrey Jr. *et al.* (1966); Cohen & Erneux (1988); Mitchell & O'Brien (2012).

Our work is motivated by a set of experiments performed at W. L. Gore and Associates, Inc., which revealed a significant increase in the volume of a sample of sulphuric acid exposed to an environment of high relative humidity for several months. Our goal is to obtain a model that explains the experimental data and can be used to quantify the hygroscopy effect in the layers of sulphuric acid produced in the GMCS device. In these devices, water vapour is absorbed from the flue gas by the sulphuric acid layers. The additional volume attributed to hygroscopy further reduces device efficiency and leads to swifter clogging. Understanding the amount of moisture uptake in such devices is crucial in understanding their performance and the time it takes for them to clog. However, the fundamental parameter controlling hygroscopy, the mass transfer coefficient associated with water transport across the interface, is

not readily available in the literature. Thus, in this chapter, we will present a simple mathematical model to describe the hygroscopy of a layer of sulphuric acid, compare the solutions to the model against experimental data, and determine this coefficient. We will then demonstrate that this formulation of the problem with a mass transfer coefficient is equivalent to the framework in terms of Henry's law for conservation of chemical potential that we have already developed in the previous chapters, and use this to derive a model for the GMCS device that incorporates hygroscopy of sulphuric acid. Unlike Delgado *et al.* (2006), we will incorporate diffusion of water, and, therefore, track the spatially non-uniform water concentration in the sulphuric acid layer. In addition, we do not calculate the water concentration at the gas–liquid interface separately, as in Sweijen *et al.* (2017), but couple it with the diffusion process in the bulk of the solution. The plan for the chapter is as follows. In Section 6.2, we will describe the experiments performed at W. L. Gore and Associates, Inc. that motivated our work. In Section 6.3, we will present the governing equations and boundary and initial conditions for a model that describes the concentration of water in a layer of aqueous sulphuric acid with thickness that can change as water is absorbed. In Section 6.3.1, we will present the steady-state solution to the problem. In Section 6.3.2, we will non-dimensionalise the model, and introduce three key dimensionless parameters. In Section 6.3.3, we will consider a distinguished limit of the model in which diffusion is the dominating process. We will present numerical results, compare these with asymptotic results and experimental data, and determine the mass transfer coefficient in Section 6.4. In Section 6.5, we will briefly show how this model can be equivalently formulated using the framework in the previous chapters, and, in Section 6.6, we will use this to formulate a model for the GMCS device that incorporates hygroscopy of sulphuric acid. Finally, we will draw conclusions in Section 6.7.

6.2 Experimental Set-Up

We now describe the experiments carried out by W. L. Gore and Associates, Inc. in order to understand the effect of hygroscopy in sulphuric acid. The experimental set-up shown in figure 6.1(a), consists of a cylindrical glass vial with a flat bottom and an O-ring seal joint at the top connected to an open tube with an O-ring seal joint at the bottom. The diameter of the vial is 2.5 cm and its height is approximately 4.5 cm. An ePTFE membrane is secured between the vial and the tube using the O-ring and a metal clamp, which separates the vial from the tube. A small amount of sulphuric

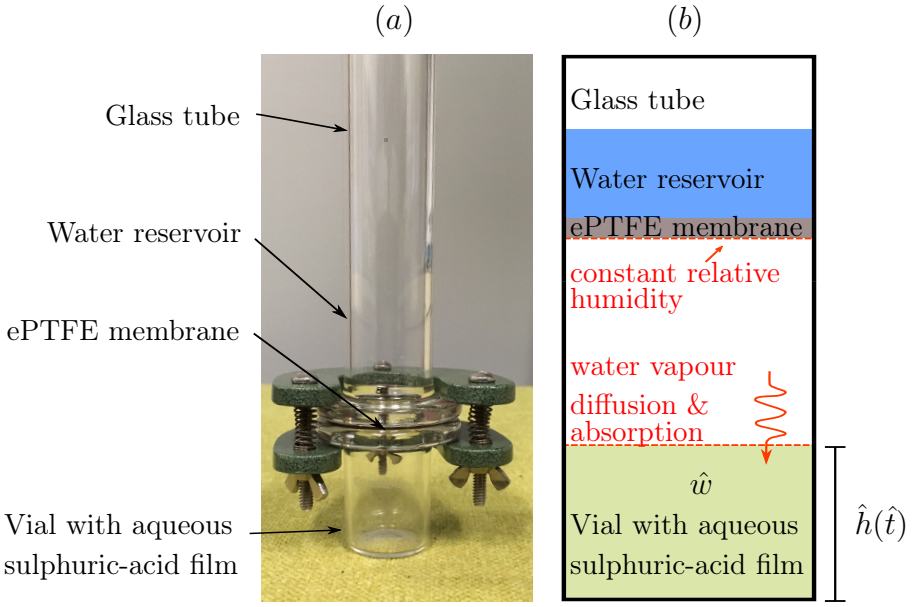

Figure 6.1: (a) Picture of the experimental set-up before filling it with liquid juxtaposed with (b) a schematic of the experiment.

acid with prescribed initial thickness and water concentration is placed in the vial (see table 6.1). The section above the membrane is filled with water to create a reservoir. The ePTFE membrane properties are such that liquid water does not penetrate and wet the membrane, but molecules of water vapour are free to diffuse through the porous structure. This set-up creates a constant-relative-humidity boundary at the bottom of the membrane surface. The overall set-up is shown schematically in figure 6.1(b). The layer of sulphuric acid absorbs water vapour and creates a gradient in the bottom section of the vial that drives further diffusion of water molecules. Two experiments, each performed in two trials and lasting six months, were conducted at 95% relative humidity with the same thickness $h_0 = 1.9 \times 10^{-3}\,\mathrm{m}$, but with two different starting concentrations, namely (a) $w_0 = 3.6 \times 10^3\,\mathrm{mol\,m^{-3}}$ (concentrated acid) and (b) $w_0 = 4.0 \times 10^4\,\mathrm{mol\,m^{-3}}$ (dilute acid). The water uptake was quantified by periodically measuring the weight of the acid solution in the vial (the measurements were taken 2–3 times a week in the first two months, and then once a week for the remaining four months of the experiment). Each measurement took 2–3 minutes and consisted of emptying the water from the glass tube (the acid was never removed from the vial), removing the top section, and weighing the bottom section (glass vial and liquid). The weight of the liquid is determined as the difference of the measured weight and the weight of the empty vial. The quantities of interest, namely, the sulphuric acid concentration and the film thickness, are then calculated from the

initial concentration and weight uptake. We will present the experimental results and a comparison with our model in Section 6.4.

6.3 Mathematical Model

We now present a model that describes the hygroscopy of sulphuric acid. We consider a liquid layer of sulphuric acid residing on an impermeable substrate, with its upper surface exposed to an atmosphere containing water at a constant relative humidity, as shown in figure 6.2. We suppose that the liquid film has initial thickness $\hat{x} = h_0$ (measured in m) and contains water with concentration w_0 (measured in $\mathrm{mol\,m^{-3}}$). Across the gas–liquid interface, we assume that the flux of water into the film, $-\hat{Q}$ (measured in $\mathrm{mol\,m^{-2}\,s^{-1}}$), caused by the hygroscopy of the sulphuric acid, is proportional to the difference between the concentration of dissolved water at the gas–liquid interface and the equilibrium concentration, w_{eq}, which is the concentration of water in the sulphuric acid associated with a balance in chemical potentials across the interface at a given relative humidity. For simplicity, we assume that this relationship is linear in the concentration difference, and thus we write $\hat{Q} = k_w(\hat{w}|_{\hat{x}=\hat{h}} - w_{\mathrm{eq}})$, where k_w (measured in $\mathrm{m\,s^{-1}}$) is the mass transfer coefficient associated with water absorption, assumed to be constant. We acknowledge the fact that this is a different formulation of the boundary conditions at the gas–liquid interface presented in the previous chapters. Here, we use a mass transfer coefficient, which is often used by industrialists and can be compared to experimental data. In Section 6.5, we will show that this formulation can be obtained equivalently from the framework developed in Chapter 3.

In practice, w_{eq} can be experimentally determined (Wilson, 1921) and depends on the relative humidity and temperature of the surrounding air. For simplicity, we assume isothermal conditions so that w_{eq} is a constant. In the liquid film, we assume that water is transported by diffusion with constant diffusivity D_{w_l} (measured in $\mathrm{m^2\,s^{-1}}$), and that volume changes due to mixing are negligible. In practice, the diffusivity may vary with concentration but we will find that, for the parameter regime of interest, this does not play a role, while for other regimes, which we consider in Appendix D, we will show that a concentration-dependent diffusivity has a minimal effect on the behaviour.

We also note that, since the water vapour absorbed at the top of the liquid film is less dense than the sulphuric acid, convective effects due to density variations are negligible. Given that we expect the surface tension of the liquid layer to keep the

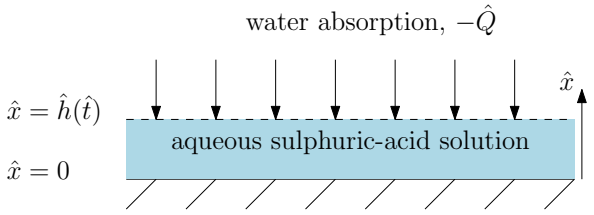

Figure 6.2: Schematic of the model system.

air–liquid interface flat, we restrict ourselves to a one-dimensional model with changes only occurring in the vertical direction. Of course, small menisci exist at the edges of the layer, but we anticipate that their influence will be confined to a small boundary layer near the walls and expect that these will have negligible effect on the mass transfer. Thus, we write down the following model for the water concentration within the film, $\hat{w}$, and the thickness of the film, $\hat{h}$,

$$\frac{\partial \hat{w}}{\partial \hat{t}} = D_{w_l} \frac{\partial^2 \hat{w}}{\partial \hat{x}^2}, \tag{6.1}$$

$$\frac{\mathrm{d}\hat{h}}{\mathrm{d}\hat{t}} = k_w V_{\mathrm{m},w} (w_{\mathrm{eq}} - \hat{w}|_{\hat{x}=\hat{h}}), \tag{6.2}$$

where $V_{\mathrm{m},w}$ (measured in $\mathrm{m}^3\,\mathrm{mol}^{-1}$) is the molar volume of water.

At the gas–liquid interface, we conserve flux relative to the moving interface and write

$$-D_{w_l} \frac{\partial \hat{w}}{\partial \hat{x}} - \hat{w} \frac{\mathrm{d}\hat{h}}{\mathrm{d}\hat{t}} = k_w (\hat{w} - w_{\mathrm{eq}}) \qquad \text{at} \qquad \hat{x} = \hat{h}(\hat{t}). \tag{6.3}$$

At the surface of the substrate, $\hat{x} = 0$, we impose no flux of water, and, thus, we write

$$-D_{w_l} \frac{\partial \hat{w}}{\partial \hat{x}} = 0 \qquad \text{at} \qquad \hat{x} = 0. \tag{6.4}$$

We assume that, initially, the concentration of water is known and uniform, and that the thickness of the film is given, and, thus, we write

$$\hat{w} = w_0, \quad \hat{h} = h_0 \qquad \text{at} \qquad \hat{t} = 0. \tag{6.5}$$

We note that, for situations of practical interest, $w_0 < w_{\mathrm{eq}}$. To summarise, equations (6.1) and (6.2) with boundary conditions (6.3) and (6.4), and initial conditions (6.5) form a closed system for the concentration of water and the height of the film.

We list the known dimensional parameters for the two experiments in table 6.1, and note that the mass transfer coefficient k_w is unknown *a priori*.

Parameter	Definition	Value	Units
h_0	Initial liquid thickness	1.9×10^{-3}	m
w_0	Initial water concentration	(a) 3.6×10^3	$\mathrm{mol\,m^{-3}}$
		(b) 4.0×10^4	
A	Cross-section of glass vial	4.9×10^{-4}	$\mathrm{m^2}$
w_{eq}	Equilibrium water concentration	5.4×10^4	$\mathrm{mol\,m^{-3}}$
M_w	Molar mass of water	1.8×10^{-2}	$\mathrm{kg\,mol^{-1}}$
D_{w_l}	Diffusivity of water	1.6×10^{-9}	$\mathrm{m^2\,s^{-1}}$
	in aqueous sulphuric acid		
$V_{\mathrm{m},w}$	Molar volume of water	1.8×10^{-5}	$\mathrm{m^3\,mol^{-1}}$

Table 6.1: Dimensional parameters (taken from Wilson, 1921; Brini *et al.*, 2017; Leaist, 1984).

6.3.1 Steady State

Before proceeding, we look for the steady-state solutions $\hat{w}_{ss} = \hat{w}_{ss}(\hat{x})$ and $\hat{h}_{ss} = \hat{h}_{ss}(\hat{x})$ to (6.1)–(6.5). Equation (6.2) tells us that

$$\hat{w}_{ss}|_{\hat{x}=\hat{h}} = w_{\mathrm{eq}}, \tag{6.6}$$

which we use to solve (6.1) along with (6.4) to find that

$$\hat{w}_{ss} = w_{\mathrm{eq}}. \tag{6.7}$$

We appeal to conservation of mass of sulphuric acid in order to find the final thickness of the liquid layer. Denoting by N the total initial moles of substance present in the layer, and the total number of moles of sulphuric acid by S, we have that

$$S = N - Aw_0h_0 \qquad \text{at} \qquad \hat{t} = 0, \tag{6.8}$$

where A is the cross-sectional area of the layer, measured in $\mathrm{m^2}$.

Once the system has settled into the steady state, since the change in thickness of the liquid layer is due purely to the increase in water molecules, the total number of moles of sulphuric acid remains the same and is given now by

$$S = N - Aw_{\mathrm{eq}}\hat{h}_{ss} + \frac{A(\hat{h}_{ss} - h_0)}{V_{\mathrm{m},w}}. \tag{6.9}$$

Equating (6.8) and (6.9) and rearranging, we find that

$$\hat{h}_{ss} = \frac{h_0(1 - V_{\mathrm{m},w}w_0)}{1 - V_{\mathrm{m},w}w_{\mathrm{eq}}}. \tag{6.10}$$

We note that the steady-state layer thickness is independent of the mass transfer coefficient k_w.

6.3.2 Dimensionless Model

In order to find the key parameters that determine the behaviour of the system, we non-dimensionalise (6.1)–(6.5) using the following scalings

$$\hat{w} = w_{\mathrm{eq}} w, \quad (\hat{x}, \hat{h}) = h_0(x, h), \quad \hat{t} = (h_0^2/D_{w_l})t, \tag{6.11}$$

where we have chosen to scale with the timescale associated with diffusion across the layer (rather than the timescale associated with the interface motion). This proves useful when comparing our model with experimental results as we have a good estimate of both h_0 and D_{w_l}. Furthermore, we have chosen w_{eq} as the scale for $\hat{w}$, since this parameter remained the same in the experiments (the same relative humidity was maintained throughout the experiments). The resulting dimensionless equations, together with the boundary and initial conditions, are

$$\frac{\partial w}{\partial t} = \frac{\partial^2 w}{\partial x^2}, \tag{6.12}$$

$$\frac{\mathrm{d}h}{\mathrm{d}t} = \alpha_{w,\mathrm{eq}} \,\mathrm{Sh}(1 - w|_{x=h}), \tag{6.13}$$

subject to

$$-\frac{\partial w}{\partial x} - w\frac{\mathrm{d}h}{\mathrm{d}t} = \mathrm{Sh}(w-1) \qquad \text{at} \qquad x = h(t), \tag{6.14}$$

$$\frac{\partial w}{\partial x} = 0 \qquad \text{at} \qquad x = 0, \tag{6.15}$$

$$w = n, \quad h = 1 \qquad \text{at} \qquad t = 0, \tag{6.16}$$

where we have introduced three dimensionless parameter groups, namely,

$$\alpha_{w,\mathrm{eq}} = w_{\mathrm{eq}} V_{\mathrm{m},w}, \qquad n = \frac{w_0}{w_{\mathrm{eq}}}, \qquad \mathrm{Sh} = \frac{h_0 k_w}{D_{w_l}}. \tag{6.17}$$

Here, $\alpha_{w,\mathrm{eq}}$ represents the thickness change associated with the equilibrium concentration, n is the ratio of the initial concentration to the equilibrium concentration, assumed to be less than one (since the initial concentration is lower than the equilibrium concentration), and Sh is the Sherwood number for water absorption, which compares the diffusive and the absorptive timescales. We also note that $\alpha_{w,\mathrm{eq}} < 1$, since the equilibrium concentration of water is less than the molar concentration of water. We list the known dimensionless parameters for the two experiments in table 6.2, and note that the Sherwood number Sh is unknown *a priori*, since it depends on the unknown mass transfer coefficient k_w.

Parameter	Value
$\alpha_{w,\mathrm{eq}}$	0.97
n	(a) 0.067, (b) 0.74

Table 6.2: Dimensionless parameters.

6.3.3 The Case of Small Sherwood Number

Although the problem (6.12)–(6.16) is not very difficult to solve numerically, it is nonetheless a moving-boundary problem that requires a careful treatment. Before solving numerically, we would like to gain insight into the qualitative behaviour of the solutions for limiting values of the Sherwood number, since this is the number that we do not know *a priori*. To that end, we consider the limit in which $\mathrm{Sh} \ll 1$, which will provide substantial simplifications to the problem and, as we will see in Section 6.4, it will prove relevant to the experiments we described in Section 6.2. This limit corresponds to the situation when diffusion of water is much faster than water absorption, respectively. We treat both $\alpha_{w,\mathrm{eq}}$ and n as $O(1)$ parameters, so that our model has the richest structure. We also briefly discuss the large-Sherwood-number limit in Appendix D, where we are also able to make some simplifications.

When $\mathrm{Sh} \ll 1$, we see from (6.13) that, in this case, the right-hand side becomes small, and, to a good approximation, the film does not grow. This is not surprising since, in this limit, the diffusion timescale is much shorter than the absorptive timescale. Moreover, if we solve (6.12)–(6.16) neglecting the terms multiplied by Sh, equation (6.14) tells us that the flux of water from the atmosphere is zero, and, thus, the concentration remains at its initial value. In order to explore the film growth, we rescale time by $t = \tau/\mathrm{Sh}$, where $\tau = O(1)$, which corresponds to using the absorptive timescale, on which diffusion happens very fast. With this scaling, the model becomes

$$\mathrm{Sh}\frac{\partial w}{\partial \tau} = \frac{\partial^2 w}{\partial x^2}, \tag{6.18}$$

$$\frac{\mathrm{d}h}{\mathrm{d}\tau} = \alpha_{w,\mathrm{eq}}(1 - w|_{x=h}), \tag{6.19}$$

subject to

$$-\frac{\partial w}{\partial x} - \mathrm{Sh}\, w\frac{\mathrm{d}h}{\mathrm{d}\tau} = \mathrm{Sh}(w-1) \qquad \text{at} \qquad x = h(\tau), \tag{6.20}$$

$$-\frac{\partial w}{\partial x} = 0 \qquad \text{at} \qquad x = 0, \tag{6.21}$$

$$w = n, \quad h = 1 \qquad \text{at} \qquad \tau = 0. \tag{6.22}$$

Neglecting terms of $O(\mathrm{Sh})$, we see that (6.18), (6.20), and (6.21) yield a spatially uniform solution

$$w = w(\tau). \tag{6.23}$$

Thus, diffusion acts fast enough that the water concentration is uniform in the bulk liquid, but is not in equilibrium, and this gives rise to film growth. In order to solve for $w(\tau)$, we integrate (6.18) across the layer, and apply (6.20) and (6.21) to find that

$$\frac{\mathrm{d}(wh)}{\mathrm{d}\tau} = 1 - w|_{x=h} = \frac{1}{\alpha_{w,\mathrm{eq}}}\frac{\mathrm{d}h}{\mathrm{d}\tau}. \tag{6.24}$$

Integrating (6.24) and applying (6.22) gives a relationship between w and h, namely,

$$w = \frac{h - 1 + \alpha_{w,\mathrm{eq}} n}{\alpha_{w,\mathrm{eq}} h}. \tag{6.25}$$

Substituting from (6.25) into (6.19), we arrive at an ordinary differential equation for h,

$$\frac{\mathrm{d}h}{\mathrm{d}\tau} = \frac{(\alpha_{w,\mathrm{eq}} - 1)h + 1 - \alpha_{w,\mathrm{eq}} n}{h}, \tag{6.26}$$

which has to be solved subject to (6.22). The implicit solution for h reads

$$\tau = \frac{1}{\alpha_{w,\mathrm{eq}} - 1}\left(h - 1 - \frac{1 - \alpha_{w,\mathrm{eq}} n}{\alpha_{w,\mathrm{eq}} - 1}\log\left(\frac{(\alpha_{w,\mathrm{eq}} - 1)h + 1 - \alpha_{w,\mathrm{eq}} n}{(1-n)\alpha_{w,\mathrm{eq}}}\right)\right). \tag{6.27}$$

From (6.26), we see that, as $\tau \to \infty$, h tends to a steady-state thickness given by

$$h_{\mathrm{eq}} = \frac{1 - \alpha_{w,\mathrm{eq}} n}{1 - \alpha_{w,\mathrm{eq}}}, \tag{6.28}$$

and, consequently, that $w \to 1$. We note that (6.28) is the dimensionless version of (6.10). Equation (6.28) further simplifies to $h_{\mathrm{eq}} = 1/(1 - \alpha_{w,\mathrm{eq}})$ when $n \ll 1$, providing a simple formula for the equilibrium film thickness in this regime.

6.4 Numerical Results

We now solve the full system (6.12)–(6.16) numerically and compare the results with the asymptotic reductions presented in Section 6.3.3 and the experimental results from Section 6.2. In order to solve the problem numerically, we map the time-dependent spatial domain $0 \le x \le h(t)$ to the fixed domain $0 \le \xi \le 1$ using the transformation $x = h(t)\xi$, discretise the system in space, and solve the problem using the method of lines. In figure 6.3, we present the solutions for h and w for sample parameter values $\mathrm{Sh} = 1, \alpha_{w,\mathrm{eq}} = 0.5, n = 0.1$ in order to visualise the generic behaviour of

the system, and, in particular, the saturation of the film thickness with time. We see that, in figure 6.3(a), the film thickness evolves to an equilibrium value of 1.9, which agrees with the prediction from (6.28) if we substitute these parameter values, while in figure 6.3(b), we see that the water concentration first develops a moderate gradient near the gas–liquid interface due to water absorption before smoothing out as the concentration becomes uniform across the liquid film due to diffusion.

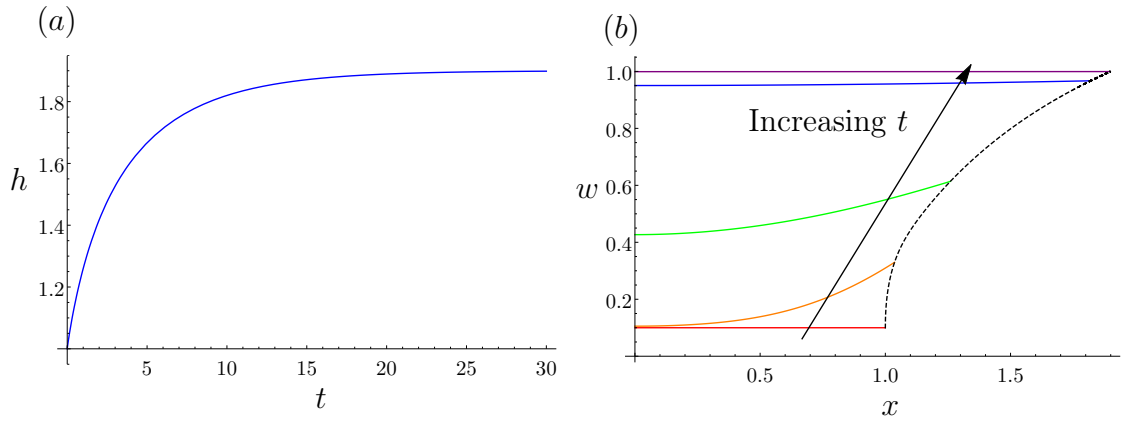

Figure 6.3: Graphs showing (a) the temporal profile of h, satisfying (6.12)–(6.16) and (b) the spatial profile of w for various times: $t = 0$ (red), 0.1 (orange), 1 (green), 10 (blue), 30 (purple). The position of the gas–liquid interface is shown with a dashed line. The parameters are $\alpha_{w,\mathrm{eq}} = 0.5$, $\mathrm{Sh} = 1$, and $n = 0.1$.

Having seen the general behaviour of the system, we now explore how the solution changes as the parameters change. Firstly, we vary w_{eq}, which changes both $\alpha_{w,\mathrm{eq}}$ and n, and the results are shown in figure 6.4(a). We see that increasing w_{eq} results in a larger equilibrium film thickness. This is because the larger the w_{eq} the more water uptake is required to reach equilibrium. Secondly, we vary w_0 by varying n as shown in figure 6.4(b). We see that increasing w_0 leads to a decrease in the equilibrium film thickness. This is to be expected, since increasing w_0 means that the initial concentration becomes closer to the equilibrium value w_{eq}, and so less water needs to be absorbed until equilibrium is reached. Thirdly, in figure 6.5, we present the film thickness versus time for decreasing values of Sh between 1 and 0.1, and we see that there is excellent agreement between the numerical results and our asymptotic prediction from Section 6.3.3, shown as a dashed line, as $\mathrm{Sh} \to 0$. We note that we have plotted the results versus the scaled time τ to be consistent with the result in Section 6.3.3. Since changing Sh only alters the relative strength of absorption over diffusion, variations in this parameter determine the *approach* of the thickness to its

equilibrium, including the time it takes to reach it, but not its actual value, which is given by (6.28).

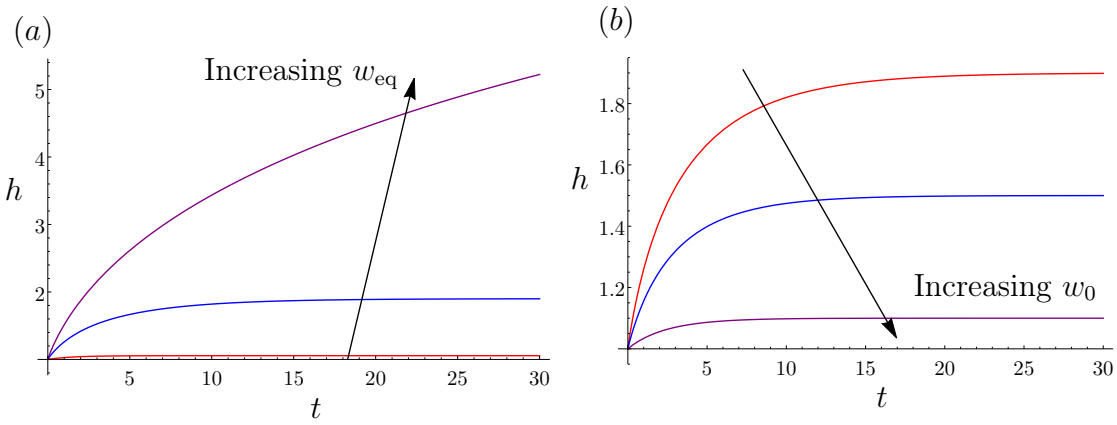

Figure 6.4: Graphs showing the temporal profile of h varying (a) w_{eq} by varying both $(\alpha_{w,eq}, n)$: (0.1, 0.5) (red), (0.5, 0.1) (blue), (0.9, 0.06) (purple) and (b) w_0 with $n =$ 0.1 (red), 0.5 (blue), 0.9 (purple), and $\alpha_{w,eq} = 0.5$. Here, Sh $= 1$.

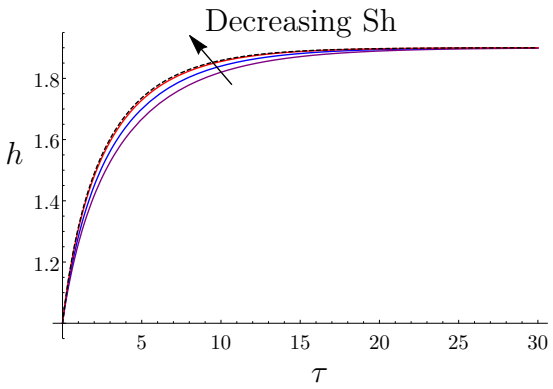

Figure 6.5: Graph showing how h varies with time for various values of Sh: Sh $= 1$ (purple), 0.5 (blue), 0.1 (red), asymptotic result from Section 6.3.3 (dashed). The other parameters are $\alpha_{w,eq} = 0.5, n = 0.1$.

We also investigate the behaviour of the water concentration in the film in the limiting case of small Sh using the asymptotic reductions in Section 6.3.3. When Sh $\ll 1$, we see in figure 6.6 that, as discussed in Section 6.3.3, the concentration is spatially uniform across the film for all time under the influence of the dominating diffusion process, and equilibrium at the interface is reached over a longer timescale.

Finally, we compare our numerical results against experimental data. We use the experiments with initial water concentration $w_0 = 3.6 \times 10^3\,\mathrm{mol\,m^{-3}}$ to determine the

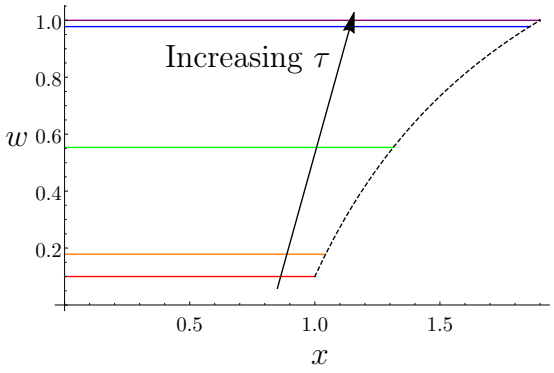

Figure 6.6: Graph showing how w varies with x for the small-Sh limit from Section 6.3.3 for various times: $\tau = 0$ (red), 0.1 (orange), 1 (green), 10 (blue), 30 (purple); the position of the gas–liquid interface is shown with a dashed line. The other parameters are $\alpha_{w,\mathrm{eq}} = 0.5$, $n = 0.1$.

Sherwood number, which we find by fitting the experimental values of the mass, $\hat{M}$, of water in the liquid layer against

$$\hat{M}(\hat{t}) = AM_w \int_0^{\hat{h}(\hat{t})} \hat{w}\,\mathrm{d}\hat{x} = h_0 w_{\mathrm{eq}} AM_w \int_0^{h(t)} w\,\mathrm{d}x, \tag{6.29}$$

where M_w is the molar mass of pure water (measured in $\mathrm{kg\,mol^{-1}}$), and w and h are taken from the numerical simulation. Using least squares, our fitting procedure gives that $\mathrm{Sh} = 0.1$, and we show the comparison between the dimensional data, the output of our model, and our small-Sh formula in figure 6.7(a). We then use the fitted value of Sh to make a prediction when $w_0 = 4.0 \times 10^4\,\mathrm{mol\,m^{-3}}$, and we show the results from the model, the small-Sh approximation, and the dimensional experimental data in figure 6.7(b). We see excellent agreement, which validates our model. We use the fitted value of the Sherwood number to determine the value of the parameter k_w, which we find to be $k_w = 8.8 \times 10^{-8}\,\mathrm{m\,s^{-1}}$ (at this value of the relative humidity). A similar order of magnitude was found for the equivalent coefficient for ternary systems of aluminium chlorohydrate, glycerol and water in Hennessy *et al.* (2017).

6.5 An Equivalent Formulation

We now show that the model presented in Section 6.3 is equivalent to the formulation we used for sulphur dioxide transport in Chapter 3. We model diffusion of water vapour, as in the experimental set-up in Section 6.2, in a tube of length $L \approx 5 \times 10^{-2}\,\mathrm{m}$ that has a layer of aqueous sulphuric acid of thickness $\hat{h}$ at the bottom with initial water concentration w_0 and initial thickness h_0. We assume there is a source of water

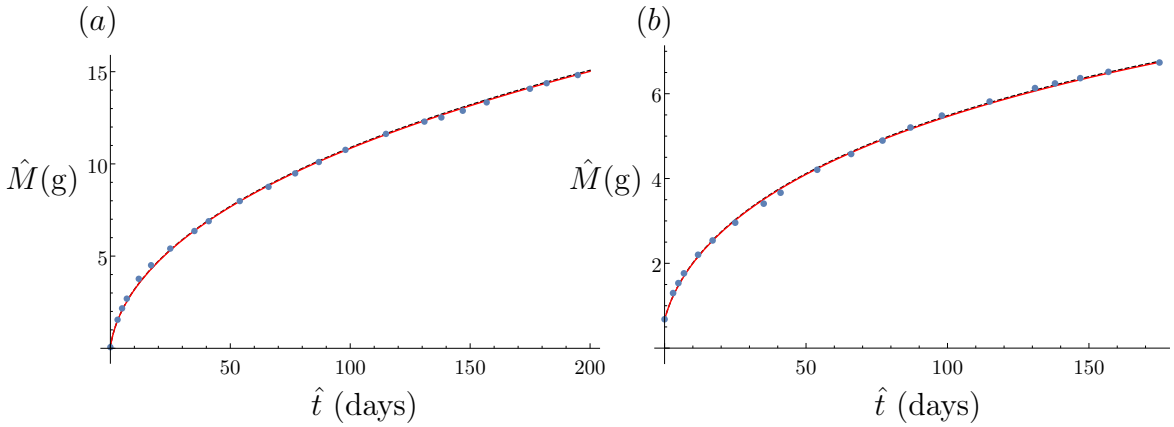

Figure 6.7: Graphs showing how $\hat{M}$, measured in g, varies with time, measured in days, from the numerical simulation (red), compared with the asymptotic result from Section 6.3.3 (dashed), and experimental data (blue dots) for (*a*) $w_0 = 3.6 \times 10^3\,\mathrm{mol\,m^{-3}}$ with $\alpha_{w,\mathrm{eq}} = 0.97, n = 0.74$, and (*b*) $w_0 = 4.0 \times 10^4\,\mathrm{mol\,m^{-3}}$ with $\alpha_{w,\mathrm{eq}} = 0.97, n = 0.067$. We fit the data to the model to find $\mathrm{Sh} = 0.1$.

vapour of concentration w_1 at the top of the tube. We note that specifying the water vapour concentration at the top of the tube is equivalent to prescribing the relative humidity. The governing equations are

$$\frac{\partial \hat{w}_g}{\partial \hat{t}} = D_{w_g} \frac{\partial^2 \hat{w}_g}{\partial \hat{x}^2}, \tag{6.30}$$

$$\frac{\partial \hat{w}_l}{\partial \hat{t}} = D_{w_l} \frac{\partial^2 \hat{w}_l}{\partial \hat{x}^2}, \tag{6.31}$$

$$\frac{\mathrm{d}\hat{h}}{\mathrm{d}\hat{t}} = V_{\mathrm{m},w} \hat{Q} = V_{\mathrm{m},w} \left(D_{w_g} \frac{\partial \hat{w}_g}{\partial \hat{x}} + \hat{w}_g \frac{\mathrm{d}\hat{h}}{\mathrm{d}\hat{t}} \right) \Bigg|_{\hat{x}=\hat{h}}, \tag{6.32}$$

where $\hat{w}_g$ and $\hat{w}_l$ are the concentrations of water in the gas and in the liquid, respectively, D_{w_g} and D_{w_l} are the diffusivities of water in the gas and in the liquid, respectively, $V_{\mathrm{m},w}$ is the molar volume of water, and $\hat{Q}$ is the flux of water vapour through the gas–liquid interface. Following the modelling approach in Chapter 3, these equations are subject to

$$\hat{w}_g = w_1 \qquad \text{at} \qquad \hat{x} = L, \tag{6.33}$$

$$D_{w_g} \frac{\partial \hat{w}_g}{\partial \hat{x}} + \hat{w}_g \frac{\mathrm{d}\hat{h}}{\mathrm{d}\hat{t}} = D_{w_l} \frac{\partial \hat{w}_l}{\partial \hat{x}} + \hat{w}_l \frac{\mathrm{d}\hat{h}}{\mathrm{d}\hat{t}} \qquad \text{at} \qquad \hat{x} = \hat{h}, \tag{6.34}$$

$$\hat{w}_g = \beta_w \hat{w}_l \qquad \text{at} \qquad \hat{x} = \hat{h}, \tag{6.35}$$

$$\frac{\partial \hat{w}_l}{\partial \hat{x}} = 0 \qquad \text{at} \qquad \hat{x} = 0, \tag{6.36}$$

$$\hat{w}_g = w_1 \qquad \text{at} \qquad \hat{t} = 0, \tag{6.37}$$

$$\hat{w}_l = w_0 \qquad \text{at} \qquad \hat{t} = 0, \tag{6.38}$$

$$\hat{h} = h_0 \qquad \text{at} \qquad \hat{t} = 0, \tag{6.39}$$

where β_w is Henry's Law constant, and h_0 is the initial thickness of the liquid layer. We do not know β_w *a priori*, but expect it to be small, since sulphuric acid has high affinity to water. We note that (6.34) has additional advective terms compared to (3.9) from Chapter 3, for example, due to the fact that there is a gas-to-liquid transition, and hence liquid condensation, at the gas–liquid interface.

We non-dimensionalise the system using

$$\begin{gathered} \hat{x} = h_0 x \, (0 < \hat{x} < \hat{h}), \quad \hat{x} = LX \, (\hat{h} < \hat{x} < L), \quad \hat{h} = h_0 h, \\ \hat{t} = (h_0^2/D_{w_l})t, \quad \hat{w}_g = w_1 w_g, \quad \hat{w}_l = (w_1/\beta_w) w_l, \end{gathered} \tag{6.40}$$

where we have non-dimensionalised space differently in the gas and in the liquid. The resulting equations are

$$\frac{\eta_w}{\epsilon^2} \frac{\partial w_g}{\partial t} = \frac{\partial^2 w_g}{\partial X^2}, \tag{6.41}$$

$$\frac{\partial w_l}{\partial t} = \frac{\partial^2 w_l}{\partial x^2}, \tag{6.42}$$

$$\frac{\mathrm{d}h}{\mathrm{d}t} = \frac{\alpha_{w,1}\epsilon}{\eta_w} \frac{\partial w_g}{\partial X} + \alpha_{w,1} w_g \frac{\mathrm{d}h}{\mathrm{d}t}, \tag{6.43}$$

subject to

$$w_g = 1 \qquad \text{at} \qquad X = 1, \tag{6.44}$$

$$\frac{\partial w_g}{\partial X} + \frac{\eta_w}{\epsilon} w_g \frac{\mathrm{d}h}{\mathrm{d}t} = \frac{\eta_w}{\beta_w \epsilon} \frac{\partial w_l}{\partial x} + \frac{\eta_w}{\beta_w \epsilon} w_l \frac{\mathrm{d}h}{\mathrm{d}t} \qquad \text{at} \qquad X = \epsilon h, x = h, \tag{6.45}$$

$$w_g = w_l \qquad \text{at} \qquad X = \epsilon h, x = h, \tag{6.46}$$

$$\frac{\partial w_l}{\partial x} = 0 \qquad \text{at} \qquad x = 0, \tag{6.47}$$

$$w_g = 1 \qquad \text{at} \qquad t = 0, \tag{6.48}$$

$$w_l = n \qquad \text{at} \qquad t = 0, \tag{6.49}$$

$$h = 1 \qquad \text{at} \qquad t = 0, \tag{6.50}$$

where we have introduced four dimensionless parameters

$$\alpha_{w,1} = w_1 V_{\mathrm{m},w} \approx 10^{-5}, \quad \epsilon = \frac{h_0}{L} \approx 0.4 \times 10^{-1}, \quad \eta_w = \frac{D_{w_l}}{D_{w_g}} \approx 10^{-4}, \quad n = \frac{\beta_w w_0}{w_1}, \tag{6.51}$$

where n is anticipated to be small, since the initial water concentration is small compared to the water vapour concentration in the tube (or, alternatively, the relative

humidity) used in the experiments. Since $\eta_w/\epsilon^2 \ll 1$, we obtain from (6.41), (6.44), and (6.46) that the leading-order approximation to w_g is

$$w_g = 1 - (1 - X)(1 - w_{l,i}), \tag{6.52}$$

where $w_{l,i} = w_{g,i}$ is the concentration of water at the interface. So, at the interface

$$\frac{\partial w_g}{\partial X} = 1 - w_{l,i}. \tag{6.53}$$

Thus, using (6.43) and noting that $\alpha_{w,1} \ll \alpha_{w,1}\epsilon/\eta_w$

$$\frac{\mathrm{d}h}{\mathrm{d}t} = \frac{\alpha_{w,1}\epsilon}{\eta_w}(1 - w_{l,i}). \tag{6.54}$$

This is equivalent to (6.13) from Section 6.3.2. The dimensional equilibrium concentration is thus $\hat{w}_l = w_{\mathrm{eq}} = w_1/\beta_w$. We, thus, see that $\alpha_{w,1}/\beta_w$ is equivalent to $\alpha_{w,\mathrm{eq}}$, $\beta_w\epsilon/\eta_w$ is equivalent to the Sherwood number, and, therefore, $\beta_w D_{w_g}/L$ is equivalent to the mass transfer coefficient k_w from Section 6.3.

We now also recover the small-Sherwood-number limit considered in Section 6.3.3. Since $\alpha_{w,1}\epsilon/\eta_w \ll 1$, we obtain from (6.43) that h is stationary. In order to understand its evolution, we rescale time as before, using the new version of the Sherwood number

$$t = \frac{\eta_w}{\beta_w\epsilon}\tau, \tag{6.55}$$

where $\tau = O(1)$. The governing equations become

$$\frac{\beta_w}{\epsilon}\frac{\partial w_g}{\partial \tau} = \frac{\partial^2 w_g}{\partial X^2}, \tag{6.56}$$

$$\frac{\beta_w\epsilon}{\eta_w}\frac{\partial w_l}{\partial \tau} = \frac{\partial^2 w_l}{\partial x^2}, \tag{6.57}$$

$$\frac{\mathrm{d}h}{\mathrm{d}\tau} = \frac{\alpha_{w,1}}{\beta_w}\frac{\partial w_g}{\partial X} + \alpha_{w,1} w_g \frac{\mathrm{d}h}{\mathrm{d}\tau}, \tag{6.58}$$

subject to

$$w_g = 1 \qquad \text{at} \qquad X = 1, \tag{6.59}$$

$$\frac{\partial w_g}{\partial X} + \beta_w w_g \frac{\mathrm{d}h}{\mathrm{d}\tau} = \frac{\eta_w}{\beta_w\epsilon}\frac{\partial w_l}{\partial x} + w_l\frac{\mathrm{d}h}{\mathrm{d}\tau} \qquad \text{at} \qquad X = \epsilon h, x = h, \tag{6.60}$$

$$w_g = w_l \qquad \text{at} \qquad X = \epsilon h, x = h, \tag{6.61}$$

$$\frac{\partial w_l}{\partial x} = 0 \qquad \text{at} \qquad x = 0, \tag{6.62}$$

$$w_g = 1 \qquad \text{at} \qquad \tau = 0, \tag{6.63}$$

$$w_l = n \qquad \text{at} \qquad \tau = 0, \tag{6.64}$$

$$h = 1 \qquad \text{at} \qquad \tau = 0. \tag{6.65}$$

Since we expect β_w to be very small, $\eta_w/\beta_w\epsilon$ is a large parameter. Thus, to leading order, using (6.57), (6.60), and (6.62) yields

$$w_l = w_l(\tau) \tag{6.66}$$

is a function of time only. We integrate (6.57) form $x = 0$ to $x = h$ and obtain, using Leibniz rule and (6.62),

$$\frac{\beta_w\epsilon}{\eta_w}\frac{\mathrm{d}}{\mathrm{d}\tau}\int_0^h w_l\,\mathrm{d}x - \frac{\beta_w\epsilon}{\eta_w}\frac{\mathrm{d}h}{\mathrm{d}\tau}w_{l,i} = \left.\frac{\partial w_l}{\partial x}\right|_{x=0}^{x=h} = \left.\frac{\partial w_l}{\partial x}\right|_{x=h}. \tag{6.67}$$

Multiplying (6.67) by $\eta_w/\beta_w\epsilon$, rearranging and applying (6.58) and (6.60), we find that

$$\frac{\mathrm{d}}{\mathrm{d}\tau}(hw_l) - w_l\frac{\mathrm{d}h}{\mathrm{d}\tau} = \frac{\eta_w}{\beta_w\epsilon}\left.\frac{\partial w_l}{\partial x}\right|_{x=h} = \frac{\partial w_g}{\partial X} + \beta_w w_g\frac{\mathrm{d}h}{\mathrm{d}\tau} - w_l\frac{\mathrm{d}h}{\mathrm{d}\tau} = \frac{\beta_w}{\alpha_{w,1}}\frac{\mathrm{d}h}{\mathrm{d}\tau} - w_l\frac{\mathrm{d}h}{\mathrm{d}\tau}, \tag{6.68}$$

i.e.,

$$\frac{\mathrm{d}}{\mathrm{d}\tau}(hw_l) = \frac{\beta_w}{\alpha_{w,1}}\frac{\mathrm{d}h}{\mathrm{d}\tau}. \tag{6.69}$$

Solving (6.69) and using (6.64) and (6.65), we obtain

$$w_l = \frac{h - 1 + \alpha_{w,\mathrm{eq}}n}{\alpha_{w,\mathrm{eq}}h}, \tag{6.70}$$

where $\alpha_{w,\mathrm{eq}} = \alpha_{w,1}/\beta_w$. This is an analogous equation to (6.25) from Section 6.3.3. Substituting (6.55) and (6.70) in (6.54), we obtain

$$\frac{\mathrm{d}h}{\mathrm{d}\tau} = \frac{(\alpha_{w,\mathrm{eq}} - 1)h + 1 - \alpha_{w,\mathrm{eq}}n}{h}, \tag{6.71}$$

subject to (6.65), which is the same equation as (6.26), from which we can obtain the solution (6.27). Thus, the mass transfer coefficient formulation and the full diffusion model are equivalent in the relevant limit.

6.6 Microscale Model of the GMCS Device with Hygroscopy

In this chapter, we have formulated a one-dimensional model describing the hygroscopy of a layer of sulphuric acid, which is an important mechanism for the accumulation of liquid within the filter sheets of the GMCS device. However, the

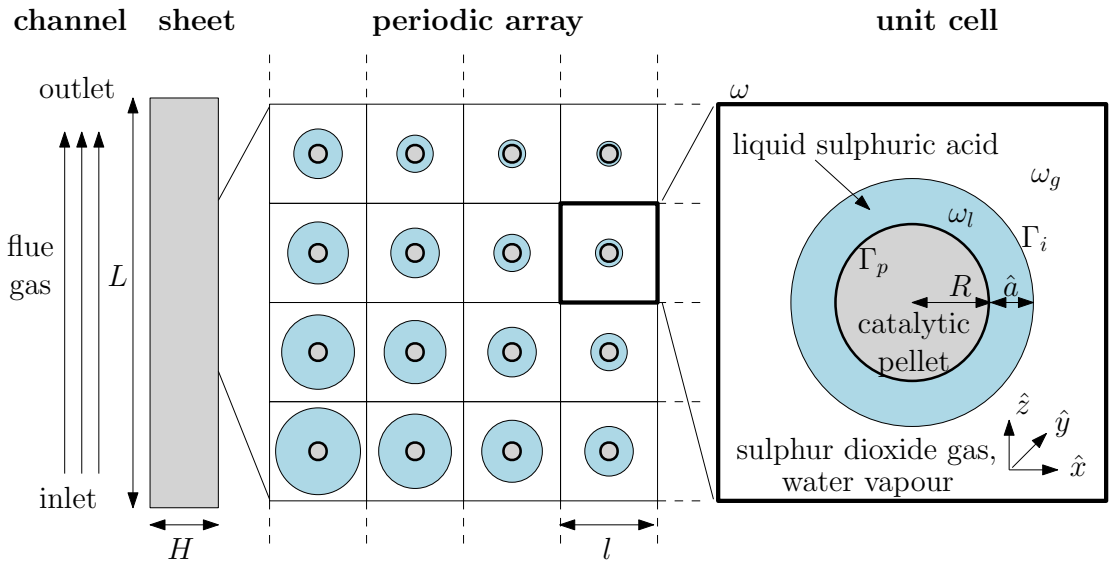

Figure 6.8: Schematic cross-sectional representation of the porous structure of the filter.

homogenised model we considered in Chapter 3 does not include hygroscopy. Thus, in this section, we extend our microscale model to include the effect of hygroscopy. We recall that water is also a reactant in (1.1), and so its concentration affects the chemical kinetics of the model.

We follow the approach that has already been developed in Chapter 3 for sulphur dioxide and incorporate an equivalent formulation for water. Throughout the derivation of the revised model, we omit some details and explanations, since the general principles have been covered previously. As well as sulphur dioxide, we now explicitly track the concentration of water in the gas and in the liquid sulphuric acid. Following the notation introduced in Chapter 3 and in figure 6.8, the governing equations for the concentration of sulphur dioxide and water in the gas and in the liquid are

$$\frac{\partial \hat{s}_g}{\partial \hat{t}} + \nabla \cdot (\hat{\boldsymbol{u}}_{\boldsymbol{g}} \hat{s}_g) = D_{s_g} \nabla^2 \hat{s}_g \qquad \text{in} \qquad \omega_g, \tag{6.72}$$

$$\frac{\partial \hat{s}_l}{\partial \hat{t}} + \nabla \cdot (\hat{\boldsymbol{u}}_{\boldsymbol{l}} \hat{s}_l) = D_{s_l} \nabla^2 \hat{s}_l \qquad \text{in} \qquad \omega_l, \tag{6.73}$$

$$\frac{\partial \hat{w}_g}{\partial \hat{t}} + \nabla \cdot (\hat{\boldsymbol{u}}_{\boldsymbol{g}} \hat{w}_g) = D_{w_g} \nabla^2 \hat{w}_g \qquad \text{in} \qquad \omega_g, \tag{6.74}$$

$$\frac{\partial \hat{w}_l}{\partial \hat{t}} + \nabla \cdot (\hat{\boldsymbol{u}}_{\boldsymbol{l}} \hat{w}_l) = D_{w_l} \nabla^2 \hat{w}_l \qquad \text{in} \qquad \omega_l. \tag{6.75}$$

We assume that the fluid in both phases is incompressible but, as before, will not write in full the equations satisfied by $\hat{\boldsymbol{u}}_{\boldsymbol{g}}$ and $\hat{\boldsymbol{u}}_{\boldsymbol{l}}$, since the advection terms in (6.72) – (6.75) will be negligible in the physical limit that we consider in which the liquid

layer around the catalytic pellet grows slowly. We use a mass-action rate law to determine the fluxes, $\hat{Q}_s$ and $\hat{Q}_w$, of sulphur dioxide and water, respectively, removed from the system at the surface of the pellets, which gives us that

$$\hat{Q}_s = \hat{Q}_w = \hat{Q} = 2k \left(\hat{s}_l|_{|\hat{\boldsymbol{x}}|=R}\right)^2 \left(\hat{w}_l|_{|\hat{\boldsymbol{x}}|=R}\right)^2, \tag{6.76}$$

We close the system using a global conservation law that links the growth of the liquid layer to the amount of liquid produced on the surface of the catalytic pellet and the amount of water absorbed at the gas–liquid interface. Since the density does not change much, for simplicity, we assume that the density of the liquid phase is constant, as in the previous sections. At the pellet surface, the velocity of the liquid is given by its production rate

$$\hat{\boldsymbol{u}}_{\boldsymbol{l}} \cdot \boldsymbol{n}_p = V_{\mathrm{m}} \hat{Q} = 2kV_m \hat{s}_l^2 \hat{w}_l^2, \tag{6.77}$$

where $\boldsymbol{n}_p$ denotes the outwards-pointing unit normal to the surface of the pellet, which is in the radial direction $\boldsymbol{e}_r$. Due to radial symmetry and incompressibility, and applying (6.77), we obtain

$$\hat{\boldsymbol{u}}_{\boldsymbol{l}} = \frac{2kR^2V_m \left(\hat{s}_l|_{|\hat{\boldsymbol{x}}|=R}\right)^2 \left(\hat{w}_l|_{|\hat{\boldsymbol{x}}|=R}\right)^2}{r^2} \boldsymbol{e}_r. \tag{6.78}$$

Furthermore, we do not expect any buoyancy-induced instabilities, since the denser sulphuric acid is produced on the surface of the pellets, while water is absorbed at the gas–liquid interface. Since we assume constant liquid density (and neglect the mass of the dissolved sulphur dioxide and volume changes due to mixing of sulphuric acid and water, as before), mass conservation can be written in terms of volume as

$$\begin{aligned} \frac{\mathrm{d}}{\mathrm{d}\hat{t}} \left(\frac{4\pi}{3} \left((R+\hat{a})^3 - R^3 \right) \right) &= \int_{\Gamma_p} V_{\mathrm{m}} \hat{Q} \, \mathrm{d}\hat{S} + \int_{\Gamma_i} V_{\mathrm{m},w} \hat{Q}_{w,i} \, \mathrm{d}\hat{S} \\ &= 4\pi R^2 V_{\mathrm{m}} \hat{Q} + 4\pi (R+\hat{a})^2 V_{\mathrm{m},w} \hat{Q}_{w,i}, \end{aligned} \tag{6.79}$$

where $\hat{Q}_{w,i}$ is the flux of water vapour through the gas–liquid interface, given by

$$\hat{Q}_{w,i} = D_{w_l} \frac{\partial \hat{w}_l}{\partial \hat{n}} - \left(\hat{\boldsymbol{u}}_{\boldsymbol{l}} \cdot \boldsymbol{n}_i - \frac{\mathrm{d}\hat{a}}{\mathrm{d}\hat{t}} \right) \hat{w}_l = D_{w_l} \frac{\partial \hat{w}_l}{\partial \hat{n}} - \left(\frac{2kR^2 V_{\mathrm{m}} \hat{s}_l^2 \hat{w}_l^2}{(R+\hat{a})^2} - \frac{\mathrm{d}\hat{a}}{\mathrm{d}\hat{t}} \right) \hat{w}_l, \tag{6.80}$$

where $\boldsymbol{n}_i$ is the outwards-pointing unit normal to the interface Γ_i, and we have used (6.78) noting that $\boldsymbol{n}_i = \boldsymbol{e}_r$. We rewrite (6.79) and rearrange as

$$\frac{\mathrm{d}\hat{a}}{\mathrm{d}\hat{t}} = \frac{2kV_{\mathrm{m}} \left(\hat{s}_l|_{|\hat{\boldsymbol{x}}|=R}\right)^2 \left(\hat{w}_l|_{|\hat{\boldsymbol{x}}|=R}\right)^2}{(1+\hat{a}/R)^2} + \frac{D_{w_l} V_{\mathrm{m},w}}{(1 - V_{\mathrm{m},w} \hat{w}_l|_{|\hat{\boldsymbol{x}}|=R+\hat{a}})} \left. \frac{\partial \hat{w}_l}{\partial \hat{n}} \right|_{|\hat{\boldsymbol{x}}|=R+\hat{a}}. \tag{6.81}$$

At the surface of the pellet, we balance the flux of sulphur dioxide and water into the pellet with the amount being consumed by the reaction, i.e.,

$$(D_{s_l}\nabla\hat{s}_l - \hat{\boldsymbol{u}}_{\boldsymbol{l}}\hat{s}_l)\cdot\boldsymbol{n}_p = 2k\hat{s}_l^2\hat{w}_l^2, \tag{6.82}$$

$$(D_{w_l}\nabla\hat{w}_l - \hat{\boldsymbol{u}}_{\boldsymbol{l}}\hat{w}_l)\cdot\boldsymbol{n}_p = 2k\hat{s}_l^2\hat{w}_l^2, \tag{6.83}$$

which we can rewrite, using (6.77), to be

$$D_{s_l}\nabla\hat{s}_l\cdot\boldsymbol{n}_p = 2k(1+V_{\mathrm{m}}\hat{s}_l)\hat{s}_l^2\hat{w}_l^2, \tag{6.84}$$

$$D_{w_l}\nabla\hat{w}_l\cdot\boldsymbol{n}_p = 2k(1+V_{\mathrm{m}}\hat{w}_l)\hat{s}_l^2\hat{w}_l^2. \tag{6.85}$$

At the gas–liquid interface, we impose continuity of flux of sulphur dioxide and water, and we assume local thermodynamic equilibrium (which leads to Henry's law) and, thus, we write

$$D_{s_g}\nabla\hat{s}_g\cdot\boldsymbol{n}_i - \left(\hat{\boldsymbol{u}}_{\boldsymbol{g}}\cdot\boldsymbol{n}_i - \frac{\mathrm{d}\hat{a}}{\mathrm{d}\hat{t}}\right)\hat{s}_g = D_{s_l}\nabla\hat{s}_l\cdot\boldsymbol{n}_i - \left(\hat{\boldsymbol{u}}_{\boldsymbol{l}}\cdot\boldsymbol{n}_i - \frac{\mathrm{d}\hat{a}}{\mathrm{d}\hat{t}}\right)\hat{s}_l, \tag{6.86}$$

$$D_{w_g}\nabla\hat{w}_g\cdot\boldsymbol{n}_i - \left(\hat{\boldsymbol{u}}_{\boldsymbol{g}}\cdot\boldsymbol{n}_i - \frac{\mathrm{d}\hat{a}}{\mathrm{d}\hat{t}}\right)\hat{w}_g = D_{w_l}\nabla\hat{w}_l\cdot\boldsymbol{n}_i - \left(\hat{\boldsymbol{u}}_{\boldsymbol{l}}\cdot\boldsymbol{n}_i - \frac{\mathrm{d}\hat{a}}{\mathrm{d}\hat{t}}\right)\hat{w}_l, \tag{6.87}$$

$$\hat{s}_g = \beta_s\hat{s}_l, \tag{6.88}$$

$$\hat{w}_g = \beta_w\hat{w}_l, \tag{6.89}$$

where

$$\boldsymbol{n}_i = \frac{\nabla\left(|\hat{\boldsymbol{x}}| - R - \hat{a}\right)}{|\nabla\left(|\hat{\boldsymbol{x}}| - R - \hat{a}\right)|} \tag{6.90}$$

denotes the outwards-pointing unit normal to the liquid layer. We note that the Henry's law constant β_w can be calculated knowing the concentration of water in the gaseous and aqueous phase at thermodynamic equilibrium. For a relative humidity of 99%, we can calculate that $\beta_w \approx 2\times10^{-5}$ (Wilson, 1921). From table 1.1, we thus see that $\beta_w \ll \beta_s$, which reflects the high affinity of sulphuric acid to water (i.e., its hygroscopy). We also note that, this time, unlike in Chapter 3, the terms in brackets in (6.86) and (6.87) are not zero, since water is condensing at the moving interface.

To close the microscale model as before, we prescribe periodicity of $\hat{s}_g$ and $\hat{w}_g$ along the boundary of each cell of the periodic microstructure and also assume

$$\hat{s}_g = S_0, \quad \hat{w}_g = W_0, \quad \text{and} \quad \hat{a} = 0 \qquad \text{at} \qquad \hat{t} = 0, \tag{6.91}$$

where S_0 and W_0 are the concentrations of sulphur dioxide and water in the incoming flue gas.

Equations (6.72)–(6.75) and (6.81), subject to (6.84)–(6.91) are a closed model describing the evolution of a layer surrounding a pellet, and form the building blocks for future homogenisation.

6.7 Conclusions

In this chapter, we derived a one-dimensional model to describe the tendency of sulphuric acid to absorb water from its environment, motivated by a set of experiments performed at W. L. Gore and Associates, Inc. We considered a uniform liquid film of aqueous sulphuric acid residing on an impermeable substrate which absorbs water through its surface from a constant-relative-humidity environment above. We assumed that the rate of absorption of water vapour is proportional to the difference between the water concentration at the surface and the equilibrium concentration. We identified three dimensionless numbers. Two of these correspond to properties that are easily measured experimentally, and involve the initial and equilibrium water concentrations. The third, the Sherwood number, is the ratio between the diffusive and the absorptive timescales, which cannot be extracted from a direct experimental measurement without using a model. We used the model to make a simple prediction about the final thickness of the liquid layer. In the small-Sherwood-number regime, we found that diffusion dominates over absorption, and the concentration of water is spatially uniform across the liquid layer. We obtained an explicit solution for the film thickness and concentration in this regime. We solved the full system of equations numerically, explored the behaviour of the system as the parameters vary, and observed an excellent agreement with our asymptotic prediction in the appropriate limit.

We compared our results to experimental data from two experiments, namely, high and medium initial concentration of sulphuric acid at close to 100% relative humidity. The mathematical model gave excellent agreement in both cases for a fit to a single mass transfer coefficient, $k_w = 8.8 \times 10^{-8}\,\mathrm{m\,s^{-1}}$, validating the model and determining the previously unknown value of k_w. The model can now be used, with this value of k_w, with confidence in other settings.

The diffusivity of water in sulphuric acid in our experiment varies between 1.2×10^{-9} and 2.0×10^{-9} $\mathrm{m^2 s^{-1}}$, according to Leaist (1984); Umino & Newman (1993). If we use these values of D_{w_l} along with the fitted value for Sh, our range of estimates for k_w is $6.6 \times 10^{-8} - 11 \times 10^{-8}$ $\mathrm{ms^{-1}}$. The associated Sherwood number was small, and the data was also well fitted using the small-Sherwood-number results. This suggests that our simple analytical solution (6.27) can be used to predict the amount of absorbed water without having to solve any differential equations numerically. Further, we showed that the mass transfer formulation is equivalent to the formulation used in Chapter 3, where we applied Henry's law at the gas–liquid interface, and found that

the equivalent parameter to the mass transfer coefficient k_w is $\beta_w D_{w_g}/L$. We also formulated a microscale model for the GMCS device in analogy to Chapter 3, which incorporates the effect of hygroscopy and serves as an essential ingredient in obtaining a homogenised model for a system of macroscale equations that track both sulphur dioxide and water concentration within the device. To test the model predictions further it would be useful to perform more experiments with different values of the relative humidity, but we acknowledge that these are difficult to carry out.

Our simple model can be readily used for other systems where water or indeed other substances are absorbed from the environment before diffusing through a liquid film. Examples include alcohols, such as ethanol, methanol, glycerol, and also sodium hydroxide, paints, and coatings.

Our experimental results showed that there was a notable increase in the thickness of the sulphuric acid layer by the end of our six-month-long experiments, confirming the presence of volume change by this mechanism and that hygroscopy will play a key role in sulphuric acid layer growth in industrial settings where the relative humidity is high.

Chapter 7

Conclusions

7.1 Summary

In this thesis, we considered the problem of removal of sulphur dioxide using filters made from a catalytic porous medium. These filters, called Gore Mercury Control System (GMCS) devices and designed by W. L. Gore and Associates, Inc., consist of multiple filter sheets that are folded into a series of open channels. The flue gas, which contains sulphur dioxide and a plentiful supply of oxygen and water vapour, flows through the channels and diffuses into the porous sheets, where sulphur dioxide reacts with oxygen and water on the surface of microscopic catalytic pellets to produce liquid sulphuric acid. The pellets are embedded in a network of fibres, which constitute the internal structure of the porous filter sheets. This method of removal of sulphur dioxide is beneficial in many ways, including a flexible installation process, a lower total cost of ownership, and production of sulphuric acid, without generating waste, which can be used for commercial purposes. However, over time, the liquid sulphuric acid produced accumulates within the filter and reduces its efficiency. In Chapters 2–6, we developed a suite of detailed mathematical models for various aspects of this problem, incorporating elements from the relevant physics and chemistry, yet retaining generality wherever possible.

Inspired by this problem, we began by studying a paradigm problem in fundamental fluid dynamics in Chapter 2. We considered the problem of spreading of a viscous film under surface tension and injection of liquid through part of the substrate. This was designed to mimic the production and spreading of sulphuric acid at the surface of the catalytic pellets and along the fibres, where we represented the pellets as flat regions of liquid injection. In the subsequent analysis, we assumed the existence of a precursor layer to resolve the stress singularity at the contact line. In particular,

this assumption is valid for hydrophilic substrates. We performed asymptotic analysis for early and late time for constant injection and found that the film thickness grew linearly for early time, while the contact line did not move. For late time, we obtained a power-law relationship, where the maximum film thickness scaled like $t^{3/7}$, while the position of the contact line scaled like $t^{4/7}$ for time t. We also discussed the full late-time behaviour of the film spreading in the context of classical results, such as the Cox–Voinov law. We then considered three generalisations in terms of the rate of liquid injection: power-law, point-source, and thickness-inhibited injection rate. For the power-law injection, we considered rates of the form t^c for $-1 < c < 1$. We found that, for late time, the film thickness grew when $c > -3/4$, tended to constant when $c = -3/4$, and decreased for $c < -3/4$. We used this to formulate an inverse problem of finding the exact exponent of the injection rate given the observed position of the apparent contact line. For the point-source injection, we established that the late-time behaviour is the same as for constant injection. Finally, for the thickness-inhibited injection, we considered rates of the form $1/h^q$ for $q > 0$. We found that, unlike the power-law injection, there was unbounded growth of the film in this case, and that, as q increased, there was slowing down of the film growth and front spreading.

In the second part of the chapter, we also considered a coupled model for the film growth and the diffusion of sulphur dioxide through the gas and the liquid, which dictates the rate of liquid injection through the reaction kinetics. We identified a key dimensionless number, namely, the ratio of the reaction rate to the diffusive rate, and found that increasing this parameter promotes film growth and removal of more sulphur dioxide. Furthermore, in the case of infinite reaction rate, there is not a complete removal of sulphur dioxide, and the concentration only reaches zero at the centre of the injection region. In addition, we found that the injection rate in this limit is inversely proportional to the film thickness, as in the thickness-inhibited injection, considered in the first part of the chapter, and linearly proportional to the sulphur dioxide concentration. However, when the reaction was slower than diffusion, the injection rate was proportional to the square of the sulphur dioxide concentration. We also explored the effect of non-constant oxygen concentration on the behaviour of the system in Appendix C.

We moved on to develop a microscale model of the filter that can then be upscaled, using the theory of homogenisation, to a device-scale model. As in the classic homogenisation approach, we assumed that a filter sheet could be represented as a periodic array of cubic unit cells with a catalytic pellet in the middle of each one

of them. We derived the governing equations for sulphur dioxide transport in the gas and in the liquid phase in a single cell and used Henry's law, which follows from conservation of chemical potential, to relate the concentration of sulphur dioxide on either side of the gas–liquid interface. We assumed a particular mass-action rate law using the stoichiometry of the reaction and obtained the corresponding equations for sulphur dioxide transport and growth of the liquid layer of sulphuric acid. We then systematically upscaled the governing equations to derive a set of macroscale equations that captured the effect of the complicated microstructure via the presence of an effective "sink" term and an effective diffusivity in the equation of sulphur dioxide concentration. We also considered two distinguished limits based on the order of magnitude of two dimensionless numbers, κ_s and σ_s, which measure the ratio of reaction rate to diffusive rate, and the relative mass transfer of sulphur dioxide on either side of the gas–liquid interface, respectively. For the first limit, we assumed that $\kappa_s = O(1)$ and σ_s is sufficiently small, i.e., the reaction proceeded at a moderate rate, but there was little mass transfer of sulphur dioxide from the gas phase to the liquid phase. In this limit, the sink term in the equation for sulphur dioxide concentration was a complicated non-linear function of the sulphur dioxide concentration and the thickness of the liquid layer of sulphuric acid. For the second limit, we assumed that $\sigma_s = O(1)$, while κ_s was sufficiently small, i.e., there was a moderate mass transfer of sulphur dioxide across the gas–liquid interface, but the reaction was very slow. In this limit, the sink term simplified significantly, but retained non-linearity. However, the effective diffusivity was more difficult to calculate, since the moderate mass transfer resulted in the cell problem depending on two cell functions, one in the gas and one in the liquid domain. Based on realistic parameter values, we then identified a physically relevant limit where both the reaction rate and the mass transfer were small. In each of these limits, we established a quasi-static evolution of the sulphur dioxide concentration. Finally, we used a spherically symmetric version of the microscale model for a single pellet to fit the results to existing observations on the rate of liquid transport within the filter and be able to infer the magnitude of the unknown reaction rate. We solved the model numerically and found the value of the reaction rate constant, which we used throughout the thesis. We also analysed the relationship between the reaction rate and the time taken for the liquid sulphuric acid to be expelled on the surface of the filter sheets, and found that there is a minimum non-zero such time indicating that the process is limited by diffusion transport whenever the reaction rate is infinite.

In Chapter 4, we coupled the macroscale equations for gas and liquid transport within a filter sheet with an advection–diffusion equation for the sulphur dioxide concentration in an open channel, where the flue gas originates. Based on the filter geometry, we assumed that the aspect ratio of the filter sheet is small, i.e., its thickness is much smaller than its length and width. This introduced a small parameter, the aspect ratio, which we exploited to make asymptotic predictions in two separate limits, based on the values of two dimensionless parameters. The first parameter measures the change in volume in the gas-to-liquid transition in the chemical reaction and is a measure of the amount of sulphur dioxide in the flue gas. The second parameter is the aspect ratio of the filter channel. In the first limit, we assumed that there was little sulphur dioxide in the system and that the channel was longer than its width. As a result, we obtained a simplified quasi-static equation for the sulphur dioxide concentration both in the filter sheet and in the channel. In the second limit, we assumed that there was a moderate amount of sulphur dioxide in the system and that the channel was much longer than its width. In this case, we were able to obtain an explicit solution for the concentration of sulphur dioxide and the void fraction in the filter sheet. The solutions were monotonically decreasing and increasing, respectively, with the depth of the sheet. The explicit solutions allowed us to estimate the critical time when the first coalescence between neighbouring liquid layers occurs. We saw that increasing the inter-pellet distance in the porous sheet increased this critical time, and, thus, increased the time for device operation. We then solved the full macroscale model numerically and found very good agreement with the asymptotic solutions, which suggested that we could use the simplified equations whenever the device was operating in the corresponding regime. We obtained numerical solutions to an extended model, valid beyond the point of first liquid-layer coalescence, and observed that the operating time of the filter significantly increased, while its removal capacity decreased until the whole device stopped working. In addition, we found that the device did not clog uniformly across the filter sheet. We also explored the effect of varying the dimensionless parameters in the governing equations and found that, given a target sulphur dioxide concentration at the outlet of the filter channel, or a percentage of sulphur dioxide to be removed, our model could be used to find the maximum speed of the gas that would achieve this. All this modelling was performed in the case of rectangular channels made of parallel sheets. To explore the effect of having closed channels, which is the original design of the GMCS device, since it maximises surface area, we also considered a radially symmetric model for cylindrical channels. We found that the qualitative behaviour of the solutions was the same

as for the rectangular channels, but the outlet concentration of sulphur dioxide was lower due to the larger surface area.

We then considered the problem of two neighbouring catalytic pellets, the first of which was completely submerged in liquid sulphuric acid, while the second was not. We introduced a source of sulphur dioxide on the side of the first pellet to recreate the asymmetry present in the real GMCS device, where sulphur dioxide emerges from the filter channels. The goal of this model was to understand how the amount of liquid produced around the second pellet depends on the amount of liquid produced around the first pellet, and how the two gas–liquid interfaces move relative to each other. This problem was motivated by the question of what would happen with the long-term operation of the device once a continuous layer of liquid sulphuric acid formed near the surface of the filter sheets, given that diffusion of sulphur dioxide in the liquid was much slower than in the gas. We found that, using realistic parameter values for the GMCS device, much more liquid was produced around the first pellet, and thus the first gas–liquid interface moved faster than the interface around the second pellet. This suggested that the time when the filter sheets would be completely filled with liquid was dictated by the rate of propagation of the continuous layer of liquid near the surface of the sheets, and since the diffusion in this layer was much slower than in the gas, we expect that the efficiency of the device would drop once such a continuous layer formed. We also investigated the effect of varying the reaction rate and found that, as the reaction rate decreased, the amount of liquid produced around each pellet approached a common value, and the time until coalescence of the two interfaces increased.

One feature of this model is that we ignored the presence of the fibres between the pellets, assuming that they were hydrophobic, and, thus, the liquid would tend to accumulate around the pellets. The GMCS device is indeed manufactured with hydrophobic fibres, but there exist techniques of coating these fibres with hydrophilic material. Therefore, in Chapter 5, we considered a simplified one-dimensional model of a filter sheet made of hydrophilic fibres to explore their effect on the liquid transport. We modelled the liquid flow using a version of Richards equation with a source term due to the chemical reaction. We identified a dimensionless parameter that measured the ratio of the chosen timescale over which the liquid grew and the natural timescale associated with the wetting of the sheet. This parameter was large, indicating that the filter sheet would wet long before any appreciable liquid growth would be observed. This suggested that, over the chosen timescale, the saturation within the filter sheet was spatially uniform and increased until the whole sheet was

filled with liquid. We obtained an asymptotic prediction for the saturation and the sulphur dioxide concentration as well, which showed an excellent agreement with the full numerical solution. This behaviour is in stark difference with the case from the previous chapter, where the region of the filter sheet nearest to the filter channel saturates with liquid sulphuric acid first. This means that, in the case of hydrophilic fibres, choosing a thicker sheet would be more beneficial as it would increase the time until full clogging.

Finally, we derived a one-dimensional mathematical model for the hygroscopy of sulphuric acid. This is relevant to the operation of the GMCS device, since sulphuric acid is hygroscopic, and water absorption provides another mechanism of liquid growth within the filter sheets. We considered a uniform liquid layer of aqueous sulphuric acid, which resided on an impermeable substrate. We assumed that the rate of water absorption at the gas–liquid interface was proportional to the difference between the water concentration at the interface and the equilibrium concentration at which there was no more absorption. We derived the governing equations and identified one of the key dimensionless parameters to be the Sherwood number, which measures the ratio between absorption rate and diffusive rate and can only be estimated by an experiment. We then solved the model numerically and compared our results with experimental data from two experiments performed by W. L. Gore and Associates, Inc., which motivated our model. The first one was for a high initial concentration of sulphuric acid, while the second was for a medium concentration, where both experiments were performed at a relative humidity close to 100%. The model gave an excellent agreement in both cases for a fit to a single mass transfer coefficient (or, equally, the Sherwood number in dimensionless terms). We also noticed that the Sherwood number was small for the experiments of interest, which inspired us to perform small-Sherwood-number asymptotic analysis. We obtained an explicit solution for the film thickness and water concentration, and a simple formula for the final value of the thickness, replacing the need to solve any differential equations. Since a small Sherwood number indicates diffusion dominating over absorption, we observed a spatially uniform concentration profiles across the liquid layer. In all comparisons, we obtained excellent agreement between the numerical solutions and the asymptotic predictions. At the end of the chapter, we also showed that the mass transfer formulation is equivalent to the formulation used in the previous sections, where Henry's law was used at the gas–liquid interface, and formulated a microscale model, analogous to the model from Chapter 3, which tracks the water concentration within the device and incorporates hygroscopy of sulphuric acid.

7.2 Practical Results

Our models provide the basis for exploration of the performance of reactive filters and for optimisation in order to minimise the amount of sulphur dioxide released by the device into the atmosphere, while ensuring longevity. One of the most important model outputs is the concentration of sulphur dioxide at the outlet of the filter, since this is often regulated by a given concentration threshold before being deemed safe to release into the atmosphere. We derived a simplified model that captures a physically relevant operating regime for a sulphur dioxide flue gas filter, and is significantly easier to solve than the full model. The model set-up was appropriate for a filter made from hydrophobic material. Using our results, we found that the outlet concentration of sulphur dioxide reduces to about 20% or less of the inlet concentration, depending on the amount of sulphur dioxide in the flue gas. We also explored the effect of changing various system parameters on the outlet sulphur dioxide concentration. Specifically, our results can be used to estimate the maximum speed the flue gas can be flowed at, or the maximum width of the filter channels, that ensure the outlet concentration does not exceed the given threshold. For a maximum outlet concentration of 20% of the inlet concentration in a 1-metre long filter, for example, we found that the maximum speed of the gas was $0.1\,\mathrm{m\,s^{-1}}$. Similar analysis applies to another quantity of interest, namely, the percentage of unfiltered sulphur dioxide, which is useful when there is a requirement for a minimum fraction of the incoming sulphur dioxide to be filtered.

Another important criterion for the device performance is its lifetime. We found that the time until the first clogging in the filter, which occurs when two liquid layers growing around neighbouring pellets coalesce, is linearly proportional to the ratio of the timescale associated with liquid growth to the diffusive timescale in the gas across the filter. This was further supported by the explicit solution to a reduced model we considered. Our reduced model gave an estimated clogging time of around 100 days in the case of low sulphur dioxide concentration, which provides the correct order of magnitude in the case of the real filter, as observed by W. L. Gore and Associates, Inc. Furthermore, we presented an extended model that described the filter operation until it ceased working altogether. This revealed a significant increase in the lifetime of the filter and suggested that the filter did not clog uniformly everywhere in the filter sheets. Based on an explicit solution to one of our reduced models, we also established a weak dependence of the clogging time of the filter on the number of pellets per unit length within the filter. In all this analysis, we used an estimate for

the reaction rate constant, which we inferred from a simple model for liquid growth around a single pellet.

Unlike the aforementioned results that apply to hydrophobic material, the model we considered to describe filters made from hydrophilic material suggested that the liquid sulphuric acid would spread uniformly across the filter sheets. This means that it will take longer for hydrophilic filters with thicker sheets to be filled with liquid.

Finally, we also developed a model for the hygroscopy of sulphuric acid, which plays a crucial role in dictating the clogging rate. We estimated the mass transfer coefficient associated with water absorption from sulphuric acid and found that, even in the case of diluted acid, the initial layer of sulphuric acid can increase its volume seven times. Our theory was validated by experiments performed by W. L. Gore and Associates, Inc. This means that hygroscopy is an important effect, and, due to the additional water absorption, it will reduce the clogging time of the filter.

7.3 Future Work

There are various extensions to this work that we believe would be interesting. One would be to replace the flat substrate in Chapter 2 with a cylinder and the injection cite with a sphere to better represent the pellet–fibre configuration (see figure 7.1). This has the potential of introducing the well-known Rayleigh–Plateau instability, and a key question would be how the two principal curvatures affect the flow. Also of interest would be to study multiple fluid injection sites and the interaction between the resulting flows.

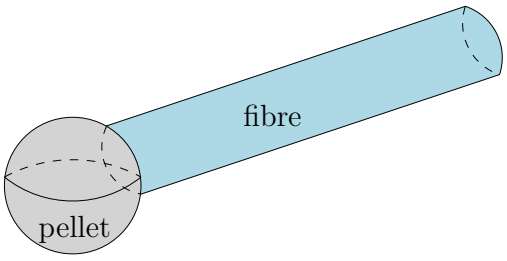

Figure 7.1: Schematic of a cylindrical fibre and a spherical pellet.

In addition, we want to incorporate the effect of the fibre network in the porous sheets, since these fibres can be manufactured to be either hydrophilic or hydrophobic, which may enhance or inhibit the liquid transport within the filter. A possible modelling approach would be to incorporate the capillary model from Chapter 2 into a more complex, possibly hexagonal, unit cell (see figure 7.2) with a catalytic pellet

in the middle and fibres attached to it, which can then be used in a homogenisation procedure to obtain an upscale model for the whole device.

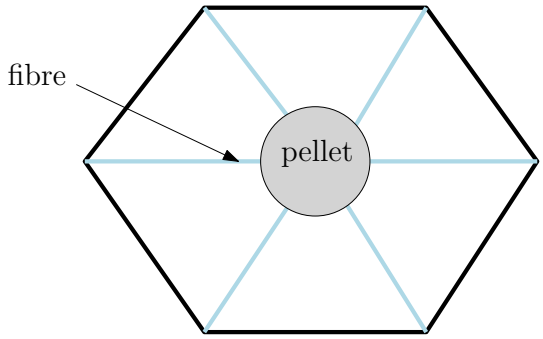

Figure 7.2: Schematic of a hexagonal unit cell with a pellet and fibres attached to it.

Our model in Chapter 4 captures the initial stage of operation of the filter device before neighbouring liquid layers in the filter sheets coalesce, and a continuous layer of liquid forms along the channels walls. As hypothesised in Section 4.8, after this point the efficiency of the filter will drop significantly, since the rate of diffusion of sulphur dioxide in liquid is much lower than in gas. A possible mechanism that may account for the long lifetime of the filters is the continuous flow of liquid out of the filter sheets and the eventual drainage along their surface. This will prevent the full clogging of the region near the filter sheets and will provide the necessary gas pathways for the sulphur dioxide to diffuse through and keep the filter running. Our model could be extended to include gravity-driven drainage of liquid along the surface of the filters. Another key extension would be to develop a model that accounts for the change in the diffusive pathway in the liquid and involves a moving front of liquid inside the filter sheets (see figure 7.3). Coupled with the effect of a fibrous network of varying wettability properties, such a model would be useful in accurately tracking the gas and liquid pathways of sulphur dioxide in the filter. Ultimately, we would like to compare the results of such a long-term model with future experimental data from W. L. Gore and Associates, Inc.

With regards to Chapter 5, a more realistic two- or three-dimensional model incorporating flow in the channels will provide more insight into the advantages or disadvantages of having a filter made of hydrophilic fibres. Our preliminary results suggested that over the timescale of liquid growth, the liquid saturation within the filter sheets will be spatially uniform. This indicated that thicker sheets would seem more useful, since this would increase the time until clogging. A higher-dimensional model will introduce a more complicated flow in directions other than across the sheets

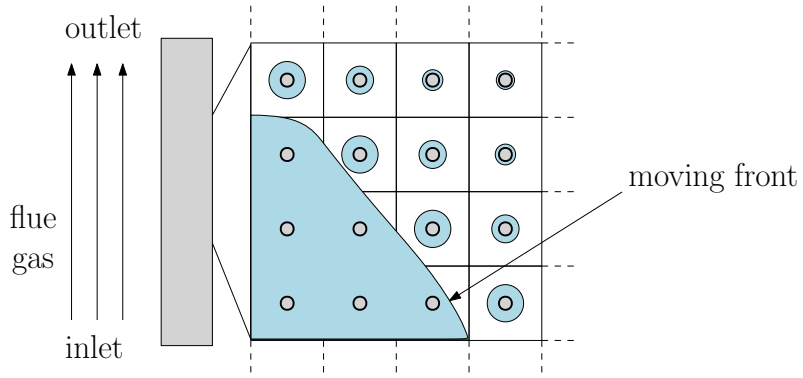

Figure 7.3: Schematic of a moving liquid-acid front in a porous filter sheet.

only, which could further increase the operating time of the filter. More importantly, we could use such a model to explore a hybrid filter made of both hydrophobic and hydrophilic regions, which could provide an optimal liquid drainage in the filter sheets. This could be achieved by directing the flow in a way that creates gas pathways through the sheets that last as long as possible and allow for an easy access for the diffusion of sulphur dioxide.

An immediate extension to our work in Chapter 6 is to homogenise the model in Section 6.6 to evaluate the effect of hygroscopy on the device performance. We expect that the solution to this model will reveal earlier clogging than in Chapter 4, due to water absorption by the sulphuric acid. A simplifying assumption we made throughout this chapter and the thesis was that the sulphur dioxide and water diffusivities were constant. In practice the diffusivity can vary with the corresponding concentration. However, in the case of water, we found that concentration-dependent variations in diffusivity played no role in the small-Sherwood-number limit of interest, since here the behaviour was limited by mass transfer. In Appendix D, our preliminary study showed that a concentration-dependent diffusivity also had little effect on the system behaviour for larger Sherwood numbers. However, a more comprehensive study of these effects would be worthwhile. Further, since the catalytic reaction and absorption of water are exothermic reactions, we are also interested in relaxing our isothermal assumptions and incorporating heat transfer into our model. In particular, in both these cases, small changes may become important if lateral temperature or concentration gradients are established at the gas–liquid interface, since these can generate significant Marangoni flows. In such cases, our one-dimensional approximation in Chapter 6 would break down and we would need to consider the two-dimensional analogue and incorporate the fluid flow.

In this thesis, we created a suite of novel mathematical models that described removal of sulphur dioxide using porous catalytic filters, and the results we obtained provide significant theoretical and practical insight into the way the industrial process is carried out. Our results were not only limited to industrial applications, but had impact in fundamental research in fluid dynamics and industrial chemistry. One of the purposes of our modelling is to provide a rigorous mathematical framework that retains generality in applications and can be used to analyse and simplify a seemingly complex real-world problem without the need for expensive and time-consuming experiments and computations. We anticipate that our models will be of wide applicability to other industrial processes and catalytic systems, such as carbon capture and storage, purification in fuel cells, and removal of nitric oxides, where similar reaction types take place, and our methodology can be applied successfully.

Appendix A

Determining Henry's Law Constants from Experimental Data

Henry's law can be used to relate the concentration of a chemical species on either side of an interface in the case when the interface is in thermodynamic equilibrium. The constant of proportionality in Henry's law is defined differently in different research papers. In Sander (2015), for example, four different ways of expressing Henry's law are given. Here, we present these ways, and give a simple method for converting between them, and thus show how the values in table 1.1 can be obtained from values found in the literature.

The main expression of Henry's law that we use in this thesis presents Henry's law constants as dimensionless constants of proportionality between the concentrations of a chemical in liquid (c_l) and in gas (c_g). To be consistent with Sander (2015) and for the purposes of comparing the various definitions, we will denote this constant by H^{cc} (where we use double-letter indices to indicate the variable we measure on either side of the gas–liquid interface; here, c stands for concentration). Thus,

$$H^{cc} = \frac{c_l}{c_g}. \tag{A.1}$$

In this thesis, we use $\beta_s = 1/H_s^{cc}$, where s stands for sulphur dioxide, and similarly for oxygen and water. A second definition connects concentration in the liquid to partial pressure in the gas (p). This Henry's law constant is denoted by H^{cp}. So, we have

$$H^{cp} = \frac{c_l}{p}. \tag{A.2}$$

The relationship between these two definitions for an ideal gas is given by the ideal gas law and reads

$$H^{cp} = \frac{H^{cc}}{RT}, \tag{A.3}$$

where R is the universal gas constant, and T is the absolute temperature. The third definition is in terms of molar mixing ratio (x) in the liquid and partial pressure in the gas. Here, we have

$$H^{xp} = \frac{x}{p}. \tag{A.4}$$

The general relationship between H^{xp} and H^{cp} is complex but for a dilute aqueous solution it can be written as

$$H^{xp} = \frac{M_{\text{sol}} H^{cp}}{\rho_{\text{sol}}} = \frac{M_{\text{sol}} H^{cc}}{\rho_{\text{sol}} RT}, \tag{A.5}$$

where M_{sol} is the molar mass of the solution, and ρ_{sol} is the density of the solution (Sander, 2015). Finally, the fourth definition relates the molality, b, of the chemical in the liquid solution to the partial pressure in the gas.

$$H^{bp} = \frac{b}{p}. \tag{A.6}$$

Again to establish the relationship between this definition and the others, we assume a dilute solution, and we have (Sander, 2015)

$$H^{bp} = \frac{H^{cp}}{\rho_{\text{sol}}} = \frac{H^{cc}}{\rho_{\text{sol}} RT}. \tag{A.7}$$

Drawing the distinction between these definitions is important, since they each give Henry's law constants in different units.

Appendix B

A Suitable Change of Coordinates for Numerical Solution

When solving numerically (2.23) together with (2.24)–(2.26), we employ the following coordinate transformation

$$\eta = \frac{x}{t^{1/4}}, \qquad \tau = \log(t). \tag{B.1}$$

In terms of η and τ, our problem for $h(x,t) = F(\eta,\tau)$ becomes

$$\frac{\partial F}{\partial \tau} - \frac{1}{4}\eta\frac{\partial F}{\partial \eta} + \frac{1}{3}\frac{\partial}{\partial \eta}\left(F^3\frac{\partial^3 F}{\partial \eta^3}\right) = \mathrm{e}^{\tau}\Theta(1-\mathrm{e}^{\tau/4}\eta), \tag{B.2}$$

subject to

$$\frac{\partial F}{\partial \eta} = \frac{\partial^3 F}{\partial \eta^3} = 0 \qquad \text{at} \qquad \eta = 0, \tag{B.3}$$

$$F \to \delta \qquad \text{as} \qquad \eta \to \infty, \tag{B.4}$$

$$F = \delta \qquad \text{at} \qquad \tau \to -\infty. \tag{B.5}$$

If we discretise this problem using an implicit linear Euler scheme and a sufficiently small time step, then our time domain for τ is much smaller than that for t due to the exponential nature of the transformation in time. Enlarging the τ-domain marginally gives a large increase in the t-domain.

When solving the problem numerically, we require that the spatial step is bounded by the film height in order to ensure that the region near the capillary ripple is well resolved (Diez *et al.*, 2001). Clearly, this presents computational issues as $\delta \to 0$. We employ the transformation

$$F = \mathrm{e}^{G}, \tag{B.6}$$

and the problem for $G(\eta, \tau)$ becomes

$$\frac{\partial G}{\partial \tau} - \frac{1}{4}\eta\frac{\partial G}{\partial \eta} + \frac{\mathrm{e}^{-G}}{3}\frac{\partial}{\partial \eta}\left(\mathrm{e}^{4G}\left(\left(\frac{\partial G}{\partial \eta}\right)^3 + 3\frac{\partial G}{\partial \eta}\frac{\partial^2 G}{\partial \eta^2} + \frac{\partial^3 G}{\partial \eta^3}\right)\right) = \mathrm{e}^{\tau - G}\Theta(1 - \mathrm{e}^{\tau/4}\eta), \tag{B.7}$$

subject to

$$\frac{\partial G}{\partial \eta} = \frac{\partial^3 G}{\partial \eta^3} = 0 \qquad \text{at} \qquad \eta = 0, \tag{B.8}$$

$$G \to \log(\delta) = \Upsilon \qquad \text{as} \qquad \eta \to \infty, \tag{B.9}$$

$$G = \log(\delta) = \Upsilon \qquad \text{at} \qquad \tau \to -\infty. \tag{B.10}$$

Since $|\log(\delta)| > \delta$, the requirement on the spatial step is less restrictive in the transformed version of the problem (B.7)–(B.10) than in the original formulation (B.2)–(B.5).

Appendix C

The Case of Non-Constant Oxygen Concentration

Mathematical Model

If we allow the concentration of oxygen in the flue gas to vary, we have to explicitly track the oxygen concentration in the gas, denoted by $\hat{c}_g$, and in the liquid, denoted by $\hat{c}_l$, respectively. Skipping the details and following the analysis in Section 2.7.1, the model reads

$$\frac{\partial \hat{s}_g}{\partial \hat{t}} = D_{s_g}\left(\frac{\partial^2 \hat{s}_g}{\partial \hat{x}^2} + \frac{\partial^2 \hat{s}_g}{\partial \hat{z}^2}\right) \qquad \text{in } \hat{z} > \hat{h}(\hat{x},\hat{t}), \tag{C.1}$$

$$\frac{\partial \hat{c}_g}{\partial \hat{t}} = D_{c_g}\left(\frac{\partial^2 \hat{c}_g}{\partial \hat{x}^2} + \frac{\partial^2 \hat{c}_g}{\partial \hat{z}^2}\right) \qquad \text{in } \hat{z} > \hat{h}(\hat{x},\hat{t}), \tag{C.2}$$

$$\frac{\partial \hat{s}_l}{\partial \hat{t}} + \nabla\cdot(\hat{\boldsymbol{u}}_{\boldsymbol{l}}\hat{s}_l) = D_{s_l}\left(\frac{\partial^2 \hat{s}_l}{\partial \hat{x}^2} + \frac{\partial^2 \hat{s}_l}{\partial \hat{z}^2}\right) \qquad \text{in } \hat{z} < \hat{h}(\hat{x},\hat{t}), \tag{C.3}$$

$$\frac{\partial \hat{c}_l}{\partial \hat{t}} + \nabla\cdot(\hat{\boldsymbol{u}}_{\boldsymbol{l}}\hat{c}_l) = D_{c_l}\left(\frac{\partial^2 \hat{c}_l}{\partial \hat{x}^2} + \frac{\partial^2 \hat{c}_l}{\partial \hat{z}^2}\right) \qquad \text{in } \hat{z} < \hat{h}(\hat{x},\hat{t}), \tag{C.4}$$

where $\hat{\boldsymbol{u}}_{\boldsymbol{l}} = (\hat{u}_{l,1}, \hat{u}_{l,2})$ $\hat{u}_{l,1}$ is the liquid velocity, $\hat{h}(\hat{x},\hat{t}\,)$ is the thickness of the liquid layer, D_{s_g} and D_{c_g} are the diffusivities of sulphur dioxide and oxygen in the gas, and D_{s_l} and D_{c_l} are the corresponding diffusivities in the liquid. The boundary condition on $\hat{z} = 0$, which takes account of the sulphuric acid production due to the chemical reaction that takes place there, is modified to

$$\hat{w} = 2kV_{\mathrm{m}}\hat{s}_l^2\hat{c}_l\Theta(L_R - \hat{x}) \qquad \text{on} \qquad \hat{z} = 0, \tag{C.5}$$

where we have used a mass-action rate law with coefficients given by the stoichiometry of the reaction, i.e., for each molecule of oxygen, two molecules of sulphur dioxide

react to produce two molecules of sulphuric acid. Thus, the evolution equation for $\hat{h}$ becomes

$$\frac{\partial \hat{h}}{\partial \hat{t}} + \frac{\gamma}{3\mu}\frac{\partial}{\partial \hat{x}}\left(\hat{h}^3\frac{\partial^3 \hat{h}}{\partial \hat{x}^3}\right) = 2kV_{\mathrm{m}}\hat{s}_l^2|_{\hat{z}=0}\hat{c}_l|_{\hat{z}=0}\Theta(L_R - \hat{x}). \tag{C.6}$$

At the substrate surface, we use local conservation of mass to balance the total flux of chemical species into the reaction region with the amount being consumed by the reaction. These can be written as

$$D_{s_l}\frac{\partial \hat{s}_l}{\partial \hat{z}} - \hat{u}_{l,2}\hat{s}_l = 2k\hat{s}_l^2\hat{c}_l\Theta(L_R - \hat{x}), \quad D_{c_l}\frac{\partial \hat{c}_l}{\partial \hat{z}} - \hat{u}_{l,2}\hat{c}_l = k\hat{s}_l^2\hat{c}_l\Theta(L_R - \hat{x}) \qquad \text{at} \qquad \hat{z} = 0. \tag{C.7}$$

At the gas–liquid interface, we assume that the flux of sulphur dioxide and oxygen is conserved, and that the concentrations on either side of the interface are related via Henry's law, with constants related to the ratio of the solubility of each of the species in the gas and the liquid (see discussion in Section 1.2.4 and Appendix A). Thus, we write

$$D_{s_g}\frac{\partial \hat{s}_g}{\partial \hat{n}} = D_{s_l}\frac{\partial \hat{s}_l}{\partial \hat{n}}, \quad D_{c_g}\frac{\partial \hat{c}_g}{\partial \hat{n}} = D_{c_l}\frac{\partial \hat{c}_l}{\partial \hat{n}} \qquad \text{at} \qquad \hat{z} = \hat{h}(\hat{x}, \hat{t}), \tag{C.8}$$

$$\hat{s}_g = \beta_s\hat{s}_l, \quad \hat{c}_g = \beta_c\hat{c}_l \qquad \text{at} \qquad \hat{z} = \hat{h}(\hat{x}, \hat{t}), \tag{C.9}$$

where $\partial/\partial\hat{n}$ denotes the directional derivative in the direction of the outwards-pointing unit normal to the film profile, and β_s and β_c are Henry's law constants for sulphur dioxide and oxygen, respectively. Using the symmetry about $\hat{z} = H_f$, we have the no-flux conditions

$$\frac{\partial \hat{s}_g}{\partial \hat{z}} = \frac{\partial \hat{c}_g}{\partial \hat{z}} = 0 \qquad \text{at} \qquad \hat{z} = H_f. \tag{C.10}$$

We assume that the reaction region is symmetric about $\hat{x} = 0$, and so we also write

$$\frac{\partial \hat{s}_g}{\partial \hat{x}} = \frac{\partial \hat{c}_g}{\partial \hat{x}} = \frac{\partial \hat{s}_l}{\partial \hat{x}} = \frac{\partial \hat{c}_l}{\partial \hat{x}} = \frac{\partial \hat{h}}{\partial \hat{x}} = \frac{\partial^3 \hat{h}}{\partial \hat{x}^3} = 0 \qquad \text{at} \qquad \hat{x} = 0. \tag{C.11}$$

We assume that, away from the reaction region, the concentrations of sulphur dioxide and oxygen are given by the corresponding constant concentrations, S_0 and C_0, respectively, in the gas stream. Furthermore, we require that, away from the reaction region, the film thickness approaches that of the precursor film, h_∞. Thus, we have

$$\hat{s}_g \to S_0, \quad \hat{c}_g \to C_0, \quad \hat{s}_l \to \frac{S_0}{\beta_s}, \quad \hat{c}_l \to \frac{C_0}{\beta_c}, \quad \hat{h} \to h_\infty \qquad \text{as} \qquad \hat{x} \to \infty. \tag{C.12}$$

We use initial conditions that are consistent with the boundary conditions (C.12), so that we write

$$\hat{s}_g = S_0, \quad \hat{c}_g = C_0, \quad \hat{s}_l = \frac{S_0}{\beta_s}, \quad \hat{c}_l = \frac{C_0}{\beta_c}, \quad \hat{h} = h_\infty \qquad \text{at} \qquad \hat{t} = 0. \tag{C.13}$$

Dimensionless Model

We non-dimensionalise the model (C.1)–(C.13) using

$$\hat{x} = Lx, \quad (\hat{z}, \hat{h}) = H_f(z, h), \quad \hat{t} = (\mu L_R^4/\gamma H_f^3)t, \hat{u}_{l,1} = (kLS_0^2 V_{\mathrm{m}}/\beta_s^2 H_f)u_{l,1},$$
$$\hat{u}_{l,2} = (kS_0^2 V_{\mathrm{m}}/\beta_s^2)u_{l,2}, \quad \hat{s}_g = S_0 s_g, \quad \hat{c}_g = C_0 c_g, \quad \hat{s}_l = (S_0/\beta_s)s_l, \quad \hat{c}_l = (C_0/\beta_c)c_l. \tag{C.14}$$

The corresponding equations, and initial and boundary conditions become

$$\eta_s \tau_s \frac{\partial s_g}{\partial t} = \left(\epsilon^2 \frac{\partial^2 s_g}{\partial x^2} + \frac{\partial^2 s_g}{\partial z^2}\right) \qquad \text{in} \qquad z > h(x,t), \tag{C.15}$$

$$\eta_c \eta_l \tau_s \frac{\partial c_g}{\partial t} = \left(\epsilon^2 \frac{\partial^2 c_g}{\partial x^2} + \frac{\partial^2 c_g}{\partial z^2}\right) \qquad \text{in} \qquad z > h(x,t), \tag{C.16}$$

$$\tau_s \frac{\partial s_l}{\partial t} + \alpha_s \kappa_s \nabla \cdot (\boldsymbol{u_l} s_l) = \left(\epsilon^2 \frac{\partial^2 s_l}{\partial x^2} + \frac{\partial^2 s_l}{\partial z^2}\right) \qquad \text{in} \qquad z < h(x,t), \tag{C.17}$$

$$\eta_l \tau_s \frac{\partial c_l}{\partial t} + \alpha_s \eta_l \kappa_s \nabla \cdot (\boldsymbol{u_l} c_l) = \left(\epsilon^2 \frac{\partial^2 c_l}{\partial x^2} + \frac{\partial^2 c_l}{\partial z^2}\right) \qquad \text{in} \qquad z < h(x,t), \tag{C.18}$$

and

$$\frac{\partial h}{\partial t} + \frac{1}{3}\frac{\partial}{\partial x}\left(h^3 \frac{\partial^3 h}{\partial x^3}\right) = \frac{2\alpha_s \kappa_s}{\tau_s} s_l^2|_{z=0} c_l|_{z=0} \Theta(1-x), \tag{C.19}$$

where $\boldsymbol{u_l}$ is obtained from a similar expression to (2.162) but this time using (C.5) instead of (2.149). These equations are subject to the boundary conditions

$$\begin{aligned} \frac{\partial s_l}{\partial z} - \alpha_s \kappa_s u_{l,2} s_l &= 2\kappa_s s_l^2 c_l \Theta(1-x), \\ \frac{\partial c_l}{\partial z} - \alpha_s \eta_l \kappa_s u_{l,2} c_l &= \kappa \kappa_s s_l^2 c_l \Theta(1-x) \qquad \text{at} \qquad z = 0, \end{aligned} \tag{C.20}$$

$$\begin{aligned} \frac{\partial s_g}{\partial z} - \epsilon^2 \frac{\partial h}{\partial x}\frac{\partial s_g}{\partial x} &= \sigma_s \left(\frac{\partial s_l}{\partial z} - \epsilon^2 \frac{\partial h}{\partial x}\frac{\partial s_l}{\partial x}\right), \\ \frac{\partial c_g}{\partial z} - \epsilon^2 \frac{\partial h}{\partial x}\frac{\partial c_g}{\partial x} &= \sigma\sigma_s \left(\frac{\partial c_l}{\partial z} - \epsilon^2 \frac{\partial h}{\partial x}\frac{\partial c_l}{\partial x}\right) \qquad \text{at} \qquad z = h(x,t), \end{aligned} \tag{C.21}$$

$$s_g = s_l, \quad c_g = c_l \qquad \text{at} \qquad z = h(x,t), \tag{C.22}$$

$$\frac{\partial s_g}{\partial z} = \frac{\partial c_g}{\partial z} = 0 \qquad \text{at} \qquad z = 1, \tag{C.23}$$

$$\frac{\partial s_g}{\partial x} = \frac{\partial c_g}{\partial x} = \frac{\partial s_l}{\partial x} = \frac{\partial c_l}{\partial x} = \frac{\partial h}{\partial x} = \frac{\partial^3 h}{\partial x^3} = 0 \qquad \text{at} \qquad x = 0, \tag{C.24}$$

$$s_g \to 1, \quad c_g \to 1, \quad s_l \to 1, \quad c_l \to 1, \quad h \to \delta \qquad \text{as} \qquad x \to \infty, \tag{C.25}$$

and the initial conditions

$$s_g = 1, \quad c_g = 1, \quad s_l = 1, \quad c_l = 1, \quad h = \delta \qquad \text{at} \qquad t = 0, \tag{C.26}$$

where we have introduced 11 dimensionless parameters

$$\alpha_s = \frac{S_0 V_{\mathrm{m}}}{\beta_s} \approx 10^{-5},\ \delta = \frac{h_\infty}{H_f} \approx 2\times 10^{-3},\ \epsilon = \frac{H_f}{L_R} \approx 3\times 10^{-2},\ \eta_c = \frac{D_{c_l}}{D_{c_g}} \approx 10^{-4},$$
$$\eta_l = \frac{D_{s_l}}{D_{c_l}} \approx 1,\ \eta_s = \frac{D_{s_l}}{D_{s_g}} \approx 2\times 10^{-4},\ \kappa_s = \frac{kC_0 H_f S_0}{\beta_c \beta_s D_{s_l}} \approx 2\times 10^{-4},\ \kappa = \frac{\beta_c D_{s_l} S_0}{\beta_s C_0 D_{c_l}} \approx 5,$$
$$\sigma_s = \frac{D_{s_l}}{\beta_s D_{s_g}} \approx 5\times 10^{-3},\ \sigma = \frac{\beta_s D_{c_l} D_{s_g}}{\beta_c D_{c_g} D_{s_l}} \approx 7\times 10^{-4},\ \tau_s = \frac{\gamma H_f^5}{\mu D_{s_l} L_R^4} \approx 4\times 10^{-3}, \tag{C.27}$$

where we have used the parameter values from table 1.1.

Distinguished Limit: $\kappa_s = O(1), \alpha_s, \sigma_s, \tau_s = O(\epsilon^2)$ and Sub-Limits

We note that, had we not assumed c_g to be constant, following the same steps as in Section 2.7.3 and noting that $\sigma \ll 1$ in (C.21), the right-hand side of the equivalent equation to (2.193) for c_g would be zero. This would lead to the solution $c_g = 1$. Thus, the oxygen concentration is indeed constant in the gas. Further, provided $\kappa \ll 1$, the flux at $z = 0$ given by (C.20) will be zero, and, thus, the oxygen concentration in the liquid will also be constant, $c_l = 1$. This is the case, for example, for flue gas with a low concentration of sulphur dioxide, or where the oxygen content is large (which is often the case in real applications), so that $S_0/C_0 \ll 1$. With the quoted value in (2.170) of $\kappa = 5$, however, we cannot conclude that oxygen concentration is constant in the liquid. Nevertheless, if we follow the previous steps, integrate (2.174) and the analogous equation for c_l, and apply (C.20) and (C.22), remembering that $c_g = 1$, we find that

$$s_l^{(0)} = 2\kappa_s \mathcal{G}(x,t)^2 \mathcal{F}(x,t) z + \mathcal{G}(x,t) \qquad \text{in} \qquad 0 \le x \le 1, \tag{C.28}$$
$$c_l^{(0)} = 2\kappa\kappa_s \mathcal{G}(x,t)^2 \mathcal{F}(x,t) z + \mathcal{F}(x,t) \qquad \text{in} \qquad 0 \le x \le 1, \tag{C.29}$$

where

$$\mathcal{F}(x,t) = \frac{1}{2\kappa\kappa_s h \mathcal{G}(x,t)^2 + 1}, \tag{C.30}$$

and $\mathcal{G}(x,t)$ satisfies the following cubic equation

$$2\kappa\kappa_s h \mathcal{G}(x,t)^3 + 2\kappa_s(1 - \kappa s_g) h \mathcal{G}(x,t)^2 + \mathcal{G}(x,t) - s_g = 0. \tag{C.31}$$

The relevant equations for s_g and h are then

$$\eta_s \tilde{\tau}_s (1-h)\frac{\partial s_g}{\partial t} - \frac{\partial}{\partial x}\left((1-h)\frac{\partial s_g}{\partial x}\right) = -\frac{2\tilde{\sigma}_s \kappa_s \mathcal{G}(x,t)^2}{2\kappa\kappa_s h \mathcal{G}(x,t)^2 + 1}\Theta(1-x), \tag{C.32}$$

$$\frac{\partial h}{\partial t} + \frac{1}{3}\frac{\partial}{\partial x}\left(h^3\frac{\partial^3 h}{\partial x^3}\right) = \frac{2\tilde{\alpha}_s\kappa_s\mathcal{G}(x,t)^2}{\tilde{\tau}_s(2\kappa\kappa_s h\mathcal{G}(x,t)^2+1)}\Theta(1-x). \tag{C.33}$$

In principle, one could explicitly solve (C.31), but, due to the similar structure, we do not anticipate a qualitative difference in the solution, compared to (2.186), and for the purposes of this analysis, we assume the oxygen concentration is constant everywhere. However, we will comment on the limiting behaviour when $\kappa_s \ll 1$ and $\kappa_s \gg 1$.

In the limit $\kappa_s \to 0$, we note that, in the case of non-constant oxygen concentration in the liquid, from (C.31), we again obtain the solution $\mathcal{G}(x,t) \to s_g$ as $\kappa_s \to 0$, which leads to the same set of equations for s_g and h considered in Section 2.7.4, namely, (2.198) and (2.199).

In the limit $\kappa_s \to \infty$, we note that, in the case of non-constant oxygen concentration in the liquid, in order to obtain the correct behaviour of $\mathcal{G}(x,t)$ as $\kappa_s \to \infty$, we scale $\mathcal{G}(x,t) = \tilde{\mathcal{G}}(x,t)/\sqrt[3]{\kappa_s}$. Then, from (C.31), to leading order in $1/\sqrt[3]{\kappa_s}$, we obtain

$$\tilde{\mathcal{G}}(x,t) = \sqrt[3]{\frac{s_g}{2\kappa h}}. \tag{C.34}$$

Thus, substituting in (C.32) and (C.33) and taking the limit as $\kappa_s \to \infty$, we obtain

$$\eta_s\tilde{\tau}_s(1-h)\frac{\partial s_g}{\partial t} - \frac{\partial}{\partial x}\left((1-h)\frac{\partial s_g}{\partial x}\right) = -\frac{\tilde{\sigma}_s}{\kappa h}\Theta(1-x), \tag{C.35}$$

$$\frac{\partial h}{\partial t} + \frac{1}{3}\frac{\partial}{\partial x}\left(h^3\frac{\partial^3 h}{\partial x^3}\right) = \frac{\tilde{\alpha}_s}{\kappa\tilde{\tau}_s h}\Theta(1-x). \tag{C.36}$$

Therefore, in this case, we again obtain the thickness-inhibited injection inversely proportional to h, as in Section 2.7.4, but no dependence on the sulphur dioxide concentration in the gas.

Appendix D

Large-Sh Limit and Non-Constant Diffusivity

The large-Sherwood-number limit is not physically relevant for explaining the hygroscopy of sulphuric acid, but is useful to study for systems in which the absorption process dominates the diffusion process. When $\mathrm{Sh} \gg 1$, equation (6.13) gives

$$w|_{x=h} = 1, \tag{D.1}$$

neglecting the small terms. Unlike in Section 6.3.3, here, equilibrium happens at the interface much faster than diffusion takes place. Substituting (6.13) and (D.1) into (6.14), the problem for w and h becomes

$$\frac{\partial w}{\partial t} = \frac{\partial^2 w}{\partial x^2}, \tag{D.2}$$

$$\frac{\mathrm{d}h}{\mathrm{d}t} = \frac{\alpha_{w,\mathrm{eq}}}{1-\alpha_{w,\mathrm{eq}}} \frac{\partial w}{\partial x}\Big|_{x=h}, \tag{D.3}$$

subject to (6.15), (6.16), and (D.1).

These equations cannot be further simplified, and they have to be solved numerically. In figure D.1, we present the film thickness versus time for larger values of Sh between 1 to 100 found by numerically solving (6.12)–(6.16). We also show an asymptotic solution in the large-Sh limit, found by numerically solving the reduced problem (D.2), (D.3), with (6.15), (6.16), and (D.1). We see that there is excellent agreement between the numerical results from the full model and the asymptotically reduced problem as Sh increases. We note that the large-Sherwood-number limit corresponds to the case when water absorption dominates over diffusion, which gives rise to a sharper gradient in the film thickness for early time since water is absorbed at a faster rate than it can be transported away from the surface.

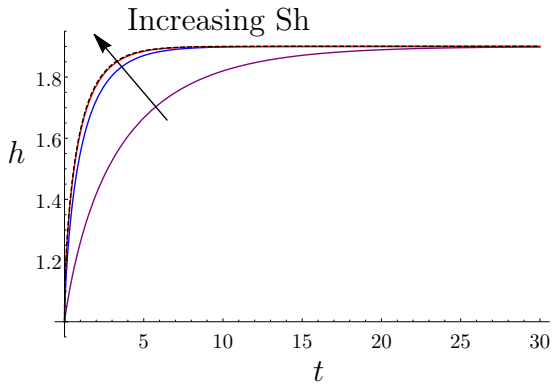

Figure D.1: Graph showing how h varies with time for various values of Sh: Sh $= 1$ (purple), 10 (blue), 100 (red), along with the solution to (D.1)–(D.3), (6.15), and (6.16) (dashed). Here, $\alpha_{w,\mathrm{eq}} = 0.5, n = 0.1$.

In figure D.2, we show how the concentration of water varies across the film for various times in the large-Sh limit. We see that it takes a long time for the concentration to become uniform. This is different from the small-Sherwood-number regime, presented in Section 6.3.3, when the concentration quickly becomes uniform, and then gradually approaches equilibrium at the interface.

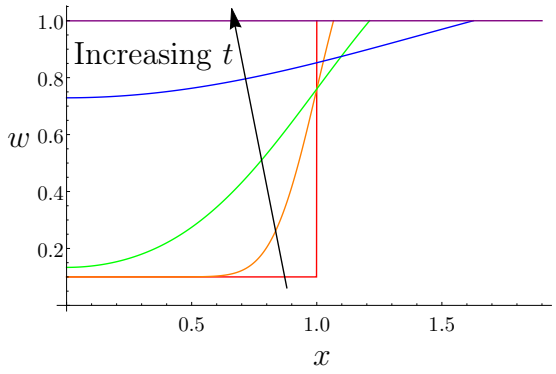

Figure D.2: Graph showing how w varies with x in the large-Sh limit for various times: $t = 0$ (red), 0.01 (orange), 0.1 (green), 1 (blue), 10 (purple). The other parameters are $\alpha_{w,\mathrm{eq}} = 0.5$, $n = 0.1$.

Finally, we consider the case in which we replace the constant diffusivity D_{w_l} in our analysis with a linear concentration-dependent diffusivity $D_{w_l}(1.15w + 0.1)$ where $n \leq w \leq 1$ in the experiments, motivated by observations of concentration-dependent diffusivity in Leaist (1984) and Umino & Newman (1993). Comparing the predicted layer growth in each case shows a negligible difference between the two (figure D.3), which indicates that assuming a constant diffusivity provides a suitable approximation to the behaviour.

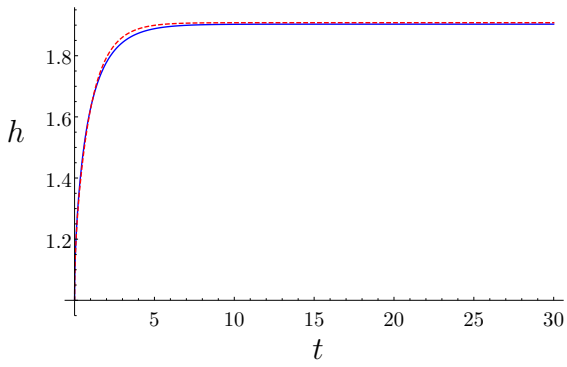

Figure D.3: Graph showing how h varies with time for $\alpha_{w,\mathrm{eq}} = 0.5$ and $n = 0.1$ for a constant diffusivity D_{w_l} (blue) and concentration-dependent diffusivity $D_{w_l}(1.15c + 0.1)$ (red dashed), where $D_{w_l} = 1.6 \times 10^{-9}\mathrm{m}^2\,\mathrm{s}^{-1}$.

Bibliography

Ajaev, V. S. (2012) *Interfacial Fluid Mechanics: A Mathematical Modelling Approach*. Springer.

Alfrey Jr., T., Gurnee, E.F. & Lloyd, W.G. (1966) Diffusion in glassy polymers. *J. Polym. Sci. C* **12** (1), pp. 249–261.

Allaire, G., Mikelić, A. & Piatnitski, A. (2010) Homogenization approach to the dispersion theory for reactive transport through porous media. *SIAM J. Math. Anal.* **42** (1), pp. 125–144.

Allaire, G. & Piatnitski, A. (2010) Homogenization of nonlinear reaction–diffusion equation with a large reaction term. *Ann. Univ. Ferrara* **56** (1), pp. 141–161.

Anderson, D. M., Angel, J., Breward, C. J. W., Dubovski, P., Duffy, D., Evans, R., Grant, Z., Janett, A., Jiang, J., Khamala, B., Liu, R., Niroobakhsh, Z., Platini, T., Sanaei, P. & Zhong, L. (2015) Flooding in porous media. *Tech. Rep*. Thirty-First Annual Workshop on Mathematical Problems in Industry.

Anderson, D. M. & Davis, H. (1995) The spreading of volatile liquid droplets on heated surfaces. *Phys. Fluids* **7** (2), pp. 248–265.

Andrade Jr., J. S., Street, D. A., Shibusa, Y., Havlin, S. & Stanley, H. E. (1997) Diffusion and reaction in percolating pore networks. *Phys. Rev. E* **55** (1), pp. 772–777.

Bear, Jacob (1979) *Hydraulics of Groundwater*. Dover Publications, Inc.

Beavers, G. S. & Joseph, D. D. (1967) Boundary conditions at a naturally permeable wall. *J. Fluid Mech.* **30** (1), pp. 19–207.

Ben-Avraham, D. (1991) Diffusion in disordered media. *Chemometr. Intell. Lab. Syst.* **10** (1-2), pp. 117–122.

Bender, C. & Orszag, S. (1999) *Advanced Mathematical Methods for Scientists and Engineers: Asymptotic Methods and Perturbation Theory*. Springer.

Benilov, E. S., Chapman, S. J., McLeod, J. B., Ockendon, J. R. & Zubkov, V. S. (2010) On liquid films on an inclined plate. *J. Fluid Mech.* **663**, pp. 53–69.

Bensoussan, A., Lions, J.-L. & Papanicolaou, G. (1978) *Asymptotic Analysis for Periodic Structures*. North-Holland.

Beuscher, U. & Venkateshwaran, V. (2019) W. L. Gore and Associates. Personal communication.

Blunt, M., King, M. J. & Scher, H. (1992) Simulation and theory of two-phase flow in porous media. *Phys. Rev. A* **46** (12), pp. 7680–7699.

Blunt, M. J. (2001) Flow in porous media – pore-network models and multiphase flow. *Curr. Opin. Colloid Interface Sci.* **6** (3), pp. 197–207.

Bonn, D., Eggers, J., Indekeu, J., Meunier, J. & Rolley, E. (2009) Wetting and spreading. *Rev. Mod. Phys.* **81** (2), pp. 739–805.

Borsi, Iacopo, Farina, A. & Fasano, A. (2004) On the infiltration of rain water through the soil with runoff of the excess water. *Nonlinear Analysis: Real World Applications* **5**, pp. 763–800.

Bourne, A., LaVia, L. C., Moeller, A., Severin, D., Fowler, D., Manar, A., Schimpf, P., Messina, A., Benner, T., Matuscak, W., Daniels, A., Brown, D. & Gonet, P. (2018) Analysis of the Illinois coal industry and electrical generation in Illinois. *Tech. Rep*. Flue Gas Desulfurization Task Force Report.

Breivik, R. A. (2020) SNOX Brochure. *Tech. Rep*. Haldor Topsoe.

Bringedal, C., Berre, I., Pop, I. S. & Radu, F. A. (2016) Upscaling of non-isothermal reactive porous media flow with changing porosity. *Transp. Porous Med.* **114**, pp. 371–393.

Bringedal, C. & Kumar, K. (2017) Effective behavior near clogging in upscaled equations for non-isothermal reactive porous media flow. *Transp. Porous Med.* **120**, pp. 553–577.

Brini, E., Fennell, C. J., Fernandez-Serra, M., Hribar-Lee, B., Lukšič, M. & Dill, K. A. (2017) How water's properties are encoded in its molecular structure and energies. *Chem. Rev.* **117** (19), pp. 12385–12414.

Brinkman, H. C. (1949) A calculation of the viscous force exerted by a flowing fluid on a dense swarm of particles. *Appl. Sci. Res.* **1** (27), pp. 27–34.

Brown, T. P., Rushton, L., Mugglestone, M. A. & Meechan, D. F. (2003) Health effects of a sulphur dioxide air pollution episode. *J. Public Health Med.* **25** (4), pp. 369–371.

Bruna, M. & Breward, C. J. W. (2014) The influence of non-polar lipids on tear film dynamics. *J. Fluid Mech.* **746**, pp. 565–605.

Bruna, M. & Chapman, S. J. (2015) Diffusion in spatially varying porous media. *SIAM J. Appl. Math.* **75** (4), pp. 1648–1674.

Campbell, E. & Edwards, D. (2015) Desulfurization of natural gas for fuel cells. *Tech. Rep*. Thirty-First Annual Workshop on Mathematical Problems in Industry.

Canuto, H. M. P., Afonso, M. R. A. & da Costa, J. M. C. (2013) Hygroscopic behavior of freeze-dried papaya pulp powder with maltodextrin. *Acta Scientiarum-Technology* **36** (1), pp. 179–185.

Cao, Q. & Nastac, L. (2019) Mathematical modelling of slag–metal reactions and desulphurization behaviour in gas-stirred ladle based on the DPM-VOF coupled model. *Ironmaking and Steelmaking* pp. 1–9.

Carlson, A., Mandre, S. & Mahadevan, L. (2015) Elastohydrodynamics of contact in adherent sheets , arXiv: 1508.06234.

Chapman, S. J. & Shabala, A. (2017) Effective transport properties of lattices. *SIAM J. Appl. Math.* **77** (5), pp. 1631–1652.

Chen, C.-T. & Tan, W.-L. (2012) Mathematical modeling, optimal design and control of an SCR reactor for NO_x removal. *J. Taiwan Inst. Chem. E.* **43** (3), pp. 409–419.

Chernyavsky, I. L., Leach, L., Dryden, I. L. & Jensen, O. E. (2011) Transport in the placenta: Homogenizing haemodynamics in a disordered medium. *Phil. Trans. Soc. A* **369** (1954), pp. 4162–4182.

Cieplak, M. & Robbins, M. O. (1990) Influence of contact angle on quasistatic fluid invasion of porous media. *Phys. Rev. B* **41**, pp. 11508–11521.

Cohen, D. S. & Erneux, T. (1988) Free boundary problems in controlled release pharmaceuticals. I: Diffusion in glassy polymers. *SIAM J. Appl. Math.* **48** (6), pp. 1451–1465.

Conca, C., Díaz, J. I., Liñán, A. & Timofte, C. (2004) Homogenization in chemical reactive flows. *Electron. J. Differ. Eq.* **2004** (40), pp. 1–22.

Cooper, L. J., Daly, K. R., Hallett, P. D., Naveed, M., Koebernick, N., Bengough, A. G., Koebernick, N., Bengough, A. G., George, T. S. & Roose, T. (2017) Fluid flow in porous media using image-based modelling to parametrize Richards' equation. *Proc. R. Soc. A* **473**, pp. 1–20.

Cox, R. G. (1986) The dynamics of the spreading of liquids on a solid surface. Part 1. Viscous flow. *J. Fluid Mech.* **168**, pp. 169–194.

Craster, R. V. & Matar, O. K. (2009) Dynamics and stability of thin liquid films. *Rev. Mod. Phys.* **81**, pp. 1131–1198.

Dahiya, S. & Myllyvirta, L. (2019) Global SO_2 emission hotspot database. *Tech. Rep*. Greenpeace Environment Trust.

Dalwadi, M. P., Bruna, M. & Griffiths, I. M. (2016) A multiscale method to calculate filter blockage. *J. Fluid Mech.* **809**, pp. 264–289.

Dalwadi, M. P., Griffiths, I. M. & Bruna, M. (2015) Understanding how porosity gradients can make a better filter using homogenization theory. *Proc. R. Soc. A* **471**, pp. 1–20.

Dalwadi, M. P., Wang, Y., King, J. R. & Minton, N. P. (2018) Upscaling diffusion through first-order volumetric sinks: A homogenization of bacterial nutrient uptake. *SIAM J. Appl. Math.* **78** (3), pp. 1300–1329.

Daly, K. R. & Roose, T. (2015) Homogenization of two fluid flow in porous media. *Proc. R. Soc. A* **471** (2176), pp. 1–20.

Damle, A. S. (1986) Modeling of SO_2 removal in spray-dryer flue-gas desulfurization system. *Tech. Rep*. United States Environmental Protection Agency.

Davis, S. H. & Hocking, L. M. (1999) Spreading and imbibition of viscous liquid on a porous base. *Phys. Fluids* **11** (1), pp. 48–57.

Davis, S. H. & Hocking, L. M. (2000) Spreading and imbibition of viscous liquid on a porous base. II. *Phys. Fluids* **12** (7), pp. 1646–1655.

De Blasio, C., Carletti, C., Westerlund, T. & Järvinen, M. (2013) On modelling the dissolution of sedimentary rocks in acidic environments. An overview of selected mathematical methods with presentation of a case study. *J. Math. Chem.* **51** (8), pp. 2120–2143.

Delgado, J. M. P. Q., Ramos, N. M. M. & De Freitas, V. P. (2006) Can moisture buffer performance be estimated from sorption kinetics? *J. Build. Phys.* **29** (4), pp. 281–299.

Deng, B. & Wang, J. (2017) Saturated–unsaturated groundwater modeling using 3D Richards equation with a coordinate transform of nonorthogonal grids. *Appl. Math. Model.* **50**, pp. 39–52.

Diez, J. A., Kondic, L. & Bertozzi, A. (2001) Global models for moving contact lines. *Phys. Rev. E* **63**, pp. 1–13.

Duffy, B. R. & Moffatt, H. K. (1997) A similarity solution for viscous source flow on a vertical plane. *Eur. J. Appl. Math.* **8**, pp. 37–47.

Duffy, B. R. & Wilson, S. K. (1997) A third-order differential equation arising in thin-film flows and relevant to Tanner's law. *Appl. Math. Lett.* **10** (3), pp. 63–68.

Dunn, G. J., Wilson, S. K., Duffy, B. R., David, S. & Sefiane, K. (2008) A mathematical model for the evaporation of a thin sessile liquid droplet: Comparison between experiment and theory. *Colloids Surf. A* **323** (1), pp. 50–55.

Ehrhard, P. & Davis, S. H. (1991) Non-isothermal spreading of liquid drops on horizontal plates. *J. Fluid Mech.* **229**, pp. 365–388.

Farthing, M. & Ogden, F. (2017) Numerical solution of Richards' equation: A review of advances and challenges. *Soil Sci. Soc. Am. J.* **81**, pp. 1257–1269.

Fasano, A. & Mikelić, A. (2000) On the filtration through porous media with partially soluble permeable grains. *Nonlinear Differ. Equ. Appl.* **7**, pp. 91–105.

Ferrell, R. T. & Himmelblau, D. M. (1967) Diffusion coefficients of nitrogen and oxygen in water. *J. Chem. Eng. Data* **12** (1), pp. 111–115.

Fioletov, V. E., McLinden, C. A., Krotkov, N., Li, C., Joiner, J., Theys, N., Carn, S. & Moran, M. D. (2016) A global catalogue of large SO_2 sources and emissions derived from the Ozone Monitoring Instrument. *Atmos. Chem. Phys.* **16**, pp. 11497–11519.

Fraysse, N. & Homsy, G. M. (1994) An experimental study of rivulet instabilities in centrifugal spin coating of viscous Newtonian and non-Newtonian fluids. *Phys. Fluids* **6** (4), pp. 1491–1504.

Gahn, M., Neuss-Radu, M. & Knabner, P. (2016) Homogenization of reaction–diffusion processes in a two-component porous medium with nonlinear flux conditions at the interface. *SIAM J. Appl. Math.* **76** (5), pp. 1819–1843.

Gallagher, K., Darling, R., Patterson, T. & Perry, M. (2008) Capillary pressure saturation relations for PEM fuel cell gas diffusion layers. *J. Electrochem. Soc.* **155**, pp. 1225–1231.

Gaur, V., Asthana, R. & Verma, N. (2006) Removal of SO_2 by activated carbon fibers in the presence of O_2 and H_2O. *Carbon* **44**, pp. 46–60.

van Genuchten, M. (1980) A closed-form equation for predicting the hydraulic conductivity of unsaturated soils. *Soil Sci. Soc. Am. J.* **44**, pp. 892–898.

Gilding, B. (1991) Qualitative mathematical analysis of the Richards equation. *Transport Porous Med.* **6**, pp. 651–666.

Govindarao, V. M.H. & Gopalakrishna, K. V. (1993) Solubility of sulfur dioxide at low partial pressures in dilute sulfuric acid solutions. *Ind. Eng. Chem. Res.* **32** (9), pp. 2111–2117.

Govindarao, V. M. H. & Gopalakrishna, K. V. (1995) Oxidation of sulfur dioxide in aqueous suspensions of activated carbon. *Ind. Chem. Eng. Res.* **34** (7), pp. 2258–2271.

Greenewalt, C. H. (1926) Absorption of water vapor by sulfuric acid solutions. *J. Ind. Eng. Chem.* **18** (12), pp. 1291–1295.

Güthenke, A., Chatterjee, D., Weibel, M., Waldbüsser, N., Kočí, P., Marek, M. & Kubíček, M. (2007) Development and application of a model for a NO_x storage and reduction catalyst. *Chem. Eng. Sci.* **62** (18), pp. 5357–5363.

Guttikunda, S. K. & Jawahar, P. (2014) Atmospheric emissions and pollution from the coal-fired thermal power plants in India. *Atmos. Environ.* **92**, pp. 449–460.

Guzman, R. & Vasquez, D. A. (2016) Surface tension driven flow on a thin reaction front. *Eur. Phys. J. Spec. Top.* **225** (13-14), pp. 2573–2580.

Halpern, D. & Grotberg, J. B. (1992) Fluid–elastic instabilities of liquid-lined flexible tubes. *J. Fluid Mech.* **244**, pp. 615–632.

Hashemi, S. M. H., Mehrabani-Zeinabad, A., Zare, M. H. & Shirazian, S. (2019) SO_2 removal from gas streams by ammonia scrubbing: Process optimization by response surface methodology. *Chem. Eng. Technol.* **42** (1), pp. 45–52.

Hayduk, W., Asatani, H. & Lu, B. C. Y. (1988) Solubility of sulfur dioxide in aqueous sulfuric acid solutions. *J. Chem. Eng. Data* **33** (4), pp. 506–509.

Hennessy, M. G., Ferretti, G. L., Cabral, J. T. & Matar, O. K. (2017) A minimal model for solvent evaporation and absorption in thin films. *J. Colloid Interface Sci.* **488**, pp. 61–71.

Herrada, M., Martín, G. & Montanero, J. (2014) Modeling infiltration rates in a saturated/unsaturated soil under the free draining condition. *J. Hydrol.* **515**, pp. 10–15.

Hetherington, P. J. (1968) Absorption of sulphur dioxide into aqueous media: A mechanism study. PhD thesis, University of Tasmania.

Hocking, L. M. (1980) Sliding and spreading of two-dimensional drops. *Q. J. Mech. Appl. Math.* **34** (1), pp. 37–55.

Hocking, L. M. (1983) The spreading of a thin drop by gravity and capillarity. *Q. J. Mech. Appl. Maths* **36** (1), pp. 55–69.

Hocking, L. M. (1992) Rival contact-angle models and the spreading of drops. *J. Fluid Mech.* **239**, pp. 671–681.

Hornung, U. (1997) *Homogenization and Porous Media*. Springer.

House, J. E. (2013) *Inorganic Chemistry*, 2nd edn. Academic Press.

Howell, P. D. (2010) Surface-tension-driven flow on a moving curved surface. *J. Engng Maths* **45** (3), pp. 283–308.

Howell, P. D., Robinson, J. & Stone, H. A. (2013) Gravity-driven thin-film flow on a flexible substrate. *J. Fluid Mech.* **732**, pp. 190–213.

Howison, S. D. (2005) *Practical Applied Mathematics: Modelling, Analysis, Approximation*. Cambridge University Press.

Howison, S. D., Moriarty, J. A., Ockendon, J. R., Terrill, E. L. & Wilson, S. K. (1997) A mathematical model for drying paint layers. *J. Engng Maths* **32** (4), pp. 377–394.

Hsu, H. C., Hsu, Y. T., Hsich, W. L., Weng, M. C., Zhang Jian, S. T., Hsu, F. J., Chen, Y. F. & Fu, S. L. (2008) Hygroscopic swelling effect on polymeric materials and thermo-hygro- mechanical design on finger printer package. *2008 3rd International Microsystems, Packaging, Assembly and Circuits Technology Conference, IMPACT* (1), pp. 291–294.

Huh, C. & Scriven, L. E. (1971) Hydrodynamic model of steady movement of a solid/liquid/fluid contact line. *J. Colloid Interface Sci.* **35** (1), pp. 85–101.

Huppert, H. E. (1982) The propagation of two-dimensional and axisymmetric viscous gravity currents over a rigid horizontal surface. *J. Fluid Mech.* **121**, pp. 43–58.

Ishakoglu, A. & Baytas, A. F. (2005) The influence of contact angle on capillary pressure–saturation relations in a porous medium including various liquids. *Int. J. Eng. Sci.* **43** (8), pp. 744–755.

Jiang, X., Liu, Y. & Gu, M. (2011) Absorption of sulphur dioxide with sodium citrate buffer solution in a rotating packed bed. *Chinese J. Chem. Eng.* **19** (4), pp. 687–692.

Johnson, K. A. & Goody, R. S. (2011) The original michaelis constant: Translation of the 1913 michaelis–menten paper. *Biochemistry* **50** (39), pp. 8264–8269.

Joshi, B. K. & Kandpal, N. D. (2007) Volumetric and transport properties of aqueous sulphuric acid. *Phys. Chem. Liq.* **45** (4), pp. 463–470.

Kaskiala, T. (2002) Determination of oxygen solubility in aqueous sulphuric acid media. *Miner. Eng.* **15** (11), pp. 853–857.

Kiil, S., Michelsen, M. L. & Dam-Johansen, K. (1998) Experimental investigation and modeling of a wet flue gas desulfurization pilot plant. *Ind. Chem. Eng. Res.* **37** (7), pp. 2792–2806.

King, J. R. & Bowen, M. (2001) Moving boundary problems and non-uniqueness for the thin film equation. *Eur. J. Appl. Maths* **12** (3), pp. 321–356.

Kiradjiev, K. B., Breward, C. J. W. & Griffiths, I. M. (2018) Surface-tension- and injection-driven spreading of a thin viscous film. *J. Fluid Mech.* **861**, pp. 765–795.

Kiradjiev, K. B., Breward, C. J. W., Griffiths, I. M. & Schwendeman, D. W. (2020*a*) A homogenised model for a reactive filter. *SIAM J. Appl. Math.* In print.

Kiradjiev, K. B., Nikolakis, V., Beuscher, U., Venkateshwaran, V., Griffiths, I. M. & Breward, C. J. W. (2020*b*) A simple model for the hygroscopy of sulfuric acid. *Ind. Eng. Chem. Res.* **59**, pp. 4802–4808.

Kiss, A. A., Bildea, C. S. & Grievink, J. (2010) Dynamic modeling and process optimization of an industrial sulfuric acid plant. *Chem. Eng. J.* **158** (2), pp. 241–249.

Klaassen, R. (2003) Achieving flue gas desulphurization with membrane gas absorption. *Filtration and Separation* **40** (10), pp. 26–28.

Knotts, J. & Gueniou, K. (2017) A complete mercury control system. *Tech. Rep.* W. L. Gore and Associates, Inc.

Kropat, E. & Meyer-Nieberg, S. (2012) Homogenization of singularly perturbed diffusion-advection-reaction equations on periodic networks. *IFAC Proceedings Volumes* **45** (25), pp. 83–88.

Lacey, A. A. (1982) The motion with slip of a thin viscous droplet over a solid surface. *Stud. Appl. Maths* **67** (3), pp. 217–230.

Landa-Marbán, D., Bødtker, G., Kumar, K., Pop, I. S. & Radu, F. A. (2020) An upscaled model for permeable biofilm in a thin channel and tube. *Transp. Porous. Med.* **132**, pp. 83–112.

Leaist, D. G. (1984) Diffusion coefficient of aqueous sulfur dioxide at 25° C. *J. Chem. Eng. Data* **29** (3), pp. 281–282.

Lewandowska, J., Szymkiewicz, A., Burzyński, K. & Vauclin, M. (2004) Modeling of unsaturated water flow in double-porosity soils by the homogenization approach. *Adv. Water Resour.* **27**, pp. 283–296.

Lewis, W. K. & Whitman, W. G. (1924) Principles of gas absorption. *J. Ind. Eng. Chem.* **16** (12), pp. 1215–1220.

Lister, J. R. (1992) Viscous flows down an inclined pane from point and line sources. *J. Fluid Mech.* **242**, pp. 631–653.

Lister, J. R., Peng, G. G. & Neufeld, J. A. (2013) Viscous control of peeling an elastic sheet by bending and pulling. *Phys. Rev. Lett.* **111** (15), pp. 1–5.

Luckins, E., Breward, C. J. W., Griffiths, I. M. & Wilmott, Z. (2019) Homogenisation problems in reactive decontamination. *Eur. J. Appl. Math.* **31** (5), pp. 1–24.

Marinoschi, G. (2004) A free boundary problem describing the saturated-unsaturated flow in a porous medium. *Abstract and Applied Analysis* **2004**, pp. 729–755.

Martin, C., Perrard, A., Joly, J. P., Gaillard, F. & Delecroix, V. (2002) Dynamic adsorption on activated carbons of SO_2 traces in air I. Adsorption capacities. *Carbon* **40** (12), pp. 2235–2246.

Mason, D. P. & Momoniat, E. (2004) Axisymmetric spreading of a thin liquid drop with suction or blowing at the horizontal base. *Intl J. Non-Linear Mech.* **39**, pp. 1013–1026.

Massman, W. J. (1998) A review of the molecular diffusivities of H_2O, CO_2, CH_4, CO, O_3, SO_2, NH_3, N_2O, NO, and NO_2 in air, O_2 and N_2 near STP. *Atmos. Environ.* **32** (6), pp. 1111–1127.

McEwan, A. D. & Taylor, G. I. (1966) The peeling of a flexible strip attached by a viscous adhesive. *J. Fluid Mech.* **26** (1), pp. 1–15.

Meier, S. A., Peter, M. A. & Böhm, M. (2007) A two-scale modelling approach to reaction-diffusion processes in porous materials. *Comput. Mater. Sci.* **39** (1), pp. 29–34.

Meyer, C. & Hewitt, I. (2017) A continuum model for meltwater flow through compacting snow. *The Cryosphere* **11**, pp. 1–24.

Michalski, J. A. (2001) Equilibria in a limestone based FGD process: A pure system and with chloride addition. *Chem. Eng. Technol.* **24** (10), pp. 1059–1069.

Mitchell, S. L. & O'Brien, S. B. G. (2012) Asymptotic, numerical and approximate techniques for a free boundary problem arising in the diffusion of glassy polymers. *Appl. Math. Comput.* **219** (1), pp. 376–388.

Mochida, I., Kuroda, K., Kawano, S., Matsumura, Y., Yoshikawa, M., Grulke, E. & Andrews, R. (1997) Kinetic study of the continuous removal of SO_x using polyacrylonitrile-based activated carbon fibres: 2. Kinetic model. *Fuel* **76** (6), pp. 537–541.

Molins, S. & Knabner, P. (2019) Multiscale approaches in reactive transport modeling. *Rev. Mineral. Geochem.* **85** (1), pp. 27–48.

Momoniat, E. & Mason, D. P. (2007) Spreading of a thin film with suction or blowing including surface tension effects. *Intl J. Comp. Maths Appl.* **53** (2), pp. 198–208.

Momoniat, E., Ravindran, R. & Roy, S. (2010) The influence of slot injection/suction on the spreading of a thin film under gravity and surface tension. *Acta Mech.* **211** (1-2), pp. 61–71.

Münch, A., Wagner, B. & Witelski, Thomas (2005) Lubrication models with small to large slip lengths. *J. Eng. Math.* **53**, pp. 359–383.

Murphy, E. A. & Lee, W. T. (2017) Mathematical modelling of contact lens moulding. *IMA J. Appl. Maths* **82** (3), pp. 473–495.

Mussatti, D. C. (2002) EPA air pollution control cost manual. *Tech. Rep*. United States Environmental Protection Agency.

Myers, T. G. (1998) Thin films with high surface tension. *SIAM Rev.* **40** (3), pp. 441–462.

van Noorden, T. L. (2009*a*) Crystal precipitation and dissolution in a porous medium: Effective equations and numerical experiments. *Multiscale Model. Simul.* **7** (3), pp. 1220–1236.

van Noorden, T. L. (2009*b*) Crystal precipitation and dissolution in a thin strip. *Eur. J. Appl. Math.* **20**, pp. 69–91.

van Noorden, T. L., Pop, I. S., Ebigbo, A. & Helmig, R. (2010) An upscaled model for biofilm growth in a thin strip. *Water Resour. Res.* **46** (W06505), pp. 1–14.

O'Carroll, D. M., Mumford, K. G., Abriola, L. M. & Gerhard, J. I. (2010) Influence of wettability variations on dynamic effects in capillary pressure. *Water. Resour. Res.* **46** (1–13).

Oliver, J. M., Whiteley, J. P., Saxton, M. A., Vella, D., Zubkov, V. S. & King, J. R. (2015) On contact-line dynamics with mass transfer. *Eur. J. Appl. Maths* **26** (5), pp. 671–719.

Oron, Alexander, Davis, Stephen H. & Bankoff, S. George (1997) Long-scale evolution of thin liquid films. *Rev. Mod. Phys.* **69** (3), pp. 931–980.

Osaka, Y., Kito, T., Kobayashi, N., Kurahara, S., Huang, H., Yuan, H. & He, Z. (2015) Removal of sulfur dioxide from diesel exhaust gases by using dry desulfurization MnO_2 filter. *Sep. Purif. Technol.* **150**, pp. 80–85.

Perry, R. H. & Green, D. W. (1997) *Perry's Chemical Engineers' Handbook*. McGraw-Hill.

Peschen, N. (2002) Conversion of a wet-process flue-gas desulfurization plant from quicklime (CaO) to chalk ($CaCO_3$). *Chem. Eng. Technol.* **25** (9), pp. 896–898.

Peszynska, M., Trykozko, A., Iltis, G. & Schlueter, S. (2016) Biofilm growth in porous media: Experiments, computational modeling at the porescale, and upscaling. *Adv. Water Resour.* **95**, pp. 288–301.

Peter, M. A. & Böhm, M. (2009) Multiscale modelling of chemical degradation mechanisms in porous media with evolving microstructure. *Multiscale Model. Sim.* **7** (4), pp. 1643–1668.

Poullikkas, A. (2015) Review of design, operating, and financial considerations in flue gas desulfurization systems. *Energy Technology & Policy* **2**, pp. 92–103.

Qi, Z. & Cussler, E. L. (1985) Microporous hollow fibers for gas absorption: I. Mass transfer in the liquid. *J. Membrane Sci.* **23**, pp. 321–332.

Rattigan, O. V., Boniface, J., Swartz, E. & Davidovits, P. (2000) Uptake of gas-phase SO_2 in aqueous sulfuric acid: Oxidation by H_2O_2, O_3, and HONO. *J. Geophys. Res.* **105** (D23), pp. 29065–29078.

Ray, N., Elbinger, T. & Knabner, P. (2015) Upscaling the flow and transport in an evolving porous medium with general interaction potentials. *SIAM J. Appl. Math.* **75** (5), pp. 2170–2192.

Ray, N. & Schulz, R. (2019) Derivation of an effective dispersion model for electro-osmoticflow involving free boundaries in a thin strip. *J. Eng. Math.* **119**, pp. 167–197.

Rhodes, F. H. & Barbour, C. B. (1923) The viscosities of mixtures of sulfuric acid and water. *Ind. Eng. Chem.* **15** (8), pp. 850–852.

Richards, L. A. (1931) Capillary conduction of liquids through porous mediums. *Physics* **1** (5), pp. 318–333.

Rohling, J., Shen, J., Wang, C., Zhou, J. & Gu, C. (2007) Determination of binary diffusion coefficients of gases using photothermal deflection technique. *Appl. Phys. B: Lasers Opt.* **87**, pp. 355–362.

Sahimi, M., Gavalas, G. R. & Tsotsis, T. T. (1990) Statistical and continuum models of fluid–solid reactions in porous media. *Chem. Eng. Sci.* **45** (6), pp. 1443–1502.

Sanaei, P. & Ciocanel, V. (2016) On characterizing and simulating porous media. *Tech. Rep*. Thirty-Second Annual Workshop on Mathematical Problems in Industry.

Sander, R. (2015) Compilation of Henry's law constants (version 4.0) for water as solvent. *Atmos. Chem. Phys.* **15**, pp. 4399–4981.

Sander, U. H. F., Fischer, H., Rothe, U. & Kola, R. (1984) *Sulphur, Sulphur Dioxide and Sulphuric Acid: An Introduction to Their Industrial Chemistry and Technology*. London, The British Sulphur Corporation.

Saracco, G. & Specchia, V. (1995) Catalytic ceramic filters for flue gas cleaning. 2. Catalytic performance and modeling thereof. *Ind. Eng. Chem. Res.* **34** (4), pp. 1480–1487.

Sardar, A. & Roy, P. (2015) SO_2 emission control and finding a way out to produce sulphuric acid from industrial SO_2 emission. *J. Chem. Eng. Process Tech.* **6** (2), pp. 1–7.

Savva, N. & Kalliadasis, S. (2009) Two-dimensional droplet spreading over topographical substrates. *Phys. Fluids* **21** (9), pp. 1–12.

Savva, N. & Kalliadasis, S. (2011) Dynamics of moving contact lines: A comparison between slip and precursor film models. *EPL* **94** (6), pp. 1–6.

Savva, N. & Kalliadasis, S. (2013) Droplet motion on inclined heterogeneous substrates. *J. Fluid Mech.* **725**, pp. 462–491.

Saxton, M. A., Vella, D., Whiteley, J. P. & Oliver, J. M. (2017) Kinetic effects regularize the mass-flux singularity at the contact line of a thin evaporating drop. *J. Engng Maths* **106** (1), pp. 47–73.

Saxton, M. A., Whiteley, J. P., Vella, D. & Oliver, J. M. (2016) On thin evaporating drops: When is the d2-law valid? *J. Fluid Mech.* **792**, pp. 134–167.

Schofield, F., Wray, A., Pritchard, D. & Wilson, S. (2020) The shielding effect extends the lifetimes of two-dimensional sessile droplets. *J. Eng. Math.* **120**, pp. 89–110.

Schulz, R. & Knabner, P. (2017) Derivation and analysis of an effective model for biofilm growth in evolving porous media. *Math. Meth. Appl. Sci.* **40**, pp. 2930–2948.

Schwartz, L. W. & Michaelides, L. E. (1988) Gravity flow of a viscous liquid down a slope with injection. *Phys. Fluids* **31** (1988), pp. 397–399.

Sibley, D. N., Nold, A., Savva, N. & Kalliadasis, S. (2015) A comparison of slip, disjoining pressure, and interface formation models for contact line motion through asymptotic analysis of thin two-dimensional droplet spreading. *J. Engng Maths* **94** (1), pp. 19–41.

Sippola, H. & Taskinen, P. (2014) Thermodynamic properties of aqueous sulfuric acid. *J. Chem. Eng. Data* **59** (8), pp. 2389–2407.

Slodička, M. (1997) Mathematical treatment of point sources in a flow through porous media governed by Darcy's law. *Transport Porous Med.* **28**, pp. 51–67.

Smith, A., Keane, A., Dumesic, J. A., Huber, G. W. & Zavala, V. M. (2020) A machine learning framework for the analysis and prediction of catalytic activity from experimental data. *Appl. Catal. B* **263**, pp. 1–12.

Smith, P. C. (1973) A similarity solution for slow viscous flow down an inclined plane. *J. Fluid Mech.* **58** (2), pp. 275–288.

Suggitt, R. M., Aziz, P. M. & Wetmore, F. E. W. (1949) The surface tension of aqueous sulfuric acid solutions at 25°. *J. Am. Chem. Soc.* **71** (2), pp. 676–678.

Sweijen, T., van Duijn, C. J. & Hassanizadeh, S. M. (2017) A model for diffusion of water into a swelling particle with a free boundary: Application to a super absorbent polymer particle. *Chem. Eng. Sci.* **172**, pp. 407–413.

Tanner, L. H. (1979) The spreading of silicone oil drops on horizontal surfaces. *J. Phys. D: Appl. Phys.* **12**, pp. 1473–1484.

Thompson, A. B., Tseluiko, D. & Papageorgiou, D. T. (2015) Falling liquid films with blowing and suction. *J. Fluid Mech.* **787**, pp. 292–330.

Tuck, E. O. & Schwartz, L. W. (1990) A numerical and asymptotic study of some third-order ordinary differential equations relevant to draining and coating flows. *SIAM Rev.* **32** (3), pp. 453–469.

Umino, S. & Newman, J. (1993) Diffusion of sulfuric acid in concentrated solutions. *J. Electrochem. Soc.* **140** (8), pp. 2217–2221.

Valdés-Parada, F. J., Lasseux, D. & Whitaker, S. (2017) Diffusion and heterogeneous reaction in porous media: The macroscale model revisited. *Int. J. Chem. React. eng.* **15** (6), pp. 1–24.

Vizhemehr, A. K. (2014) Predicting the performance of activated carbon filters at low concentrations using accelerated test data. PhD thesis, Concordia University.

Voinov, O. V. (1976) Hydrodynamics of wetting. *Fluid Dynamics* **11** (5), pp. 714–721.

Weill, S., Mouche, E. & Patin, J. (2009) A generalized Richards equation for surface/subsurface flow modelling. *J. Hydrol.* **366** (1), pp. 9–20.

Wein, F., Chen, N., Iqbal, N., Stingl, M. & Avila, M. (2019) Topology optimization of unsaturated flows in multi-material porous media: Application to a simple diaper model. *Commun. Nonlinear Sci. Numer. Simul.* **78**, pp. 1–16.

Wever, N., Fierz, C., Mitterer, C., Hirashima, H. & Lehning, M. (2014) Solving Richards equation for snow improves snowpack meltwater runoff estimations in detailed multi-layer snowpack model. *The Cryosphere* **8** (1), pp. 257–274.

Wilmott, Z. (2018) Multiscale modelling of the action of low salinity. PhD thesis, University of Oxford.

Wilson, R. E. (1921) Humidity control by means of sulfuric acid solutions, with critical compilation of vapor pressure data. *J. Ind. Eng. Chem.* **13** (4), pp. 326–331.

Wilson, S. D. R. (1982) The drag-out problem in film coating theory. *J. Engng Maths* **16** (3), pp. 209–221.

Wilson, S. K., Hunt, R. & Duffy, B. R. (2000) The rate of spreading in spin coating. *J. Fluid Mech.* **413**, pp. 65–88.

Wray, A. W., Duffy, B. R. & Wilson, S. K. (2020) Competitive evaporation of multiple sessile droplets. *J. Fluid Mech.* **884**, pp. A45 1–19.

Xiong, Q., Baychev, T. G. & Jivkov, A. P. (2016) Review of pore network modelling of porous media: Experimental characterisations, network constructions and applications to reactive transport. *J. Contam. Hydrol.* **192**, pp. 101–117.

Yatim, Y. M., Duffy, B. R. & Wilson, S. K. (2012) Similarity solutions for unsteady shear-stress-driven flow of Newtonian and power-law fluids: Slender rivulets and dry patches. *J. Engng Maths* **73** (1), pp. 53–69.

Yatim, Y. M., Duffy, B. R. & Wilson, S. K. (2013) Travelling-wave similarity solutions for a steadily translating slender dry patch in a thin fluid film. *Phys. Fluids* **25** (5), pp. 1–43.

Yatim, Y. M., Wilson, S. K. & Duffy, B. R. (2010) Unsteady gravity-driven slender rivulets of a power-law fluid. *J. Nonnewton Fluid Mech.* **165** (21-22), pp. 1423–1430.

Young, T. F. & Grinstead, S. R. (1949) The surface tensions of aqueous sulfuric acid solutions. *Ann. NY Acad. Sci.* **51** (4), pp. 765–780.

Zeng, J., Zha, Y. & Yang, J. (2018) Switching the Richards' equation for modeling soil water movement under unfavorable conditions. *J. Hydrol.* **563**, pp. 942–949.

Zhang, Q., Wang, H., Dalla Lana, I. G. & Chuang, K. T. (1998) Solubility of sulfur dioxide in sulfuric acid of high concentration. *Ind. Eng. Chem. Res.* **37** (3), pp. 1167–1172.

Zheng, Z., Fontelos, M. A., Shin, S., Dallaston, M. C., Tseluiko, D., Kalliadasis, S. & Stone, H. A. (2018) Healing capillary films. *J. Fluid Mech.* **838**, pp. 404–434.

Zheng, Z., Griffiths, I. M. & Stone, H. A. (2015) Propagation of a viscous thin film over an elastic membrane. *J. Fluid Mech.* **784**, pp. 443–464.

Zhou, J., Tee, T. Y., Zhang, X. & Luan, J. E. (2006) Characterization and modeling of hygroscopic swelling and its impact on failures of a flip chip package with no-flow underfill. *Proceedings of the 2005 7th Electronics Packaging Technology Conference* **2**, pp. 561–568.

Zurmühl, T. & Durner, W. (1996) Modeling transient water and solute transport in a biporous soil. *Water Resour. Res.* **32** (4), pp. 819–829.